



The role of microstructure in the temper embrittlement of low alloy steels.

DE SOUZA BOTT, Ivani.

Available from the Sheffield Hallam University Research Archive (SHURA) at:

<http://shura.shu.ac.uk/19544/>

A Sheffield Hallam University thesis

This thesis is protected by copyright which belongs to the author.

The content must not be changed in any way or sold commercially in any format or medium without the formal permission of the author.

When referring to this work, full bibliographic details including the author, title, awarding institution and date of the thesis must be given.

Please visit <http://shura.shu.ac.uk/19544/> and <http://shura.shu.ac.uk/information.html> for further details about copyright and re-use permissions.

SHEFFIELD S1 1WB

100215417 0

TELEPEN



Sheffield City Polytechnic Library

REFERENCE ONLY

ProQuest Number: 10694425

All rights reserved

INFORMATION TO ALL USERS

The quality of this reproduction is dependent upon the quality of the copy submitted.

In the unlikely event that the author did not send a complete manuscript and there are missing pages, these will be noted. Also, if material had to be removed, a note will indicate the deletion.



ProQuest 10694425

Published by ProQuest LLC (2017). Copyright of the Dissertation is held by the Author.

All rights reserved.

This work is protected against unauthorized copying under Title 17, United States Code
Microform Edition © ProQuest LLC.

ProQuest LLC.
789 East Eisenhower Parkway
P.O. Box 1346
Ann Arbor, MI 48106 – 1346

**THE ROLE OF MICROSTRUCTURE IN THE
TEMPER EMBRITTLEMENT OF LOW ALLOY STEELS**

by

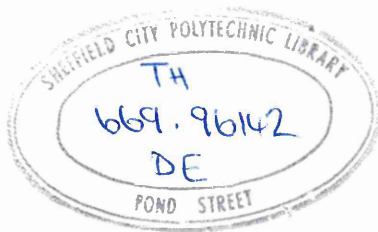
Ivani de Souza Bott, BSc, MSc

**A thesis submitted to the Council for National Academic
Awards in partial fulfilment of the requirements for the
degree of Doctor of Philosophy**

**Sponsoring Establishment: Department of Metals and Materials
 Engineering of Sheffield City
 Polytechnic**

**Collaborating Establishment: United Kingdom Atomic Energy Authority
 - Harwell**

May 1987



THE ROLE OF MICROSTRUCTURE IN THE TEMPER EMBRITTLEMENT OF LOW ALLOY STEELS

Ivani de Souza Bott

ABSTRACT

A detailed investigation has been carried out to study the effects of heat treatment on the susceptibility to temper embrittlement (Ductile-Brittle transition temperature and low energy fracture characteristics) of eleven experimental steels.

These experimental alloys represented a range of compositions related to engineering steels and corresponded to a nominal composition of 0.34 mass%C with alloying additions of Cr, Ni and Mo in varying combinations. These alloys were doped with P and Sb to study the effect of these additions on the susceptibility to temper embrittlement. These steels were investigated in the pearlitic, bainitic and tempered martensitic conditions to establish the role of microstructure.

Heat-treated alloys were characterised by fracture studies including Izod impact testing and subsequent electron microscopy.

Simultaneous Auger electron spectroscopy and energy dispersive X-ray analysis coupled with Secondary Ion Mass Spectrometry were used to study the fracture surfaces and bulk compositions of the embrittled structures.

It has been established that intergranular embrittlement in a quenched and tempered martensite microstructure was associated with the presence of P, whereas the initial intergranular embrittlement in a bainitic microstructure was associated with the segregation of Sb. It is suggested that the lower C activity produced in tempered martensite structures allows P migration to the grain boundaries causing intergranular embrittlement which was attributed to the development of M_7C_3 .

Alloys in isothermally transformed bainitic condition showed that the predominant carbide precipitate was M_3C which increased the C activity at the prior austenite grain boundaries with a resultant decrease in P concentration and consequently an absence of intergranular failure in the early stages of embrittlement. The increased C activity continued to prevent appreciable P segregation but was not sufficient to inhibit the co-segregation of Ni and Sb after extended ageing times when the bainitic alloys began to fail by intergranular fracture. After prolonged ageing increased Ni and Sb concentrations at the grain boundaries were associated with the formation of a fine grain boundary precipitate which was low in Cr. The tendency to fail by the low energy intergranular mode of failure was always greater in the tempered martensites, even when the bainites were significantly harder.

CONTENTS

CHAPTER 1	LITERATURE REVIEW	1
1.1	Introduction	1
1.2	Definition of Temper Embrittlement	3
1.3	On Temper Embrittlement, A General View	4
1.4	On Segregation	12
1.5	The Role of Microstructure in Temper Embrittlement	21
	The Role of Carbides	22
1.6	The Role of Transformed Structures	26
1.7	On Carbide Formation	28
CHAPTER 2	EXPERIMENTAL PROCEDURES	43
2.1	Manufacture of Alloys	43
2.2	Processing	43
2.3	Heat Treatments	44
2.4	Metallography	45
2.5	Mechanical Testing	45
2.5.1	Izod Impact Testing	45
2.5.2	Hardness Testing	46
2.6	Electron Microscopy	47
2.6.1	Scanning Electron Microscopy	47
2.6.2	Transmission Electron Microscopy	47
	Thin Foil Technique	48
	Replica Technique	48

2.7	Analytical Techniques	49
2.7.1	X-ray diffractometry	49
2.7.2	Surface Analysis	51
2.7.2(a)	Auger Electron Spectroscopy	51
2.7.2(b)	Secondary Ion Mass Spectroscopy (SIMS)	55
	The Physical Basis of the SIMS Process	57
	Ion Source	57
	The Mass Filter Quadrupole	59
	The Ion Detector	60
	Scanning SIMS and Depth Profiling	61
CHAPTER 3	EXPERIMENTAL RESULTS	62
	Criteria Applied to the Analysis of the Fracture Results	62
3.1	Impact Testing and Microstructural Assessment	62
3.1.1	Alloys 1 and 2 (1 mass% Cr, 3 mass% Ni; Effect of Sb)	64
	Heat Treatment A	64
	Heat Treatment B	65
	Heat Treatment C	67
	Heat Treatment D	68
3.1.2	Alloys 1 and 3 (1 mass% Cr, 3 mass% Ni 600 ppm Sb; Effect of 1 mass% Mo)	69
	Heat Treatment A	69
	Heat Treatment B	69
	Heat Treatment C	70
	Heat Treatment D	71

3.1.3	Alloys 4 and 5 (0.06 mass% Cr, 3.5 mass% Ni; Effect of Sb)	71
	Heat Treatment B	71
	Heat Treatment D	72
3.1.4	Alloys 6 and 7 (0.08 mass% Cr, 3.5 mass% Ni 600 ppm Sb; 1 mass% Mo)	72
	Heat Treatment B	73
	Heat Treatment D	73
3.1.5	Alloys 8 and 9 (0.08 mass% Cr, 0.004 mass% Ni, 4 mass% Mo) Effect of 600 ppm Sb and 60 ppm P	73
	Heat Treatment B	74
	Heat Treatment D	74
3.1.6	Alloys 10 and 11 (5 mass% Ni, 1 mass% Mo, 600 ppm Sb) Effect of Sb	75
	Heat Treatment B	75
	Heat Treatment D	76
3.2	Surface Analysis	77
3.2.1	Auger Electron Spectroscopy (AES)	77
3.2.2	Scanning Auger Microscopy (SAM)	77
3.2.3	Secondary Ion Mass Spectroscopy (SIMS)	78
	Alloy 1 (1 mass% Cr, 3 mass% Ni and 500 ppm Sb) - Heat Treatment A	79
	Alloy 1 - Heat Treatment B	81
	Alloy 7 (0.08 mass% Cr, 3.5 mass% Ni, 1 mass% Mo and 590 ppm of Sb) - Heat Treatment B	82
	Alloy 9 (0.004 mass% Ni, 4 mass% Mo and 600 ppm of Sb) As-quenched	83

CHAPTER 4	DISCUSSION	84
4.	Introduction	84
4.1	Assessment of the fracture mode	85
4.2	Criteria for the assessment of the Transition Temperature	92
4.3	Effect of Variation in Composition on Temper Embrittlement	94
4.3.1	The role of Molybdenum	95
4.3.2	Role of Nickel	97
4.3.2.1	The Cleavage-Ductile Transition	97
4.3.2.1(a)	The Effect of Mo Additions	97
4.3.2.2	The Reduction of Upper Shelf Energy	99
4.3.2.2(a)	The Effect of Mo Addition with and without Sb	99
4.3.2.3	Temper Embrittlement	101
4.3.2.3(a)	Effect of Sb addition	101
4.3.2.3(b)	Effect of Mo addition	103
4.3.2.3(c)	Effect of Mo addition in the presence of Sb	107
4.3.3	The role of nickel and chromium	111
4.3.3.1	Cleavage-Ductile Transition	111
4.3.3.1(a)	The base composition	111
4.3.3.1(b)	Effect of Sb addition in presence of Mo	112
4.3.3.2	Reduction of the Upper Shelf Energy	113
4.3.3.2(a)	Effect of Sb addition	113
4.3.3.3	Temper Embrittlement	114
4.3.3.3(a)	The base composition	114
4.3.3.3(b)	Effect of Sb addition	117
4.3.3.3(c)	Effect of Sb in presence of Mo	118

4.3.4	The role of microstructure	120
4.3.4.1	Carbide transformation in the quenched and tempered martensitic condition	120
4.3.4.2	Carbide transformation in the isothermally transformed upper bainitic condition	125
4.3.4.3	Microstructural Characteristics of Upper and Lower Bainite	127
4.4	Overview of Compositional Effects	129
CONCLUSIONS		131
REFERENCES		
TABLES		
FIGURES		

PREFACE

This thesis is submitted in part fulfilment of the requirements for the Degree of Doctor of Philosophy of the Council for National Academic Awards. The research described was carried out during the period from June 1981 to June 1986 in the Department of Metals and Materials Engineering (formerly Department of Metallurgy) at the Sheffield City Polytechnic. No part of this dissertation has been submitted for a degree at any other University or College.

Three papers have been published concerning certain aspects of the studies, the most recent being addended in the thesis:

"Simultaneous Analysis of Fracture Surfaces by Auger and Energy dispersive X-ray Mapping". Surface and Interface Analysis, Vol.9, p157-161. J. Wiley & Sons, Ltd. 1986.

Other papers are referred to in the references.

CHAPTER 1

LITERATURE REVIEW

1.1 Introduction

Material failure occurring along any interface or simple path without any considerable deformation and yielding may be termed brittle failure.

Modern electron microscopy and surface analytical techniques demonstrate that fracture can occur precisely along the grain boundary plane and across the bonds formed between the segregated impurity and matrix atoms.

The segregation levels of some impurities can now be directly related to the material and its thermo-mechanical history. The problem remains to relate fracture properties to the chemical state of the grain boundaries^[1].

In fatigue^[2] hydrogen embrittlement,^[3] stress corrosion cracking^[4, 5] and embrittlement in a liquid metal environment^[6] the fractures are also associated with the precise atomic structure of the grain boundary, but they occur according to different atomic mechanisms and so in each case, a different atomic property of the segregant is involved and a different effective segregant hierarchy is found.

Intergranular failure is also found at high temperatures, in such phenomena as overheating and hot shortness^[7] and also in the hot ductility trough problem^[8]. Some failures at high temperature are associated with the grain boundary but not with de-bonding along the precise atomic plane of segregation. In this category we find stress relief cracking^[9] and creep embrittlement^[10]

of low alloy steels. These failures occur by the formation of cavities along grain boundaries at high temperature. The cavities are thought to be nucleated on grain boundary precipitates, such as MnS and grow by vacancy supply from the grain boundary to reduce the overall strain energy.

In particular, with regard to temper embrittlement [11, 12, 13] and low temperature intergranular fracture [14], failing by impact (or tensile forces) at temperatures below 200°C and in non-aggressive or inert environments, the grain boundary chemistry may play a decisive role.

The common factor among the above intergranular failure modes is the chemical state of the grain boundary and hence the material composition.

* Carbide transformations and the precipitation of other phases can strongly influence grain boundary segregation and thus the susceptibility to temper embrittlement.

Carbide precipitation processes also influence bulk strength, which again will have an effect on the susceptibility to temper embrittlement.

To understand the factors which can influence the temper embrittlement (TE) behaviour of steel it is necessary to characterise the microstructural changes as well as mechanical properties and grain boundary segregation phenomena.*

The emphasis of the present study is placed on the discussion of the role played by microstructure in controlling the susceptibility to TE through its influence

on both solute segregation and on mechanical properties.

1.2 Definition of Temper Embrittlement (TE)

Jolivet and Vidal ^[15] found that the impact test at room temperature did not determine whether a material is embrittled or not.

They established the curves that made possible the determination of a transition temperature, which is the transition from ductile to brittle fracture mode.

Embrittlement occurs if the steels are held in or slowly cooled through the temperature range of 350° to 540°C.

Reversible temper embrittlement refers to the decrease in notch toughness when heated in or slowly cooled through a critical temperature range and the subsequent increase in this property on heating to a temperature above this range. For alloy steels this temperature range is 300-600°C whereas for higher alloy steels the embrittlement range extends to higher temperature, 750°C ^[16]. The embrittlement is manifested as an increase in the ductile-brittle transition temperature (DBTT) together with a change in the low temperature fracture mode from cleavage to intergranular. On heating above the embrittlement range and rapid cooling a decrease in the DBTT is produced together with a reversion in the fracture mode from intergranular to cleavage. This type of temper embrittlement is referred to as reversible temper embrittlement (RTE). The shift in DBTT, is related to the grain boundary segregation of major alloying elements and trace impurities in Ni-Cr steels ^[16].

1.3 On Temper Embrittlement, A General View

In 1953 Woodfine ^[17] published a critical survey of the available work on temper embrittlement up to 1952.

At that time the most outstanding investigation was dated 1925 when Greaves and Jones ^[18] reported that the embrittlement could be reduced or recovered by the addition of Mo. This finding reduced the threat of temper embrittlement from the practical point of view.

By 1944 ^[15] Jolivet and Vidal pointed out that the results of room temperature impact tests were not satisfactory for studying temper-embrittlement. They had shown that in all ferritic steels the fracture energy of notched-bar impact specimens varies with the testing temperature. Temper embrittlement did not make the steel uniformly brittle at all temperatures but displaced the energy absorption transition of the curve to higher testing temperatures.

Jolivet and Vidal defined "the position of any fracture-energy/testing temperature curve by the temperature corresponding to the point of inflexion of the curve and then took the difference between the values for the specimens with and without temper-embrittlement as a measure of the amount of the embrittlement that had occurred".

In 1947 Cohen, Hurlic and Jacobson ^[19] described an etching solution capable of differentiating between a steel in the brittle condition with one in the tough condition.

This reagent consisted of picric acid and "Zephiran Chloride" dissolved in ether, and tended to reveal

selectively the embrittled grain boundary. The intensity of this etch at grain boundaries was related to the amount of embrittlement of the alloy. About the same time (1948) McLean and Northcott ^[20] described the changes in microstructures with different reagents and times of heating suggesting a tentative theory for the mechanism of temper embrittlement. The etchants used by McLean ^[20] gave similar results to that of Cohen, in particular the aqueous picric solution. McLean pointed out that a similar British-made compound to Zephiran chloride (an American trade name for a surface active agent consisting of a mixture of high-molecular alkyl-dimethyl-benzyl ammonium chlorides) CTAB (cetyl-trimethyl ammonium bromide) produced similar results.

The main attack appeared to occur along prior austenite grain boundaries although ferrite boundaries within the prior austenite grains were sometimes revealed for steels containing P ^[13].

Preece and Carter ^[21] reported that the Zephiran chloride etch indicated the presence of embrittlement only in steels which contained chromium. In 1959 Steven and Balajiva ^[22] found that the elements primarily responsible for temper-embrittlement are Sb, P, Sn and As and that Mn and Si were also effective, but to a lesser degree.

In 1968 Low et al ^[23] examined the roles of Cr and Ni together and separately, in conjunction with the four main embrittling impurities Sb, Sn, P and As. In their investigation they included carbon extraction replicas of etched and unetched intergranular fractures, as well

as thin foil techniques. They concluded that since differences between these two conditions could not be found within the current electron microscopy techniques their suggestion was that the mechanism of embrittlement involved some form of segregation.

According to McMahon's review^[13] the direct evidence for P segregation in steel dates from 1956 by Arkharov. In 1958 Inman and Tipler^[24] reported P segregation in Iron. By 1963 these same authors^[25] had made a careful assessment of the experimental and scientific work up to that time, and gave details of the wide variety of techniques then used, including interfacial energy measurements, assessment of lattice parameter changes, and internal friction data to measure the distribution of carbon in iron-carbon alloys. Since that time the subject has advanced considerably as a result of the introduction of direct surface analytical techniques which can be used to detect and measure the species present at an exposed interface.

Subsequently in 1964 Westbrook^[26] produced a review describing a phenomenon in which the levels of apparent segregation extended to distances of the order of microns across the grain boundary and also depended upon the kinetics of cooling from high temperature. He believed that the results obtained using micro-indentation hardness traverses across grain boundaries were related to the non-equilibrium type of segregation. This type of segregation arises from the kinetics of cooling from a high temperature; the mechanism of this segregation is reportedly connected with the dragging of solute

species by a flux of vacancies towards the boundary [27].

In the late 1960's the development of a range of sophisticated electron-optical techniques for surface analysis led to an increase in the understanding of the general phenomenon of interfacial segregation. These techniques were based on a number of physical processes, such as Auger electron emission, secondary ion-mass emission, X-ray photo electron emission, ion-beam scattering and field-ion emission utilizing the atom probe.

All these are complementary techniques since there is no ideal one that can satisfy all the desired experimental requirements.

Since the introduction of AES (Auger Electron Spectroscopy), considered to be the most suitable for the study of segregation phenomena, there has been a considerable accumulation of data on species that segregate both to free surfaces and grain boundaries in a variety of metals. With regard to steels which are multicomponent systems, it is already known that more than one solute type takes part in the segregation to boundaries and yet impurities that are strongly embrittling in pure iron do not necessarily embrittle steels, because of their interaction with alloy elements.

Stein et al [28], Marcus and Palmberg [29] in 1969, and Viswanathan [30] in 1971 investigated temper embrittlement through the AES technique. Marcus and Palmberg [29] found Sb to be strongly segregated at the intergranular fracture surface. Later calibration and analysis [31] led them to conclude that the Sb concentration at the

embrittled fracture surface was about 10 atomic percent.

They also obtained spectra from the partially intergranular fracture surfaces of non-embrittled samples. There was no Sb peak in these spectra, and the intensity of Ni peaks was considerably lower indicating that less Ni and almost no Sb were present at non-embrittled grain boundaries. The Cr concentration at the embrittled fracture surface was slightly smaller than the bulk concentration.

In a similar study of P-induced embrittlement of Ni-Cr steel, Viswanathan ^[30] observed significant segregation of both Ni and P at embrittled fracture surfaces. Non-embrittled samples showed the presence of some P at the fracture surface, and interestingly, de-embrittled samples appeared to have even less P at the intergranular fracture surface than non-embrittled samples.

About the same time (1968) Low, Stein and others ^[23] reported the interaction of the alloying elements Ni and Cr with the impurity elements Sb, P, Sn and As, to produce reversible temper embrittlement in a series of high-purity steels containing 0.4 mass% C and alloyed steels containing approximately 3.5 mass % Ni, 1.7 mass % Cr and 0.05 to 0.08 mass % of the particular impurity segregated.

They stated that "the amount of embrittlement which may be caused by a specific impurity depends on the specific alloying elements present". They did not detect second-phase precipitation at the grain boundaries when in the embrittled condition.

They supported McLean's mechanism for temper embrittlement, i.e. the equilibrium segregation of impurities to grain boundaries.

These facts reinforced the earlier findings of Balajiva et al [22, 32] which demonstrated that the presence of specific impurities (P, Sn, Sb, As) was a necessary prerequisite for embrittlement of such steels.

In 1974 Rellick and McMahon^[33] made a study of the cohesion of cementite-ferrite interfaces in Fe-C alloys doped with the embrittling elements Sb, Sn, As and P. Their model is in some respect an extension of the Kula and Anctil hypothesis^[34], i.e. "The expulsion of impurities from precipitate carbides causes a transient build-up of these impurities in the cementite-ferrite interface, thereby leading to easier fracture in this region". This hypothesis is applicable to (500°F) 260°C embrittlement, but it is also consistent with the phenomenology of temper embrittlement.

In Rellick and McMahon's^[33] hypothesis the solute rejection process occurs as the carbides form during tempering and/or embrittlement ageing, i.e. the solutes are swept ahead of the advancing interface.

This model states in essence that when carbides precipitate in a steel which contains solutes more soluble in ferrite than in the carbides, some of the solute will be rejected and the rest will be trapped in the carbide. The trapped solute can then diffuse out into the ferrite at a later stage if the steel is held at an elevated temperature.

Up to 1975 several important questions concerning

temper embrittlement remained unanswered. One of them was concerned with the preferential path for fracture propagation and another with the role of the alloying elements in the segregation [35].

It was thought that segregation occurred in the austenite phase prior to the embrittling treatment [36, 37]. This assumption was shown to be inaccurate by experimental evidence [38, 39] and segregation has been shown to occur in all high angle boundaries of the ferrite phase, the previous austenite grain boundaries not being a preferential site for solute segregation [40] but only a preferential path for fracture propagation.

From AES experiments it appears that embrittling impurities, e.g. Sb, P, segregate to a much smaller extent in pure iron than in alloy steels [41]. McLean [20, 42] in his pioneering theoretical work suggested that intergranular embrittlement could be due to the segregation of solute atoms to the previous austenite grain boundaries.

McLean did not take into account the interactions between the two categories of atoms, i.e. impurities and transitional elements.

Guttman [35] presented an hypothesis for equilibrium segregation of both types of solutes, taking into account the interaction between atoms of different species.

Guttman, taking into account the M-I interaction where M (alloy element) and I (impurity element), evaluated the level of segregation for a ternary solution (Fe-M-I) through an analytical treatment based on the regular solution model, he formulated two basic hypotheses. The first one is based on the "Layer Model",

in which the interface is considered as an homogeneous two-dimensional phase (ϕ) where all the thermodynamic quantities relating to the bulk (phase B) can be defined (for instance: atomic concentrations, activities and chemical potentials).

The second hypothesis took into account the behaviour of a regular solution, as opposed to McLean, who had considered only the behaviour of an ideal solution for both grains and grain boundaries. This resulted from the fact that the intergranular layer cannot be taken as an ideal solution and the interaction between atoms cannot be neglected.

The chemical interaction between the atoms present depends on their total concentration in the system ($B-\phi$) and the system takes into account the driving force for segregation, i.e. induced by a chemical reaction.

In the case of repulsive interactions between solute and solvent atoms, one element strongly segregates and repels the other one from the interface. In the case of an attractive interaction, strong segregations are also observed and both segregations enhance each other, in this case impurities elements (I) interact more with alloying elements (M), at concentration levels large enough to involve precipitation. It is emphasised by Eyre et al ^[43] that although Guttman's ternary solution model represents an important advance over proceeding binary solution models it cannot be readily applied to more complex multicomponent systems such as commercial steels.

1.4 On Segregation

Solute segregation to grain boundaries in polycrystalline solids is a phenomenon that is widely acknowledged to influence a variety of technologically important processes in these materials [11, 16].

The segregation of solute species to grain boundaries often appears to be of the equilibrium type as contrasted to non-equilibrium types of segregation that have been discussed by Aust [44] and Anthony [45].

The equilibrium type of segregation occurs because certain locations for solute atoms at grain boundaries are energetically more favourable than the normal sites for solute atoms in the solvent lattice. The attraction of a solute atom to a site at a grain boundary can be characterised in terms of the amount by which the energy of the system is lowered (ΔE) when a solute atom in the solvent lattice changes place with the solvent atom occupying that grain boundary site. This energy (ΔE) is called the "binding energy" of that solute species for that particular grain boundary site.

The binding energies of solute atoms for grain boundaries are believed to result from a variety of factors. The sites which solute atoms occupy at the grain boundaries will have co-ordination numbers and interatomic spacings that are different from the bulk lattice. In addition the physical and chemical properties of the grain boundary material are different from those of the bulk lattice.

Any of these differences may result in a decrease in potential energy for a solute atom as it segregates

to the grain boundary region.

Hondros^[45] has shown that a general correlation exists between the degree to which a solute is enriched at a grain boundary and the reciprocal of its solid solubility in a given solvent lattice. Enrichment factors (ratio of solute concentration at the grain boundaries to that in the solvent lattice) of the order of 10^3 to 10^4 are reported^[46, 47] for elements such as S, P, N, Sb and Sn dissolved in polycrystalline metals.

White and Coghlan^[48] developed a model for estimating the spectrum of binding energies. They used the approach of a dislocation model for the elastic interaction of solutes with grain boundaries based on Eshelby's calculations^[49] of the elastic binding energy between an ellipsoidal inclusion and a source of internal stress. The solute atom was treated as a misfitting sphere having elastic constants different from the matrix. The binding energy ΔE , is then the sum of two terms, ΔE_s , the size effect and ΔE_m , the modulus effect. The size interaction results from the ability of a misfitting solute atom to lower the strain energy associated with itself, as well as the strain energy of the grain boundary, by migrating to appropriately distorted regions near the grain boundary.

The modulus interaction results from the influence of a solute atom on the elastic constants of the adjacent regions. Since the elastic energy of a strained region is directly proportional to its elastic constants, solute atoms which tend to lower the elastic moduli will be attracted to highly strained regions while those that

increase the moduli will be repelled. White and Coghlan^[48] suggest that the significant contribution of the modulus effect to grain boundary solute concentration may be a possible explanation for the segregation of certain elements in solvent lattices where they appear to have relatively small misfit parameters.

Phosphorus is known to segregate strongly to grain boundaries in α iron^[50, 51] and yet its lattice parameter is reported to be unchanged by taking phosphorus into solid solution. Thus not causing any significant misfit strain.

S is also known to segregate to grain boundaries in Fe^[47, 51], Ni^[52] and several nickel base alloys. While changes in lattice parameter as a function of bulk S concentration do not appear to have been measured (probably due to the extremely low solubility of S in these alloys), the difference in atomic diameter between S and Fe or Ni does not appear to account for its strong tendency to segregate in these alloys.

This non misfit-related tendency to segregate has typically been placed in the vague category of a "chemical effect".

Stark and Marcus^[53] assumed that initially the solute concentration and not the chemical potentials are the same in the lattice and in the boundary and that segregation attains an equilibrium as a final state, equating chemical potentials in the lattice and grain boundary, they developed two models based upon a non-equilibrium thermodynamic analysis of grain boundary segregation.

In this analysis the grain boundary is viewed as

composed of a "boundary" region of homogeneous matter subjected to a surface tension (σ^B), between the boundary and the lattice there are two regions each called a "matrix-boundary interface", which is subjected to a surface tension (σ^{BM}). There are two ways to decrease a surface tension: The cohesive energy at the surface may decrease (Model 1) leaving a smaller energy barrier to separation of atoms from the interface. Secondly, the bonds may become highly directional at the surface so that the extent of bonding between the close surfaces being separated is decreased because the bonding is directed parallel to the surface leaving few electrons to bond between two surfaces (Model 2).

In the case of the second model, Stark and Marcus hypothesize that the complex bonds formed between Fe-I (As, P, Sn or Sb) and M (Mn, Ni or Cr) segregated at a grain boundary take the form of a covalent glass with its bonding electrons providing a highly directional bond parallel to the interface.

The formation of such a glassy segregate is possible since the surrounding iron lattice inhibits long range order within the boundary and since the formation of such glasses from these elements is feasible.

This model questions how the combined enrichment (due to the interaction coefficients), as discussed by Guttman [35] causes embrittlement.

The first model is based on the fact that many solutes which segregate to the grain boundary do so independently. The simultaneous segregations of S and Sn to iron grain boundaries were found to be independent of each other [47].

Considering a binary alloy they suggested that the segregation of impurity elements (e.g. Sn, S) to the grain boundary of a metal like iron, would clearly reduce the cohesive energy at the boundary. If in addition, these two solutes tend to form compounds with other solutes (alloy elements, such as Cr, Ni, Mn) the impurity elements may segregate to the boundary thus lowering the chemical potential of the alloy elements and providing a driving force for their segregation. They in turn provide a further decrease in the chemical potential of the low cohesive energy solute at the boundary giving a driving force for further segregation of the element which is decreasing the cohesive energy of the boundary.

The existence of chemical interactions of the impurities with the metallic alloying components at the grain boundaries, suggests that electrons and their bond characteristics are responsible for the embrittlement. In order to understand the reduction of metallic cohesion, a model [54, 55] based on the electronic structure of the impurities and metallic alloying components and its rearrangement after chemical interaction is suggested.

In this model there is the assumption that chemical reactions at free surfaces and grain boundaries are similar [56, 57] and that localised electron states describe these chemical reactions best [58].

More recently [59] an attempt to give a more physical basis to the mechanism of decohesion has been made. The ideas, underlying the description of chemisorption at free surfaces, were taken as a basis to describe the chemical bonding of impurities at interfaces within the

bulk. They considered two semi-infinite metal chains, each one representing a metallic grain, with one substitutional impurity atom forming a bridge in between (grain boundary). The electronic structure of impurities known to induce temper embrittlement is characterised by an incomplete valence p shell, e.g. $\text{Si}(3s^2 3p^2)$, $\text{P}(3s^2 3p^3)$, $\text{S}, (3s^2 3p^4)$. As a consequence they show a tendency to form strong covalent bonds, which are rigid and directional as opposed to metallic (isotropic and weaker) bonds. This model predicted that upon increasing strength of the impurity-metal bond, the cohesion energy corresponding to the metal-metal bond in the immediate vicinity of the impurity, decreases. This is a reflection of the fact that after forming the covalent bond with the impurity the participation of the "metallic" orbital on the bond of its neighbouring metallic atom is strongly reduced. A sophisticated calculation including electron-electron correlations, several electronic orbitals and geometrical effects was proposed. The basis of the Hamiltonian model employed was that the metal can be represented by a one-dimensional chain of atoms where a tight-binding first nearest neighbour basis of non-degenerate Wannier orbitals are used to obtain the electronic eigenfunctions.

Seah ^[14] proposed a numerical estimate of the effects of different segregated chemical species on the strength of grain boundaries. This approach is concerned with predicting the effect of the segregant on the ideal strength of the grain boundary. He suggested that in the case of low temperature fracture it be assumed that

the grain boundary separates without redistribution of the solute atoms. The pair-bonding or quasi-chemical approach gives an easy numerical evaluation of the behaviour of embrittlement, or otherwise, for the grain boundary segregation of some seventy solutes in the same number of solvent matrices.

The actual energy required to break the bonds across the grain boundary may be simply determined by counting up the number of "dangling" bonds per unit area and summing their energies.

These energies may be calculated from the sublimation enthalpies. A fair numerical estimate by this approach may be made using nearest neighbour bond terms. This theory did not take into account any bulk precipitation or changes in microstructure caused by embrittling elements.

A different theory proposed by Machlin ^[60] is based on the suggestion that decohesion is a consequence of the segregation of certain impurities to the grain boundaries where the mechanism by which these segregated impurities induce decohesion differs from case to case. He described in this way a mechanism for grain boundary decohesion in temper embrittled specimens.

The proposed grain boundary decohesion process corresponds to a metal-covalent bond transition for the bonds associated with the segregant atoms during the process of intercrystalline fracture, in which the covalent bonds formed are completely saturated by atoms belonging to only one of the two surfaces produced by

the fracture. Since it is reasonable to expect the energy associated with the bonds of the segregant atoms to decrease as stress is applied and the segregant atom moves towards its equilibrium site on a free surface, the segregated atoms at the grain boundary act to provide a positive pressure tending to separate the grains adjoining the grain boundaries and in this manner lowers the fracture strength of the grain boundaries.

This analysis is concerned with the state of bonding of the segregant atom at a grain boundary site. Machlin^[60] suggests that EXAFS studies of grain boundary fracture surfaces should reveal an average co-ordination number for the segregant at the surface that is less than that for the average surface host atom or less than that expected for the average atom of a surface of that crystal orientation. Further, the segregant - host bond lengths corresponding to surface sited segregant should be less than those corresponding to the same atoms but at grain boundary sites.

This mechanism is more consistent with the theory of the mechanics of intercrystalline crack propagation.

Jokl et al^[61] proposed for this latter mechanism the basic assumption that the bond breaking and dislocation emission at the microcrack tip are all concomitant processes.

It has been noted^[35] that the embrittling elements are often from groups IV to VI of the periodic table, and that the embrittling power of the element increases as one moves from group IV to VI in a given row of the periodic table. Therefore, impurities which are more

electronegative with respect to their transition metal hosts are stronger embrittlers.

Messmer and Briant^[62] focussed on the chemical bonding aspect of embrittlement. Their suggestion is that to understand the chemical bonding aspect of grain boundary embrittlement at its most fundamental level, it is necessary to perform fully quantum mechanical calculations which will describe the bonding at the grain boundary.

A molecular orbital cluster approach is suggested, since the chemical bonding for clusters has atomic arrangements representative of those of the grain boundary and determine changes in the bonding which occur when an embrittling element is introduced.

Messmer and Briant^[62] reported calculations for five different clusters. In three of these Fe is the host metal and in two Ni is the host.

They show that the strongly embrittling elements are indeed very electronegative with respect to the host metal and draw charge from the metal atom onto themselves. Thus, the metal-impurity bond is heteropolar. In contrast, a cohesive enhancer, such as B in Ni, does not deplete the metal atoms of charge and the impurity-metal bond is much more homopolar. Such an element will then provide additional bonding at the grain boundary while not destroying the metal-metal bonds.

More recently Viefhaus et al^[63] studied an alloy of Fe-0.064% P austenitized at 1050°C, recrystallised at 850°C and held at 500°C for ten days. They found strong P segregation and questioned whether fracture occurs

by breaking of metal-impurity bonds directly in the segregated layer or by breaking of metal-metal bonds in an adjacent layer.

They examined both fracture surfaces of the broken specimens and the concentration of P was about equally high on the corresponding fracture faces, suggesting that the value obtained can be doubled to obtain the approximate grain boundary concentration.

From observations on the behaviour of P segregated on iron during slow evaporation of Ni atoms on to the surface, they concluded that upon fracture the segregated P atoms change their place with metal atoms in order to be on the outer surface.

Further, they suggest that it is not possible to derive from the Auger spectrum after fracture whether the rupture of a grain boundary with segregated impurity atoms occurs by breaking of metal-impurity bonds or by breaking of metal-metal bonds.

1.5 The Role of Microstructure in Temper Embrittlement

A range of different microstructures may be produced in heavy section components due to differences in cooling through the section thickness. Examples are turbine rotors and pressure vessels.

It is generally concluded that tempered martensitic structures are more susceptible to temper embrittlement than tempered bainite which in turn is more susceptible than a pearlitic structure. A limited number of studies have been undertaken to clarify how these susceptibilities are correlated.

There are a large number of variables involved, including carbide composition, size, shape and distribution, phase morphologies, matrix-strength levels and initial DBTT values prior to ageing.

The Role of Carbides

Grossman ^[64] first suggested that carbides might play a role in intergranular cracking, Lement et al ^[65] who studied the microstructural changes accompanying the tempering of martensite showed that near 205°C-230°C ϵ -carbide dissolves in the low-carbon martensitic matrix and cementite begins to precipitate as elongated films at martensite boundaries, and as platelets and globular particles within the martensite.

Klinger et al ^[66] showed that irrespective of the time and temperature of tempering, the initiation of embrittlement coincided with the nucleation and growth of cementite platelets and the disappearance of ϵ -carbide.

The intergranular fracture along the prior austenite grain boundaries could not be explained by this mechanism, since the ϵ -carbide \rightarrow cementite transformation is not localised at these boundaries. One possibility was that the cracks which nucleated near the thin carbide platelets at the high-angle prior austenite grain boundaries had a better chance for propagation along the continuous path provided by these boundaries. Grossman ^[64] questioned whether these cracks were nucleated by the brittle fracture of thin cementite platelets or by the ductile rupture of the soft ferrite surrounding the carbide plates.

Until this time little had been known about the effects of alloying elements and residual impurity on this form of embrittlement. Segregation of impurity and alloying elements has been extensively studied and it is a well established fact that its occurrence can promote embrittlement, or not, to an extent which depends on the particular combination of alloying elements and impurities involved.

Segregation at grain boundaries could occur as equilibrium segregation either during tempering or austenitisation or by carbide rejection during tempering.

Briant and Banerji^[12] suggested that grain boundary segregation during tempering is unlikely, N being the only embrittling element able to diffuse at this temperature^[3, 67] while P, S and N do have sufficient mobility at the austenitising temperature for equilibrium segregation to the grain boundaries. There are also several experimental results which show this to be true. One of these is the observation of quench cracks along the prior austenite grain boundaries in martensite^[37]. It was observed that these quench cracks can be attributed to P segregation in the parent austenite^[68, 69].

To relate both carbides and impurities Kula and Anctil^[34] suggested that certain impurities which are more soluble in α -ferrite than in the carbide will be rejected after the carbide has precipitated in an elongated film or plate form. This build-up of impurities at the ferrite-carbide interface could reduce impact strength either by lowering the ferrite carbide interfacial energy or by local solid-solution strengthening,

impeding dislocation movement.

Rellick and McMahon [33] proposed that solute rejection processes during carbide formation, tempering and/or embrittlement ageing are important as solutes will be pushed along in front of the advancing interface. Their model states in essence that when carbides precipitate in a steel which contains solutes, more soluble in ferrite than in carbide, some of the solute will be rejected and the rest will be trapped in the carbide. The trapped solute can diffuse out into the ferrite at a later time if the steel is held at an elevated temperature.

When a quenched steel is tempered at successively high temperatures, precipitation and coarsening of cementite occurs above $\sim 200^{\circ}\text{C}$ and solute rejection occurs. If enough of the solute is an embrittling element, cohesion of the carbide-ferrite interface is lowered. Since precipitation and coarsening occurs more rapidly in high angle boundaries, the steel has a tendency to fracture with low toughness along these boundaries.

Kula and Anctil [34] considered that the outward diffusion of trapped impurities after carbide precipitation caused the embrittlement, whereas Rellick and McMahon's model suggested that impurities rejected during carbide precipitation should be at least equally important. The latter authors modified Kula and Anctil's model in order to account for the non-equilibrium segregation, because the embrittlement found was neither stable nor reversible. They assumed that the embrittling elements have negligible solubility in Fe_3C and that a precipitating carbide would, therefore, tend to reject

such foreign atoms, thereby causing a build-up of the element in the ferrite alongside the carbide-ferrite interface.

Edwards et al ^[16] gave some direct evidence concerning the relation between segregation behaviour and changes in microstructure. They showed that it is possible to obtain increases in embrittlement whilst matrix hardness is decreasing. They concluded that the extent of embrittlement is determined by the balance achieved between grain boundary weakening due to segregation and grain interior strength changes. Their studies were conducted on a commercial Ni-Cr steel (EN30A) and a high purity Ni-Cr steel (BE10) doped with 425 ppm of Sn. They showed that the embrittlement of both was associated with the segregation of Ni, Sn and P to the prior austenitic boundaries.

Using the shift in DBTT relative to ageing time at 500°C as a guide they identified three main phases in the embrittlement behaviour. Phase I was characterised by an increase in the DBTT to the first maximum, Phase II corresponds to the decrease in DBTT to the first minimum and Phase III corresponds to the secondary increase in DBTT, this being associated with the transformation of M_3C to Cr-rich M_7C_3 which releases P to segregate to the boundaries. This was observed even in the "pure" steel in which the bulk P concentration was only 35 ppm by mass. King and Knott ^[70] explained the ductile failure of EN30A, which consisted of fine tempered martensite, in terms of the weakening of the carbide/matrix interface by these impurity elements (P and/or Sn). It was suggested that the segregation of these impurity elements occurred during

the embrittling heat treatment. They concluded that in low-alloy steels, where the inclusions are widely separated the carbides become involved in the ductile failure mechanism, because impurity element segregation can weaken the carbide interface and so produce large reduction in the strain required to grow a fibrous crack.

1.6 The Role of Transformed Structures

The degree to which degradation of toughness occurs due to temper embrittlement can be a function of the microstructure of the steel. Microstructure can influence the segregation behaviour of impurity elements by modifying either the driving force or kinetics of segregation. The various factors that are considered important are the chemistry of the ferrite matrix, grain boundary structure, the nature of other interfaces to which partitioning of the impurities can occur, and the dislocation density [71].

It is well known that the amount, type, and composition of the carbides in steels vary with heat treatment. This means that the composition of the ferrite matrix would also vary correspondingly for a given constant bulk composition of the steel.

The solubilities as well as the diffusivities of the impurity elements in the matrix are dependent on the composition of the matrix and can thus be modified by changes in microstructure [72].

Joshi [73] has shown that the segregation of impurities and alloying elements can occur preferentially to some boundaries and not to others, presumably due to differences in boundary structure.

Othani and McMahon reported that the fracture path in temper embrittled bainitic steels follow ferrite-ferrite and ferrite-bainite boundaries, while in martensitic steels, the fracture path follows the prior austenitic boundaries^[74]. For a given tempering treatment and strength level, marked differences still exist in the carbide morphology between bainitic and martensitic steels. Viswanathan and Sherlock^[75] reported that the bainitic structure of Cr-Mo-V steel contained lenticular carbides in contrast to rounded carbides in the martensitic structure.

They assumed that the diameter of the lenticular carbides is one half that of the rounded carbides. Calculations made on this basis show that for a given total volume of carbides the carbide-ferrite interface area can be as much as 50% higher for the lenticular carbides. This means that a significantly higher proportion of impurities may segregate to the carbide-ferrite interfaces in bainite than in martensite, with a concomitantly reduced segregation to prior austenite grain boundaries. The initial DBTT and its shift on embrittlement ageing is a function of both the type of transformed structure and on the degree of tempering (as reflected by hardness). The difference in the initial DBTT's is believed to be related to different carbide sizes and shapes in the two types of microstructures (tempered martensite and bainite). The higher DBTT of the tempered bainite structures is a consequence of the larger crack nuclei assuming that cracked carbides nucleate brittle fracture.

The general trend for the susceptibility to TE to increase with increasing hardness is partly due to the

increased stresses across grain boundaries as the matrix hardens [76]. This effect will, therefore, be additive to any increased embrittlement due to segregation.

1.7 On Carbide Formation

Carbides may influence solute segregation to boundaries:

- (i) By the rejection of impurity and alloy elements into the boundaries from the carbides formed during tempering and embrittlement.
- (ii) By the type of carbide present initially and the transformation of one carbide to another during embrittlement influencing matrix composition and hence the thermodynamic driving force.
- (iii) By the carbide-matrix interface itself acting as a preferred site for trace impurities.

* When low alloy steels are quenched and tempered, the equilibrium carbide to form is cementite. The morphology of Fe_3C is dependent on its nucleation site, and three main modes of precipitation can be recognised, namely, grain boundary films, or discrete grain boundary particles, matrix-nucleated Widmanstätten laths, and twin-nucleated laths [77]. *

The predominance of any of these forms depends to a large extent on the nature of the as-quenched martensite [77, 78, 79].

In low-carbon steels where the martensite consists of packets of aligned needles, the first form

predominates [77, 79] .

In high-carbon steels, however, where the martensite consists mainly of internally twinned plates, the third form predominates [77, 78] although the Widmanstätten laths have also been observed to nucleate in twin-free regions [80] .

The occurrence of the carbide $M_7C_3 = (Cr, Fe)_7C_3$ in alloy steels has been the subject of a number of studies [81-85] . Particular interest attaches to this question whether this carbide forms in a ferrite matrix already containing cementite by in situ nucleation or from completely separate nuclei.

It has been suggested that the mode of formation does in fact depend on the relative amount of iron and chromium [83] . The subsequent replacement of M_7C_3 by another carbide $M_{23}C_6$ appears to occur by separate nucleation [86] .

Dyson and Andrews [87] studied a low-chromium steel (Cr-Mo-V) in which the iron chromium carbide M_7C_3 and the replacement of Fe_3C by M_7C_3 was suggested to occur by separate nucleation. They found that up to times of 1 hour at 500°C, the cementite remains in a Widmanstätten pattern and does not spheriodize, but at higher temperatures and longer times the cementite begins to dissolve and becomes ragged in appearance. At the same time M_7C_3 begins to precipitate and the hardness decreases. Initially, the M_7C_3 carbide was found to precipitate in the bulk of the grains.

Viswanathan and Joshi [88] investigated the effects of transformation product and strength level (or hardness) on temper embrittlement susceptibility of a Cr-Mo-V steel

doped with P and Sn. They found that even at identical strength levels, the morphology and distribution of carbides are distinctly different between tempered martensite and bainite.

Following a one hour tempering treatment at 704°C, the tempered martensite structure contains a uniform distribution of fine, rounded carbides. Carbides in tempered bainite, on the other hand, are lenticular, larger in size and non-uniform in distribution. Consequently, the size of the ferrite islands, relatively free of carbides, is much larger in bainite. Following tempering the area fraction of carbides in the matrix decreases and coarsening of the carbides at the austenite grain boundaries takes place.

After very short tempering times ($\frac{1}{4}$ hour) both bainite and martensite contain predominantly M_3C with minor amounts of M_2C . With increased tempering, the amount of M_2C in the martensitic steels increases; for martensite tempered for 70 hours the presence of large amounts of M_7C_3 type alloy carbides were also observed.

In the case of bainitic steels, increased tempering results in a progressive increase in the amount of M_2C as well as $M_{23}C_3$ type alloy carbides. The changes in the carbides are also reflected by the progressive depletion of the ferrite matrix in Mo and Cr. The depletion of the element Cr in ferrite, which is known to accentuate embrittlement due to P segregation, may cause increased segregation at high hardness levels. An opposite effect would be exerted by Mo on the other hand, in view of its retarding influence on the diffusion of P.

Viswanathan and Sherlock [76] investigated Ni-Cr-Mo-V steels, of commercial purity, heat treated to produce a tempered bainitic structure to various strength levels and then isothermally aged at 315°, 400° and 450°C for times up to 35,000 hours. They found that the carbide morphology in the grain boundaries does not change with the progress of embrittlement. Further, the morphology of carbides in the grain boundaries is the same as that in the matrix. The major difference seemed to be the higher density and larger size of the grain boundary carbides, due perhaps to earlier nucleation and faster growth (higher diffusion rates) of carbides at grain boundaries. This provides a continuous ferrite-cementite interface which, when weakened by segregation of various impurity elements, would result in preferential fracture at the grain boundaries.

The result obtained from the Cr-Mo-V steel revealed a number of features relating to the rôle played by microstructure in controlling the nucleation and growth of cleavage cracks in the unembrittled states and its possible influence on segregation and embrittlement through its link with matrix chemistry. More precisely, the differences in the initial DBTT's can be attributed to the larger carbide sizes and less uniform distribution in the tempered bainite structures.

Moreover, whereas the predominant carbide in both structures is iron rich M_3C following tempering, for short times (high hardness), these transform to $M_2C + M_7C_3$ in the martensite structure and to $M_2C + M_{23}C_6$ in the bainitic structure with increasing tempering time.

Considering Ni-Cr steels and Fe-C alloys the role played by the carbide types relating to the mechanism of temper embrittlement Ohtani et al [89] suggested that a central feature of temper embrittlement is redistribution of solute during carbide precipitation. They found that the embrittlement in Fe-C alloys could be removed by reheating for a short time above 600°C and quenching to room temperature. Subsequent heating at 480°C produced re-embrittlement of grain boundaries. This was found to be a result of precipitation of fine carbides in the ferrite grain boundaries; the carbides partially dissolved at 600°C reprecipitated at 480°C mainly at high angle grain boundaries. This latter embrittlement occurred with all the dopants studied, i.e. P, Sn, Sb, As.

The embrittlement effects were found not to be stable since they disappeared after prolonged heating in the temper embrittling range. At higher temperatures the de-embrittlement was more rapid, based on the comparison of results obtained from Ni-Cr steels with Fe-C alloys containing 0.04 mass% C.

They explained the phenomena in terms of the rejection of the impurities from grain boundary regions where the carbides formed. This rejection occurs because of the low solubility of such elements in Fe_3C . The suggestion is that the origin of the impurity build up is solute redistribution during carbide precipitation, rather than equilibrium segregation.

Rellick and McMahon [33] suggested a model assuming that the embrittling elements have negligible solubility in Fe_3C and that a precipitating carbide would, therefore,

tend to reject such foreign atoms, thereby causing a build-up of the element in the ferrite alongside the carbide-ferrite interface.

When quenched steel is tempered at successively high temperatures above $\sim 200^{\circ}\text{C}$ precipitation, coarsening of cementite and solute rejection occurs. If enough of the solute is an embrittling element, cohesion of the carbide ferrite interface is lowered. Since precipitation and coarsening occurs more rapidly in high angle grain boundaries, and since the prior austenite grain boundaries form a continuous, coarse network of high angle boundaries, the steel has a tendency to fracture with low toughness along these boundaries.

Rellick and McMahon ^[33] suggest that the formation of alloy carbides such as M_7C_3 and M_{23}C_6 would make this process more complex, if they behave differently from M_3C with respect to their solubility for various embrittling elements and to the cohesion of the carbide ferrite interface. Additionally, the alloying elements will affect not only the nature of the microstructure and hardness but also the nature of the carbides of heat treated steels, and the kinetics of dispersion of impurity elements. Ohtani and McMahon ^[74] studied a low carbon steel 0.008-0.007 mass% C, 3.5 mass% Ni and 1.7 mass% Cr doped with Sb or P. For the Sb-doped steel the microstructure which resulted from austenitization (at 1200°C), brine quenching and tempering at 650°C was a mixture of blocky ferrite and a lath type structure resembling upper bainite. After ageing at 480°C for 1,000 hours the microstructure underwent a certain amount of recovery. The fracture path followed

the boundaries of the transformed and recovered ferritic microstructure. Areas of this fracture had a very rough topography whilst others were somewhat smooth. Particles of these surfaces were identified as M_3C and $M_{23}C_6$ carbides and were presumed to have precipitated at 480°C . These grain boundaries corresponded to the blocky ferrite formed during the initial quench.

No particles at grain boundaries were reported for the P-doped alloy. McMahon et al [90] observed the process of carbide precipitation and growth in grain boundaries of Sb-doped alloys expanding the work mentioned above [74]. He found that the boundaries were initially free of precipitate but that carbide platelets formed and increased in size and number with ageing time. The early carbides tended to be M_3C and the later ones M_7C_3 and $M_{23}C_6$. No evidence of a film-like phase at grain boundaries was found but some of the grain boundary carbides appear to have another phase formed in association with them. This phase was described as having a flat, tongue-like shape which seemed to grow out into the matrix from the carbide-ferrite interface. Examples of duplex carbides were found, mixtures of M_7C_3 and $M_{23}C_6$ but these appeared different from the tongue-like phase, whose identity was not found. He suggested that the carbides which were in solution at the 675°C tempering (and recrystallization) temperature, formed in grain boundaries during ageing at 520°C (for times up to 8,400 hours) and caused an increase in the grain boundary concentration of Ni. This occurred because Ni has a low solubility in carbides and it was therefore rejected from the regions which transform to carbide.

Edwards et al [16] studied the temper embrittlement behaviour of Ni-Cr steels using a commercial low alloy steel (EN30A) and a high purity Ni-Cr steel doped with 425ppm Sn (BE10).

They studied the degree of embrittlement, relating the variation in DBTT of both steels to isothermal ageing time at 500°C, following a 1 hour temper at 650°C, indicating that the development of temper embrittlement could be subdivided into three main phases. The "phase I" extended up to tempering times of 100 hours at 500°C (following a 1 hour temper at 650°C). During this phase the transformation of the martensite to ferrite and carbides played an important role in governing the subsequent Ni segregation, which was found to be of a non-equilibrium nature.

The carbides formed in both steels after 1 hour at 650°C was Fe_3C but this transformed to a Cr rich M_7C_3 at longer tempering times.

They considered the results obtained to be consistent with that of a non-equilibrium build up of tramp and alloy elements occurring at carbide-ferrite interfaces as a result of rejection from the supersaturated solution within the carbides and diffusion to the interface, since following a temper at 650°C little further growth of carbides occurred at 500°C.

In specimens quenched from 950°C no carbides were present at the start of ageing and the carbide rejection process on subsequent ageing at 500°C is not expected to contribute significantly to the grain boundary Ni concentration. On ageing within the embrittlement regime

at 500°C, a Ni-Sn phase was observed to form [91]. The build up in grain boundary Ni concentration due to rejection from the carbide during ageing will attract Sn to the boundaries from the grain interiors in an analogous manner to that suggested by McMahon et al [90]. This phase was identified in EN30A as Ni_3Sn [91].

The "phase II" in EN30A extends from 100 to 700 hours on ageing at 500°C, following a 1 hour temper at 650°C. The carbides predominant at this stage were still M_3C type.

The time interval for "phase III" is > 700 hours. Within this stage the iron rich M_3C partially transforms to Cr-rich M_7C_3 with a continued coarsening of the Ni_3Sn .

Eyre et al [43] carried out an extensive study on the steel mentioned above. They determined the carbide population in both steels (EN30A) and Sn doped 3.3 mass%Ni-1.4mass% Cr (BE10) as a function of ageing time at 500°C after the conventional quench and temper at 650°C.

After tempering for 1 hour at 650°C the carbide population is close to 100% M_3C . Energy dispersive analysis (EDX) indicates that the composition of M varies quite widely, but it typically comprises 75mass% Fe+25mass% Cr. The M_3C transforms progressively to M_7C_3 during ageing at 500°C, reaching ~50%. The composition of M in M_7C_3 is approximately 60-70mass% Cr+30-40 mass% Fe. Thus, the change from one type of carbide to another modified the matrix composition and it is relevant to consider the effect this has on segregation.

In the EN30A steel, the grain boundary P content increased at early times when the carbides were predominantly M_3C but it underwent a secondary increase

at long times when M_7C_3 population increased and this again coincides with a secondary increase in DBTT.

At first sight, these results are surprising since the increase in M_7C_3 depletes the matrix of chromium which is predicted to increase the thermodynamic driving force for P segregation to boundaries.

The factors that may contribute to this apparent contradiction were considered [43]. Firstly, other microstructural changes are occurring at the same time as the $M_3C \rightarrow M_7C_3$ transformation. Of particular relevance is the build-up of three-dimensional Ni-Sn phases which were identified on the boundaries for ageing times of 100 hours. Secondly, there is the possibility that P has a lower solubility in M_7C_3 than in M_3C and is thus "squeezed out" into the boundary by the rejection mechanisms as the $M_3C \rightarrow M_7C_3$ transformation occurs. Thirdly, replacement of M_3C by M_7C_3 may reduce the carbon level at the boundary, which would again allow P to segregate to the vacant sites [92].

Cianelli et al [93] studied the temper embrittlement of Ni-Cr steels by Sn. The heat treatment consisted of austenization at 1100°C, water quenched and tempered at 650°C for 2 hours. The specimens were either quenched and reheated to 500°C for ageing times up to 1,000 hours or cooled at 1°C/hour to 500°C and then aged.

They found that the embrittling interaction between Sn and Ni was due to the effect of Ni lowering the solubility of Sn in α -Fe [72].

The Guttman analysis [35] suggests a rationalisation of the tendency for the Ni and Sn to segregate together

due to strong mutual attraction, and their tendency to form intermetallic compounds. This tendency is stronger between Ni and Sn than between Fe and Sn.

It was suggested that the temper embrittlement of Sn-doped Ni-Cr steels occurs by equilibrium co-segregation of Sn and Ni to grain boundaries in a manner analogous to the effects of Sb and P.

Edwards et al ^[94] using Mössbauer spectroscopy demonstrated the existence of a reversible Ni-Sn interaction by subjecting a 3 mass% Ni steel doped with Sn to a classical embrittling-de-embrittling treatment. The interaction was considered to be primarily centred at the grain boundaries and it was related to either the increased number of Ni nearest neighbours of the Sn atoms or due to a bi-dimensional compound formation of Ni_3Sn_2 or Ni_3Sn_4 .

Titchmarsh et al ^[91] reported a detailed electron microscopic analysis of the microstructures of a commercial (EN30A) Ni-Cr steel and a special laboratory made steel (BE10) having similar Ni and Cr contents, but doped specially with Sn. Both steels were oil quenched from 950°C tempered for 1 hour at 650°C and aged at 500°C for times up to 5,000 hours.

Considering the Ni-Cr steel EN30A, on ageing for 500 hours at 500°C the boundaries contained about 96% Fe_3C and 2% hexagonal M_7C_3 particles containing Fe and Cr in approximately equal amounts. In addition, about two volume percent of the particles were analysed to contain Ni and Sn. Such particles were invariably located with small clusters of particles and were apparently attached to Fe_3C particles, although frequently M_7C_3 particles were

also present in the clusters. The structure was analysed and found to be cubic with a lattice unit cell size of 0.598 ± 0.004 nm which matches a Ni_3Sn phase previously reported [95] to be stable only above 950°C . These particles contain significant amounts of Sb and Mn in addition to Sn and Ni but no P was detected, although parallel AES studies [43] have shown that P is present at the grain boundaries in significant amounts (approximately 15 at%).

On ageing for 5,000 hours at 500°C the proportion of M_7C_3 and Ni-Sn precipitates increased to 15% and 5% by volume respectively, the balance again being Fe_3C .

Clayton and Knott [96] studied the extent to which P segregates during the austenitizing cycle, in 0.3 mass% C, 2.5 mass% Ni and 1.4 mass% Cr steel. They found that segregation in the Ni-Cr steel was greater at lower austenitizing temperatures (900 – 1000°C).

They suggested that the embrittlement thoughts, at 350°C could be attributed to the formation of nucleation sites carbides in prior austenite grain boundaries which already contain segregant (P) present after austenitizing treatment. The grain-boundary P levels could be further enhanced by carbide rejection as the carbide nuclei grow.

Clark and Wirth [97, 98] worked on a 4 mass% Ni-1 mass% Cr steel analysing the microstructural and fracture data of three separate types of austenite decomposition product. For the quenched and aged materials, all treated at 425°C after initial tempering at 610°C , a fine needle like precipitate was formed on ageing at 425°C at prior austenite grain boundaries and to a lesser extent at some of the martensite lath boundaries.

For a given ageing time at 425°C the amount of fine needle like precipitate was greater for samples that had had a shorter prior temper at 610°C. The onset of precipitation was later for samples held longer at 610°C.

Prolonged ageing at 425°C had shown a gradual reduction in the amount of the fine needle like precipitate and, in some areas, its complete disappearance, which coincided with a decrease in the amount of brittle intergranular fracture and also a decrease in the DBTT.

For the isothermally transformed and aged materials, a complete transformation of the austenite to a mixture of ferrite and pearlite occurred after 12 hours at 610°C. After ageing for 8064 hours at 425°C, it was observed that no significant change had occurred in the microstructure, other than a slight growth of the carbides in the ferrite-pearlite microstructure.

They proposed that the continuous filamentary precipitate formed during the early stages of the process after a single temper of 425°C was similar to precipitate formed at the prior austenite grain boundaries after a double temper, thus providing poor cohesive strength at the prior austenite grain boundaries, giving totally brittle intergranular failure.

The globular precipitates present at prior austenite grain boundaries in the softest tempered martensite, acted as a nuclei for ductile intergranular fracture initiation. It was suggested that in the initial stages solute rejection occurred at the particle/matrix interface during tempering at the lower temperature, although there was no direct evidence to confirm this because Auger Electron Spectroscopy

did not have sufficient spatial resolution.

More recently Wirth et al ^[99] investigated a laboratory cast of vacuum melted steel (3.5 mass% Ni, 1 mass% Cr). One half of these samples were tempered for 1 hour at 600°C and aged at 430°C for up to 2 years. The other half was quenched directly to 430°C to produce bainitic structures, then aged for similar times. In the quenched and tempered martensite microstructure the grain boundary precipitation sequence was $(M_3C) \rightarrow (M_3C + M_7C_3) \rightarrow (M_3C + M_7C_3 + \text{Mn-containing G phase})$ with increasing embrittlement time.

In the embrittled isothermally transformed material the sequence was $(M_3C) \rightarrow (M_3C + \text{extremely small quantities of } M_7C_3)$.

It was suggested that, although intergranular failure was related to the observation of enhanced concentrations of Sb at grain boundaries of tempered embrittled martensite, it is clear that the initial microstructure prior to ageing at 430°C, determines the extent to which Sb can diffuse much more easily in the martensite even though the dislocation density is greater in the bainite. This indicates that the Sb is likely to be associated either with particles or atomic complexes. The levels of Sb found by EDX analysis in the M_3C particles were too small and variable to determine any consistent trends correlating composition to microstructure. However, the fact that M_7C_3 appeared much earlier in the ageing sequence of the martensitic structure is consistent with $M_3C \rightarrow M_7C_3$ reaction releasing Sb which can diffuse to boundaries.

Another possible explanation was the rejection of Ni into the grain boundaries from the M_3C particles at

these sites (formed at 600°C) during 430°C ageing. The Ni attracting the Sb to the boundaries in a manner similar to the Ni-Sn interaction described previously [91, 94] the auger analysis showed a gradual increase in Ni concentration at grain boundaries, above the matrix value, for the quenched and tempered samples. In the case of the isothermally transformed material the concentration of Ni at grain boundaries was similar to the matrix. After long-term ageing the Sb concentrations were similar in both conditions.

It is clear that the role played by the microstructure in temper embrittlement exerts a major influence on the parameters governing segregation and, more indirectly, through its effect on mechanical properties. However, much work remains to be done on this aspect. Therefore, clear connection or interaction between the mechanisms of segregation and microstructural aspect related to temper embrittlement is yet to be found.

EXPERIMENTAL PROCEDURES

2.1 Manufacture of Alloys

The alloys used in this investigation were made in a high frequency vacuum furnace as 10 kg melts and cast into cast iron moulds to produce two individual 5 kg ingots 5.5 cm x 5.5 cm x 18 cm long.

The materials used to make the alloys were Japanese electrolytic iron and carbon as graphite plus additions of Si, Al, Ni, Cr, Sb and Mo, as the spectrographically pure elements.

Alloying additions were calculated on the basis of 100% yield using a total charge weight of 10 kg. The electrolytic iron, graphite, Cr, Ni and Mo were all charged to the cold crucible prior to commencement of melting. Melting was carried out under a pressure of 200 torr of argon. On completion of melting, the furnace was evacuated to 10^{-3} torr and the melt held at this temperature for 10 minutes. The pressure was then increased to 200 torr by admission of argon and then the silicon, manganese and when appropriate, antimony added. Table I lists the chemical composition of the alloys in mass percent.

2.2 Processing

The ingot produced was then hot forged at 1250°C to 4 cm diameter round, followed by final rolling to 2 cm diameter bar. The as rolled bar was machined into Izod impact test pieces, each containing three transverse notches.

2.3 Heat Treatments

All heat treatments, austenitization, tempering and ageing were carried out in muffle furnaces.

The Izod specimens were coated with Berkatekt, a protective substance to prevent oxidation during the subsequent heat treatments.

All the specimens were austenitized at 875°C for 1 hour and then either water quenched to room temperature, quenched in a salt bath at 350°C or 430°C or transferred to another muffle furnace.

To obtain tempered martensite, after quenching to room temperature the specimens were tempered at 600°C for 1 hour and then embrittled.

The bainitic specimens were isothermally transformed after the austenitizing treatment in either a muffle furnace at 430°C or quenched in a salt bath at 430° or 350°C and then transferred to a muffle furnace for the embrittling heat treatment. To obtain pearlite the specimens were transferred from the austenitizing heat treatment to a muffle furnace at 580°C for 48 hours, and then embrittled.

The embrittling heat treatment was performed at 430°C, in a muffle furnace, for 24, 720, 2160, 8760 hours for all alloys except alloy 1 which was aged to an extent of 17,520 hours for the bainite and quenched and tempered martensite condition.

All alloys were heat treated to obtain quenched and tempered martensite and bainite microstructures except for alloys 1, 2 and 3 which were heat treated to obtain a pearlite structure as well as the bainitic and martensitic structures. Table II describes the heat

treatments applied.

2.4 Metallography

Optical microscopy proved to be insufficient due to the fine microstructure produced by the heat treatment applied, to assess this fine microstructure scanning electron microscopy (SEM) of the polished and etched samples was utilized.

The etchants used were as follows:

1. 2% Nital - 2% V/V concentrated HNO_3 in alcohol.
2. Aqueous Picric - saturated solution of picric acid in water + 5 ml HCl.
3. Ethereal Picric + CTAB - 20 g of picric acid + 100 ml of ether + 1.0 g of cetyl trimethyl ammonium bromide.

To obtain a clear outline of prior and grain boundaries double etching, for example etchant 1 followed by etchant 2, had to be applied. All the specimens were mounted in conductive bakelite to provide good electrical contact for examination under scanning electron microscopy (SEM). Standard polishing techniques down to $0.25\mu\text{m}$ diamond were used to prepare specimens for metallographic examinations. After etching the specimens were gold coated and examined by SEM.

2.5 Mechanical Testing

2.5.1 Izod Impact Testing

The impact testing was carried out on an Avery Izod

impact test machine at temperatures in the range -196 to +200°C. All the specimens were initially tested at ambient temperature and then above it and/or below as required to determine the impact transition curve, for each heat treated condition. After each fracture had been carried out examination of the fracture face using scanning electron microscopy (SEM) was undertaken. This procedure permitted the selection of the temperature for subsequent tests according to the trend followed by a specific microstructure. For instance, if the specimen had failed in a ductile mode at ambient temperature the subsequent test would be carried out at temperatures below ambient temperature regardless of the energy value obtained for the room temperature impact test. The same procedure was applied for all further tests at appropriate temperatures of testing. The examination by SEM was carried out on each specimen tested. The impact energy values obtained took into consideration two sources of error, machine reading (systematic error) ± 1 Joule and the averaging of three results giving a random error of ± 1.5 .

2.5.2 Hardness Testing

Hardness measurements were carried out using a Vickers pyramid indenter, at a load of 30 kg, on all specimens. The surface of the specimen was prepared to a 600 grit finish, hardness results were calculated by taking the average of several impressions. All sets of raw data were within ± 10 Hv₃₀, therefore an error bar for all Hv₃₀ reading of 300 will give limits of

2.6 Electron Microscopy

2.6.1 Scanning Electron Microscopy

All the fractured specimens were examined by scanning electron microscopy on a Philips PSEM 500 unit in order to elucidate the changes in fracture characteristics with varying microstructures and test temperature.

The etched specimens were gold coated (using a gold-palladium alloy) in order to produce a clear distinction of the grain boundaries. Shadowing was shown to improve the discrimination of grain boundaries..

2.6.2 Transmission Electron Microscopy

The instruments used in this investigation were a Jeol 100 CX with a side entry eucentric uniaxial tilt stage and a scanning transmission facility plus EDX analytical capability, a Philips 400T fitted with similar attachments and a dedicated scanning transmission microscope, the VGHB501.

Most of the observations have been carried out utilizing thin foil techniques and carbon replicas. The scanning transmission technique is of particular importance to the identification of the particles' chemical composition in that it allows the beam to be focussed to a small spot size compared with the usual transmission spot size. Electron diffraction (selected area and convergent beam techniques) annular dark field and normal dark field imaging were used to identify particles and phases present in a given microstructure.

Thin Foil Technique

One end of each specimen was machined into a 3mm rod. Discs of ~0.5mm in thickness were cut on a small slitting machine. These were ground on both faces using increasingly fine grades of grinding papers (240 down to 600-grit) until the thickness was reduced to about 0.08mm. A Struers unit was utilized to produce polishing, thinning and perforation of the discs in one operation. The electrolyte used was 10 or 6% V/V Perchloric acid in water-free methanol. Excellent polishing conditions were obtained when the electrolyte was cooled down to -45°C and -60°C.

Replica Technique

The specimens for replication were polished and etched, in order to obtain a clear outline of the grain boundaries, some specimens required multiple etching to facilitate a good discrimination of the grain boundaries.

Before coating, the specimen was cleaned with a sheet of replicating plastic which is applied to the etched surface using an acetone solvent and left to dry. Once dry this replicating plastic is stripped off and the sample ultrasonically cleaned for approximately 10 minutes. A sheet of replicating plastic is again applied to the surface, as described above, and only stripped off just before the specimen is placed into the carbon coating chamber. After carbon coating, a square grid is scribed onto the replicated surface. The carbon film formed on the specimen surface is

loosened by electrolytic etching using the normal standard techniques. After etching the specimen was washed in methanol and immersed in distilled water where the small square pieces of the thin film were collected on a double copper grid for further examination by TEM. This technique proved to be very efficient in determining the morphology of the carbides present in a given microstructure. In this way it was possible to undertake electron diffraction techniques without any contribution from the matrix.

2.7 Analytical Techniques

2.7.1 X-ray Diffractometry

All the alloys studied were examined by X-ray diffractometry in the as-received and heat treated (at 875°C for 1 hour and then water quenched) conditions in order to determine if there was any retained austenite in these two conditions.

This examination was made on a Philips diffractometer using monochromatic Co K α radiation. The method of analysis was based on its integrated intensities of diffracted beams by comparing the integrated intensities of reflection planes (h k l) of martensite (bcc) and austenite (fcc) phases.

The relation between concentration and intensity is not generally linear since the diffracted intensity and concentration depends markedly on the absorption coefficient of the mixture and this itself varies with concentration. To analyse a mixture of two phases α and β a particular line of the α -phase is considered.

Where I_{α} is the intensity of this line for the phase α .

The integrated intensity of a diffraction line was calculated by following the equation given by Durnin and Ridal [100].

$$I_{hkl} = n^2 V_m (LP) e^{-2M} (f.f)^2$$

where $I(hkl)$ = integrated intensity of hkl reflection

n = number of cells in cm^3

V = volume exposed to X-ray beam in cm^3

LP = Lorentz Polarization Factor

m = multiplicity of (hkl) planes

e^{-2M} = Debye-Waller temperature factor

F = structure factor

f = atomic scattering factor

2.7.2 Surface Analysis

The equipment utilized for Auger Electron Spectroscopy (AES) and Secondary Ion Mass Spectrometry (SIMS) was a V. G. Scientific MICROLAB 500. This equipment can perform scanning electron microscopy (SEM), scanning Auger microscopy (SAM), energy dispersive X-ray analysis (EDX), scanning SIMS microscopy (SSM), and depth profiling in both AES and SIMS mode. Figure 1 shows these interactions schematically.

Topographical investigation by SEM and SAM allows imaging and element mapping of a specimen from different fracture morphologies. EDX enables elemental analysis of the semi-bulk material and can be performed concurrently with AES. SIMS facilitates the determination of isotopic ratios and chemical information from the sputtered molecules. SSM permits element mapping at lower concentrations than is possible with SAM. Note that SIMS detects compounds, i.e. FeO, whereas AES detects atomic species, i.e. Fe and O.

2.7.2 (a) Auger Electron Spectroscopy (AES)

Auger electrons are produced by irradiating a sample surface with a focussed primary beam of electrons of energy (E_p) typically in the range 2-10 Kev, although in this investigation, where 500^oÅ spatial resolution was required, 20 Kev and even 30 Kev has been used.

Many elastic and inelastic scattering reactions occur to produce emitted radiation. Only ~ 1 in 10^5 of

the emitted electrons arise from the Auger process; Auger electrons are distinguished by having energies which are independent of E_p and characteristic only of the samples from which they arise.

The Auger process is illustrated schematically in Fig. 2(a) where the particular Auger electron originated from an Si atom ionized by the ejection of a K electron. The K vacancy is filled by an L_I electron and at the same time an L_{II} , L_{III} electron is emitted as an Auger electron. The nomenclature used to describe this specific process is $KL_I L_{II}, L_{III}$: the energy level from which the electron is ejected is named first, the level from which the electron falls named next, and the original level of the ejected Auger electron named last. After the emission of the Auger electron the atom is doubly ionized.

The probability of an ionized atom emitting a specific energy Auger electron is governed by two factors, the fluorescent yield (ω) (which defines the probability of an X-ray being emitted rather than an Auger electron

$$\omega_k = \frac{X_k}{X_k + A_k}$$

where X_k and A_k are the number of X-ray photons emitted and the number of Auger electrons emitted) and the number of different Auger electrons which can be emitted as an atom returns (eventually) to the ground state. To determine the number of transitions it is necessary to

know the number of initial and final electron configurations where final refers to the doubly ionized state and not to the ground state. Consideration of the energy levels in doubly ionized and singly ionized atoms shows that for the KLL Auger transitions there are six Auger transitions for low and high atomic number atoms but nine for atoms of intermediate atomic number.

The energies of Auger electrons can be determined by considering the transitions depicted in Fig. 2(a). The energy released where the L_I electron falls into the k shell is $(E_k - E_{L_I})$ but the electron has to supply the energy $(E_{L_{II}, L_{III}} + \phi)$, to escape from the sample, where ϕ is the work function. (Work function ϕ is the difference in energy between the Fermi level * of a solid and the energy of the free space outside the solid (vacuum level.) At absolute zero the work function is the minimum energy required to remove an electron from a solid. Because the atom has an extra positive charge, i.e. because it is doubly ionized, the term $E'_{L_{II}, L_{III}}$ should be approximately equal to the L_{II}, L_{III} ionization energy of the next heavier element, so that $E'_{L_{II}, L_{III}}(Z) = E_{L_{II}, L_{III}}(Z+1)$. Thus, the energy of the Auger electron $E(Z)$ is given by

$$E(Z) = [E_k(Z) - E_{L_I}(Z)] - [E_{L_{II}, L_{III}}(Z+1) + \phi] \quad (2)$$

* At absolute zero all the electrons in a solid occupy the lower levels and the valence band is filled to a certain energy, whilst no higher levels are occupied. This level of maximum energy is called the Fermi level (E_f).

The measured energy will, in fact, have an additional term $-(\phi_A - \phi)$, which is the difference between the work functions of the energy analyser ϕ_A and the sample emitting Auger electrons. Thus,

$$E(Z) = [E_k(Z) - E_{L_I}(Z)] - [E_{L_{II}, L_{III}}(Z+1) + \phi_A] \quad (3)$$

so that the work function ϕ is eliminated from the measurements.

Equation (2) is clearly limited since it predicts that $E_{kL_I L_{II}, L_{III}} \neq E_{kL_{II}, L_{III} L_I}$ although the beginning and final states are identical so that the Auger electrons must have the same energies. Refinements in equation (2) takes into account quantum mechanical effects which removes this problem and gives excellent (within 1%) agreement between experiment and theory.

The possibility of other transitions which can influence the relative intensities of Auger and X-rays must be considered. The Coster-Kronig transitions are particularly significant because they involve transitions within one shell, e.g. of the type $L_{III} \rightarrow L_{II}$ and L_I and $L_{II} \rightarrow L_I$. The effect of this is to alter the relative intensity of Auger Electrons expected from the arguments given above, and in addition, the energy available from these transitions may result in line broadening. The influence of accelerating voltage on the generation of Auger electrons is reflected in the ionization cross section.

The ionization cross section, taken in conjunction with the fluorescent yield, and the probabilities of

the various transitions, control the intensities of the Auger signals generally for a given beam current. The Auger signal generated by electron irradiation is superimposed on a high background signal made up of low energy secondary electrons [101].

The competition between the X-ray and the Auger electron is such that they are quite equal for heavy elements but increasingly biased towards the Auger process for lighter elements. The energies of Auger electron emissions are in the range 20-2500 eV and the cross-section for all the elements is such that the sensitivity of the technique varies by a factor of only 30, when the peak heights of the dominant Auger transitions are plotted as a function of atomic number. It is, therefore, possible to analyse for all elements other than H and He by making a single sweep of the analyser. Detection limits range from about 0.01 to 0.3 mass% [102].

2.7.2 (b) Secondary Ion Mass Spectrometry (SIMS)

A basic SIMS apparatus consists of a primary ion source, sample holder, secondary ion mass filter and secondary ion detector.

The interaction of energetic ions with a solid results in the production of atoms and molecules in neutral and charged states. SIMS involves measurement of the mass/charge (m/e) ratio of the ejected (secondary) positive and negative ions.

Although only a small fraction (0.1 to 10%) of the total sputtered species are ions, the high detection sensitivity for ions by mass spectrometer makes the

technique a sensitive tool for surface analysis, Elemental (including H), isotopic and molecular (hence chemical) identification is a particular asset of the technique. The depth of analysis, which is an important consideration for segregation studies, depends primarily upon the sputtered depth during the time of analysis. It typically extends beyond 5 to 50Å depth, depending upon the energy of primary ions, the ion production area (controlled by beam size and raster gating parameters) and ion detection sensitivities [103].

For surface analysis a primary beam of Argon ions at current densities greater than 1 mA cm^{-2} is used with an ion beam of 20 to 100 μm diameter.

In the static SIMS mode the minimum surface erosion is obtained using the lowest current densities, thus the technique has a very high surface sensitivity, especially to electro positive elements [104]. In surface imaging and analysis a liquid-metal ion source was also used at current densities of 0.637 mA cm^{-2} having a beam diameter varying from 500Å to 100 μm .

The sensitivity of SIMS for some elements is exceptionally high (parts per billion). At higher current densities the sample surface may be sputtered away to give depth profile information directly. For sputtered particles the total number can be counted and the sputter yield can be determined, i.e. the number of sputtered atoms per incident ion, the sputter yield can then be used to obtain relative composition against depth profile information.

The Physical Basis of the SIMS Process

When an ion beam interacts with a surface a range of interactions occurs, i.e. reflected ions, sputtered ions, neutral atoms, electrons and photons will be ejected. SIMS uses information from the sputtered ions. Figure 2(b) shows schematically the principle of SIMS. Each incident ion transfers its energy to the sample lattice through a "collision cascade" and ions escaping from the surface as a result of this disturbance are said to be sputtered. Only a fraction of the sputtered atoms are ionized and pass through the mass spectrometer. Usually it is the positive secondary ions which are collected. Not only are monatomic ions produced, but also ionized cluster of atoms. These are not necessarily fragments of the sample lattice, but may consist of arbitrary combinations of atoms, including the bombarding species (e.g. O, Ar) and contaminants (e.g. C,H), these are called 'molecular peaks' [105].

The Ion Source

It is standard practice to use argon bombardment of the sample to obtain SIMS data since this can also be used to clean the surface and establish depth profile analysis.

The ion source used was Argon ion gun type (AG61), which is a hot filament electron impact ion source producing an inert gas beam into a spot of about 20 to 100 microns of diameter and very high current densities greater than 1 mA cm^{-2} . This source can be used for static, dynamic scanning SIMS and for small area depth

profiling where operated at maximum beam current. This gun operates at accelerating voltages between 1 and 5 kV and at pressures in the analysis chamber between 3×10^{-7} - 3×10^{-6} torr. The ion current on the sample varies with both voltage and pressure, for instance, it will provide about 20 μ A at a spot of 5mm diameter at an accelerating voltage of 5 kV.

The most recently developed type of ion source is the field emission liquid-metal ion source. A needle whose tip has a radius in the range 1-10 μ m is placed with its shank passing through a close-fitting capillary tube into a reservoir of liquid metal. The material of the needle is chosen so that the liquid wets it, but does not react with it. On wetting, the liquid metal is drawn up over the protruding needle and over its tip by capillary action, any loss being made good by flow from the reservoir. A high voltage between 4 and 10 kV is then applied between the needle and an extractor electrode positioned a short distance in front of the needle, where upon the film of liquid metal covering the tip is distorted into a cusp-shaped protusion. This protusion is formed by the balance of forces due to electrostatic stress and surface tension. Due to the consequent very high electric field at the tip of the cusp, a beam of positively charged metal is formed, which is then extracted through a circular aperture in the extractor [104].

A liquid Gallium ion gun was also used in this investigation. Its performance provided much higher spatial resolution than that can be achieved with the

argon ion gun. The spot size obtained was of the order of 100 μm . Source energies of between 10-30 kV were used with specimen currents as low as 50 pA to produce the information without causing undue damage to the specimen.

The Mass Filter - Quadrupole

In SIMS a mass spectrometer is used to analyse the sputtered particles since both atomic and molecular information can appear in the sputtered ion spectra, it can, in principle, determine the surface elemental and chemical composition from the mass spectrum.

The unique advantages of SIMS are the ability to detect mass with an accuracy which allows the determination of isotope ratios and chemical information from sputtered molecules and its ability to detect all elements except He and Ne [104] .

In the V. G. MICROLAB 500 analysis of the sputtered species were undertaken using a mass quadrupole (MM12-12S) with a mass range 0-800 amu. A quadrupole consists of a group of four cylindrical rod-shaped electrodes. The basic concept of this device is to provide a potential field distribution, periodic in time and symmetrical with respect to the axis, which will transmit a selected mass group and cause ions of improper mass to be deflected away from the axis [106] . The ions enter an extraction lens and the polarity of the applied voltages determines the polarity of the secondary ions that enter the analyser. Ions of the correct polarity then pass into the spherical capacity analyser which allows only those within a narrow kinetic energy range

to pass through. All neutrals and ions above and below the kinetic energy range are absorbed. The ions then enter the quadrupole mass spectrometer which selects ions with a particular mass to charge (m/e) ratio from all others. This is achieved by applying known RF (radio frequency) and DC voltages to the quadrupole. Finally, ions with the selected mass-to-charge ratio pass through the quadrupole and are detected using the electron multiplier [107].

The resolution described by the manufacturers for the MM12-12S is of a 10% valley between adjacent peaks of equal height or a 5% width of a single peak equal to 1 amu throughout the mass range (0 to 800 amu).

Abundance sensitivity is a measure of the ability of an analyser to detect low concentrations of a trace element. It can be severely limited if the trace element's peak in the spectrum is overlapped by the 'tail' of an adjacent major peak. The abundance sensitivity of the MM12-12S is given as the ratio of the count rates at mass 38 and mass 39 (main $^{39}\text{K}^+$ peak) in a KBr positive SIMS spectrum, and is greater than 1 in 10^5 .

The Ion Detector

The electron multiplier is a very sensitive detector, the multiplication of the signal is so high that a single ion striking the collector can be detected in the output signal. The ion beam after passing through a defining slit (the collector slit as opposed to the source slit), strikes the metal collector and causes a small number of electrons to be emitted. The number of electrons is

proportional to the intensity of the ion beam. These electrons are accelerated by a voltage drop to an electrode where they promote further emission. A series of twelve to fifteen such stages results in a large build up of electron current which is finally collected, amplified further, and sent to the recorder. The voltages on the electrode series can conveniently be varied to give the desired signal multiplication ^[108].

Scanning SIMS and Depth Profiling

Scanning the ion beam across an area of interest on the specimen will clean the specimen and liberate secondary electrons. These secondary electrons can be used to display an ion induced emissive mode secondary electron micrograph (physical image) of the specimen.

In SIMS depth profiling the beam needs to be scanned slowly at low specimen current and a system of raster gating is introduced so that depth profiling information is only derived from a central position of the total etched area. This prevents spurious data from etch crater walls contributing to the depth profile. A slow scan rate is also required for chemical imaging to compensate for the relatively long flight time of ions from the specimen to the SIMS analyser ^[104].

EXPERIMENTAL RESULTS

Criteria Applied to the Analysis of the Fracture Results

In analysing the mode of fracture and the level of embrittlement the following criteria were taken into account: -

1. An alloy which did not show a complete intergranular mode of fracture, but some patches of intergranular fracture (intergranularity), either mixed with cleavage or ductile mode was considered embrittled, i.e. as a sign of embrittlement.
2. The lowering of the upper shelf energy was also taken into consideration as a loss of toughness and the shift of the impact transition temperature to higher temperatures was also used as an indication of the level of embrittlement suffered by a given alloy.

3.1 Impact Testing and Microstructural Assessment

The fracture appearance varied with the degree of embrittlement, test temperature and microstructure. There was also a variation in fracture characteristics from the notch to the end of the fracture path.

The quenched and tempered martensitic structure contained a large proportion of intergranular fracture compared with the isothermally transformed bainitic or pearlitic microstructures for alloys 1, 2 and 3.

For alloys 4 to 11 inclusive, in the quenched and

tempered martensitic condition, a large proportion of intergranular fracture was evident compared with the isothermally transformed bainite microstructure when tested at ambient temperature was also observed.

Alloy 1 showed the largest proportion of intergranular fracture for both the quenched and tempered martensitic and isothermally transformed bainitic conditions. Alloy 2 only showed intergranular fracture in the quenched and tempered martensitic microstructure. A quasi-cleavage low energy fracture morphology was observed for all the microstructures studied in alloy 3. However, a small amount of intergranular fracture was observed in the quenched and tempered martensitic condition after holding for 8,760 hours at 430°C. By contrast the mode of fracture for this alloy at a higher testing temperature (~200°C) was mainly ductile.

For alloys 5, 7 and 11 tested at ambient temperature, there was a tendency to show intergranularity after ageing for 2,160 hours at 430°C for the quenched and tempered martensitic microstructure. In the case of the isothermally transformed bainitic microstructure, with the exception of alloys 1 and 3, none of the alloys studied showed signs of intergranularity at any of the ageing times applied.

Because of the large number of variables involved, the results obtained will be considered initially by grouping the alloys into pairs. Each pair having the same base chemical composition except for the additions of Sb and/or Mo. The actual cast composition is given in Table I.

3.1.1 Alloys 1 and 2 (~1 mass% Cr, ~3 mass% Ni, effect of Sb)

Alloy 1 contained 500 ppm of Sb to permit comparison with alloy 2.

Heat Treatment A

Austenitization of 875°C for 1 hour followed by direct transfer to a muffle furnace at 430°C for isothermal ageing.

The kinetics of the processes leading to embrittlement can be greatly influenced by the first step taken immediately after the austenitization treatment. In this case (Heat Treatment A) the samples were allowed to cool to 430°C in a muffle furnace.

For heat treatment A, isothermally transformed bainite, aged for 8,760 hours, alloy 1 shows intergranular fracture even when tested at +200°C (Fig. 3). This alloy not only shows a change in the mode of fracture from cleavage to intergranular but also a lowering of the upper shelf energy (Fig. 4) with increasing ageing time.

For alloy 2 there was an increase in the upper shelf energy with increasing ageing time (Fig. 4) and this alloy did not show (for this microstructure) any intergranularity in the mode of fracture.

In alloy 1 the mode of fracture changed from cleavage for 24 hours ageing to intergranular after 8,760 hours ageing (Fig. 5) when impact tested at ambient temperature. Alloy 2 did not show any change in the mode of fracture with increasing ageing time for this microstructure at any testing temperature.

Figure 6 compares the ageing curves for alloys 1 and 2 in the isothermally transformed bainitic condition. Figure 7 shows a transmission electron micrograph of the structure obtained for alloy 1 in the isothermally transformed bainitic condition after 24 hours ageing at 430°C. Figure 8 illustrates the appearance of this same microstructure after 168 hours ageing at 430°C (treatment carried out on a parallel work ^[99]). Figure 9 shows an annular dark field image of alloy 1 after 8,760 hours ageing at 430°C, a discontinuous network of precipitates is shown and there are signs of spheroidization. Figure 10 shows the bright field image of this microstructure.

Figures 11, 12 and 13 show a scanning electron micrograph obtained for alloy 1 for heat treatment A at 24, 2,160 and 8,760 hours ageing at 430°C. Note the coarsening of the grain boundaries. Figure 14 illustrates a scanning electron micrograph of the structure obtained for alloy 2 for this heat treatment after 24 hours ageing at 430°C, showing continuous precipitation at the grain boundaries.

Heat Treatment B

Austenitization at 875°C for 1 hour followed by water quenching, tempering at 600°C for 1 hour and ageing at 430°C.

For the quenched and tempered martensitic structure, there was a decrease of the upper shelf energy with increasing ageing time for both alloys 1 and 2. Alloy 1 retained an intergranular mode of fracture even at

a high impact testing temperature ($\sim +80^{\circ}\text{C}$), as shown in Fig. 15. Figure 16 describes the DBTT curves for alloys 1 and 2 for this microstructure for all ageing times studied. Alloy 2 showed increased intergranularity with increasing ageing time. Figures 17, 18 and 19 show the mode of fracture obtained for alloy 2 at different ageing times and different testing temperatures. The common feature is the presence of intergranularity.

Figures 20 and 21 show alloy 1, aged for 2,160 hours, before and after being hydrogen embrittled for 16 hours at 200°C . The hydrogen embrittlement produced smoother grain facets.

Figure 22 compares the ageing curves for alloys 1 and 2 in the quenched and tempered martensitic condition. Figure 23 shows a transmission micrograph of the structure obtained for alloy 1 in the quenched and tempered martensitic condition after 24 hours ageing at 430°C . Figure 24 illustrates the appearance of prior austenite grain boundary precipitates after 168 hours ageing at 430°C .

Figures 25 and 26 show the scanning electron micrographs obtained from alloy 1 after heat treatment B at 24 and 8,760 hours ageing at 430°C , respectively.

Figures 27 and 28 illustrate a transmission electron micrograph of the structure obtained for alloy 1 after 8,760 and 17,520 hours ageing at 430°C , respectively, showing that there was a random distribution of lath boundary carbides at 8,760 hours and some signs of spheroidization of these carbides at 17,520 hours ageing. Previous work^[99] showed that the carbides follow the

transformation

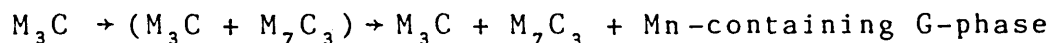


Figure 29 shows a scanning electron micrograph of the structure obtained for alloy 2 for this heat treatment after 24 hours ageing at 430°C. Figures 30 and 31 show transmission electron micrographs of this structure after 2,160 and 8,760 hours ageing at 430°C, respectively where signs of spherodization of the carbide precipitates was present and the decrease in dislocation density with increasing ageing time.

Heat Treatment C

Austenitization at 875°C for 1 hour followed by isothermal transformation at 580°C for 48 hours and ageing at 430°C.

For the pearlitic microstructure neither alloy 1 nor alloy 2 showed intergranularity, the low energy mode of fracture was cleavage. Alloy 2 retained this mode of fracture throughout the ageing sequence. Figures 32 and 33 show the mode of fracture obtained for alloy 2 at ambient temperature after 24 and 8,760 hours ageing respectively. There was a decrease of the upper shelf energy with increasing ageing time for alloy 1 and an increase for alloy 2, as shown in Fig. 34. Figure 35 compares the ageing curves for alloys 1 and 2 for this heat treatment.

Figures 36, 37, 38 and 39 show the effect of the ageing time for alloy 1 in the pearlitic condition,

comparison of the microstructures shown in these figures indicates that there was a coarsening of the cementite lamellae with increasing ageing time.

Figure 40 shows a scanning electron micrograph of the structure obtained for alloy 2 for this heat treatment after 24 hours ageing at 430°C, showing the distribution of the pearlite colonies and the continuous network of grain boundaries.

Heat Treatment D

Austenitization at 875°C for 1 hour followed by quenching into a salt bath at 350°C and ageing at 430°C (in a muffle furnace).

For this heat treatment alloy 2 showed intergranularity after 720 hours ageing at 430°C (Fig. 41). With extended ageing, alloy 2 showed a mixed (cleavage and intergranular) mode of fracture (Figs. 42 and 43). Alloy 1 showed a classical brittle intergranular mode of fracture after 2,160 hours ageing at 430°C (Fig. 44). Figure 45 shows the DBTT curve obtained for alloys 1 and 2 for this heat treatment with increasing ageing time.

Unlike heat treatments B and C, the upper shelf energy did not decrease for heat treatment D. It is interesting to note that the upper shelf energy increased with increased ageing time similar to heat treatment A. The type of fracture for the lower energy showed intergranularity, while for heat treatment A it was cleavage.

Alloy 1 showed a decrease in the upper shelf energy

with increasing ageing time for all the microstructures studied. Both alloys 1 and 2 showed signs of embrittlement, i.e. lowering of the lower shelf energy plus fracture surface intergranularity in the quenched and tempered martensitic condition (heat treatment B). Figure 46 compares the ageing curves for alloys 1 and 2 for this heat treatment.

Figures 47 and 48 illustrate the microstructures obtained for alloy 2 for 24 and 2,160 hours ageing respectively, at 430°C, showing discrete grain boundary carbides and increasing carbide precipitation with ageing time. Figure 48 clearly indicates the decrease in dislocation density.

3.1.2 Alloys 1 and 3 (~1 mass% Cr, ~3 mass% Ni, effect of ~1% mass Mo)

Alloy 3 contained 600 ppm of Sb and 0.94 mass% Mo to permit comparison with alloy 1.

Heat Treatment A

The mode of fracture for alloy 3 was only quasi-cleavage for the low energy mode, even after 8,760 hours ageing at 430°C, and the upper shelf energy remained constant throughout the ageing times (Fig. 49). Figure 50 compares the ageing curves for alloy 1 and 3 for this heat treatment.

Heat Treatment B

After 2,160 hours ageing at 430°C alloy 3 revealed some signs of embrittlement, i.e. intergranularity

(Fig. 51) and the upper shelf energy decreased with ageing time although this was at a slower rate than for alloy 1. This intergranularity increased even further with longer ageing times as shown by impact testing at ambient temperature, +80°C and +200°C (Figs. 52, 53 and 54 respectively).

Figure 55 shows the DBTT curves for these two alloys in the quenched and tempered martensite condition. In this condition regions of intergranular fracture were observed in the lower shelf fracture after 2,160 hours. There was a decrease in the upper shelf energy with increased ageing time.

Figure 56 compares the ageing curves for alloys 1 and 3 for this heat treatment.

Figure 57 illustrates the microstructure obtained for alloy 3 for this treatment after 24 hours ageing at 430°C. The microstructure clearly shows a continuous network of grain boundary carbide.

Heat Treatment C

For this heat treatment the upper shelf energy for alloy 3 remained quite constant whilst alloy 1 showed a comparatively small decrease. The mode of fracture for alloy 3 was quasi-cleavage for the low energy mode of fracture. Figure 58 shows the behaviour of these two alloys in the pearlite condition. Figure 59 compares the ageing curves for alloys 1 and 3 for this heat treatment.

Heat Treatment D

Alloy 3 did not show any significant variation in the upper shelf energy, remaining constant throughout the ageing sequence (Fig. 60). The low energy mode of fracture was quasi-cleavage, as observed in heat treatment A. Figure 61 compares the ageing curves for alloys 1 and 3 for this heat treatment. Figures 62, 63, 64 and 65 compare DBTT curves for alloys 2 and 3 for heat treatments A, B, C and D respectively.

3.1.3 Alloys 4 and 5 (0.06 mass% Cr, ~3.5 mass% Ni, effect of Sb)

Alloy 5 contained 520 ppm of Sb to permit comparison with alloy 4.

Heat Treatment B

In the quenched and tempered martensite condition, alloy ⁵/~~4~~ showed signs of embrittlement after extensive ageing (8,760 hours) at 430°C (Fig. 66). This embrittlement was present even at high temperature (~+200°C) impact testing (Fig. 67).

Alloy 5 (Fig. 68) showed a significant decrease in the upper shelf energy after 2,160 hours ageing at 430°C. Associated with the decrease in upper shelf energy was the presence of intergranularity (Fig. 69) in the low energy fracture.

Figure 70 compares the ageing curves for alloys 4 and 5 for this heat treatment. Figures 71 and 72 show a transmission electron micrograph of the structure obtained for alloy 4 after 2,160 and 8,720 hours ageing

at 430°C respectively. Both micrographs indicate the presence of globular carbides on the grain boundaries and within the grains.

Heat Treatment D

Figure 73 shows the influence of Sb on the DBTT curves after increasing ageing times for the isothermally transformed bainite condition. Alloy 5 showed a pronounced decrease of the upper shelf energy with increasing ageing time. There was no change in the low energy mode of fracture which remained quasi-cleavage from 24 hours to 8,760 hours ageing at 430 (Figs. 74 and 75). Figure 76 shows the hardness curve for alloys 4 and 5 for this heat treatment.

Figure 77 shows a scanning electron micrograph of the microstructure obtained for alloy 4 for this heat treatment after 24 hours ageing at 430°C, showing the distribution of carbides on the grain boundaries and within the grains.

Figure 78 shows a scanning electron micrograph of the microstructure obtained for alloy 5 for this heat treatment after 24 hours ageing at 430°C. This can be compared with Fig. 77 showing a finer carbide distribution and a more continuous carbide precipitation at the grain boundaries.

3.1.4 Alloys 6 and 7 (0.08 mass% Cr, ~3.5 mass% Ni, ~1 mass% Mo)

Alloy 7 contained ~600 ppm of Sb to permit comparison with alloy 6.

Heat Treatment B

In the case of the quenched and tempered martensitic condition, alloys 6 and 7 showed a significant decrease in the upper shelf energy with extended ageing, i.e. 8,760 hours at 430°C (Fig. 79). Alloy 6 did not show signs of intergranularity in the low energy fracture, but alloy 7 containing ~600 ppm showed some intergranularity after 8,760 hours ageing, as shown in Fig. 80.

Figure 81 compares the ageing curves for alloys 6 and 7 for this heat treatment.

Figure 82 shows a transmission electron micrograph of the structure obtained for alloy 6 for this heat treatment after 8,760 hours ageing at 430°C, and is compared with alloy 7 (Fig. 83) showing the influence of the additions of Mo and Sb.

Heat Treatment D

Both alloys showed similar values of Izod impact strength after extended ageing times in this condition (Fig. 84). The mode of fracture for both alloys remained quasi-cleavage for the low energy impact temperature, Figs. 85 and 86, throughout the ageing sequence. In terms of hardness values there was no significant variation for either alloy (Fig. 87).

3.1.5 Alloys 8 and 9 (0.004 mass% Ni, ~4 mass% Mo)

Alloy 9 contained ~600 ppm of Sb to permit comparison with alloy 8.

Heat Treatment B

Both alloys 8 and 9 showed a quasi-cleavage mode of fracture for the quenched and tempered condition on testing at ambient temperature (Figs. 88 and 89). There was no change in the mode of fracture after extended ageing at 430°C (Figs. 90 and 91). The upper shelf mode of fracture was ductile throughout the ageing sequence. See Figs. 92 and 93 for alloy 8 and Figs. 94 and 95 for alloy 9. The order of magnitude of the dimpling size is $\sim 2\mu$ for both alloys after 8,760 hours ageing at 430°C.

In the presence of Ni and Cr at trace levels, Mo did not produce (at ~ 4 mass%) intergranularity and there was a small decrease in the impact transition temperature (Fig. 96) confirming the absence of any tendency to embrittlement. Figure 97 compares the ageing curves for alloys 8 and 9 for this heat treatment.

Figure 98 shows a transmission electron micrograph of the structures obtained for alloy 9 for this heat treatment after 8,760 hours ageing at 430°C, showing large particle at the grain boundary. This alloy was examined in the as-quenched condition to determine if these large particles were present before the quench procedure. A carbon extraction replica of alloy 9 (Fig. 99) in the as-quenched condition showed a similar precipitate morphology to that shown in Fig. 98. This particle was identified as M_6C . Alloys 8 and 9 contained 2.3 and 3% of retained austenite for this condition.

Heat Treatment D

For the isothermally transformed bainitic condition

neither alloy (8 and 9) showed any marked difference in the DBTT curves (Fig. 100). After 8,760 hours ageing both the mode of fracture and amount of energy absorbed remained quite similar. After 720 hours there was a slight shift indicating that more energy was required to cause fracture through the mode of fracture still remained the same.

It was interesting to note that both alloys in the isothermally transformed bainitic condition (Fig. 100) and quenched and tempered martensitic condition (Fig. 96) showed similar toughness for the lower shelf energy for all ageing times studied. Figure 101 compares the ageing characteristics for alloys 8 and 9 in the isothermally transformed bainitic condition.

Figures 102 and 103 show a transmission electron micrograph of the structure obtained for alloy 8 for this heat treatment after 24 and 8,760 hours at 430°C. It was observed that after 24 hours the carbide distribution was localized at the laths boundaries. After 8,760 hours the distribution of these precipitates had become more random and globular in appearance.

3.1.6 Alloys 10 and 11 (~5 mass% Ni, ~1 mass% Mo)

Alloy 11 contained 650 ppm of Sb to permit comparison with alloy 10.

Heat Treatment B

For the quenched and tempered martensitic condition, alloy 11 was shown to be embrittled after 2,160 hours

ageing at 430°C (Fig. 104). Alloy 10 in the same condition showed intergranularity only when impact tested at $\sim -196^{\circ}\text{C}$ after 8,760 hours at 430°C (Fig. 105). Considering the transition temperature (TD) for this pair of alloys it can be seen that there was no simple impact transition from ductile to intergranular mode of failure. As shown in Fig. 106 there was a mixed region, ductile/intergranular and ductile/quasi-cleavage for alloy 11 (after 2,160 hours ageing) and alloy 10 (after 8,760 hours ageing) respectively. This mixed region made the analysis of the transition more complicated, since taking it into consideration it could be said that there was very little increase for TD in this condition.

Figure 107 shows that both alloys had approximately the same hardness values throughout the ageing sequence. Figure 108 shows a transmission electron micrograph structure obtained for alloy 11 for this heat treatment after 8,760 hours ageing at 430°C. This micrograph shows a duplex distribution of carbides with large randomly distributed globular precipitates and a fine distribution within the grains.

Heat Treatment D

In the isothermally transformed bainitic condition, alloy 11 showed a lowering in the upper shelf energy (Fig. 109), though there was no sign of intergranularity. No significant change in hardness was detected with both alloys following a similar pattern (Fig. 110). The lower shelf mode of fracture was quasi-cleavage

throughout the ageing sequence (Figs. 111, 112, 113 and 114).

Figure 115 shows a transmission electron micrograph of the structure obtained for alloy 11 for this heat treatment after 8,760 hours ageing at 430°C, with clear grain boundaries and globular carbides distributed within the grains. The hardness data is summarised in Table IIIa and IIIb.

3.2 Surface Analysis

3.2.1 Auger Electron Spectroscopy (AES)

The grain boundary composition analysis was made by obtaining intergranular cleavage, ductile or a mixture of these fractures in situ and analysing the information from the fresh surfaces thus formed. The output data is obtained in the form of a spectrum of $N(E)$ v. E which was then differentiated using a computer to produce $dN(E)/d(E)$, as a function of energy, E . The elements were identified from the characteristic energy at which the peaks occur.

The Auger spectra were obtained using 3-20 KeV electrons and specimen currents of 5-20nA.

The Auger specimens were manufactured from the remains of Izod impact samples previously fractured at ambient temperature, having 30mm in length, 5mm in diameter and notched to a 1mm depth, 15mm from one end.

All samples were fractured under a vacuum better than 10^{-9} torr and analysed under a vacuum of 10^{-8} ton.

3.2.2 Scanning Auger Microscopy (SAM)

Auger and X-ray mapping were carried out using

a 10-30 KeV electron beam energy and 5-10nA specimen current.

Scanning Auger electron microscopes utilise a spot size of <50nm as in conventional SEM and permit an Auger resolution of the order of <0.1 μ m. This microscope has magnetic lenses and uses accelerating potentials of up to 30kV and is also fitted with X-ray detectors. The X-ray spectrum can be obtained simultaneously with the Auger spectrum, because the energy dispersive detector and electronic are totally independent of the Auger collection system.

The Auger mapping information was recorded electronically and stored on the computer data system for processing when requested. The Auger map was a straightforward comparison between peak and background signal from a large number of points in the area of interest. The peak and background intensities are extremely dependent on the topography of the area being mapped and in order to reduce the topographical effect the maps were plotted from $\frac{P-B}{B}$ values, where (P = peak) and (B = background).

3.2.3 Secondary Ion Mass Spectroscopy

A basic SIMS apparatus consists of a primary ion source, sample holder, secondary ion mass filter and secondary ion detector. Secondary ion mass spectra were acquired using two primary ion sources, Argon (2-5 KeV) and the liquid metal Gallium operating at 10-30 KeV.

In an attempt to study the elemental species present on fracture surface without significant damaging the

sputtered surface, the liquid metal ion source was preferred because the specimen current could be reduced to 100 pico amps/m² and still produce an effective signal. The argon ion source was limited to examining the samples in the dynamic SIMS mode because the minimum usable specimen current was limited to 0.5 nano amps/mm². Mass data was acquired directly in a computer mode which allowed spectrum processing such as background subtraction and peak smoothing to be carried out before producing the hard copy.

Alloy 1 (~1 mass% Cr, ~3 mass% Ni and ~500 ppm Sb) -
Heat Treatment A

In order to obtain an intergranular mode of fracture for the short time ageing (720 hours), samples were embrittled for 16 hours at 200°C in a hydrogen atmosphere, by using an autoclave at a pressure of 0.22 Pa. Figure 116 shows the Auger spectrum obtained, where no impurity elements such as Sb or P was detected on this intergranular surface. Figure 117 shows the spectrum obtained for this same condition (Heat treatment A) after 8,760 hours ageing at 430°C. This spectra, obtained from an intergranular region, showed a well defined Sb peak. For a mixed (intergranular and cleavage) region (Fig. 118) the Sb peak does not appear indicating that Sb had segregated to the grain boundaries. For this same condition (Heat treatment A) after extended ageing time, 17,520 hours at 430°C, alloy 1 showed Sb and P (Fig. 119) on the intergranular fracture surface region. A spectra from the cleavage region showed that

neither Sb or P (Fig. 120) were present. Note that the Ni peak is smaller than the one found on the intergranular region.

Secondary electron image from the intergranular fracture surface of alloy 1 after 17,520 hours ageing is shown in Fig. 121. (A hard copy of the Auger map is shown in Fig. 122 for the equivalent area.)

The Auger maps show the distribution of the elements Sb, Ni, Cr and P, Fig. 123 a, b, c and d respectively. Ni and Sb were shown to have segregated to the same intergranular region (compared with Fig. 122, while P and Cr exhibited an even distribution.

The precipitates observed on the intergranular facets were examined by "Energy Dispersive X-ray Analysis" (Fig. 124, E.D.X.), indicating the presence of Cr. Secondary ion mass spectrometry (SIMS) of alloy 1 in the isothermally transformed bainite (Heat treatment A) after 1,000 hours ageing was also carried out, Fig. 125 shows the positive secondary ion mass distribution of species sputtered from a cleavage fracture surface indicating the presence of Sb ¹²¹ and Sb ¹²³ mass species.

Figure 126 shows a secondary electron image of a polished and ion etched sample in the isothermally transformed bainitic condition (Heat treatment A) aged for 1,000 hours. Figure 127 shows the topographical scanning Auger image from the ion etched image showed in Fig. 126. Figure 128 shows the Auger map of the Sb distribution in the area shown in Fig. 126, indicating a coarsening of Sb-rich regions in the bainite microstructure after prolonged ageing.

Alloy 1 - Heat Treatment B

For the quenched and tempered martensite condition (Heat treatment B), after 24 hours ageing at 430°C alloy 1 showed that P was present on the intergranular fracture surface, as shown on the Auger spectrum Fig. 129. No P, however, was found on the ductile area Fig. 130, and the Ni peak was reduced compared to the one found for the intergranular area. Further analysis produced Figure 131 showing the topographical scanning Auger image from the intergranular area analysed and Figs. 132 and 133 show the Auger maps giving the distribution of the elements Ni and P, respectively, on the intergranular surface. SIMS was carried out on samples aged for 24 hours at 430°C. Figure 134 gives the secondary electron image of the intergranular fracture surface. Figure 135 displays the EDX analysis of a particle A on the intergranular fracture surface shown in Fig. 134. Figure 136 shows the CrK_α X-ray map for the area shown in Fig. 134. Figure 137 shows the positive secondary ion mass distribution of the species sputtered from the intergranular fracture surface, after 1,000 hours ageing at 430°C. Identical Sb^{121} and Sb^{123} levels were also obtained on the cleavage fracture of the bainitic condition (Fig. 125).

In order to show that hydrogen embrittlement had not influenced the segregation of Sb in heat treatment A, samples from alloy 1 were embrittled by using the same hydrogen embrittling procedure, Fig. 138 gives the Auger spectra obtained, Sb was found on the intergranular fracture surface. Figure 139 shows the EDX

analysis obtained for alloy 1, after 8,760 hours ageing, Mn-containing G-phase was found at the prior austenite grain boundaries.

After 17,520 hours ageing at 430°C in the martensitic condition, alloy 1 did not show the same significant impurity element (such as P or Sb) segregation (Fig. 140) as previously observed in the same alloy aged for 24 hours, in the survey spectrum.

Figure 141 shows the spectrum obtained at the surface and after depth profiling for alloy 1 after 17,520 hours ageing at 430°C. Depth profiling was carried out using a Gallium liquid metal ion gun. Spectrum 1 compared with spectrum 2 show that Ni^{58} and Ni^{60} , Mn^{55} , Si^{27} decrease along with P^{31} .

Alloy 5 (0.06 mass% Cr, ~3.5 mass% Ni and ~500 ppm of Sb)-Heat treatment B

Figure 142a is the Auger spectrum obtained from a general area of the surface fracture of alloy 5, showing that no significant impurity segregation occurred for the quenched and tempered martensite condition (Heat treatment B) after 8,760 hours ageing at 430°C.

Alloy 7 (0.08 mass% Cr, ~3.5 mass% Ni, ~1 mass% Mo and ~590 ppm of Sb) - Heat treatment B

Figure 142b shows the spectrum obtained from an intergranular region of alloy 7, after 8,760 hours ageing at 430°C indicating that P had segregated for that region of the fracture surface. Figure 143 shows the spectrum obtained from a cleavage surface, confirming the absence

of P peak.

Alloy 9 - (0.004 mass% Ni, 4 mass% Mo and 600 ppm of Sb)

As-quenched

EDX analysis, Fig. 144, of the particle A shown in Fig. 99, shows that this precipitate was rich in Fe and Mo. Convergent beam electron diffraction analysis of particle A in the carbon extraction replica (Fig. 99) indicated that this carbide was M_6C with a lattice parameter of 11.2\AA units^[109].

CHAPTER 4

DISCUSSION

4. Introduction

In this work it has been established that the type of fracture observed was dependent on the microstructure which in turn influenced the segregation behaviour of impurity elements by modifying either the driving force or kinetics of segregation. The major factors influencing temper embrittlement as described in the literature survey are:

1. The chemistry of the matrix.
2. Grain boundary structure.
3. The nature of other interfaces to which partitioning of the impurities can occur.
4. The dislocation density.

As the amount, type and composition of carbides in steel vary with heat treatment it is clear that the composition of the matrix would also vary correspondingly for a given constant bulk composition of the steel. The solubility, as well as the diffusivity of impurity elements, are dependent on the composition of the matrix and can thus be modified by changes in microstructure⁽⁷²⁾.

Therefore, the resulting mode of fracture will be reliant upon several interdependent mechanisms operating in a given alloy.

4.1 Assessment of the Fracture Mode

The essential feature of temper embrittlement is that it involves a lowering of cohesion along grain boundaries regardless of the origin of the boundary⁽⁷⁴⁾. One of the basic features of this work is the assessment of the transition to such a mode of fracture. It is therefore appropriate to devote the first part of this discussion to a more detailed consideration of the transition from cleavage to intergranular mode of fracture and the philosophy of the criteria adopted to quantify the changes accompanying this phenomenon.

The fracture path in temper embrittled bainitic steels of low carbon (0.008 mass% C) content has been said to follow the ferrite-ferrite and ferrite-bainite boundaries, whilst the martensitic steels' fracture path follows the prior austenitic boundaries⁽⁷⁴⁾ and should require less energy as the boundary surfaces become smoother. In this investigation the energy required for a given mode of failure and the associated fracture appearance did not necessarily directly correlate, i.e. the amount of energy absorbed by an alloy to fracture in the intergranular mode was of the same order as that for fracture in the cleavage mode. This indicates that an alloy in the embrittled and in the temper-embrittled condition can absorb the same amount of energy on impact testing.

In considering cleavage crack propagation, low temperature and high strain rates tend to raise the yield points of metals and to suppress plastic deformation. The energy associated with plastic deformation therefore becomes less important, the lower the temperature of testing and the higher the velocity with which

the crack moves. Where slip takes place during the movement of a crack, energy is absorbed in nucleating and moving dislocations.

Cleavage takes place by the separation of atomic bonds along well defined crystal planes. Ideally a cleavage fracture would have perfectly matching faces, completely flat and featureless. However structural materials are polycrystalline with the grains (neglecting texture) more or less randomly oriented with respect to each other. Thus cleavage propagation through one grain will have to change direction as it crosses a grain or sub-grain boundary. Such changes in direction will result in the characteristic fracture surface usually observed. In addition, structural materials contain particles, precipitates or crystallographic imperfections that further complicate the fracture path. One of the principal features observed is "river patterns" which represents cleavage steps on parallel planes. Such behaviour was typical of alloys 1 and 2 (figs.32 and 33) in the isothermally transformed pearlitic conditions (heat treatment C) and in the isothermally transformed bainitic conditions (heat treatment A) alloy 2 and alloy 1 for the low energy mode of fracture.

A cleavage facet which contains a large number of steps has a large surface area and therefore an increased associated surface energy. The advance of the crack not only involves separation of the crystal along cleavage plane segments, but also entails the continued growth of the surfaces of the steps. Unless a secondary plane or slip plane is nearly normal to the surface of the primary cleavage plane, the formations of the steps can involve plastic tearing of the metal in order to form the surface of the steps.

The fracture morphology exhibited mainly by samples in the isothermally transformed bainitic condition (D) consisted of a multi-faceted block texture with some extremely fine "river" markings which are variable in orientation relative to the macroscopic failure path. These fractures were called quasi-cleavage. In the condition D these were characteristic for the following alloys; alloy 5 (fig.75), alloy 6 (fig.86(a) and 87(a)), alloy 7 (fig.86(b) and 87(b)), alloy 10 (fig.112) and alloy 11 (fig.114).

Intergranular fracture in this context usually results from the segregation of impurity elements (such as P, Sn and Sb) to grain boundaries. Attempts to explain low temperature intergranular fracture have concentrated on cracking of precipitates at grain boundaries⁽¹¹⁰⁾ and on segregation induced low temperature fracture necessitating the utilization of a quantifiable theoretical approach such as the Griffith model⁽¹¹⁾, which provides a basis for fracture strength estimation related to thermodynamic criterion for fracture by considering the total change in energy of the cracked material as the crack length increases. This may be summarized as follows:

$$\sigma_f = \frac{2 \epsilon \gamma^1}{\pi c}^{\frac{1}{2}}$$

σ_f being the stress at which a crack of length c begins to propagate in a material with elastic modulus ϵ . In a brittle material γ^1 is the total energy required per unit area of surface created by the crack and is composed of the surface energy (γ) and a plastic work term γ_p such that:

$$\gamma^1 = \gamma + \gamma_p$$

where intergranular fracture occurs, the appropriate quantity for surface energy is:

$$\gamma_b^1 = 2 \gamma_s - \gamma_b$$

where γ_s is the surface energy of the exposed boundary and γ_b the pre-existing grain boundary energy. The equation above is used by many authors to describe the effect of segregation on intergranular brittle fracture^(41,74,111,112,113,114,115).

During segregation both γ_s and γ_b are reduced. Observations of γ_s and γ_b as a function of the solute molar fraction (X_c) generally show that both fall to about half their original value at the maximum levels of segregation obtained experimentally. Therefore, according to this prediction, for any normally ductile material in which γ falls to half of its original value during segregation the grain boundary cohesion will be sufficiently reduced such that the material will exhibit extensive, segregation-induced brittle intergranular fracture. (As shown by alloy 1 (figs.20 and 121) and alloy 2 (fig.18)). Seah⁽¹¹⁾ suggested that the above considerations ignore the fact that upon fracturing the fresh surfaces do not have time to redistribute the solute and for low temperature fractures (such as occurring in temper embrittlement) the surfaces exposed have only half of the associated interfacial enrichment each. Therefore the segregation level at the surfaces causes only a small reduction in γ_s so that the net effect on γ is small, even for high values of interfacial enrichment. Thus segregation induced low temperature intergranular brittle failure cannot be explained entirely by the lowering of γ .

Other parameters need consideration such as the degree of segregation at the grain boundaries, impurity contents, grain size, the degree of misfit of solute atoms at the grain boundaries and therefore dislocation-solute interactions, diffusion rates of solutes and solvents in and to the grain boundaries.

In this work, beyond the intrinsic characteristics of each type of fracture, i.e. cleavage, intergranular and ductile, it was taken into account that the type of fracture was dependent on the specific microstructure, which in turn can influence the segregation behaviour of impurity elements by modifying either the driving force for, or kinetics of, segregation.

In practice many microstructural and microstructure-related features can play a role in determining the fracture path. The most important are:

1. second phases
2. particles and precipitates
3. grain size
4. texture due to mechanical work

The amount, type and composition of carbides in steels vary with heat treatment. Moreover the composition of the matrix can be modified by such microstructural changes, e.g. carbide transformation occurring on subsequent ageing. This will in turn affect solubility, as well as diffusivity of impurity elements, which are dependent on the matrix composition⁽⁷²⁾ since impurity elements and alloying elements can be of interest, for instance the formation of molybdenum-phosphorus phases.

Therefore, the resulting mode of fracture will be reliant upon the above factors as they operate for each particular microstructure for each alloy. This may be demonstrated by the following observations; For alloy 2, a comparison of figs.19 and 33, which shows that for the same testing temperature, after 8760 hours ageing at 430°C the quenched and tempered martensitic structure exhibited an intergranular mode of fracture (fig.19) whereas the pearlite-ferrite structure exhibited a cleavage mode of fracture (fig.33), despite their similar hardness levels (287 and 244 HV₃₀, respectively). For alloy 5, an analogous comparison shows that the quenched and tempered martensitic condition (406 HV₃₀) exhibited an intergranular mode of fracture (fig.66) whereas the isothermally transformed bainite condition (393 HV₃₀) exhibited a quasi-cleavage mode of failure (fig.75). For alloy 7 an analogous comparison shows that the quenched and tempered martensitic structure (391 HV₃₀) exhibited a mixed cleavage - intergranular type of fracture (fig.80b) whereas the isothermally transformed bainitic condition (398 HV₃₀) exhibited a quasi-cleavage mode of fracture (fig.86b). In this particular study there were numerous variations in chemical composition which had a significant influence on fracture. It was also clear that the previous thermal history, and therefore microstructure, contributed towards mechanisms of segregation which promoted embrittlement.

For the alloys in this study three types of embrittlement were observed, they were:-

(1) Changes in ductile-brittle transition temperature

A shift in transition temperature, without a change in the low energy mode of fracture (which remained cleavage) or variations of the upper shelf energy.

(2) Changes in fracture mode and toughness

A change from cleavage to intergranular for the low energy mode of fracture accompanied by a decrease of the upper shelf energy.

(3) Temper embrittlement

A shift in transition temperature together with a change from cleavage to intergranular for the low energy mode of fracture and lowering of the upper shelf energy.

Fig. 145(a) shows schematically these embrittlement types, described above.

The degree of embrittlement was measured by the difference in transition temperature between the unembrittled (24 hours ageing) and temper embrittled condition. The extent of this shift in transition temperature, ie the severity of embrittlement is represented by a histogram, fig. 145(b). Tables IVa and IVb summarises the transition temperature values for alloys 1-11 for all heat treatments applied in accord with ageing time. Likewise the low energy fracture mode is given in Tables Va and Vb.

4.2 Criteria for the assessment of transition temperature

The 'degree of embrittlement' (116), is conventionally assessed by measuring the difference in impact transition temperature between an embrittled and unembrittled steel but this shift cannot necessarily be attributed directly to the segregation phenomena, because the fracture in materials of different yield stresses will take place at different transition temperatures. For example, results on a high yield strength martensite may be similar to those of a lower strength bainite. Therefore, in this work the most reliable comparison has been made only for alloys which have similar yield strengths.

In the current work, Vickers hardness values were used as an indication of the yield strength of all the alloys in all the various heat treated and aged conditions. This provided a reliable method of gauging relative strength levels. Testing would have provided more precise data (taking into account grain size effects in particular), but such an extensive appraisal would have unduly depleted the amount of material available for the optical and electron optical assessments of microstructure and also for the X-ray diffraction and surface analytical assessments.

There are various definitions of transition temperature obtained from an energy or fracture appearance versus temperature curve. One of these is to select a temperature, corresponding to the (upper shelf) energy, above which the fracture is 100% fibrous (ductile). This transition temperature criterion is called the fracture transition plastic (FTP), though the possibility of brittle fracture is negligible above the FTP the use of this concept is highly impractical in many applications

because these values are normally too high to be realistic. An arbitrary criterion is to base the transition temperature on 50% cleavage-50% ductile, this is called fracture appearance transition temperature (FATT). A third criterion is the temperature associated with the average of the upper and lower shelf energy values. A fourth criterion is based on the temperature at which the fracture becomes 100% cleavage, known as nil ductility temperature (NDT). The fracture initiates with essentially no prior plastic deformation.

All these four criteria are well known and most of the established literature on temper embrittlement⁽¹³⁾⁽¹⁴⁾ refers to them. However, many authors either tend to refer to FATT or simply to transition temperature without a precise definition of the criteria which they used in determining the transition temperature despite the lack of a standard criterion.

In this work the change in the mode of fracture from ductile to brittle was categorised by three main criteria; one according to fracture appearance and the other two (the lowering of the upper shelf energy and a change in ductile to brittle transition temperature) according to the variation in energy absorbed on impact testing.

With reference to the impact energy curves; initially the temperature associated with the point of inflexion was estimated as a measure of the transition temperature T_{D_I} . For the impact energy curves which did not exhibit a clear point of inflexion the mean value (T_{D_M}) was calculated by considering the highest and lowest energy absorbed on impact, within a testing temperature range of -196° to $+200^{\circ}\text{C}$.

4.3 Effect of Variation in Composition on Temper Embrittlement

The influence of alloying elements such as Ni, Cr and Mn on temper embrittlement is such that they can intensify the segregation of impurity elements, though not causing embrittlement themselves. In particular Ni and Cr can intensify P, Sb, Sn and S segregation to grain boundaries⁽⁹²⁾. Such synergistic co-segregation occurs where the interaction between M(a metallic element) and I(an impurity element) enhances segregation of both types of elements to the grain boundaries.

In order to confirm the various influences of different combinations of alloy additions the compositions investigated are considered in the following groups which firstly studies the effect of molybdenum, secondly the effect of molybdenum in the presence of nickel and thirdly the effect of molybdenum in the presence of nickel and chromium.

For the purpose of the following discussion the alloys (1 to 11) will be grouped as described below.

Group 1

Alloy 8 (C - 4Mo)

Alloy 9 (C - 4Mo - Sb)

Group 2

Alloy 4 (C - 3Ni)

Alloy 5 (C - 3Ni - Sb)

Alloy 6 (C - 3Ni - 1Mo)

Alloy 7 (C - 3Ni - 1Mo - Sb)

Alloy 10 (C - 5Ni - 1Mo)

Alloy 11 (C - 5Ni - 1Mo - Sb)

Group 3

Alloy 2 (C - 1Cr - 3Ni)

Alloy 1 (C - 1Cr - 3Ni - Sb)

Alloy 3 (C - 1Cr - 3Ni - 1Mo - Sb)

4.3.1 The role of molybdenum

Alloys 8 (C-4 Mo) and 9 (C-4 Mo Sb) exhibited the cleavage-ductile transition in both quenched and tempered martensite and isothermally transformed lower bainitic condition as shown by the impact curves Figs.86 and 100 respectively, throughout the ageing sequence.

The maximum increase in transition temperature for the quenched and tempered martensitic structure had occurred by 720 hours ageing for alloy 8, in the case for alloy 9 it had occurred by 24 hours ageing at 430°C. This effect is better described by the transition temperature curves as shown in fig.146 and corresponded to a softening of 50 Hv₃₀ points (Table IIIa) for alloy 8 and 39 Hv₃₀ for alloy 9 (as compared with the as-received condition).

Figure 147 shows schematically the relationship between softening, segregation and variation in transition temperature (T_D). At a given segregation level in a given alloy the change in transition temperature increases with hardness. Therefore, during ageing the measured variation in transition temperature (T_D) which reflects both segregation and hardness levels can go through a maximum if segregation has reached equilibrium while softening is still in progress. With longer tempering times, the effect vanishes. This effect was observed in NiCr steels^(76,126)

tempered 1 hour at 650°C and aged for 1000 hours at 520°C, as seen in fig.148() and this was similar to that found in this work for alloys 8 and 9 in the quenched and tempered martensitic condition.

TEM work for alloy 9 in the quenched and tempered martensitic condition and for alloy 8 in the isothermally transformed lower bainitic condition showed the presence of large globular carbides, as seen in Figs.98 and 103, respectively. Alloy 9 in the as-quenched condition contained some carbides of identical morphology to those found in the quenched and tempered martensitic condition. These were identified as M_6C and EDX analysis (fig.144) showed them to be rich in Mo.

The addition of Mo at levels up to 0.5 mass% can be effective in suppressing temper embrittlement by reducing grain boundary segregation^(117,21) due to it promoting a decrease in the rate of P diffusion in iron⁽¹¹³⁾. Mo has strong carbide forming tendencies which result in increased carbide formation, thus diminishing the intergranular solute segregation caused by the carbide solute rejection mechanism⁽¹¹⁸⁾. However Mo additions in amounts greater than 0.5 mass% can be detrimental⁽¹¹⁹⁻¹²³⁾ and that the detrimental effect is linked with the presence of Ni and Cr in the steel. The present work suggests that the formation of more stable carbides of higher Mo:C ratio will leave less Mo in solution to interact with impurity elements such as P which could thereby have prevented temper embrittlement. More specifically the increase in P segregation at the high Mo contents of greater than 0.5 mass% would be due to increasing amounts of M_6C precipitation thus leaving less Mo in solution and reducing the level of C

solute on the boundaries (the interaction C-P is repulsive) which would be consistent with the suggestion⁽⁹²⁾ that strong carbide formers such as Mo (Cr and Ti) reduce the C activity in solution resulting in enhanced P levels at the boundaries.

Alloy 9 contained M_6C , and also a higher impurity content, 60 ppm P + 600 ppm Sb than alloy 8 (30 ppm P). However, both alloys exhibited a cleavage-ductile transition, suggesting that the presence of Mo at 5 mass% in the absence of Ni and Cr was not detrimental.

4.3.2 Role of Nickel

4.3.2.1 The Cleavage-Ductile Transition

4.3.2.1(a) The Effect of Mo Additions

From the data obtained from transition temperature (Table IVa) it can be seen that the addition of 1 mass% Mo to a C-3 mass% Ni alloy caused a shift of +150°C in transition temperature for the quenched and tempered martensite and a shift of +39°C for the isothermally transformed bainitic structure; it also increased the hardness by 142 Hv₃₀ points, for both conditions (Tables IIIa and IIIb). It is observed that these values refer to 24 hours ageing, as the unembrittled condition (compare alloy 4 with alloy 6).

Such increases in hardness due to the Mo addition⁽¹²⁵⁾ have been associated with an increase in the susceptibility to temper embrittlement which would explain the increase in transition temperature observed for alloy 6. However, this alloy failed only by quasi-cleavage for the low energy mode of fracture in both quenched and tempered martensite and isothermally transformed bainite conditions, (fig.85a and 86a). Therefore the increase in transition temperature can be associated with the increase in

hardness. The Mo addition reduced the upper shelf energy for the isothermally transformed bainitic condition as seen in the impact curves, this is clearly shown by Figs.73 and 84, for alloys 4 and 6 respectively. However, during ageing there was no further reduction of the upper shelf energy and alloy 6 exhibited a cleavage-ductile transition. The initial reduction due to the Mo addition was probably due to the refinement in carbide size as Mo-rich carbides were promoted, because the energy required for void growth and coalescence would be higher for a small number of large widely separated carbides, than for a large number of closely spaced small carbides.

The addition of 600 ppm Sb (alloy 7) to an alloy containing C-3 mass% Ni 1 mass% Mo (alloy 6) caused a shift of -164°C in transition temperature after 24 hours ageing in the isothermally transformed bainitic condition, (Table IVa). The effect of ageing on the transition temperature is better described by the curves in fig.151. It can be seen that for extended ageing (i.e. after 2160 hours) the shift in transition temperature was substantially reduced, indicating that the effect of the 600 ppm addition of Sb on transition temperature was transient.

For the impact curves obtained for alloys 6 and 7, i.e. with 1 mass% Mo plus 600 ppm Sb respectively (fig.84) it can be seen that the Sb addition did not significantly alter the behaviour of this alloy, both had similar upper and lower shelf energy values and exhibited a quasi-cleavage-ductile transition. The low energy mode of fracture was identical to that of the alloy without Sb (alloy 6) as seen in figs.85 and 86.

4.3.2.2 The Reduction of Upper Shelf Energy

4.3.2.2(a) The Effect of Mo Addition with and without Sb

For extended ageing in the quenched and tempered martensitic structure (fig.79), alloy 6 exhibited a significant loss in toughness (as indicated by a decrease of 83 joules for the upper shelf energy). This indicated that, although there was an absence of any intergranular mode of fracture, i.e. as would have been expected for temper embrittlement, the intrinsic toughness of the alloy, as measured by the shift in transition temperature due to the 1 mass% Mo addition (related to alloy 4) was increased. (Compare figs.150 and 151 for alloys 4 and 6, respectively). The reduction in upper shelf energy observed in the quenched and tempered conditions (fig.79), was probably due to the fine carbide dispersion observed in this alloy (fig.82), compared to alloy 4 (fig.72). This refinement in carbide size for alloy 6, due to the addition of 1 mass% Mo, was probably due to the transformation of the original Fe_3C precipitation to Mo based carbides.

Carbide morphology, plays a very important role regarding the lowering of the upper shelf energy because even if carbide impurity-rejection did not occur around carbides, the energy required for void growth and coalescence would be higher for a small number of large widely separated carbides than for a large number of smaller carbides (fig.149 shows this mechanism schematically). Furthermore, a preferential cleavage path will selectively traverse regions of high void concentration as suggested by Guttman et al⁽¹²⁷⁾. This explains why the low energy mode of fracture was quasi-cleavage.

The addition of 600 ppm Sb (alloy 5) to a C-3 mass% Ni alloy (alloy 4) in the isothermally transformed bainitic condition produced a decrease in transition temperature of -120°C for 24 hours ageing (Table IVa). However, after 8760 hours ageing this difference was reduced to only -2°C . This effect of the ageing time on the shift in transition temperature is better described by the transition temperature curves (fig.150) for alloys 4 and 5.

It can be seen from the impact transition curves (fig.73) that there was a decrease in upper shelf energy for alloy 5 throughout the ageing sequence. This progressive loss in toughness resulted from the microstructural changes which occurred during ageing. More specifically, the changing character of the second phase particle dispersions and their associated particle/matrix interfaces which in turn controlled void formation by decohesion and thereby determined the micromechanisms which were responsible for fracture^(128,129). The particle/matrix interfacial work of fracture (or "cohesive energy") in a given matrix is determined principally by the particle coherence and bulk chemistry⁽¹³⁰⁾. It has been suggested by some authors (129,131,132) that cohesive energy may be reduced dramatically through local changes in interfacial chemistry resulting from the segregation of surface active elements.

One possible explanation for the reduction in upper shelf energy observed for alloy 5 is that the Sb reduced the cohesion around the particle/matrix interface. However the mechanism by which Sb would enrich these interfaces requires further work.

The addition of 600 ppm Sb (alloy 11) to an alloy containing C-5 mass% Ni, 1 mass% Mo (alloy 10), caused a shift of $+46^{\circ}\text{C}$ in

transition temperature for 24 hours ageing (Table IV), in the isothermally transformed bainitic condition. It was observed that the alloys containing 5 mass% Ni (alloys 10 and 11) and 3 mass% Ni (alloys 6 and 7) with the same additions of Sb and Mo exhibited hardness values within the range 350-400 Hv₃₀. Indicating that these additions had relatively little influence in the strength level of these alloys in this condition.

From the impact energy curves it can be seen that the 600 ppm Sb additions in the presence of 1 mass% Mo caused a decrease in upper shelf energy for an alloy containing 5 mass% Ni (alloy 11). This reduction in upper shelf energy could have been associated with an increased Ni level rather than simply the presence of Sb and Mo, because for the same additions an alloy containing 3 mass% Ni did not exhibit a lowering of the upper shelf energy during the ageing sequence. Moreover for 24 hours ageing it can be seen that there was a reduction of 30 joules for the upper shelf energy with the increase in Ni content. (Compare alloys 7 and 11, figs.84 and 109 respectively).

TEM work for alloy 11 (fig.115) showed that this alloy had small globular carbides distributed within the grains and grain boundaries, clear evidence of precipitation.

4.3.2.3 Temper Embrittlement

4.3.2.3(a) Effect of Sb addition

The addition of 600 ppm Sb to a C-3 mass% Ni alloy produced a shift of +110°C in transition temperature (compare alloys 4 and 5) Table IVa, for 24 hours ageing, i.e. in the unembrittled condition.

This shift is increased further throughout the ageing sequence and after 8160 hours ageing it was +283°C.

The 600 ppm Sb addition caused classical temper embrittlement to alloy 5 because it exhibited an upward shift in transition temperature together with a change in the mode of fracture from cleavage (in this case quasi-cleavage) to intergranular and a lowering in upper shelf energy. However, it should be noted that this embrittlement was observed after 2160 hours ageing and that the mode of fracture was not totally intergranular as shown by fig.69. Further ageing (i.e. after 8160 hours) increase the severity of this embrittlement to the extent that this alloy exhibited similar modes of fracture when impact tested at -196°C (fig.66) and +200°C (fig.67). Therefore Sb not only increases the severity of embrittlement for alloy 5 but also increased the rate at which this alloy embrittles, because for an alloy of the same base chemical composition without Sb (alloy 4) temper embrittlement due to P was manifested only after 8160 hours ageing (Table Va). This increase in the rate of embrittlement, observed in alloy 5 compared which alloy 4 was probably due to the fact that both alloys contained 30 ppm P, and that for alloy 5 there was competition between Ni-P and Ni-Sb interactions. For alloys containing Ni the interaction Ni-Sb co-segregation was observed at grain boundaries. This synergistic effect basically arises from the preferential attractive interaction between Ni and Sb in Fe. For a Ni-Cr alloy it has been found^(76,126) that Sb segregation was strongly promoted in the presence of Ni. The Ni-Sb interaction coefficient is considerably higher (27 K.cal/g atom) than for Ni-P (18 K.cal/g atom)⁽³⁵⁾, however the intrinsic

segregation energy of Sb is appreciably smaller than that found for P⁽¹³⁴⁾ which thermodynamically expresses that the segregation potency of Sb is much weaker than that of P as already observed for various steels^(126,133). Therefore, the site competing mechanism between P and Sb was probably the cause of temper embrittlement in alloy 5.

4.3.2.3(b) Effect of Mo addition

The increase in Ni content from 3 to 5 mass% Ni for an alloy containing 1 mass% Mo, alloy 10, induced temper embrittlement after extended ageing time (8760 hours). This was manifested as an increase in transition temperature (fig.152) throughout the ageing sequence and a mixed quasi-cleavage/intergranular fracture for the low energy mode (fig.105) after 8760 hours ageing. However, for ageing times before the onset of temper embrittlement this alloy exhibited a decrease in upper shelf energy, as seen in fig.106, which decreased further after the onset of temper embrittlement. Therefore the increase in Ni content the presence of 1 mass% Mo will be discussed in terms of these two effects.

Although Ni additions are stated to generally confer toughness improvements^(135,136) for the alloys, in this study this did not prove to be the case, as shown by the decrease in upper shelf energy.

Norström and Vingsbo⁽¹³⁵⁾ investigating low carbon alloys found that Ni additions conferred powerful intrinsic toughness improvements and that it may decrease the impact transition temperature by as much as 20°C per percent of Ni, the main

contribution being attributed to improvements in cleavage fracture strength.

The above authors did not, however, consider the decrease of the upper shelf energy (fig.153) presented for their steel accompanying the increase in Ni content from 5 to 9 mass% Ni. this reduction of 40 Joules indicates a decrease in toughness, whilst an unqualified improvement was claimed for their alloys.

Although the Mo content of their alloys was considerably less than that of the alloy in this study, the comparison is limited to the unembrittled condition. For this condition (aged for 24 hours) it can be seen that the increase in Ni content from 3 to 5 mass% produced a reduction of 35 joules in the upper shelf energy. Compare alloys 6 (3 mass% Ni) and alloy 10 (5 mass% Ni), figs.79 and 106 respectively.

Yield strength as indicated by the hardness values reported in Table IIIa and IIIb showed that there was a reduction of 36 Hv₃₀ points for the increase in Ni content and that the transition temperature decreased by -71°C (Table IVa) which is in agreement with the work of Norström and Vingsbo⁽¹³⁸⁾. However, the increase in cleavage fracture resistance (toughness improvement) attributed to the increase in Ni content was not verified by the alloy in this study. Alloy 10 exhibited quasi-cleavage for the low energy mode of fracture and the energy absorbed on impact was 30 Joules (fig.106), the same being observed (for alloy 6), before the increase Ni content (fig.79). Therefore for the alloy in this study the increase in Ni content did not improve the 'intrinsic' ductile fracture toughness or the cleavage strength as claimed by Norström and Vingsbo⁽¹³⁵⁾, for their alloys.

The improvement in toughness associated with the increase in Ni content was an indirect effect, since it seems to be associated with special heat treatments (e.g. double-austenitizing, i.e. high temperature austenitizing and quenching followed by low-temperature austenitizing)^(136,137) which would produce duplex microstructures, i.e. martensite and retained austenite when the latter would confer the improvement in toughness. For the alloy in this study no retained austenite was detected by from the X-ray diffractometry measurements made for this alloy (alloy 10) in the as-quenched condition. Norström and Vingsbo, normalized their alloys at 900°C and then austenitized at 800°C, however, they reported no retained austenite for the as-quenched condition. Therefore it is possible that the decrease in ductile fracture toughness for alloy 10 was due to lowering of the carbide/matrix interfacial strength by impurity (probably P) rejection.

Geniets et al showed that alloying elements such as Ni (and Si) raise the C activity in martensite⁽¹³⁸⁾ because the activation energy for the diffusion of C in martensite is mainly associated with the energy barrier opposing the passage of the carbon atoms through the prohibited octahedral sites. Therefore the effect of the interaction of Ni is that it can influence this activation energy and consequently the activity coefficient of the dissolved C. Furthermore, elements such as Ni (and Si) when in solution in iron increase the stability of graphite relative to carbide phases, indicating that these elements raise the C activity in martensite as they are known to do in austenite⁽¹³⁹⁾.

Therefore, Ni will raise the C activity which in turn can prevent P segregation⁽⁹²⁾. For alloys containing Mo (alloy 10) the effect will be further complicated since Mo can suppress P segregation by a transient Mo-P compound formation. However, during long term ageing Mo is precipitated as the more stable carbides (e.g. M_3C) with subsequent P rejection and hence segregation can occur.

In the case of alloy 10 it is likely that the onset of temper embrittlement was determined by the mechanism described above, i.e. during ageing, cementite was replaced by more stable Mo based carbides thereby releasing P to segregate to the grain boundaries.

The increase in Ni content, therefore increased the susceptibility to temper embrittlement, since temper embrittlement was not present for an alloy of otherwise identical chemical composition containing 3 mass% Ni (alloy 6) and it was manifested after the increase in Ni content to 5 mass% Ni (alloy 10). This suggests that Ni strongly promotes the process of embrittlement⁽⁹⁰⁾.

Nickel has low solubility in carbides⁽⁹⁰⁾ and therefore can be rejected into solution during precipitation and growth. Moreover, Ni can interact with P increasing its activity or diffusivity in Fe⁽³⁰⁾ suggesting that Ni increases the P embrittling potency. thus, for alloy 10, several interdependent mechanisms are likely to have been in operation, contributing to the embrittlement of this alloy. First a carbide rejection mechanism probably involving P, caused the decohesion of the carbide-matrix interface leading to the lowering of the upper shelf energy. Secondly during ageing the replacement of cementite

by the more stable Mo based carbides, released P which in turn exhibited an increase in embrittling potency due to the level of Ni.

4.3.2.3(c) Effect of Mo addition in the presence of Sb

The addition of 1 mass% Mo (alloy 7) to an alloy containing 600 ppm Sb (alloy 5) produced a shift of +35°C in transition temperature, in the quenched and tempered martensitic condition (Table IVa), for 24 hours ageing.

After 8760 hours ageing alloy 7 showed an upward shift in transition temperature together with cleavage as the low energy mode of fracture from quasi-cleavage to quasi-cleavage/intergranular (fig.80) and a lowering of the upper shelf energy, indicating that this alloy was temper embrittled. Therefore, the 1 mass% Mo addition to alloy 7 had merely retarded the onset of embrittlement, because a comparison between alloy 5 (without Mo) and alloy 7 (Table Va) shows that the onset of embrittlement was detected after 2160 hours ageing for the alloy without Mo.

Auger analysis for alloy 7 detected P (fig.142) as the embrittling element. It appears that in spite of the strong attractive interaction between Ni and Sb, the bulk contents required to achieve grain boundary saturation are much larger for Sb than for P. Note that alloy 7 contained 600 ppm Sb, 300 ppm P and 1 mass% Mo, the latter of which has a strong affinity for P and can apparently act as an effective scavenger, thereby preventing P segregation. Guttman et al, suggest that Mo is also a strong carbide former and this reaction can negate the P scavenging effect⁽¹⁴⁰⁾.

A possible explanation for the mechanism of embrittlement of alloy 7 is that on ageing, microstructural changes involving the replacement of the original Fe_3C precipitation by Mo-based carbides, removing Mo from solid solution reduced its role in inhibiting embrittlement by P. Since carbide transformations also have some effect on the matrix composition and hence influence the thermodynamic driving force for segregation to boundaries. The kinetics of the process of embrittlement during ageing are controlled by the diffusion rate of the less mobile species taking part in the process at the temperature studied⁽¹⁴¹⁾. It is possible that the release of P by the formation of Mo-based carbides a site competition mechanism is established between P and Sb, which eventually leads to P segregation to grain boundaries as detected by auger analysis.

Another possible explanation for the embrittlement detected for alloy 7 involves the Ni-Sb interaction.

The transition from one type of carbide to another modifies the matrix composition and it is relevant to consider the effect of this modification on segregation. The change in carbide type has been correlated^(16,30,141) with grain boundary P content, however, no correlation with Sb has been reported.

For a Ni-Cr steel⁽¹⁶⁾ the increase of P segregation was associated with microstructural changes in carbide transformations and the growth of a Ni-Sn phase. The precipitation of these phases requires the segregated Sn to cluster, resulting in an initial decrease of the transition temperature followed by an increase as P segregates to the vacated boundary sites.

In view of the similarity between the behaviour of Sn and Sb in iron⁽¹³⁴⁾, their similar atomic radii (atomic radii for Sn and Sb are 1.57 and 1.61Å respectively⁽⁷²⁾), the formation of Ni-Sb⁽¹⁴²⁾ and that the presence of this phase has been associated with temper embrittlement⁽³⁵⁾, it is reasonable to suggest that the 600 ppm Sb addition for alloy 7 resulted in the formation of a Ni-Sb phase similarly to a Ni-Sn phase and during ageing this increased the grain boundary P segregation. Alloy 7 exhibited an initial decrease in transition temperature which could be associated with Sb segregation in clusters, followed by an increase in transition temperature after 2160 hours ageing, as shown in fig.151.

For an alloy of the same chemical base composition of alloy 7 without Sb (alloy 6) no embrittlement was observed. This would have been due to the fact that in the absence of a site competition mechanism the amount of P segregated was sufficient to cause a decrease of the upper shelf energy (fig.79) but not cause an intergranular mode of fracture. The fine carbide distribution probably contributed for this lowering by the mechanism previously described and schematically represented in fig.149.

The same effect was observed during the ageing sequence for alloy 7, however in the presence of 600 ppm Sb the P segregation was possibly enhanced by the formation of a Ni-Sb phase, similar to Ni-Sn phases observed in Ni-Cr alloys, leading to an intergranular mode of fracture. The increase in Ni content from 3 mass% in alloy 7 to 5 mass% in alloy 11, increased the susceptibility to embrittlement for an alloy containing 600 ppm Sb and 1 mass% Mo. As indicated by the ageing times required to induce any intergranularity in the low energy fracture mode (2160 hours for alloy 11 as opposed to 8760 hours for

alloy 7, see Table IVa). In fact a shift of +158°C in transition temperature was evident even for the sample aged for 24 hours which exhibited quasi-cleavage for the low energy mode of fracture (compare alloys 7 and 11, Table IVa). The kinetics of embrittlement were observed to be modified significantly when both P and Sb were present, as opposed to that in the presence of P, since for alloy 11 the onset of embrittlement was after 2160 hours ageing and for an alloy of identical chemical composition but without Sb, this occurred after 8160 hours ageing. A similar effect was observed for alloys containing 3 mass% Ni, alloys 4 and 5.

Alloy 11 exhibited similar behaviour to alloy 10 (i.e. a decrease in upper shelf energy for the earlier ageing times). However after extended ageing times, there was an increase in transition temperature (Table IVa) and a further decrease in upper shelf energy (fig.106) together with a mixed cleavage/intergranular fracture for the low energy mode.

Similarly for alloy 7, it is probable that on ageing the precipitation of Mo based carbides replacing the original Fe_3C , removed Mo from solid solution, releasing P, then a site competition mechanism would have been established between P and Sb. Since Ni can increase P activity and subsequently its segregation to grain boundaries it follows that Ni will increase the embrittling potency of P(30).

Another factor that may have contributed to the embrittlement of alloy 11 is the carbide distribution which consisted of a duplex distribution of carbides with large randomly distributed precipitates and a fine distribution within the grains (fig.108). This duplex distribution could have contributed to the overall

embrittlement. As discussed previously, a fine carbide distribution is likely to contribute to the lowering of the upper shelf energy because of the mechanism of void growth and coalescence for a large number of small carbides would require less energy than for a small number of large carbides (as described in fig.149). Furthermore, for this alloy the carbides were sited on grain boundaries. Therefore the impurity build-up (probably P) by rejection from carbides and diffusion out along the grain boundaries would have been sufficient to produce a mixed mode of fracture including cleavage and intergranular for the low energy mode of fracture.

4.3.3 The role of nickel and chromium

4.3.3.1 Cleavage-ductile transition

4.3.3.1(a) The base composition

The 3 mass% Ni, 1 mass% Cr alloy (alloy 2) exhibited the classical cleavage-ductile transition in the isothermally transformed upper bainite and ferrite-pearlite conditions throughout the ageing sequence as shown by the impact curves, figs.4 and 34 respectively.

The increase in hardness observed for alloy 2 (Table III(b)) in the ferrite-pearlitic condition with increasing ageing time was probably due to the fact that the material was not fully transformed. It is possible that on ageing at 430°C some bainite may have been formed, which contributed to the observed increase in hardness.

From transition temperature curves (fig.154) it can be seen that alloy 2, in the ferritic-pearlitic condition, exhibited an

upward shift in transition temperature, which perfectly fits the criterion from the cleavage-ductile transition. However, when considering alloy 2 in the isothermally transformed upper bainitic conditions, it can be seen that there is a decrease in transition temperature.

4.3.3.1(b) Effect of Sb addition in presence of Mo

The 3 mass% Ni 1 mass% Cr alloy containing 600 ppm Sb and 1 mass% Mo (alloy 3) in the isothermally transformed upper and lower bainite and in the ferrite-pearlite condition exhibited the cleavage-ductile transition, throughout the ageing sequence as shown by the impact transition curves figs.62, 65 and 64, respectively, the low energy mode of fracture being quasi-cleavage for all the microstructures describe above.

The higher hardness values observed in alloy 3 ranging from 393-468 Hv₃₀ in the ferrite-pearlite condition could have been due to the presence of 1 mass% Mo, since Mo additions increase hardness due to the solution strengthening effect.

The additions of Mo(1 mass%) and Sb (600 ppm) together reduced the uppershell energy exhibited by alloy 3 as compared to alloy 2 (base alloy) in the upper bainitic (fig.62), lower bainitic (fig.65) and ferritic pearlitic conditions. This indicates that the reduction described above was not associated with a specific heat treatment but rather with an effect of these additions on the intrinsic ductile fracture strength of alloy 3.

The 1 mass% Mo and 600 ppm Sb addition produced a shift of +128°C in transition temperature after 24 hours ageing, when compared with alloy 2 (Table IVa).

4.3.3.2 Reduction of the upper shelf energy

4.3.3.2(a) Effect of Sb addition

The 600 ppm Sb addition to an alloy containing 3 mass% Ni, 1 mass% Cr (alloy 1) produced a shift of +155°C in transition temperature after 24 hours ageing, in the ferrite-pearlite condition. During ageing there was an upward shift in transition temperature and a decrease in upper shelf energy, as seen in fig.34.

It has been reported⁽¹⁴³⁾ that the thickness of pearlitic-cementite lamellar and interlamellar spacing are expected to influence upper shelf energy via their influence on void nucleation and coalescence (though no unequivocal experimental data are available to support this view at present). Figures 36-39 however confirm that no significant changes occurred in such parameters for alloy 1 during the ageing sequence. The pearlitic cementite lamellar thickness will influence lamellar carbide cracking and thus void nucleation, moreover the lamellar spacing is also expected to affect upper shelf energy because it will influence the ease of void coalescence.

A comparison between alloy 2 and alloy 1 in the ferrite-pearlite condition (fig.34) showed that after Sb had been added there was a decrease in upper shelf energy and that it decreased further throughout the ageing sequence. However, to determine the mechanism that led to this lowering of the upper shelf energy further investigation is required.

4.3.3.3. Temper Embrittlement

4.3.3.3(a) The base composition

Alloy 2 (3 mass% Ni, 1 mass% Cr) in the quenched and tempered martensite condition exhibited an intergranular mode of fracture at different impact testing temperatures throughout the ageing sequence, e.g. at -196°C after 24 hours ageing (fig.17), at $+80^{\circ}\text{C}$ aged for 2160 hours (fig.18) and at ambient temperature after 8760 hours ageing (fig.19). Intergranular fracture was also observed for the low energy mode throughout the ageing sequence for this alloy (alloy 2) in the isothermally transformed lower bainite condition as seen in figs.41, 42 and 43.

The Cr:C ratio present in alloy 2 indicates that both M_3C and M_7C_3 can be expected to form, as reported by other authors^(87,144). Carbide transformations such as $\text{M}_3\text{C} \rightarrow \text{M}_7\text{C}_3$ have been associated with P segregation^(10,30,141), because P is more soluble in M_3C than in M_7C_3 ⁽¹⁶⁾, confirming P as the embrittling agent for alloy 2 in the quenched and tempered martensite condition, since the alloy contained 30 ppm P and the etching technique previously discussed (p.45) as seen in fig.29, using an etchant which mainly attacked grain boundaries containing P exhibited deep etching at the grain boundaries, a similar finding to that of Ogura et al⁽¹⁴⁵⁾ and Woodfine⁽¹⁴⁶⁾.

The transition temperature curve for alloy 2 in the quenched and tempered martensitic condition was almost constant throughout the ageing sequence, as seen in fig.155. Indicating that the P segregation to grain boundaries achieved some degree of equilibrium after 24 hours ageing at 430°C . Comparable results were obtained for a similar NiCr steel doped with P⁽⁷⁶⁾, where

grain boundary P saturation was achieved with 24 hours on ageing at 500°C (fig.156) further confirming the above hypothesis.

The rate of embrittlement as measured by the shift in transition temperature as a function of time has been related to the amount of impurity segregation (such as P) to the grain boundaries^(75,126) and this has been observed to decrease⁽⁷⁵⁾ with increasing ageing time.

It has been shown⁽⁴²⁾ that during diffusion controlled equilibrium segregation, the grain boundary concentration of solute builds-up relatively quickly to about half of its equilibrium value, but the rate then slows down as higher concentrations are reached. Furthermore, the C-curve behaviour of the time-temperature kinetics of temper embrittlement and the decrease in embrittlement rate with time are qualitatively consistent with a diffusion controlled equilibrium impurity segregation model.

It is likely that a similar mechanism of embrittlement occurred for the base composition (alloy 2) in the isothermally transformed lower bainitic structure, however in this case the impurity segregation equilibrium was not reached since the transition temperature increased with increasing ageing time, as seen in fig.155. Therefore it appears that the rate of carbide transformations that leads to temper embrittlement were slower in the isothermally transformed lower bainite than that occurring in the quenched and tempered martensitic condition. It is shown that the onset of temper embrittlement for the isothermally transformed lower bainite occurred after 720 hours ageing at 430°C while it occurred after only 24 hours for the quenched and tempered martensitic condition.

From TEM work for alloy 2 in the lower bainitic condition, it was observed that there was a change in carbide distribution from 24 hours (fig.47) to 2160 hours ageing (fig.48), showing discrete grain boundary carbides, increasing carbide precipitation and a decrease in dislocation density with ageing time. In this case the change in carbide distribution appears to be the dominant effect, because the increased precipitation at the grain boundaries certainly contributed to the embrittlement of this alloy.

The fact that temper embrittlement was present in alloy 2 in the lower bainitic condition shows that the presence of Ni and Cr were necessary to promote impurity segregation to a level at which the alloy would fail by an intergranular mode of fracture. Since for a C-3 mass% Ni alloy (alloy 4) containing 30 ppm P as impurity (the same as alloy 2) temper embrittlement did not occur in the lower bainitic condition.

Carbide in lower bainites are distributed mainly within the laths though also on the lath and prior austenitic grain boundaries. The impurity enrichment at the grain boundaries will depend on the embrittlement potency of the elements present in the alloy. Thus on ageing the embrittling species rejected (such as P) due to carbide transformation, e.g. M_3C M_7C_3 will interact with alloying elements in solution, such as Cr which will enhance P segregation⁽⁹²⁾. As a result of the interaction of Cr and C, the decrease in C activity will enhance P segregation leading to temper embrittlement.

4.3.3.3(b) Effect of Sb addition

For the alloy of identical base chemical composition to alloy 2 but containing 600 ppm Sb (alloy 1) temper embrittlement was present in the quenched and tempered martensitic condition after 24 hours ageing at 430°C (fig.16) moreover, this alloy exhibited an intergranular mode of fracture even at high temperature (+80°C) impact testing, as seen in fig.15, indicating severe embrittlement. Figure 20 shows the typical mode of fracture exhibited by alloy 1 in the quenched and tempered martensitic condition.

Temper embrittlement was also present in the isothermally transformed lower bainitic condition after 2160 hours ageing at 430°C (fig.44), and in the upper bainitic condition after 8760 hours ageing at 430°C, fig.5. Observe that alloy 1 in the upper bainitic condition exhibited a mixed mode of fracture at +200°C impact testing temperature including cleavage and intergranular, as seen in fig.3.

The transition temperature data obtained for alloy 1 in the quenched and tempered martensitic condition, isothermally transformed upper and lower bainite were only approximate since this alloy did not exhibit any true ductile fracture and, therefore, not a true upper shelf energy. Thus the decrease in transition temperature observed for the upper and lower bainitic condition (Table IVa) cannot be considered as a real effect, such as de-embrittlement. However, the apparent transition temperature for the quenched and tempered martensitic condition exhibited an increase with increasing ageing time. This effect could have been due to the fact that, in spite of this alloy exhibiting an intergranular mode of fracture on high temperature

impact testing, it maintained high energy values. Therefore, the transition temperature values are apparently consistent with the presence of temper embrittlement in these alloys.

4.3.3.3(c) Effect of Sb in presence of Mo

In the case of alloy 3 (of otherwise identical chemical composition to alloy 1), the presence of 1 mass% Mo merely retarded the onset of temper embrittlement, which was manifest after 2160 hours ageing (fig.51) and increased further with increasing ageing time since this alloy exhibited an intergranular mode of fracture at high temperature impact testing e.g. at +80°C (fig.53) and even at +200°C (fig.54).

Molybdenum has a strong affinity for P and it can apparently act as an effective scavenger thereby preventing P segregation to grain boundaries. Once precipitation of Mo containing carbides takes place however, and Mo is taken out of solution, P segregation to grain boundaries is likely to occur. By contrast, the hardness increased by 116 Hv₃₀ points (as compared with alloy 1 in the quenched and tempered martensitic condition, after 24 hours ageing (see Table IIIa) and such increases in hardness due to Mo additions are considered to increase temper embrittlement susceptibility⁽¹²⁵⁾ since this increases the difficulty of relaxing stress concentrations at grain boundaries and intergranular cracks by plastic deformation. The increase in hardness, per se, did not increase the susceptibility to embrittlement because this then would have been present after 24 hours ageing at 430°C, coinciding with the fact that for this ageing time the microstructure was relatively free of precipitation (fig.57).

After extended ageing (2160 hours) this alloy exhibited an intergranular mode of fracture, indicating that temper embrittlement developed, probably due to the formation of the Mo-rich carbides.

Alloy 3 contained 1 mass% Cr, both Cr and Mo are comparatively strong carbide formers. Therefore, it can be expected that the development of temper embrittlement in this alloy would be a function of the carbide population since changes in dissolved Cr and Mo levels will have an effect on segregated P at the boundaries⁽¹⁵⁵⁾ e.g. increases in dissolved Mo and decreases in dissolved Cr combine to reduce P segregation up to 0.6-0.7 mass% Mo, while the increase in dissolved Cr level increases P segregation for Mo contents 0.6-0.7 mass%.

However, it is difficult to separate the effects associated with Cr and Mo since Mo may stop segregation of P by forming Molybdenum Phosphorus phases when in solution whereas a decrease in dissolved Cr could produce a similar result. Additionally P segregation at high Mo contents can be due to increasing amounts of M_6C precipitation reducing the level of C solute on the boundaries, which would be consistent with the results of Erhart and Grabke⁽⁹²⁾ regarding grain boundary site competition between C and P.

The role of Sb in the embrittlement process of alloy 3 is not clear, it is possible that a Ni-Sb interaction occurs, as described previously for an alloy with Sb (alloy 1) or a site competition between P and Sb as suggested for alloy 7 (C-3 Ni). Further work is required to determine the mechanism.

4.3.4 The role of microstructure

4.3.4.1 Carbide transformation in the quenched and tempered martensitic condition

In the quenched and tempered martensitic condition the grain boundary precipitation sequence for alloy 1 was:

(M_3C) ($M_3C + M_7C_3$) ($M_3C + M_7C_3 + Mn$ containing G-phase), with increasing ageing time⁽⁹⁹⁾. This sequence is similar to those found in Ni-Cr alloys^(74,75,90,141,147) more precisely the presence of M_7C_3 is associated with the enhancement of temper embrittlement and generally found to be a carbide rich in Cr in this type of alloy^(90,141) which is in agreement with the findings of this work as shown by the EDX analysis, fig.135.

The presence of M_7C_3 was associated with P segregation, this element having been consistently detected by Auger analysis (e.g. fig.129) on the same area of fracture surface as the carbide. Ni was apparently associated with P segregation because, as shown by the Auger spectra, there was an increase in the Ni peak for the intergranular area when compared with the ductile area, as seen in figs.129 and 130 respectively. Indicating that Ni was segregated with P to the grain boundaries. However, Auger maps from the area described above, (fig.131), show the distribution of Ni (fig.132) and P (fig.133) on the intergranular surface. These show that Ni was evenly distributed over the entire area whereas P was clearly present only on the intergranular surfaces suggesting that Ni was not co-segregated with P to the grain boundaries. After extended ageing times (2160 hours at 430°C), it was observed that Sb had segregated to the grain boundaries, as shown in fig.138, and that after 17,520 hours (fig.140) this alloy showed both P and apparently Sb (though a very small peak) segregated to the grain

boundaries, though not to levels as significant as shown previously for 24 hours ageing.

Therefore, it appears that the change from one type of carbide to another modifies the matrix composition sufficiently to alter the segregation behaviour of impurity elements. For instance the depletion of the matrix of Cr by the formation of M_7C_3 increases the thermodynamic driving force for P segregation to grain boundaries. Taking into account other microstructural changes occurring at the same time as the $M_3C \rightarrow M_7C_3$ transformation, for instance a phase such as NiSn as reported by Edwards et al⁽¹⁶⁾. It is relevant to consider that these changes, occurring in the matrix composition, can lead to the segregation of other impurities present in the steel, such as Sb.

The influence of alloying elements^(88,92,136) such as Cr (or V) which form carbides more stable than cementite will decrease the carbon activity allowing extensive P at the grain boundaries. The beneficial role of C is complex⁽¹⁴⁸⁾ since it drives alloying elements (M) to the grain boundaries as a result of the large M-C attraction, but it opposes P segregation because of the large repulsive P-C interaction. In most steels⁽¹²⁶⁾, C behaviour is extremely complex since its concentration is well in excess of the solubility limit in ferrite, therefore both the soluble and precipitated carbon are involved in the segregation process.

Therefore, the replacement of M_3C by a Cr-rich M_7C_3 reduces the solute C level at the boundary (decreasing C activity) which then allows P to segregate to the vacated sites⁽⁹²⁾ as observed for alloy 1 in the quenched and tempered martensitic condition after 24 hours ageing.

The variation in Ni, Sb and P peak heights as a function of ageing time (fig.157) show a simultaneous decrease in segregation for these elements with increasing ageing time. Sb segregation was detected only after 2160 hours ageing and this coincides with a large increase in Ni segregation, suggesting that Sb segregation was directly related to that of Ni and there are indications that Ni and Sb formed a compound type Ni_xSb_y analogous to Ni_3Sn found in Ni-Cr alloy, as suggested by Edwards et al⁽¹⁶⁾. SIMS data for alloy 1 in the quenched and tempered martensitic condition (fig.137) showed that $Sb^{(121)}$ and $Sb^{(123)}$ mass species were present on the intergranular fracture surface indicating that Sb was present in the compound form because of the shift in energy as indicated by the arrows in fig.137, as well as in the atomic form as shown in the Auger graphs.

After prolonged ageing, 8760 hours, in addition to the Sb is a compound form as indicated by the SbL peak in fig.139, there was also Mn-containing G-phase found at the prior austenite grain boundary. Considering Mn-containing G-phase as an intermetallic compound⁽¹⁴⁹⁾ it can be related to the type of intermetallic compound suggested by Guttman^(35,124) which promote embrittlement.

Mn-containing G-phase contains Si and the presence of Mn and Si⁽¹⁵⁰⁾ at the grain boundaries of a Ni-Cr has been associated with tempered embrittlement. It also has been reported⁽¹⁵¹⁾ that in tempered martensite, for Si-containing steels, a Si-rich layer forms at the cementite-ferrite interface. The solubility of Si in cementite is extremely low. SIMS analysis for alloy 1, aged for 17,520 hours (fig.141), showed that Ni, Mn, Si and P were

present on the intergranular fracture surface and confirmed the presence of Mn-containing G-phase, at that surface.

However, the presence of the Mn-containing G-phase did not seem to play any relevant role in the process of temper embrittlement since the increase of C activity caused by Si and Ni in martensite⁽¹³⁸⁾ did not inhibit P segregation, as seen in the Auger spectra, fig.140, and confirmed by SIMS analysis, fig.141.

From the results obtained for alloy 1 (fig.157) it can be suggested that the temper embrittlement detected was not a result of equilibrium segregation, since Sb and Ni grain boundary concentrations decrease with increasing ageing time. McMahon et al⁽⁹⁰⁾ reported a similar type of embrittlement, though in his alloys, Ni and Sb concentrations at grain boundaries reached an equilibrium after 2000 hours ageing and the transition temperature was observed to increase by inference, as seen in fig.158a and 158b. Although there is a small decrease in the grain boundary concentration of Sb and P as indicated in fig.157, the low energy mode of fracture was intergranular for all ageing times. Therefore, the decrease in grain boundary impurity levels observed did not affect the severity of embrittlement.

The Ni/Sb atom fraction at the grain boundaries was found to decrease with ageing time, from 3.5 at 2160 hours to the same level as the bulk concentration at 17,520 hours, in accordance with McMahon et al⁽⁹⁰⁾. There are suggestions however⁽¹⁵²⁾ that the Ni/Sb ratio increases with increasing ageing temperature. Therefore, the Ni/Sb ratio will be dependent on the microstructural changes, such as carbide transformations, since

Cr depletion in the matrix due to carbide formation can have a potent effect in limiting the segregation of Ni and Sb⁽¹²⁶⁾. Furthermore Ni depresses the solubility of Sb in Fe much more than Cr does⁽¹⁵³⁾ and an alloying element with a strong attraction for Sb, such as Ni/Sb interaction will promote co-segregation of these elements⁽¹³⁴⁾.

It appears from the data obtained in this work, that there is a strong interaction between Ni and Sb, because the onset of Sb segregation coincides with an increase in Ni segregation, as shown in fig.157, and that P segregation is directly related to the type of carbide present, i.e. M_7C_3 (Cr-rich), which is in agreement with Edwards et al⁽¹⁶⁾.

Extended ageing (17,520 hours) showed that grain boundary concentration of Ni and Sb decreased, as seen in fig.157. This behaviour is analogous to that observed for a Ni-Sn phase⁽¹⁶⁾ (fig.159)

According to fig.157 Sb could have been expected to be detected on the intergranular fracture surface of alloy 1 after 2160 hours ageing, however, this was not shown by the Auger spectrum fig.138. One possible explanation is that preferential segregation occurred to the prior austenite boundaries when the steel was held in the embrittling temperature range⁽⁷³⁾. Studies on structure-dependent intergranular segregation of P in a Ni-Cr steel⁽¹⁴⁵⁾ revealed that the degree of P segregation can vary greatly from one boundary to another and along individual stepped boundaries. In the above study⁽¹⁴⁵⁾ the degree of segregation was associated with the degree of grain boundary coherency. High energy boundaries were found to be depleted in P with respect to

low energy boundaries. Therefore it is possible that P was not detected as a result of a preferential segregation phenomena.

Si segregation was significant as seen in figs.129 and 140. There was an increase in Si segregation with increasing ageing time, as seen in fig.157. Therefore it seems likely that Si has an important influence on the segregation process since it can interact with other elements including C⁽¹⁶⁾ and the major alloying elements. Furthermore, Si is virtually insoluble in the carbides⁽¹⁵⁴⁾ and may have a very large effect upon rate of growth of carbides. Since the build-up of Si around the growing particle causes an increase in the activity of C in this region, thereby decreasing the flux of C to the particle.

Since P segregation is directly related to the microstructural changes it is possible that there is a relationship between these two effects. However, a more complete understanding of the role played by Si would require further work.

4.3.4.2 Carbide transformation in the isothermally transformed upper bainitic condition

The precipitation sequence in the isothermally transformed upper bainitic condition for alloy 1 was $M_3C \rightarrow M_3C + M_7C_3$. M_7C_3 was present in very small quantities⁽⁹⁹⁾. The predominant carbide M_3C was low in Cr as shown by the EDX analysis, fig.124. In this, lay one of the main differences between the bainitic and the martensitic structure. Since the intergranular mode of fracture, was observed only after 8760 hours ageing (Table Va) for the upper bainite indicating that the rate of embrittlement was slower for this structure than for the martensitic condition.

Phosphorus was detected after extended ageing (17,560 hours) at 430°C as seen in the Auger spectra, fig.119. Although the P peak was somewhat small it was not detected at all for a cleavage region of the sample, indicating that P was segregated at the grain boundaries. Observe that though M_7C_3 was present in very small amounts, it was likely to influence the amount of P segregated. Auger mapping of this region showed that Ni and Sb segregated to the same region, i.e. to the grain boundaries, as seen in fig.123.

The Ni/Sb ratio increased with ageing time from 1.4 at 8760 hours to 2.7 at 17,520 hours indicating that, similarly to the martensitic condition, a compound type Ni_xSb_y was likely to have been precipitated. The suggestion is further supported by an Auger map of an iron etched surface, fig.128, of the same sample aged for 8760 hours, which show a localised enrichment in Sb distribution, suggesting that Sb was in the form of clusters, probably with Ni, as indicated by the increasing Ni/Sb ratio. Sb was also segregated in the form of clusters to the cleavage facets, as indicated by SIMS analysis in fig.125, suggesting that possibly similar mechanisms of carbide impurity rejection were in operation for the interlath carbides which lay on the cleavage facets.

Therefore, it appears that, from the results obtained for the isothermally transformed upper bainitic condition, Sb was co-segregated with Ni to the grain boundaries and also in the form of a compound probably Ni_xSb_y similar to the quenched and tempered martensite conditions. The difference in rate of embrittlement compared with that observed in the martensitic

structure appears to be due to the small amount of M_7C_3 . This is in agreement with Othani et al⁽¹⁵²⁾ findings, i.e. that embrittlement process started by carbide transformation should proceed initially at a faster rate than that started by Sb segregation.

4.3.4.3 Microstructural Characteristics of Upper and Lower Bainite

In comparing the transition temperature data obtained for the isothermally transformed upper bainite and lower bainite (Table IVa), it can be seen that an alloys without Sb (alloy 2), followed the classical model i.e. they showed a higher ductile brittle transition temperature in the upper bainitic than in the lower bainitic condition. This difference is attributed to the wider transition range in lower bainite than in upper bainite⁽¹⁴³⁾ due in turn to:

- (1) the easy initiation of cleavage cracking in upper bainite due to the large inter lath carbides, and the inability of the low-angle bainitic ferrite lath boundaries to impede cleavage crack propagation, and
- (2) the fine carbides within laths of lower bainite which impede cleavage crack propagation.

However, the same behaviour was not observed for the alloy containing 600 ppm Sb (alloy 1), the DBTT values being higher for lower bainite than for upper bainite. Observe, that the relative strength (Table IIIa and IIIb) for both conditions were comparable.

It appears that in the bainitic structure the carbide distribution and the alloy composition are of extreme importance. Alloy 1 was shown to be more susceptible to temper embrittlement in the lower bainitic condition than in the upper bainitic condition. Since the onset of intergranular mode of fracture (Table Va and Vb) was detected after 2160 hours ageing at 430°C for the lower bainite and after 8760 hours for the upper bainite. TEM work for alloy 1 in the upper bainite condition showed that the long axis of the carbides was perpendicular to the grain boundaries implying that they grew into the grains rather than along the boundaries as seen in figs.7, 8 and 9. This type of carbide distribution could have favoured cleavage instead of an intergranular mode of fracture, because the acicular shape of these carbides would act as a stress-raiser enhancing propagation and even nucleation of cleavage cracks.

The microstructural characteristics of upper bainite which favours, and of lower bainite which impede, cleavage crack propagation are consistent with the findings of this work. Since in lower bainite, for alloy 1 containing 600 ppm Sb, the onset of temper embrittlement was detected at earlier ageing times (2160 hours) than that found in the upper bainite (8760 hours), it seems that subtle variations in carbide distribution, allied to alloy composition, can greatly increase the susceptibility to embrittlement of bainitic structures since temper embrittlement was not detected in the upper bainitic condition for an alloy with Sb (alloy 2).

4.4 Overview of Compositional Effects

From the data obtained in this work it was clear that, for the alloys studied, the quenched and tempered martensitic condition was more susceptible to embrittlement than the bainitic or the pearlitic condition. It was suggested that the difference in susceptibility of the martensitic condition to temper embrittlement compared with the bainitic condition was associated with the carbide morphology and distribution, intrinsic to the formation of these microstructures, together with bulk composition and microstructural changes occurring during ageing at 430°C. Ni containing alloys (group 2) were shown to be susceptible to temper embrittlement when in the quenched and tempered martensitic condition, but not in the isothermally transformed pearlitic or bainitic condition. However, Ni-Cr alloys (group 3) were susceptible to temper embrittlement in both conditions, quenched and tempered martensitic and isothermally transformed bainitic, thus indicating that the carbide morphology and distribution, intrinsic to a given microstructure and the associated changes during ageing, were dependent upon the bulk composition. The precipitation sequence for a C-3Ni 1Cr Sb (alloy 1) in the martensitic condition was identified as $(M_3C) (M_3C + M_7C_3) (M_3C + M_7C_3 + \text{Mn containing G-phase})$. The carbide transformation from M_3C to M_7C_3 decreased C activity which in turn favoured P segregation to grain boundaries which led to an intergranular mode of failure together with an upward shift in transition temperature. In the case of the isothermally transformed bainitic condition the dominant carbide, for the same alloy 1 (C-3Ni, 1Cr Sb) was M_3C and Sb was found to co-segregate

with Ni to the prior austenitic grain boundaries, forming a Ni_xSb_y compound similar to NiSn , producing an intergranular mode of fracture. Therefore, it seems that temper embrittlement, for the alloys in this study, was not only a phenomenon dependent on impurity segregation to grain boundaries, but also a phenomenon which will depend on the microstructure present and the bulk composition. These will then be responsible for the interactions between impurities and alloying elements occurring as a consequence of the microstructural changes during ageing.

CONCLUSIONS

1. The quenched and tempered martensitic condition was the most susceptible to temper embrittlement, followed in turn, by the bainitic and pearlitic microstructures.
2. The quenched and tempered martensitic condition embrittled at a faster rate than the isothermally transformed bainitic structure.
3. The precipitation sequence with increasing ageing time for alloy 1 in the quenched and tempered martensitic condition was (M_3C) $(M_3C + M_7C_3)$ $(M_3C + M_7C_3 + \text{Mn-containing G-phase})$.
4. The precipitation sequence in the isothermally transformed bainitic condition for alloy 1 was (M_3C) $(M_3C + \text{extremely small quantities of } M_7C_3)$.
5. Alloy 1 (0.3 mass% C, 1 mass% Cr, 3 mass% Ni) in the quenched and tempered martensitic condition aged for 24 hours at 430°C was embrittled by P segregated at the grain boundaries due to the decrease in C activity promoted by the formation of Cr-rich carbide (M_7C_3) .
6. At later ageing times (17,520 hours) for alloy 1 in the quenched and tempered martensitic condition, Ni and Sb co-segregated to the grain boundaries.

7. The dominant carbide in the bainitic microstructure (M_3C) increased the C activity at the prior austenitic grain boundaries preventing P segregation and intergranular failure in the early stages of the ageing treatment.
8. Mo was not effective in preventing embrittlement in the quenched and tempered martensitic condition, except for alloys 8 and 9 containig high Mo (4 mass%) and negligible amounts of Ni and Cr.
9. The rate of embrittlement for the tempered martensitic condition increased with increasing Ni content.
10. The bainitic microstructure was less susceptible to temper embrittlement because, the carbide morphology and distribution intrinsic to the formation of these microstructures, together with bulk composition and microstructural changes occurring during ageing are more likely to favour a cleavage mode of fracture in the bainitic condition than in the quenched and tempered martensitic condition.

REFERENCES

1. M. P. Seah and E. D. Hondros Proceedings of NATO Advanced Research Institute "Atomistic of Fracture", 22-21 May 1981, San Bastiano, Corsica, Plenum, New York.
2. P. R. Irving, M. P. Seah and K. Kurzfeld, Proc. 2nd Int. Conf. on Mech. Behav. of Materials, Boston ASM (1976), 563.
3. S. K. Banerji, C. J. McMahon and H. C. Feng, Met. Trans. 9A (1978), 237.
4. C. Lea, Met. Sci. 14 (1980), 107.
5. E. D. Hondros and C. Lea, Nature 289 (1981), 663.
6. M. G. Nicholas and C. F. Old, J. Mat. Sci. 14 (1979), 1.
7. D. A. Melford, Phil. Trans. R. Soc. Lond. A295 (1980), 89.
8. C. Lea, R. Sawle and C. M. Sellars, Phil. Trans. R. Soc. Lond., A295 (1980), 121.
9. B. L. King, Phil. Trans. R. Soc. Lond. A295 (1980), 235.
10. H. R. Tipler, Phil. Trans. R. Soc. Lond. A295 (1980), 213.
11. M. P. Seah, Surface Science 53 (1975), 168.
12. C. L. Briant and S. K. Banerji, Int. Met. Rev. No.4, 232 (1978), 164.
13. C. J. McMahon, Jr., ATM STP 407 (1968), 127.
14. M. P. Seah, Acta Met. 28 (1980), 955.
15. H. Jolivet, G. Vidal, Rev. Met. 41 (1944), 378.
16. B. C. Edwards, B. L. Eyre and C. Gage, Acta Metall.

- 28 (1980), 335.
17. B. C. Woodfine, JISI, 173 (1953), 229.
 18. R. H. Greaves, J. A. Jones, JISI III (1925), 231.
 19. J. B. Cohen, A. Hurlich, M. Jacobson Trans. ASM, 39 (1947), 109.
 20. D. McLean and L. Northcott, JISI, 158 (1948), 169.
 21. A. Preece and R. D. Carter, JISI, 173 (1953), 387.
 22. W. Steven and K. Balajiva, JISI, 193 (1959), 141.
 23. J. R. Low, D. F. Stein, A. M. Turkalo and L. P. Laforce, Trans. of Metall. Soc. of AIME, 242 (1968), 14.
 24. M. C. Inman and H. R. Tipler, Acta Met. 6 (1958), 73.
 25. M. C. Inman and H. R. Tipler, Metall. Review 8 (1963), 105.
 26. J. H. Westbrook, Metallurgical Reviews, No.36, 9 (1964), 415.
 27. E. D. Hondros and M. P. Seah, International Metals Reviews, December (1977), 262.
 28. D. P. Stein, A. Joshi and R. P. Laforce, Trans ASM 62 (1969), 776.
 29. H. L. Marcus and P. W. Palmberg, Trans AIME, 245 (1969), 1664.
 30. R. Viswanathan, Met. Trans., 2 (1971), 809.
 31. P. W. Palmberg and H. L. Marcus, Trans ASM, 82 (1969), 1016.
 32. K. Balajiva, R. M. Cook and D. K. Worn, Nature, 178 (1956), 433.
 33. J. R. Rellick and C. J. McMahon, Jr., Metall. Trans. 5 (1974), 2439.

34. E. B. Kula and A. A. Anctil, J. Mater ASTM 14 (1969), 817.
35. M. Guttman, Surface Science 53 (1975), 213.
36. C. J. McMahon, ASTM STP 407 (1968), 3.
37. G. Clark, O. Ritichie and J. F. Knott, Nature Phys. Sci., 239 (94), (1972), 104.
38. P. R. Krahe and M. Guttman, Scripta Met. 7 (1973), 387.
39. M. Guttman, P. R. Krahe, F. Abel, G. Amsel, M. Bruneaux and C. Cohen, Met. Trans. 5 (1973), 167.
40. M. Guttman and P. R. Krahe, Mem. Sci., Rev Met., 70 (1973), 657.
41. P. V. Ramasubramanian and D. F. Stein, Met. Trans. 3 (1972), 2939.
42. D. McLean, Grain Boundaries in Metals, Oxford (1956), Ch.5.
43. B. L. Eyre, B. C. Edwards and J. M. Titchmarsh, (Advances in the Physical Metallurgy and Application of Steel), Proc. Int. Conf. Metals Society, University of Liverpool, 21-24 September (1981) 246.
44. K. T. Aust and J. H. Westbrook, Lattice Defects in Quenched Metals, 1965, p.771, Academic Press.
45. T. R. Anthony, Acta Met., 17 (1969), 603.
46. E. D. Hondros and D. McLean, Grain Boundary Structure and Properties, G. A. Chadwick and D. A. Smith, Academic Press, New York (1976), 265.
47. M. P. Seah and E. D. Hondros, Proc. Roy. Soc., A335 (1973), 191.
48. C. L. White and W. A. Coghlan, Metall. Trans.,

8A Sept. (1977), 1403.

49. J. P. Eshelby, Proc. Roy. Soc. London, A 241 (1957), 376.
50. E. D. Hondros, Proc. Roy. Soc. A286 (1965), 479.
51. P. V. Ramasubramanian and D. F. Stein, Met. Trans., 4 (1973), 1735.
52. A. W. Thompson, Grain Boundaries in Engineering Materials, J. L. Walter, J. H. Westbrook and D. A. Woodford, Eds., Proc. 4th Bolton Landing Conf., (1974), 607.
53. J. P. Stark and H. L. Marcus, Metall. Trans. A, 8A (1977), 1423.
54. W. Losch, Scripta Met. 13 (1979), 661.
55. W. Losch, Acta Met. 27 (1982), 1885.
56. W. Losch and I. Andreoni, Scripta Met. 12 (1978), 277.
57. W. Losch, Acta Met., 27 (1979), 567.
58. S. P. Walch, W. A. Goddard, III Surface Sci. 72, (1978), 645.
59. E. Anda, W. Losch, N. Majlis and J. E. Ure, Acta met. 30 (1982), 611.
60. E. S. Machlin, Scripta Met. 15 (1981), 413.
61. H. L. Joki, V. Vitek and C. J. McMahon, Jr., Acta Met., 28 (1980), 1479.
62. R. P. Messmer and C. L. Briant, Acta Met., 30 (1982), 457.
63. H. Viefhaws, R. Moller, H. Erhart and H. S. Grabke, Scripta Met., 17 (1983), 165.
64. M. A. Grossman, Trans AIME 39 (1946), 167.
65. B. S. Lement, B. L. Averbach, M. Cohen, Trans ASM

46 (1954), 851.

66. L. J. Klinger, W. J. Barnett, R. P. Frohberg and A. R. Troiano, 46 (1954), 1557.
67. T. Inoue, Grain Boundaries in Engineering Materials, (4th Bolton Landing Conference), (ed. J. L. Walter et. al.) (1975), 553, Baton Rouge, Claiborne's Publishing Division.
68. B. J. Schultz and C. J. McMahon, Jr., ASTM STP 499 (1972), 104.
69. T. Inoue, K. Yamamoto and S. Sekiguchi, Trans. ISI jpn, 14 (1974), 957.
70. J. E. King and J. F. Knott, Metal Science, January (1981), 1.
71. R. Viswanathan, ASTM STP 672 (1978), 169.
72. M. Nageswara Rao, C. J. McMahon, Jr., A. Herman, Met. Trans. 5 (1974), 1061.
73. A. Joshi, Scripta Met., 9 (1975), 251.
74. H. Othani and C. J. McMahon, Jr., Acta Metall., 23 (1975), 377.
75. R. Viswanathan and T. P. Sherlock, Metall. Trans. 3 (1972), 459.
76. R. A. Mulford, C. J. McMahon, D. P. Pope and H. C. Feng, Met. Trans., 7A (1976), 1183.
77. A. J. Baker, P. M. Kelly and J. Nutting, Electron Microscopy and Strength of Crystals, (1961), 899, Interscience.
78. M. G. Wells, Acta Met., 12 (1964), 389.
79. C. J. Barton, Acta Met., 17 (1969), 1085.
80. E. Tekin and P. M. Kelly, Precipitation from Iron Base Alloys, (1965), 173, Gordon and Breach

Science Publishers, London.

81. R. W. Baluffi, et. al., Trans ASM 43 (1951), 497.
82. E. Smith and J. Nutting, JISI, 187 (1957), 314.
83. F. B. Pickering, 4th International Conf. on Electron Microscopy, 1958, Berlin.
84. A. K. Seal and R. W. K. Honeycombe, JISI, 188 (1958), 9.
85. K. C. Mills et. al., JISI, 197 (1961), 9.
86. J. Beech and D. H. Warrington, JISI 204 (1966), 460.
87. D. J. Dyson and K. W. Andrews, JISI Feb. (1969), 208.
88. R. Viswanathan and A. Joshi, Metall. Trans., 6A (1975), 2289.
89. H. Othani, H. C. Feng and C. J. McMahon, Jr., Metall Trans., 5 (1974), 516.
90. C. J. McMahon, Jr., E. Furubayashi, H. Othani and H. C. Feng, Acta Metall., 24 (1976), 695.
91. J. M. Titchmarsh, B. C. Edwards, G. Gage and B. L. Eyre, Nature, 38 (1979), 278.
92. H. Erhart and H. J. Grabke, Met. Sci., 15 Sept. (1981), 401.
93. A. K. Cianelli, H. C. Feng, A. H. Vcisik and C. J. McMahon Jr., Met. Trans. A, 8A July (1977), 1059.
94. B. C. Edwards, B. L. Eyre, T. E. Cranshaw, Nature 269, Sept. (1977), 47.
95. R. P. Elliott, Constitution of Binary Alloys, 1st Suppl. (McGraw-Hill, New York), (1965), 674.
96. J. Q. Clayton and J. F. Knott, Metal Science 16

- (1982), 145.
97. B. Clark and A. Wirth, Proc. Int. Conf. Metals Society, University of Liverpool, 21-24 September (1981), 272.
 98. A. Wirth and B. Clark, Metals Technology, April (1981), 161.
 99. A. Wirth, I. Andreoni and J. Tichmarsh, Inst. Phys. Conf. Ser. No. 68, Chapter 9, (1983), 297.
 100. J. Durnin and R. A. Ridal, JISI, January (1968), 60.
 101. M. H. Loretto, Electron Beam Analysis of Materials, Chapter 2, Pub. Chapman and Hall, (1984).
 102. C. Lea, Metal Science, 17 (1983), 357.
 103. A. Joshi, Interfacial Segregation Seminar, ASTM (1977), 39.
 104. D. Briggs and M. P. Seah, Practical Surface Analysis, Ed. John Wiley and Sons, 1983.
 105. A. W. Czanderna, Methods of Surface Analysis, Elsevier (1975).
 106. F. A. White, Mass Spectroscopy in Science and Technology, Ed. John Wiley and Sons, Chapter 2, (1968), 40.
 107. P. E. J. Flewitt and R. K. Wild, Microstructural Characterisation of Metals and Alloys, The Institute of Metals, 1985.
 108. S. R. Shrader, Introductory Mass Spectroscopy, Ed. D. H. Busch and H. Shull, 1974.
 109. A. Wirth, J. Tighmarsh, I. Bott, (unpublished work).

110. F Smith Proc. Conf. Phys., Basis on yield and fracture, 36, Inst. Phys. Soc., Oxford, 1966.
111. A Joshi and D F Stein, ASTM, STP, 499 (1972), 59.
112. A Joshi and D F Stein, J. Inst. Metals, 99 (1971), 178.
113. J M Capus, ASTM, STP, 407 (1968), 3.
114. J R Low, Trans., AIME, 245 (1969), 2481.
115. E D Hondres and D McLean, Phil. Mag., 29 (1964), 771
116. F Knott, Fundamentals of Fracture Mechanics, Ed. Butterworths, 1973.
117. G W Austin, A R Entwistle, G C Smith, JISI, 173 (1953), 376.
118. P A Restaino, C S McMahon Jr, Trans. ASM, 60 (1967), 699.
119. A E Powers, Trans. ASM, 48 (1956), 149.
120. A E Powers, JISI, 186 (1957), 323.
121. G Vidal, Rev. Met., 42 (1945), 149.
122. D L Newhouse and H G Holtz, ASTM, STP, 407 (1968), 106.
123. J Common, P F Martin, P G Bastien, ASTM, STP, 407 (1968), 74.
124. M Guttman, Metal. Sci., 10 (1976), 337.
125. M L Wayman, P de Moulin, M Guttman, Can. Metall. Q, 16 (1977), 57.
126. R A Mulford, C J McMahon Jr., D P Pope, H C Feng, Metall. Trans., 7A (1976), 1269.
127. T Gladman, B Holmes, I D McIver, Proc. Conf. Effect of second phase particles on the mechanical properties of steel, 151, 24-25 March 1971.
128. G T Hahn and A R Rosenfield, Metall. Trans., 6A (1975), 653.
129. S H Goods and L H Brown, Meta. Metall., 27 (1979), 1.

130. H F Fischmeister, E Navara and K E Easterling, Metals. Sci., 6 (1972), 211.
131. J E King and J F Knott, Metals. Sci., 15 (1981), 1.
132. J F Fischer and J Gurland, Metals. Sci., 15 (1981), 193.
133. M Tuttmann, Phil. Trans. & Sco., London, A.295 (1980), 169.
134. P Fias, M Guttman and J Bernardini, Acta. Met., 30 (1982), 1309.
135. C A Norstrom, O Vingsbo, Metal. Sci., December (1979), 677.
136. B V Narashima Rao and G Thomas, Metall. Trans., 11A (1980), 557.
137. M Sarikava, B G Steinberg and G Thomas, Metall. Trans., 13A (1982), 2227.
138. H W King and S Glover, JISI, 1960 (1960), 281.
139. R P Smith, Trans. AIME, 218 (1960), 62.
140. C J McMahon Jr., A K Cianelli and H C Feng, Metall. Trans. A, Vol.8A (1977), 1055.
141. J I Ustinovshiko, Metal. Sci., 18 (1984), 545.
142. M C Cadeville, M Maurier and S M Friedt, Mater. Sci. Eng., 51 (19810), 147.
143. T Gladmann and F B Pickering, Chapter 9, pl41, Yield, Flow and Fracture of Polycrystals, Ed. T N Baker (1982).
144. S W K Shaw and A G Quarrell, J" I " S " I., 185 (1957), 10.
145. T Ogura, C S McMahon Jr., H C Feng and Vitek, Acta. Met. 26 (1978), 1317.
146. B C Woodfine, J.I.S.I., March (1956), 240.
147. M Wada, S Fukase and O Nishikawa, Scripta. Met., 16 (1982) 1373.
148. M Cuttmann, Ph du Moulin, M Wayman, Metall. Trans., 13A (1982), 1693.

149. H J Goldschmidt, Interstitial Alloys, Chapter 7, p329, Ed. Butterworths, 1967.
150. A Joshi, P W Palmberg and D F Stein, Metall. Trans., 6A (1975), 2160.
151. G Krauss, Phase Transformations in Ferrous Alloys, Proc. A.S.M. (A.I.M.E) Conf. (1983), 101.
152. H Othani, H C Feng, C J McMahon, R A Mulford, Metall. Trans. 7A (1976), 87.
153. M Nageswarao, C J McMahon, H Herman, Metall. Trans. 5 (1974), 1061.
154. I Olesford, International Metals Reviews, No.4 (1978), 149.
155. J Yu and C J McMahon, Met. Trans., 11A (1980), 277.

Element Alloy	C	Cr	Ni	Mn	Si	Mo	Al	S	P	Sb
	mass%						ppm			
1	0.34	0.97	3.01	0.37	0.37	-	-	50	30	500
2	0.30	0.95	2.96	0.41	0.30	-	30	40	30	-
3	0.32	1.0	3.05	0.53	0.37	0.94	40	40	30	600
4	0.30	0.06	3.54	0.45	0.33	-	30	40	30	-
5	0.30	0.06	3.54	0.45	0.33	-	30	30	30	520
6	0.31	0.08	3.60	0.47	0.35	0.93	40	30	30	-
7	0.31	0.08	3.60	0.47	0.35	0.93	40	30	30	590
8	0.31	0.08	0.004	0.45	0.39	3.87	40	30	30	-
9	0.30	0.08	0.004	0.43	0.39	3.91	50	60	60	600
10	0.35	-	5.06	0.45	0.39	0.93	50	20	30	-
11	0.35	-	5.06	0.42	0.38	0.96	50	20	30	650

Table I


HEAT TREATMENT	CODE
875°C 1h + 430°C for 24, 168, 720, 2160, 8760 & 17520 hours	A
875°C 1h WQ + 600°C 1h + 430°C for equivalent ageing times	B
875°C 1h + 580°C 48h + 430°C for equivalent ageing times	C
875°C 1h + 350°C SB 48h + 430°C for equivalent ageing times	D

A (slow cooling) = isothermally transformed bainite
 B = quenched and tempered martensite
 C = isothermally transformed pearlite
 D (fast cooling) = isothermally transformed bainite
 SB = salt bath

Table II

TABLE III(a)

For the alloys 1 to 11 in the quenched
and tempered martensitic and
isothermally transformed lower bainitic
condition.

Key  samples exhibiting temper
embrittlement

Hardness Values (Hv₃₀)

[illegible]

TABLE III(b)

For alloy 1 to 3 in the isothermally transformed ferrite-pearlite and upper bainitic condition.

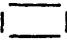
Key |  | samples exhibiting temper embrittlement

TABLE III(b)

HT		C(Ferritic-pearlitic)				A(Upper Bainite)			
Alloys	Ageing Times [h]	24	720	2160	8760	24	720	2160	8760
² C 1Cr 3Ni		209	222	304	244	294	294	293	282
¹ C 1Cr 3Ni Sb		255	257	254		339		290	<u>286</u>
³ C 1Cr 3Ni 1Mo Sb		394	465	393	468	409	441	420	421

TABLE IV(a) Transition temperature values for alloys
1 to 11 for all heat treatments applied
according with ageing time.

T_{D_I} - transition temperature value for
the point of inflexion criterion

Key

T_{D_M} - transition temperature for the
mean value criterion


|  | test not performed

TABLE IV(a)

HT	B (Martensitic)						D (Bainitic)					
	Ageing Time [h]	24	720	2160	8760		24	720	2160	8760		
T_{DI}	T_{DI}	T_{DI}	T_{DI}	T_{DI}	T_{DI}	T_{DI}	T_{DI}	T_{DI}	T_{DI}	T_{DI}	T_{DI}	T_{DI}
$T_{D(43J)}$	$T_{D(43J)}$	$T_{D(43J)}$	$T_{D(43J)}$	$T_{D(43J)}$	$T_{D(43J)}$	$T_{D(43J)}$	$T_{D(43J)}$	$T_{D(43J)}$	$T_{D(43J)}$	$T_{D(43J)}$	$T_{D(43J)}$	$T_{D(43J)}$
Alloy 8	-	+ 9	+80	+168	-	+200	-36	+9	-54	-186	-27	-68
9	-	-	-58	-	+20	-	-70	+11	-63	-	-5	0
4	-	-	-	-193	-	-192	-100	+11	-136	-50	-77	-50
5	-124	-50	-73	0	-27	-7	-147	-109	+23	+60	+72	+9
6	-110	-	-94	-77	-80	-	+39	+80	-107	-	+48	-
7	-32	-25	-73	-52	-11	-25	-140	-170	+43	+170	+98	-
10	-100	-71	-108	-38	-10	-10	+10	+8	+38	-	+74	-
11	+110	+123	-	-	-43	-	+109	-	+120	+39	+200	-

Continued o/leaf.....

HT		B (Martensitic)					D (Bainitic)									
Ageing Time [h]		24	720	2160	8760		24	720	2160							
$T_{D(43J)}$	$T_{D(43J)}$	$T_{D(43J)}$	$T_{D(43J)}$	$T_{D(43J)}$	$T_{D(43J)}$	$T_{D(43J)}$	$T_{D(43J)}$	$T_{D(43J)}$	$T_{D(43J)}$	$T_{D(43J)}$	$T_{D(43J)}$	$T_{D(43J)}$	$T_{D(43J)}$	$T_{D(43J)}$		
Alloys																
2	-	-	-10	-36	-54	-40	-50	-32	-47	-38	-56	-46	0	+10	-14	+22
1	-41	-29			-	0	-	+32	+143	+120	+162	+144	-	+25	-	0
3	+14	-	+146	+22	-	-27	-	+39	-	+165	+144	-	+163	-	-	-

HT	C(Ferritic-pearlitic)										A(Upper Bainite)									
Ageing Time [h]	24		720		2160		8760		24		720		2160		8760					
$T_{D(t)}$	T_D	T_{D_I}	T_D	T_{D_I}	T_D	T_{D_I}	T_D	T_{D_I}	T_D	T_{D_I}	T_D	T_{D_I}	T_D	T_{D_I}	T_D	T_{D_I}				
Alloys																				
2	-62	-35	-43	-27	-44	+9			+163	+144	+92	+88	+76	+72	+11	+22				
1	+144	+120	+147	+138	+177	+148			-	+18			-	0	-	0				
3	-	+105	-	-	-	0			-	-	-	-	-	+30	-	-24				

TABLE IV(b) Transition temperature values for alloys
1 to 11 for all heat treatments applied
according with ageing time.

T_{D_I} - transition temperature value for
the point of inflexion criterion

Key

T_{D_M} - transition temperature for the
mean value criterion

| ☐ | test not performed

TABLE IV(b)

[illegible]

TABLE V(a) Type of fracture for low energy mode, for a given ageing time, for alloys 1 to 11 in the quenched and tempered martensitic (B) and isothermally transformed lower bainitic condition (D).

TABLE V(b) For alloys 1 to 3 in the isothermally transformed ferrite-pearlite (C) and isothermally transformed upper bainitic condition (A).

Key ☐ samples exhibiting temper embrittlement

TABLE V(a)

Type of fracture for the low energy mode,
for a given ageing time

Alloys	B (Martensitic)				D (Bainitic)			
	24h	720h	2160h	8769h	24h	720h	2160h	8760h
8 C 4Mo	QC	QC	QC	QC	QC	QC	QC	QC
9 C 4Mo Sb	QC	QC	QC	QC	QC	QC	QC	QC
4 C 3Ni	QC	QC	QC	D/I/C	QC	QC	QC	QC
5 C 3Ni Sb	QC	QC	D/I	QC/I	QC	QC	QC	QC
6 C 3Ni 1Mo	QC	QC	QC	QC	QC	QC	QC	QC
7 C 3Ni 1Mo Sb	QC	QC	D/I	QC/I	QC	QC	QC	QC
10 C 5Ni 1Mo	QC	QC	D/I	QC/I	QC	QC	QC	QC
11 C 5Ni 1Mo Sb	QC	QC	I/D	C/I	QC	QC	QC	QC
2 C 3Cr 1Ni	I	I	I	I	C	C/I	I	C/D/I
1 C 3Cr 1Ni Sb	I		I	I	C	C	I	C/D/I
3 C 3Cr 1Ni 1Mo Sb	QC	QC	QC	QC	QC	QC	QC	QC

TABLE V(b)

Type of fracture for the low energy mode,
for a given ageing time

Alloys	C (Pearlitic)				A (Upper Bainitic)			
	24h	720h	2160h	8769h	24h	720h	2160h	8760h
2 C 3Cr 1Ni	C	C	C	C	C	C	C	C
1 C 3Cr 1Ni Sb	C	C	C	-	C	C		I
2 C 3Cr 1Ni 1Mo Sb	QC	QC	QC	QC	QC	QC	QC	QC

Fig. 1 Schematic diagram of the interactions which
can be analysed by the V.G. Scientific MICROLAB
500 used in this investigation.

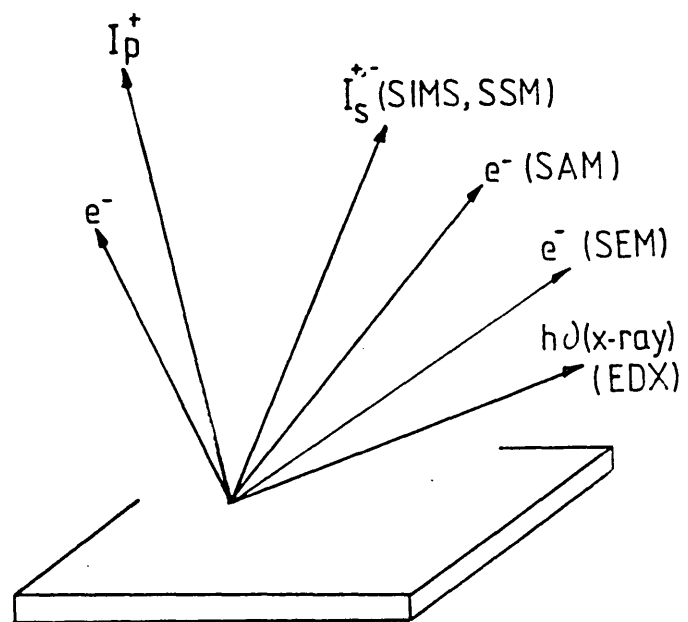


Fig. 2 Schematic diagram of the physical principle of (a) the emission of an Auger electron from an ionized Si atom ^[101], (b) the ion beam interaction with a surface (SIMS process) ^[104].

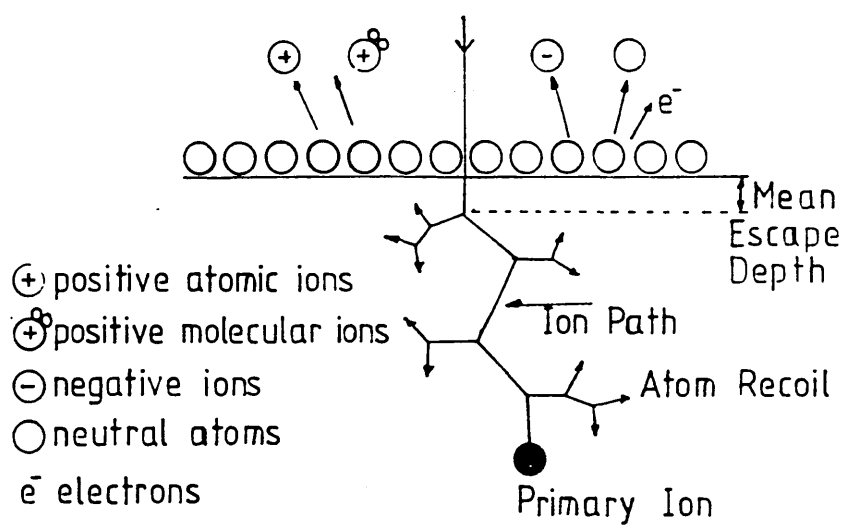
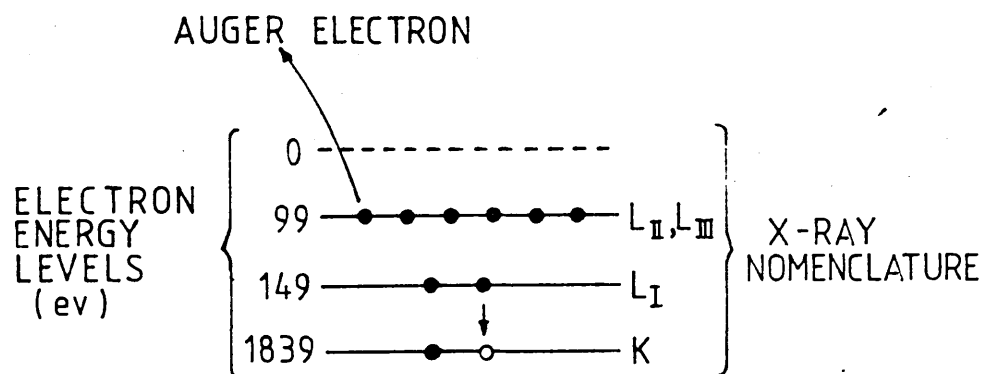


Fig. 3 Scanning electron micrograph of alloy 1 heat treatment A, aged for 8,760 hours at 430°C and impact tested at +200°C, mag. 250x.

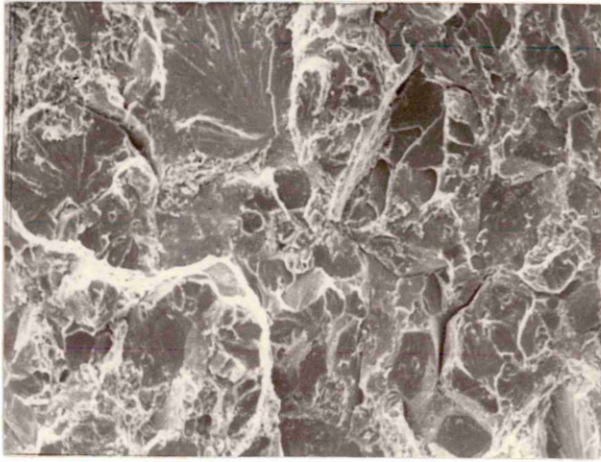


Fig. 4 DBTT curves for alloys 1 and 2 in the isothermally transformed bainitic condition (heat treatment A) with increasing ageing times, i.e. 24, 2,160 and 8,760 hours at 430°C.

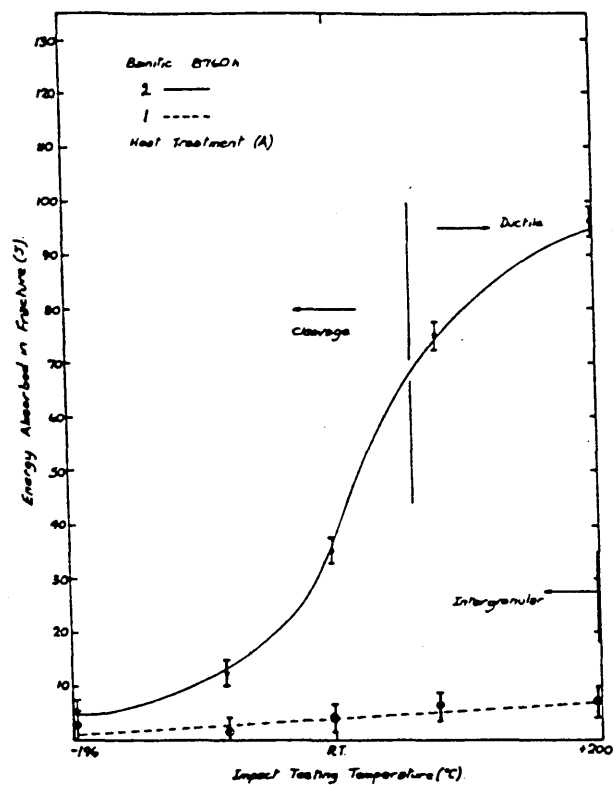
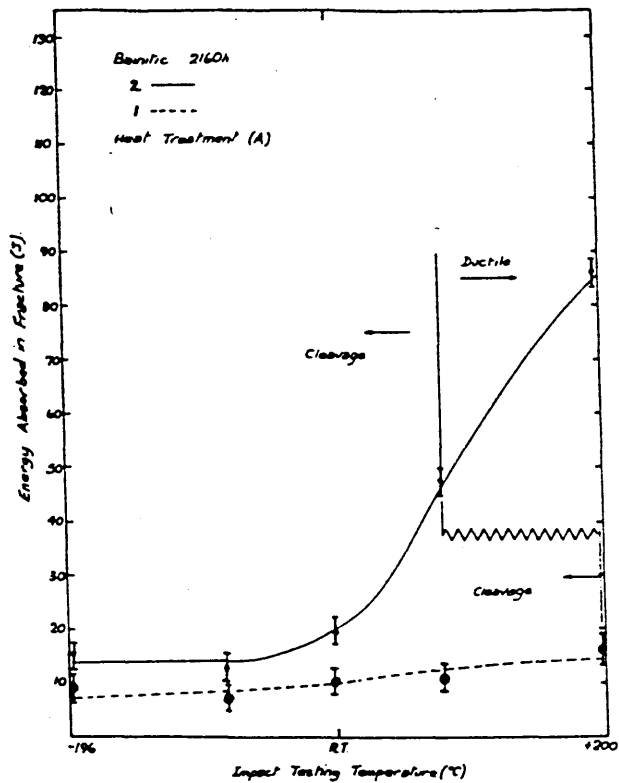
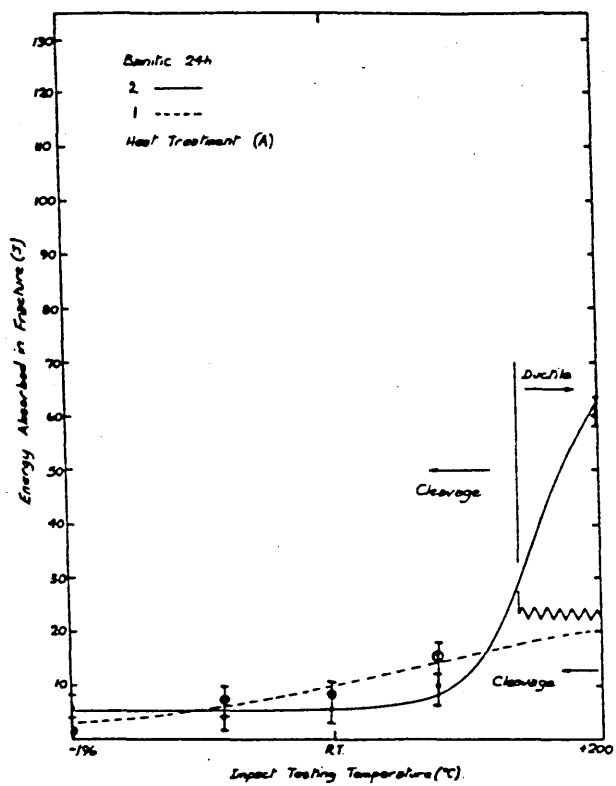


Fig. 5 Scanning electron micrograph of alloy 1 heat treatment A, aged for 8,760 hours at 430°C impact tested at ambient temperature, mag. 500x.

Fig. 6 Ageing curves for alloys 1 and 2 in the isothermally transformed bainitic condition (heat treatment A).

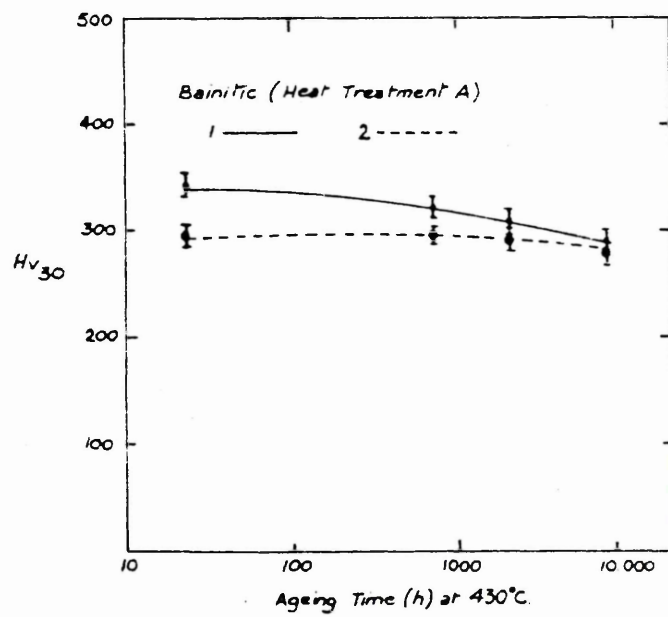
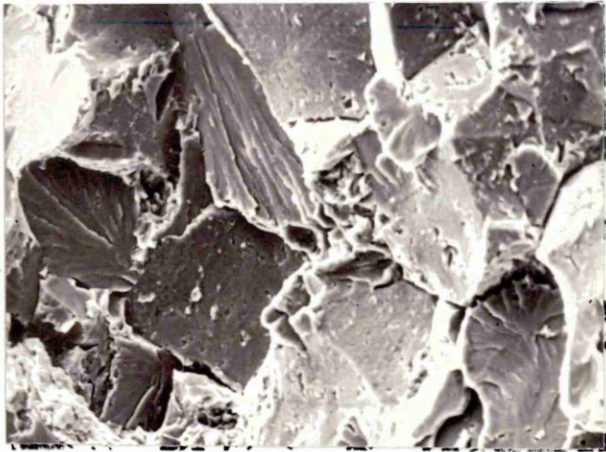


Fig. 7 Transmission electron micrograph of alloy 1 in the isothermally transformed bainitic condition (heat treatment A) aged for 24 hours at 430°C.

Fig. 8 Transmission electron micrograph of alloy 1 in the isothermally transformed bainitic condition (heat treatment A) aged for 168 hours at 430°C.

Fig. 9 Annular dark field image of alloy 1 in the isothermally transformed bainitic condition (heat treatment A) aged for 8,760 hours at 430°C.

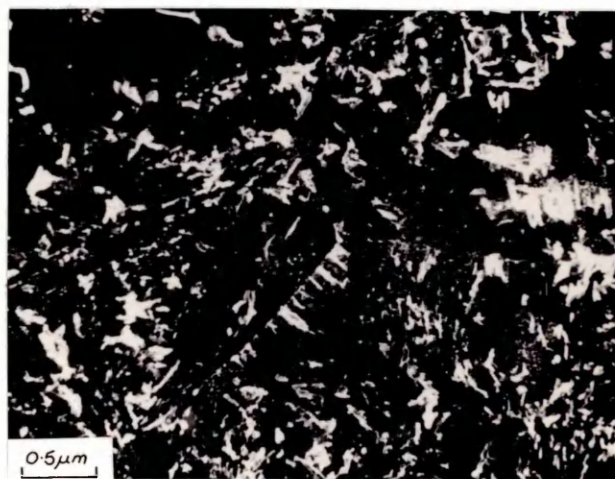
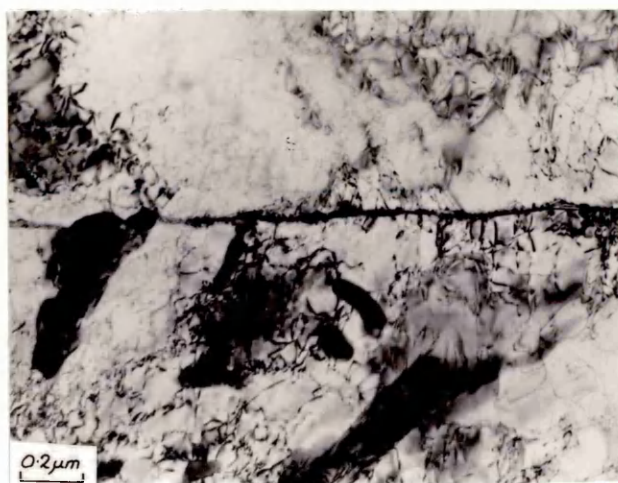


Fig. 10 Transmission electron micrograph of alloy 1 in the isothermally transformed bainitic condition (heat treatment A) aged for 8,760 hours at 430°C.

Fig. 11 Scanning electron micrograph of alloy 1 in the isothermally transformed bainitic condition (heat treatment A) aged for 24 hours at 430°C, mag. 1000x.

Fig. 12 Scanning electron micrograph for alloy 1 in the isothermally transformed bainitic condition (heat treatment A) aged for 2,160 hours at 430°C, mag. 1000x.

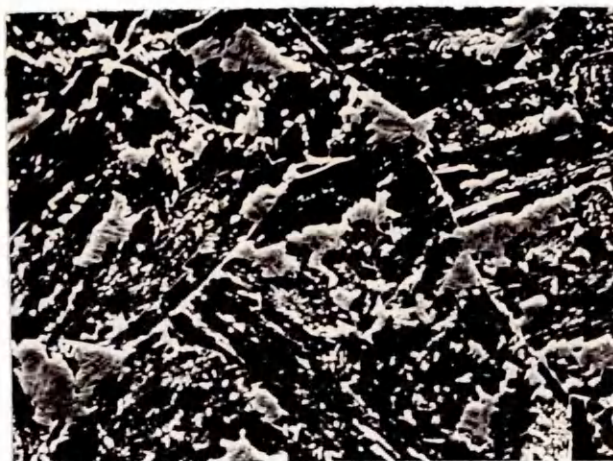
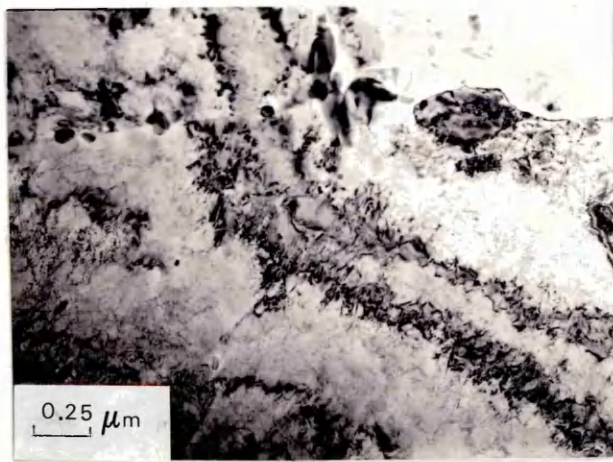


Fig. 13 Scanning electron micrograph of alloy 1 in the isothermally transformed bainitic condition (heat treatment A) aged for 8,760 hours at 430°C, mag. 1000x.

Fig. 14 Scanning electron micrograph of alloy 2 in the isothermally transformed bainitic condition (heat treatment A) aged for 24 hours at 430°C, mag. 1000x.

Fig. 15 Alloy 1 heat treatment B, aged for 24 hours at 430°C, impact tested at +80°C, mag. 1100x.

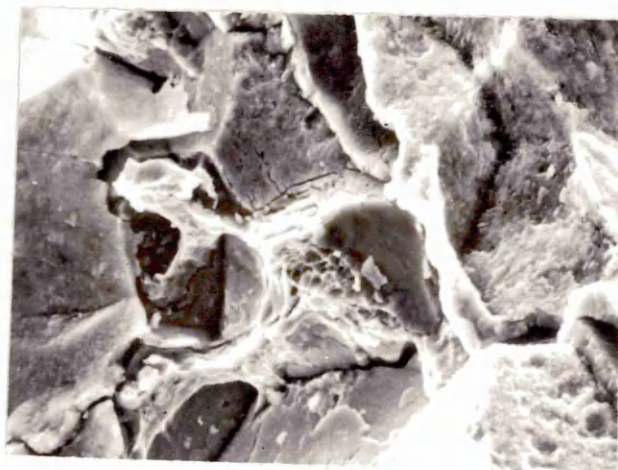
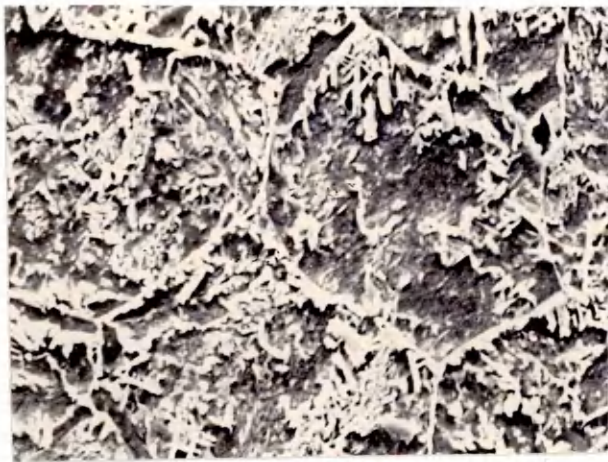


Fig. 16 DBTT curves for alloys 1 and 2 in the quenched and tempered martensitic condition (heat treatment B) with increasing ageing times.

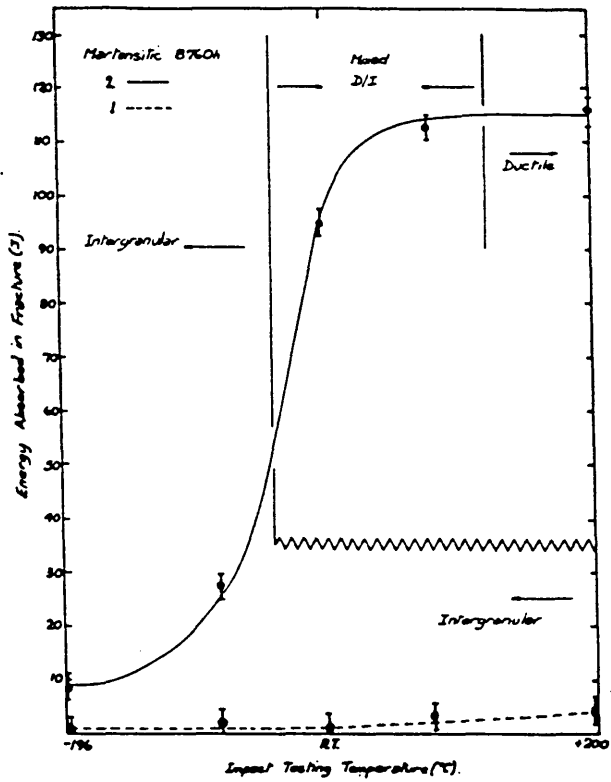
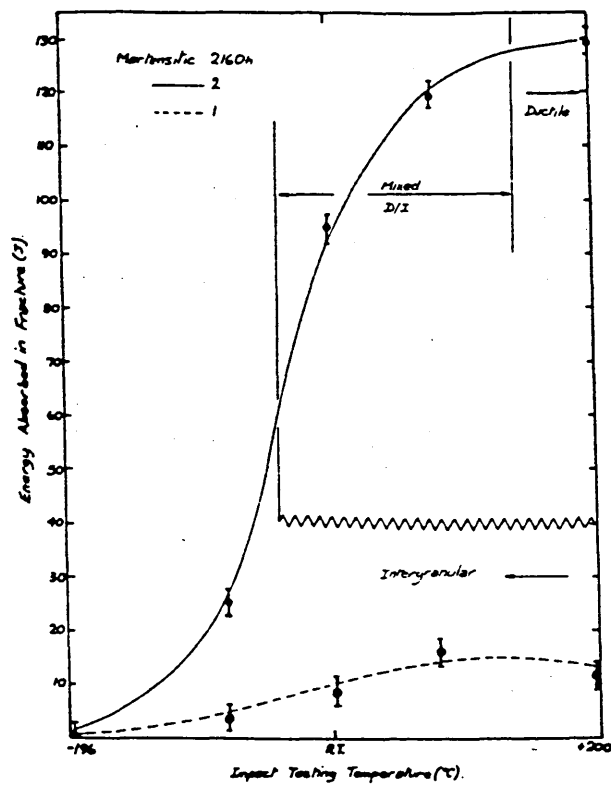
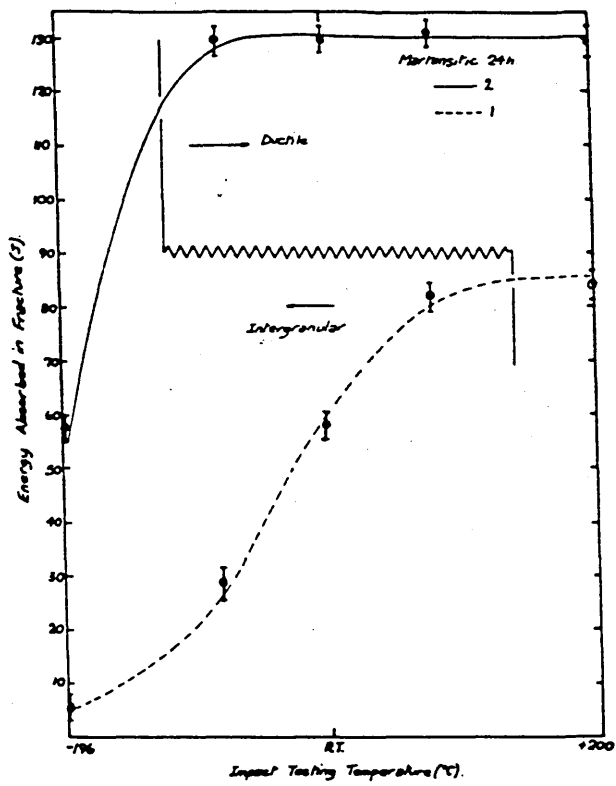


Fig. 17 Scanning electron micrograph of alloy 2, heat treatment B, aged for 24 hours at 430°C, impact tested at -196°C, mag. 550x.

Fig. 18 Scanning electron micrograph of alloy 2, heat treatment B, aged for 2,160 hours at 430°C, impact tested at +80°C, mag. 650x.

Fig. 19 Scanning electron micrograph of alloy 2, heat treatment B, aged for 8,760 hours at 430°C, impact tested at ambient temperature, mag. 400x.

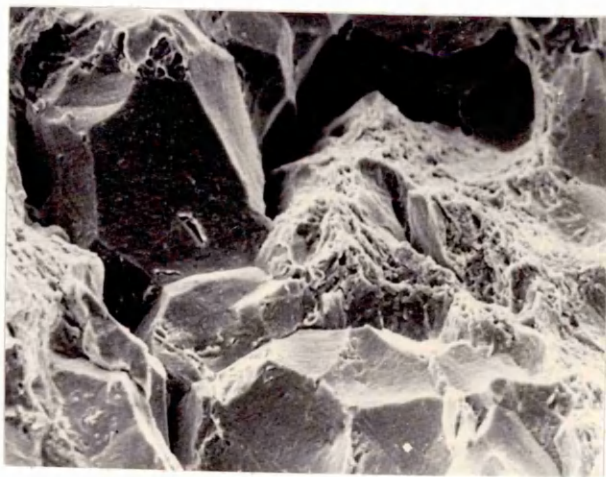
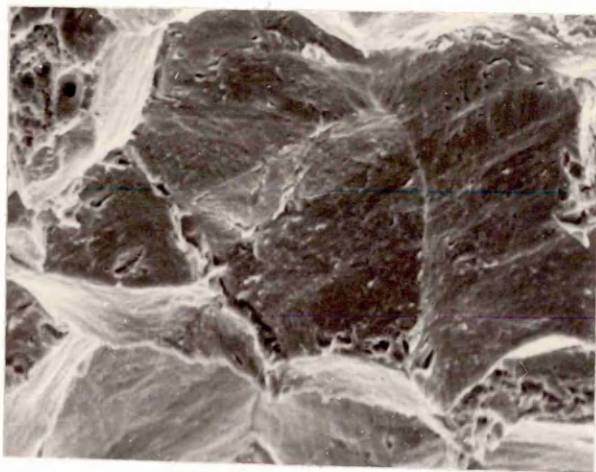
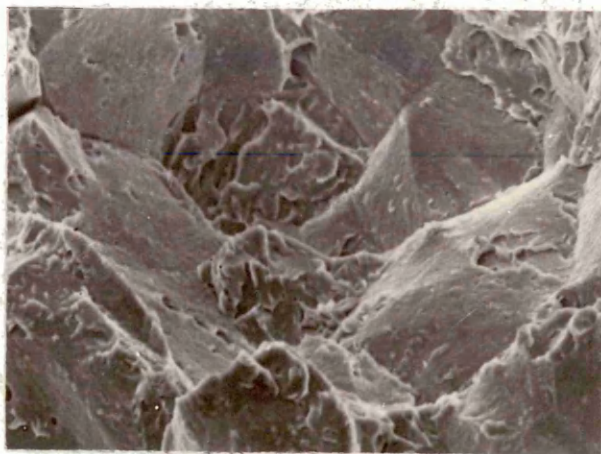


Fig. 20 Scanning electron micrograph of alloy 1, heat treatment B, aged for 2,160 hours, impact tested at ambient temperature, mag. 1000x.

Fig. 21 Scanning electron micrograph of alloy 1, heat treatment B, aged for 2,160 hours further hydrogen embrittled for 16 hours at 200°C and impact tested at -140°C, mag. 1000x.

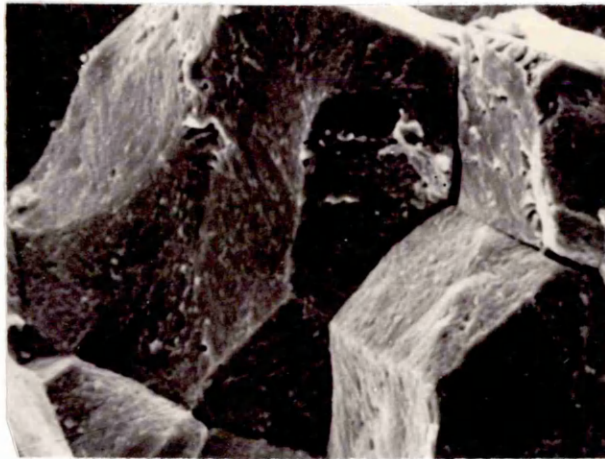
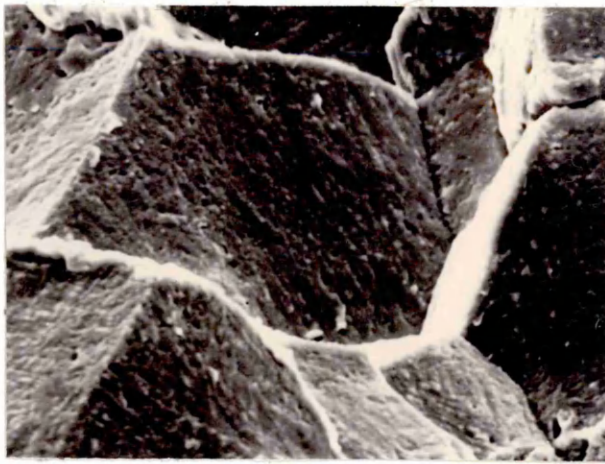


Fig. 22 Ageing curves for alloys 1 and 2 in the quenched and tempered martensitic condition (heat treatment B).

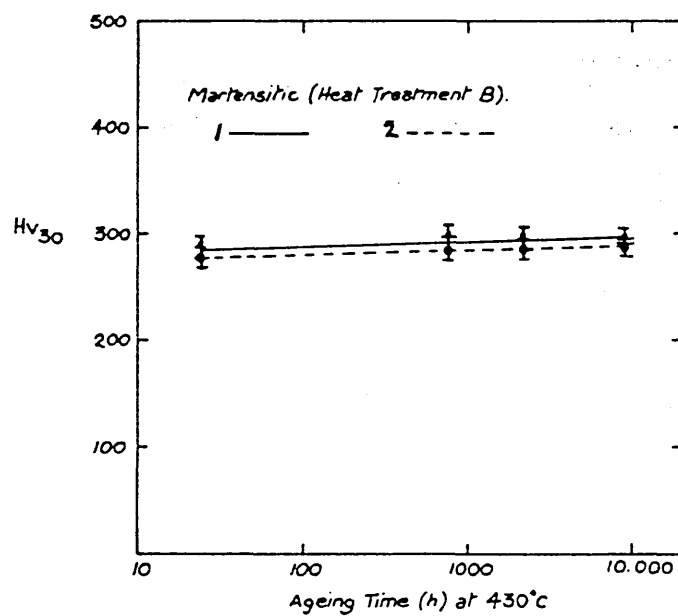


Fig. 23 Transmission electron micrograph of alloy 1 in the quenched and tempered martensitic condition (heat treatment B) aged for 24 hours at 430°C.

Fig. 24 Transmission electron micrograph of alloy 1 in the quenched and tempered martensitic condition (heat treatment B) aged for 168 hours at 430°C.

Fig. 25 Scanning electron micrograph of alloy 1 in the quenched and tempered martensitic condition (heat treatment B) aged for 24 hours at 430°C, mag. 1000x.

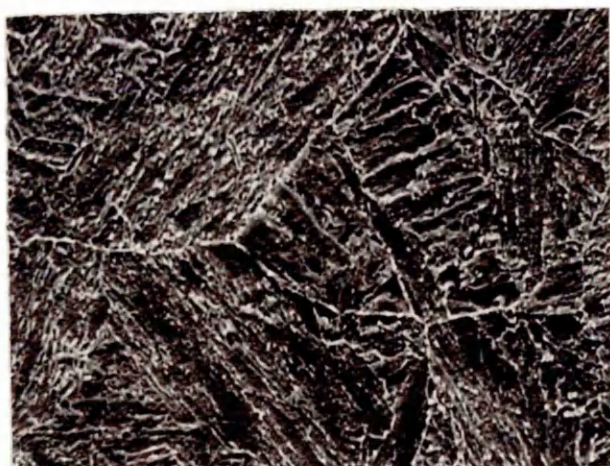
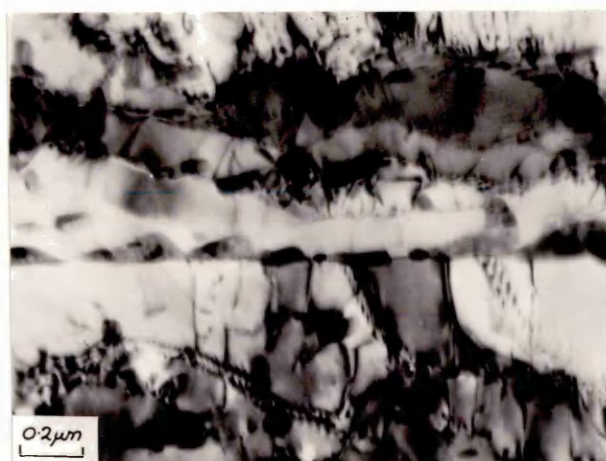
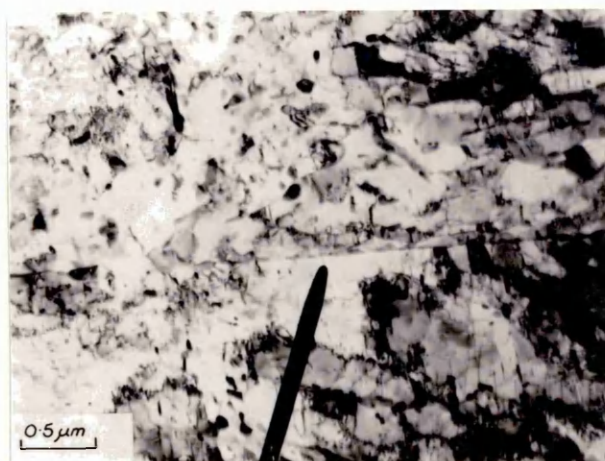


Fig. 26 Scanning electron micrograph of alloy 1 in the quenched and tempered martensitic condition (heat treatment B) aged for 8,760 hours, mag. 1000x.

Fig. 27 Transmission electron micrograph of alloy 1 in the quenched and tempered martensitic condition (heat treatment B) aged for 8,760 hours.

Fig. 28 Transmission electron micrograph of alloy 1 in the quenched and tempered martensitic condition (heat treatment B) aged for 17,520 hours.

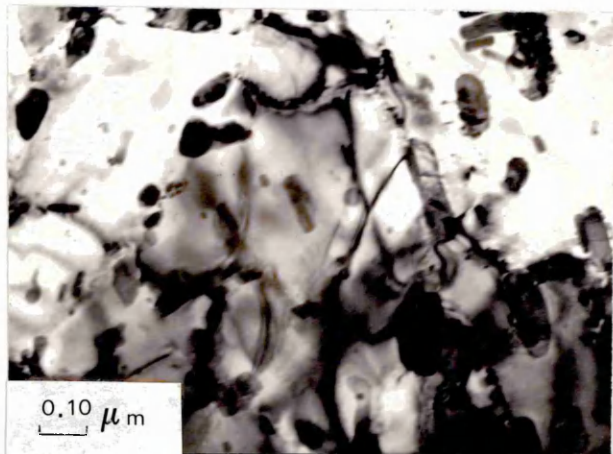
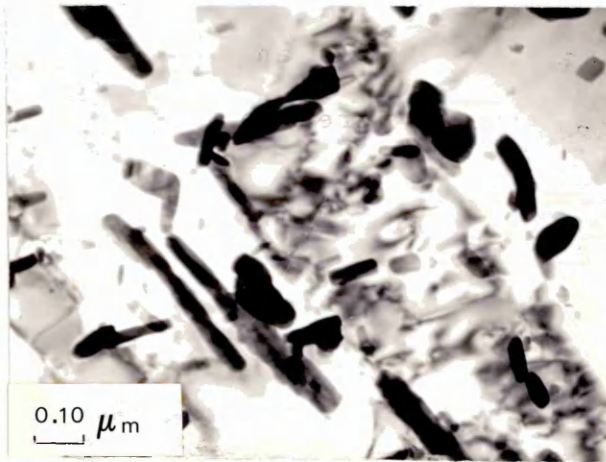
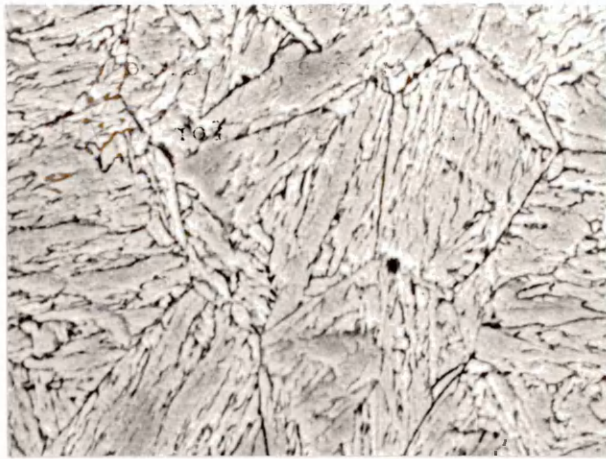


Fig. 29 Scanning electron micrograph of alloy 2 in the quenched and tempered martensitic condition (heat treatment B) aged for 24 hours at 430°C, mag. 700x.

Fig. 30 Transmission electron micrograph of alloy 2 in the quenched and tempered martensitic condition (heat treatment B) aged for 2,160 hours at 430°C.

Fig. 31 Transmission electron micrograph of alloy 2 in the quenched and tempered martensitic condition (heat treatment B) aged for 8,760 hours at 430°C.

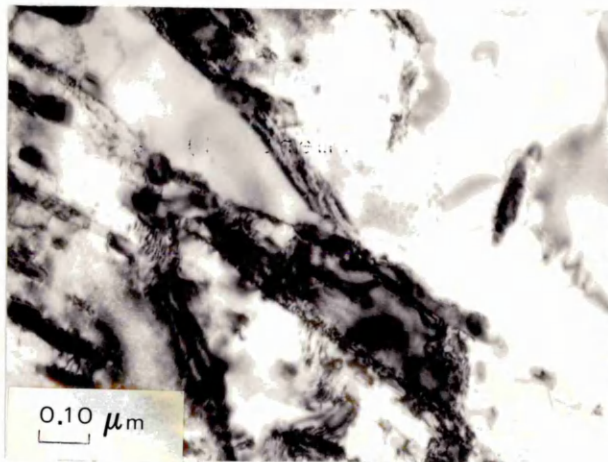
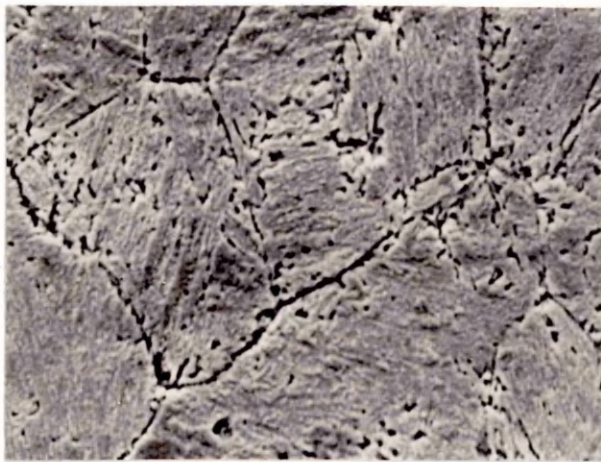
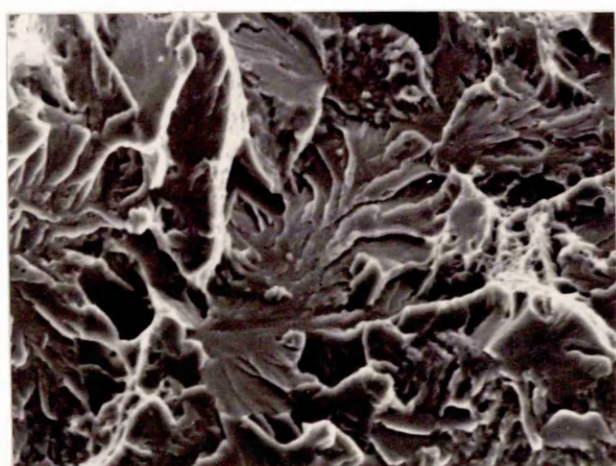
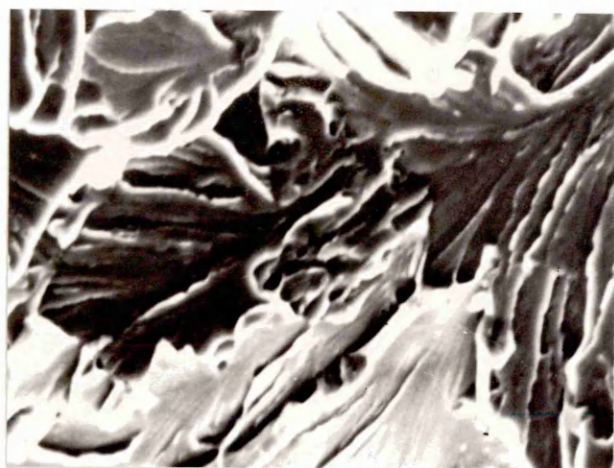


Fig. 32 Scanning electron micrograph of alloy 2, heat treatment C, aged for 24 hours at 430°C, impact tested at ambient temperature, mag. 1000x.

Fig. 33 Scanning electron micrograph of alloy 2, heat treatment C, aged for 8,760 hours at 430°C, impact tested at ambient temperature, mag. 1000x.



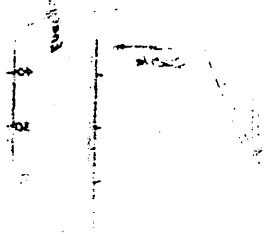


Fig. 34 DBTT curves for alloys 1 and 2 in the pearlitic condition (heat treatment C) with increasing ageing times.

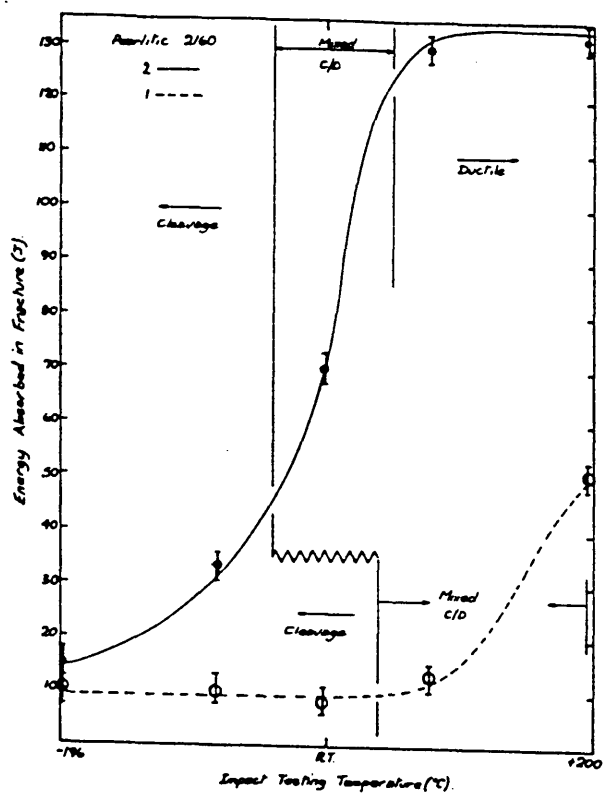
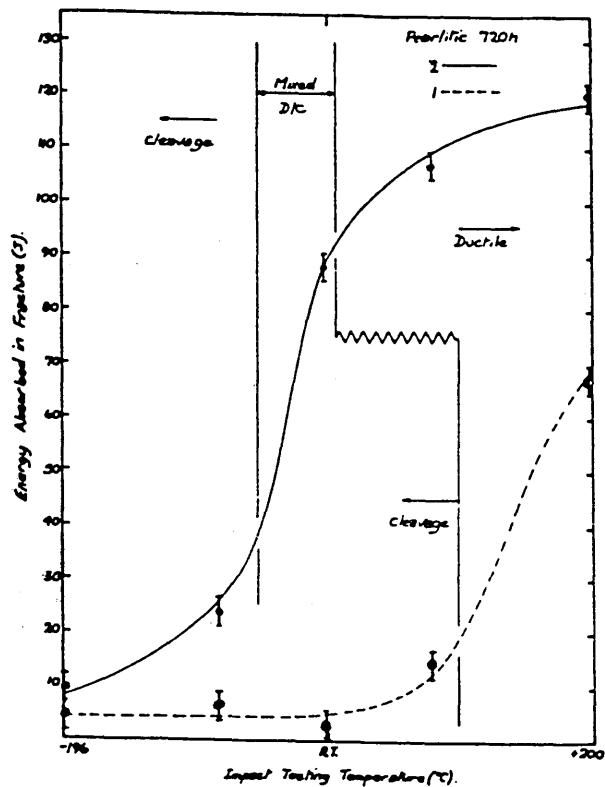
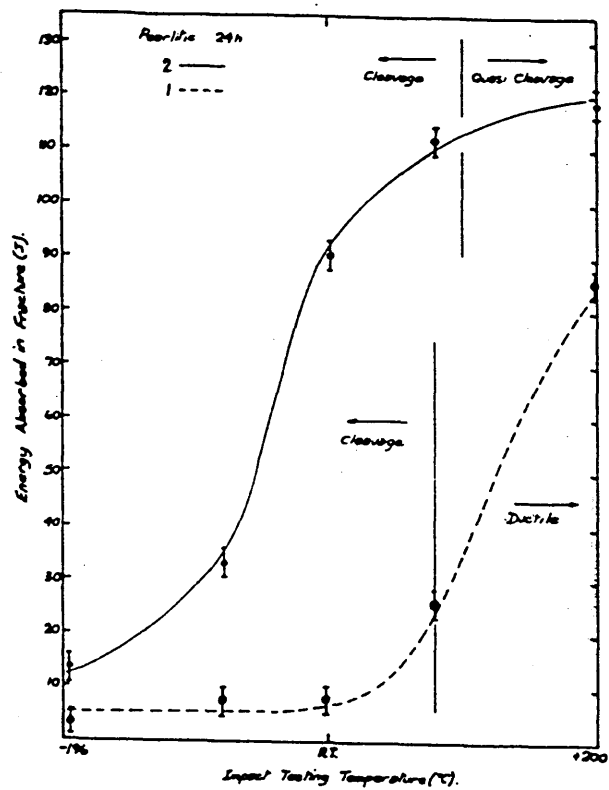


Fig. 35 Ageing curves for alloy 1 and 2 in the
pearlitic condition (heat treatment C).

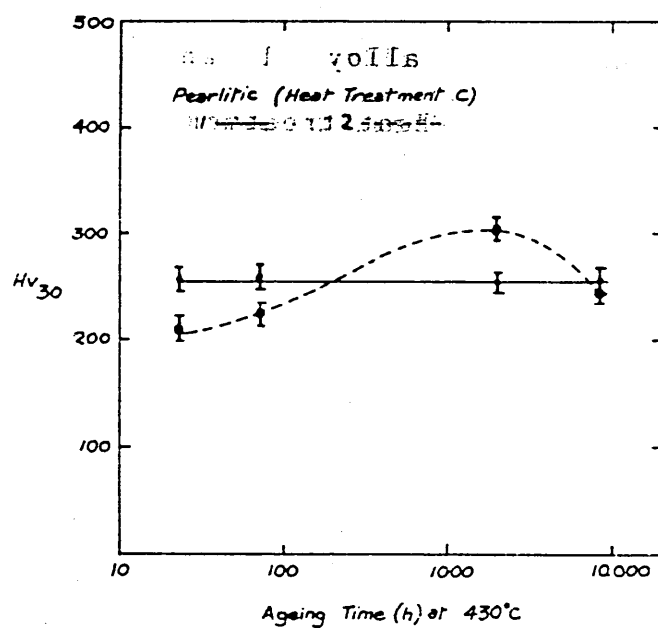


Fig. 36 Transmission electron micrograph of alloy
1 in the pearlitic condition (heat treatment
C) before ageing.

Fig. 37 Transmission electron micrograph of alloy
1 in the pearlitic condition (heat treatment
C) aged for 24 hours at 430°C.

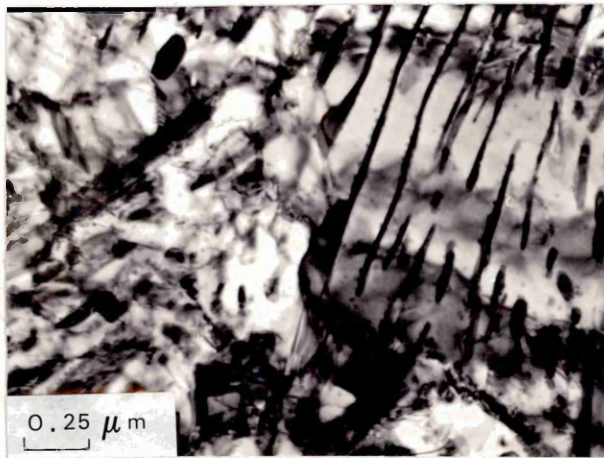
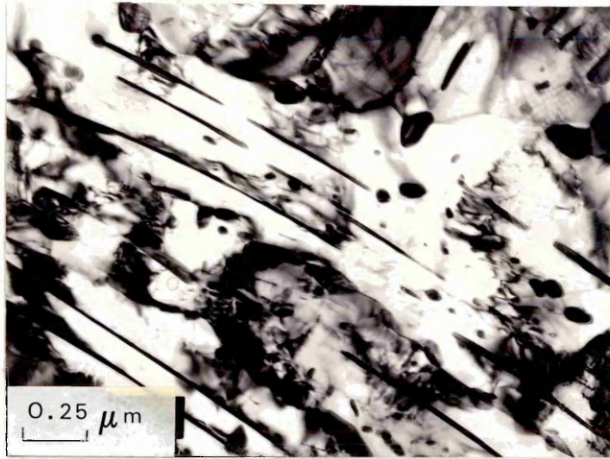


Fig. 38 Transmission electron micrograph of alloy 1 in the pearlitic condition (heat treatment C) aged for 720 hours at 430°C.

Fig. 39 Transmission electron micrograph of alloy 1 in the pearlitic condition (heat treatment C) aged for 2,160 hours at 430°C.

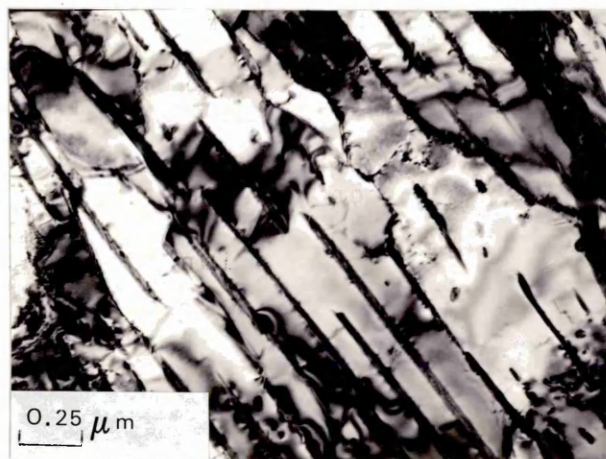
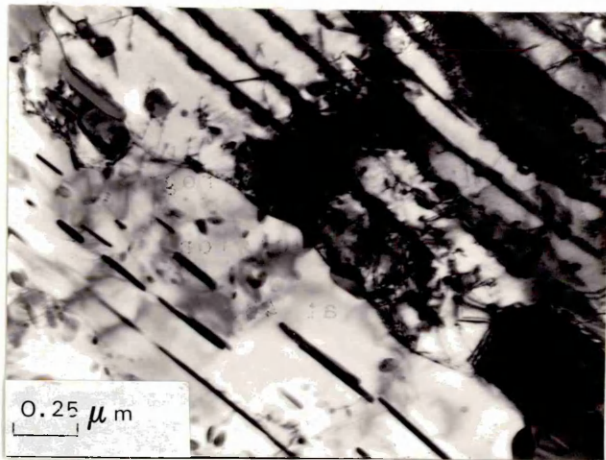


Fig. 40 Scanning electron micrograph of alloy 2 in the pearlitic condition (heat treatment C) aged for 24 hours at 430°C, mag. 1100x.

Fig. 41 Scanning electron micrograph of alloy 2, heat treatment D, aged for 720 hours at 430°C, impact tested at -70°C, mag. 1000x.

Fig. 42 Scanning electron micrograph of alloy 2, heat treatment D, aged for 2,160 hours at 430°C, impact tested at -70°C, mag. 1100x.

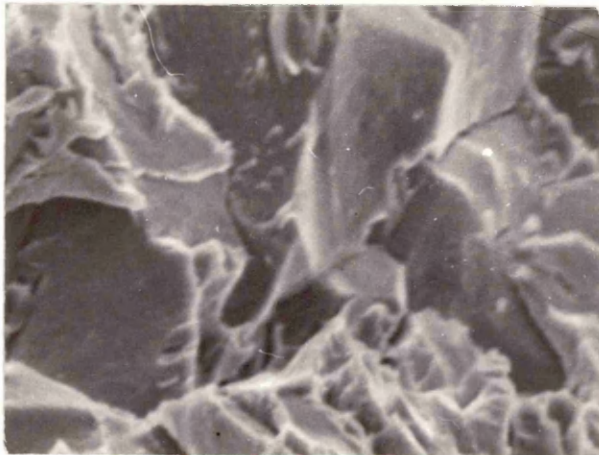
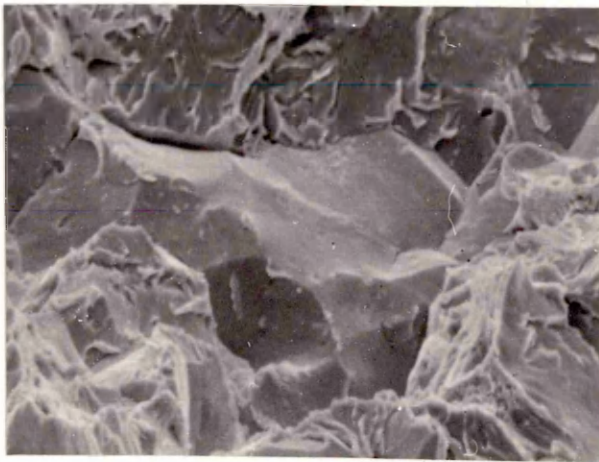
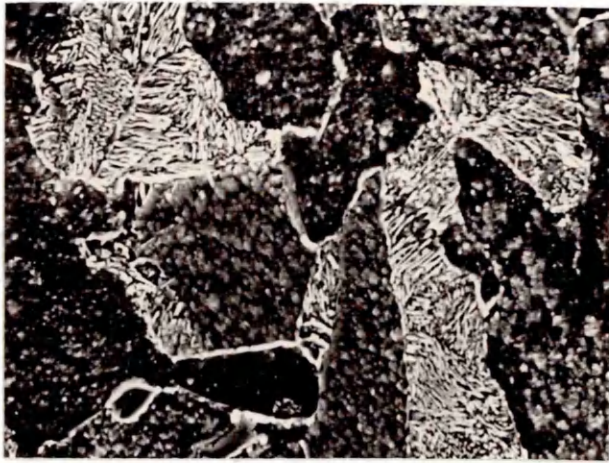
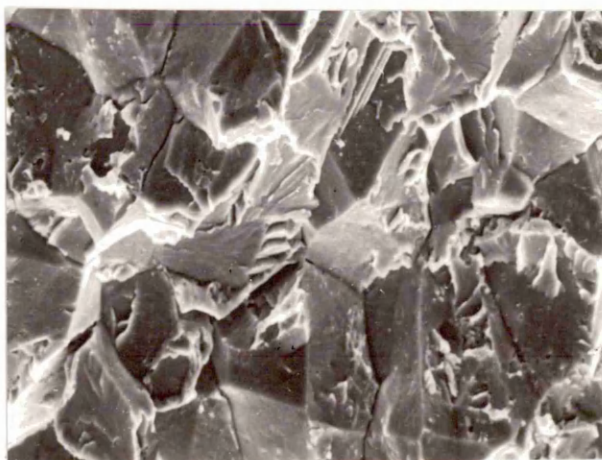
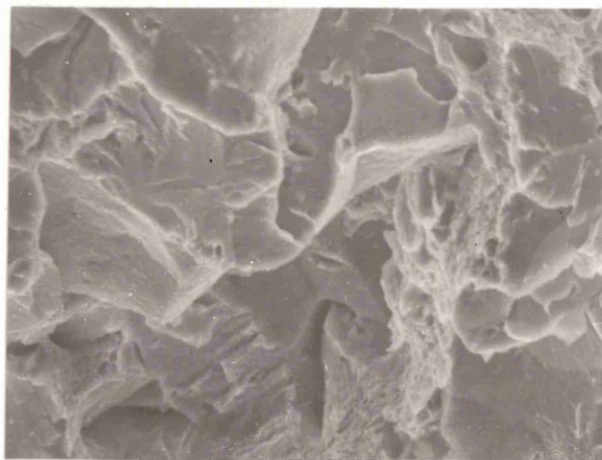


Fig. 43 Scanning electron micrograph of alloy 2, heat treatment D, aged for 8,760 hours at 430°C, impact tested at -196°C, mag. 1100x.

Fig. 44 Scanning electron micrograph of alloy 1, heat treatment D, aged for 2,160 hours at 430°C, impact tested at ambient temperature, mag. 700x.



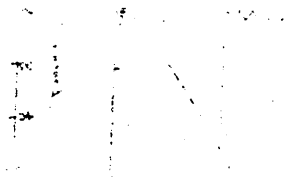


Fig. 45 DBTT curves for alloy 1 and 2 in the isothermally transformed bainitic condition (heat treatment D) with increasing ageing times.

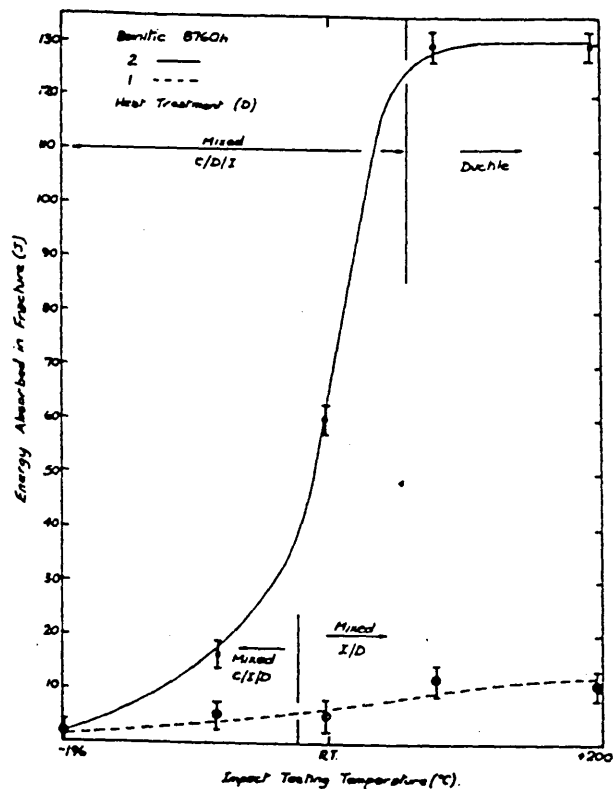
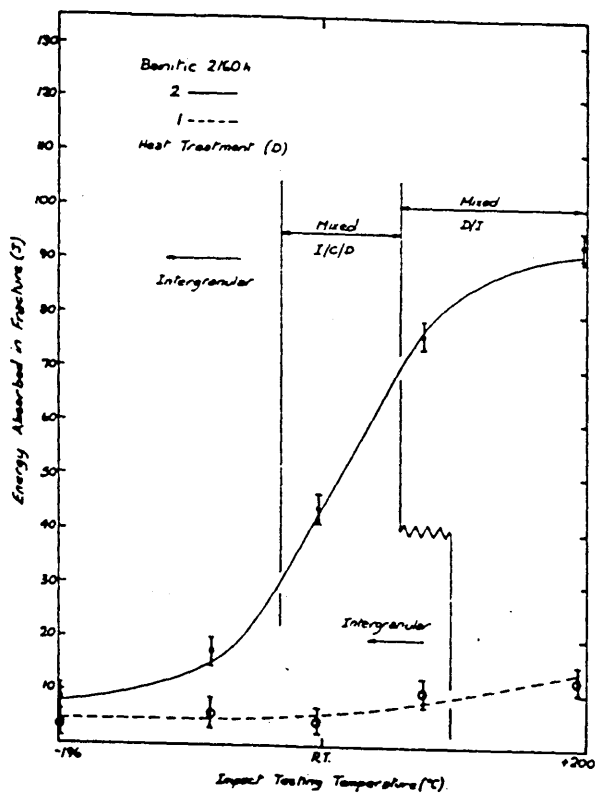
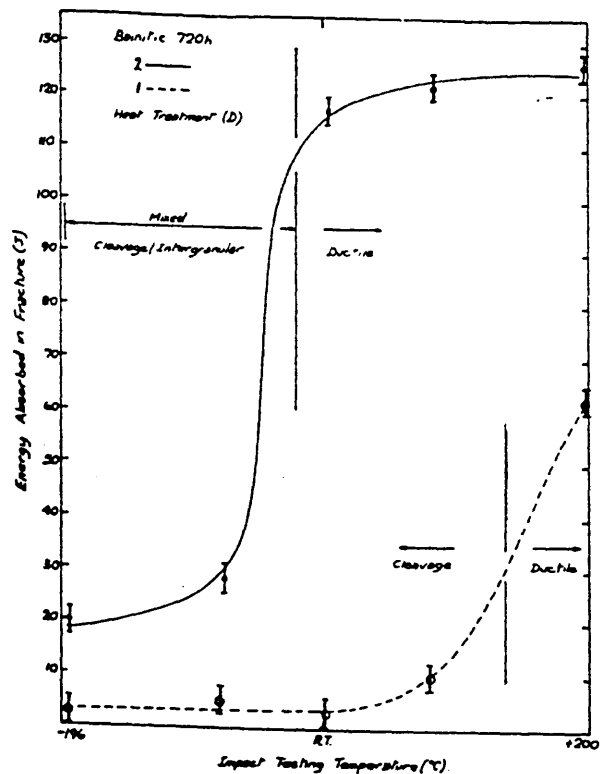
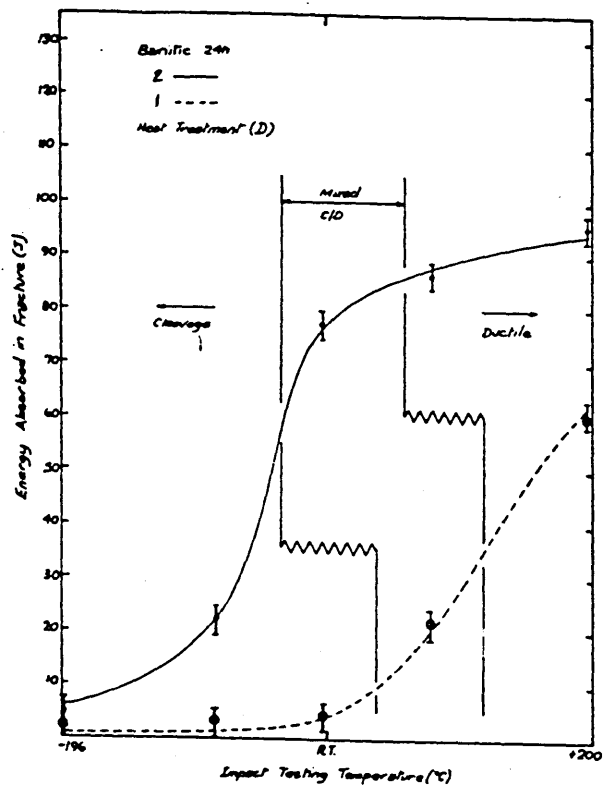


Fig. 46 Ageing curves ~~for~~ alloys 1 and 2 in the
isothermally transformed bainitic condition
(heat treatment D).

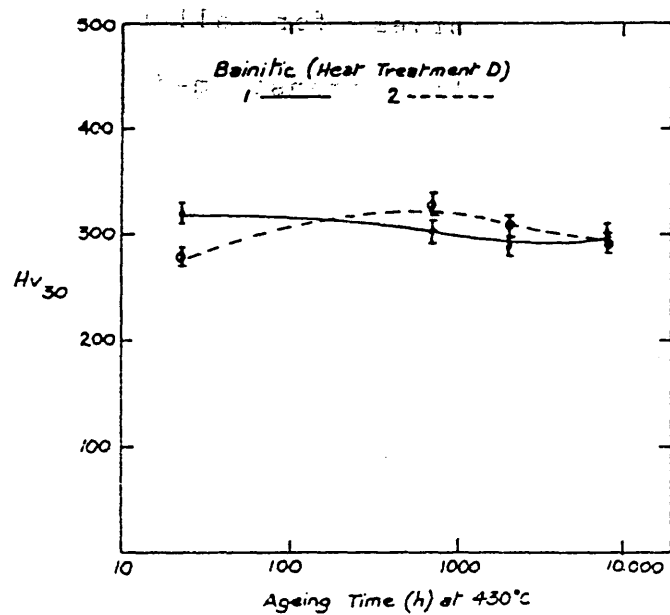


Fig. 47 Transmission electron micrograph of alloy 2 in the isothermally transformed bainitic condition (heat treatment D), aged for 24 hours at 430°C.

Fig. 48 Transmission electron micrograph of alloy 2 in the isothermally transformed bainitic condition (heat treatment D), aged for 2,160 hours at 430°C.

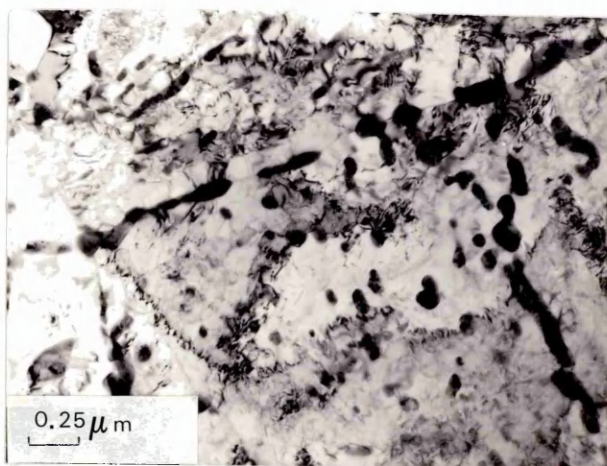
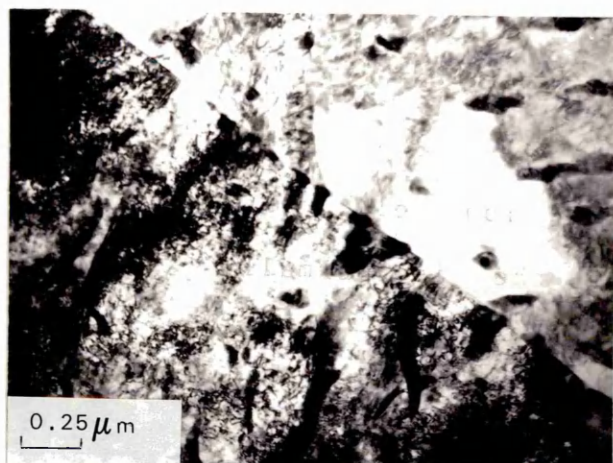


Fig. 49 DBTT curves for alloys 1 and 3 in the isothermally transformed bainitic condition (heat treatment A) with increasing ageing time.

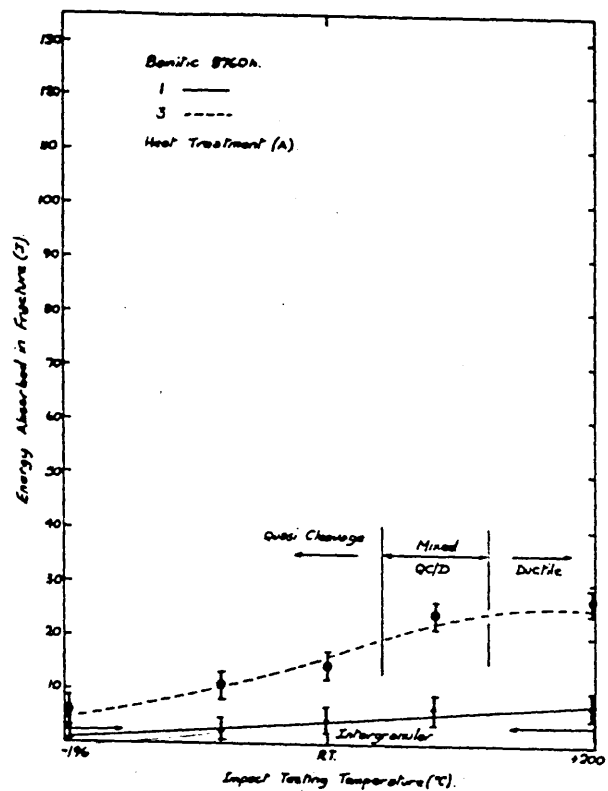
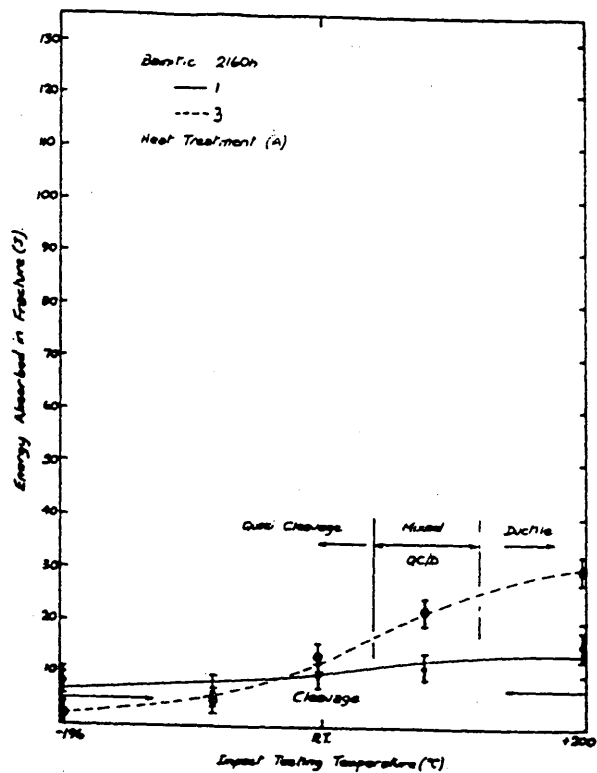
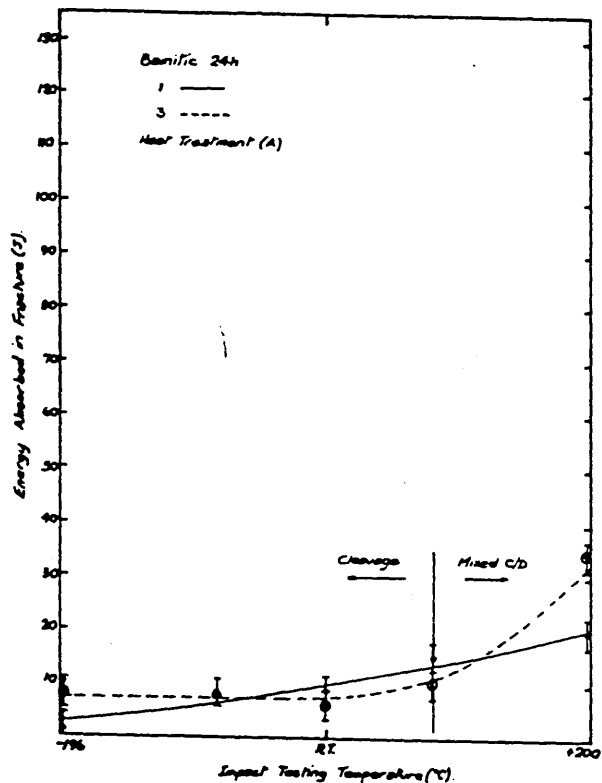


Fig. 50 Ageing curves for alloys 1 and 3 in the isothermally transformed bainitic condition (heat treatment A).

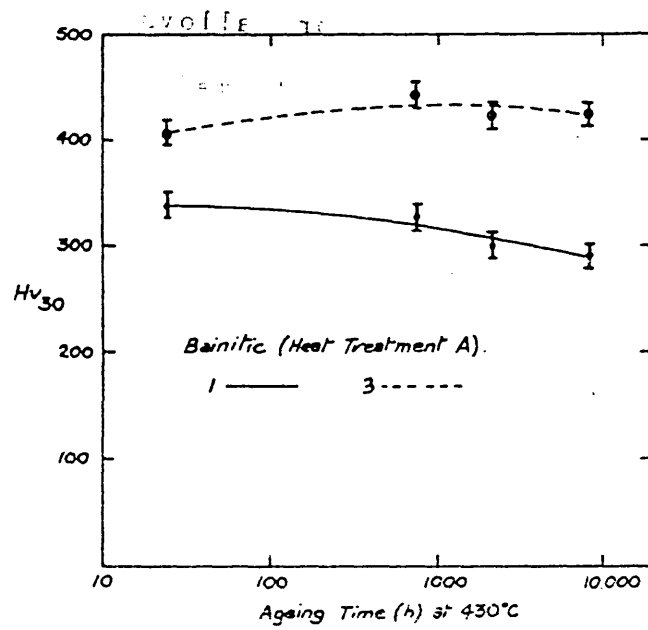


Fig. 51 Scanning electron micrograph of alloy 3, heat treatment B, aged for 2,160 hours at 430°C, impact tested at -80°C, mag. 800x.




Fig. 52 Scanning electron micrograph of alloy 3, heat treatment B, aged for 8,760 hours at 430°C, impact tested at ambient temperature, mag. 800x.

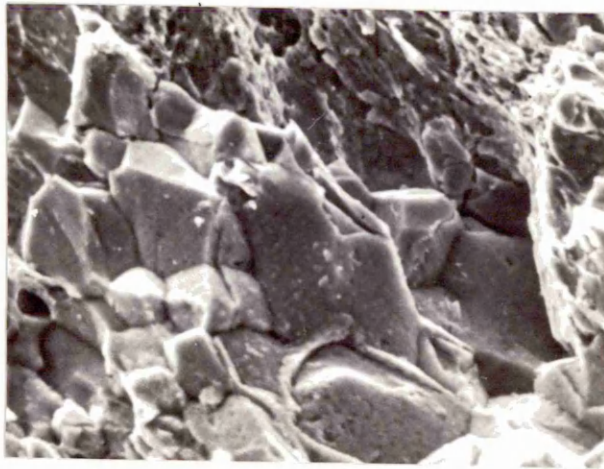
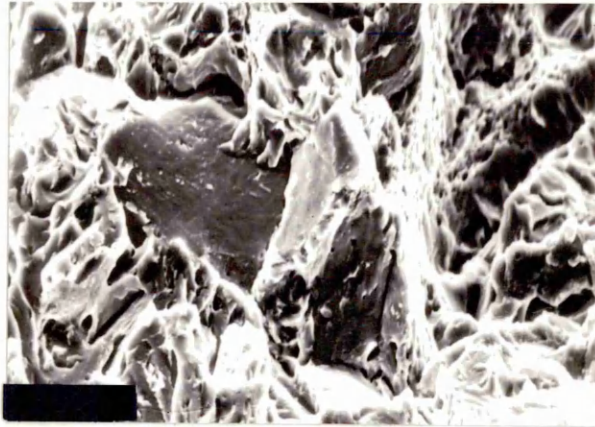
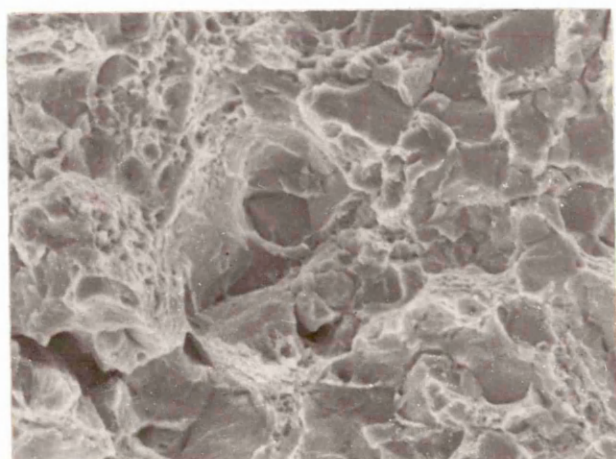
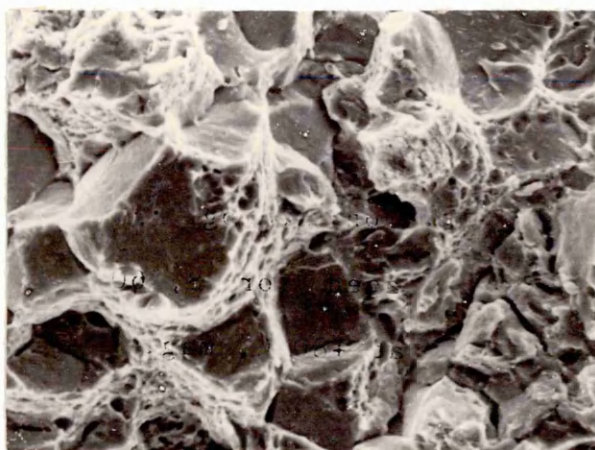


Fig. 53. Scanning electron micrograph of alloy 3, heat treatment B, aged for 8,760 hours at 430°C, impact tested at +80°C, mag. 800x.

Fig. 54 Scanning electron micrograph of alloy 3, heat treatment B, aged for 8,760 hours at 430°C, impact tested at +200°C, mag. 800x.



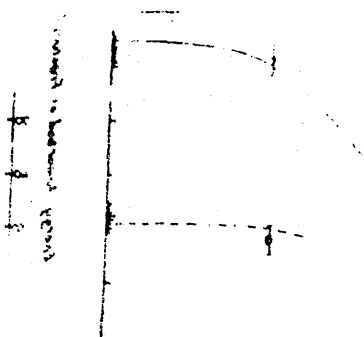


Fig. 55 DBTT curves for alloys 1 and 3 in the quenched and tempered martensitic condition (heat treatment B) with increasing ageing time.

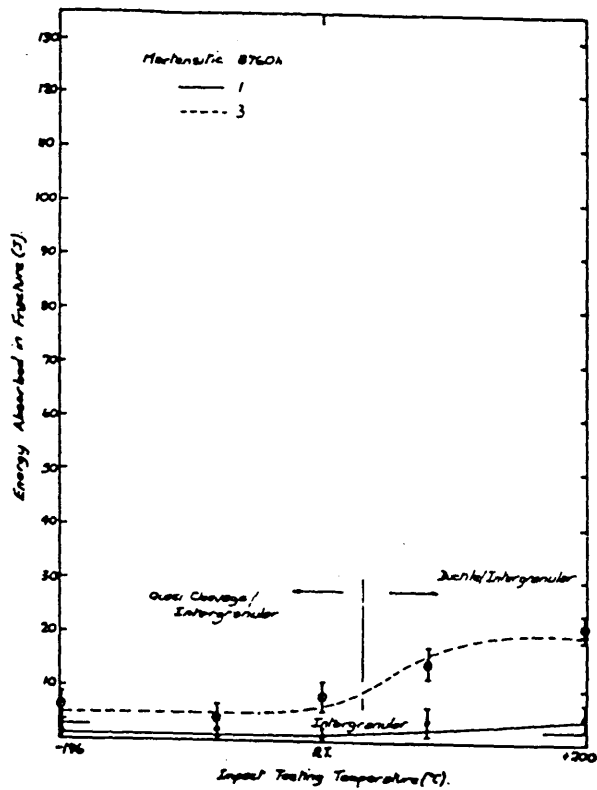
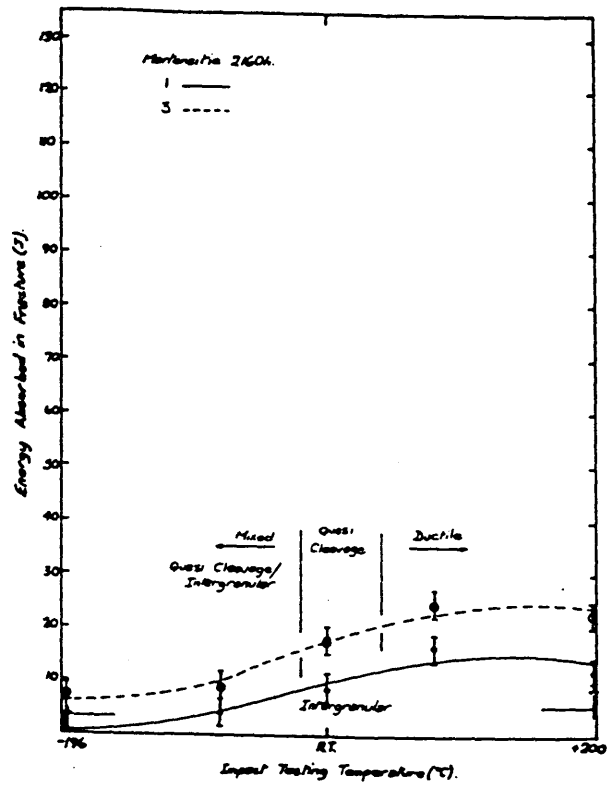
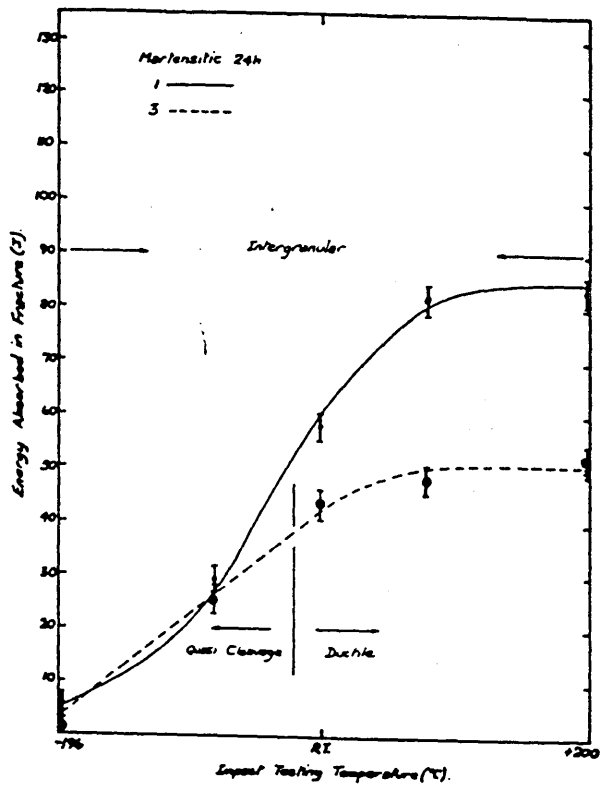


Fig. 56 Ageing curves for alloys 1 and 3 in the quenched and tempered martensitic condition (heat treatment B).

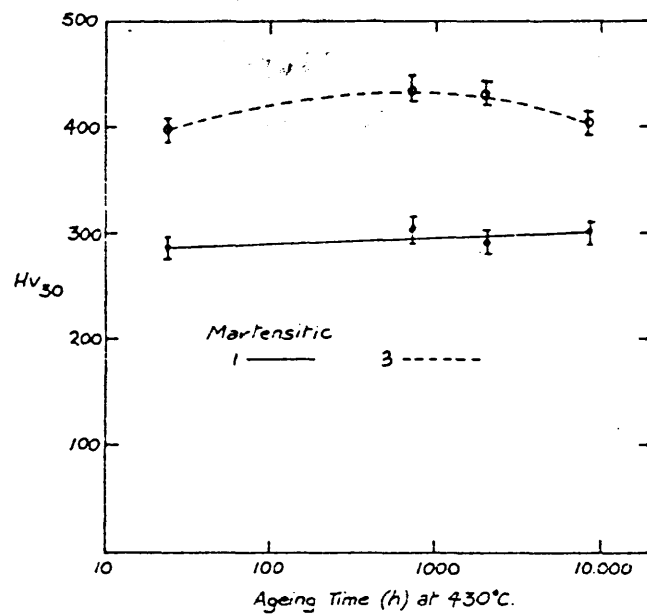
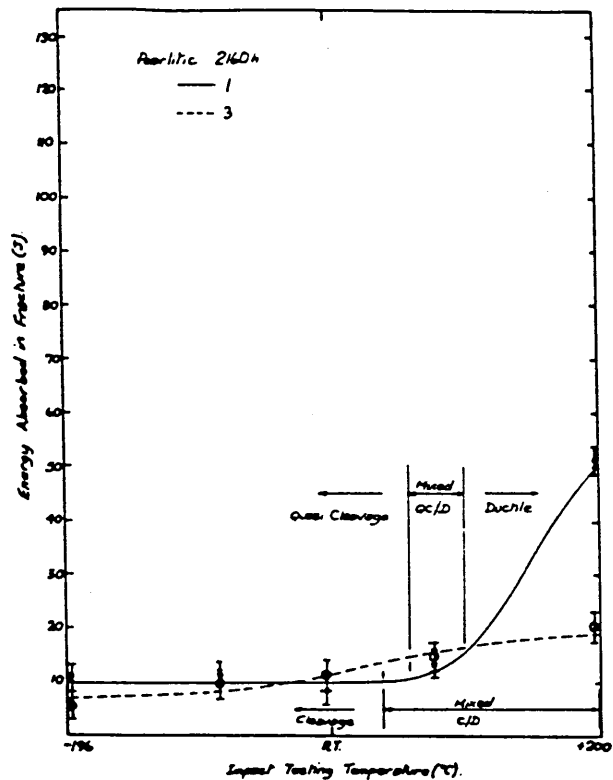
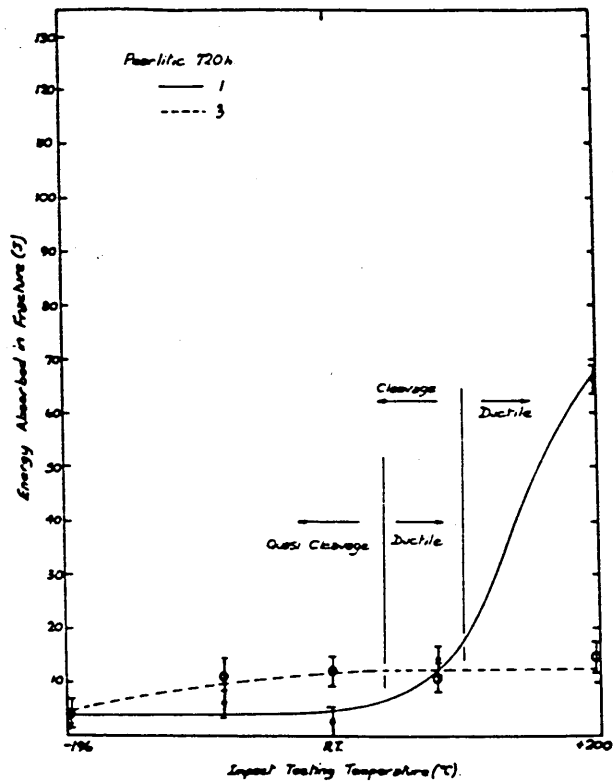
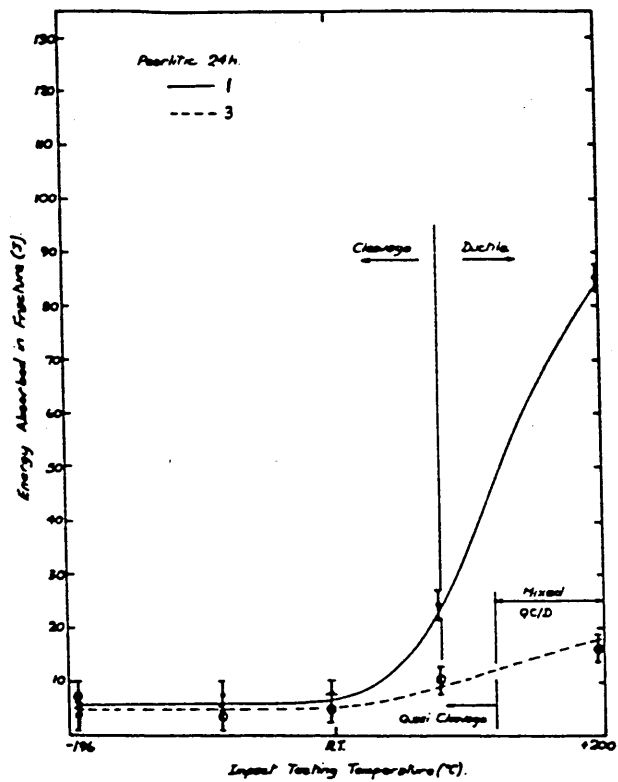


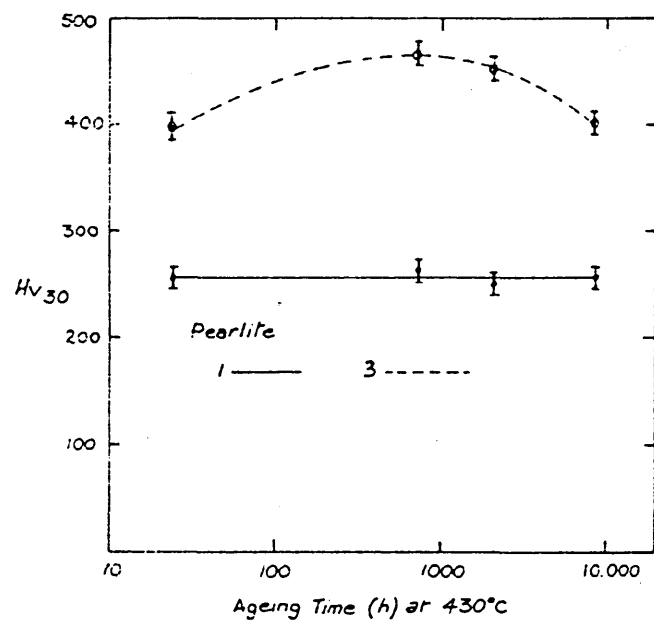
Fig. 57 Transmission electron micrograph of alloy 3 in the quenched and tempered martensitic condition (heat treatment B) aged for 24 hours at 430°C.





Fig. 58 DBTT curves for alloys 1 and 3 in the pearlitic condition (heat treatment C) with increasing ageing time.





24

Fig. 60 DBTT curves for alloys 1 and 3 in the bainitic condition (heat treatment D) with increasing ageing time.

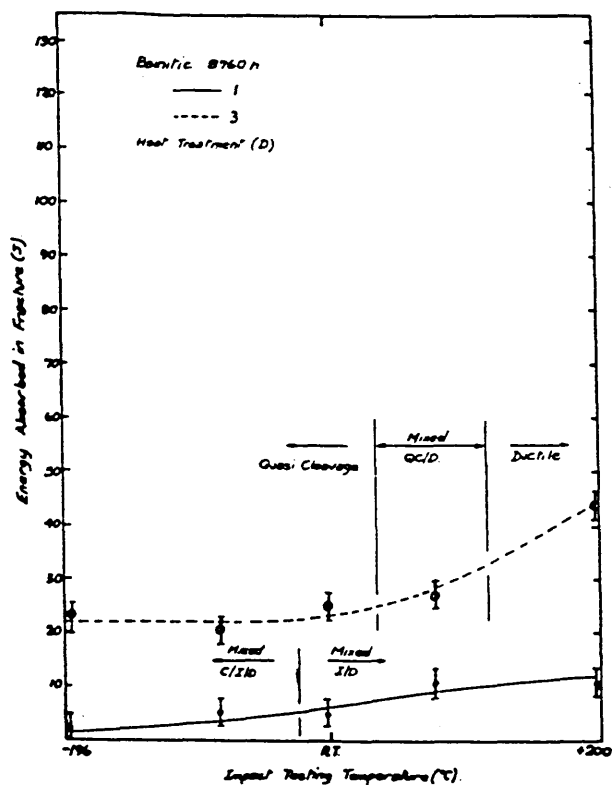
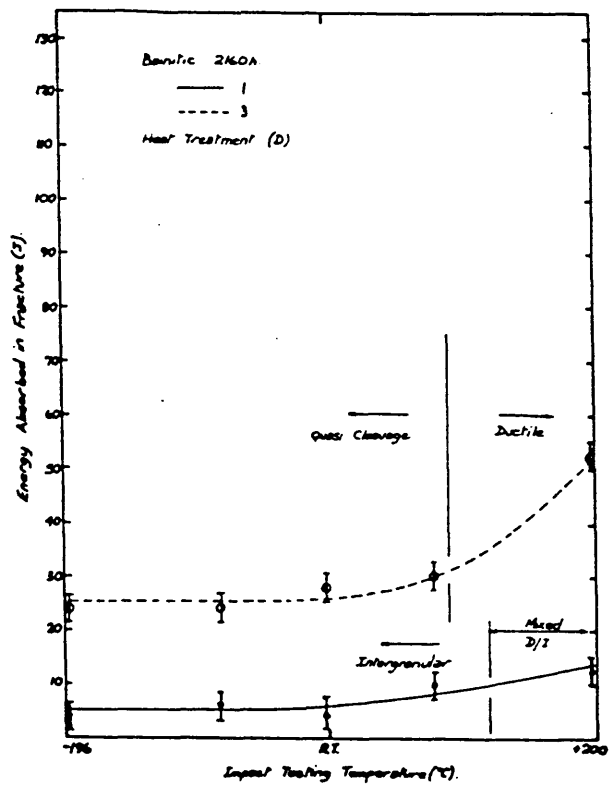
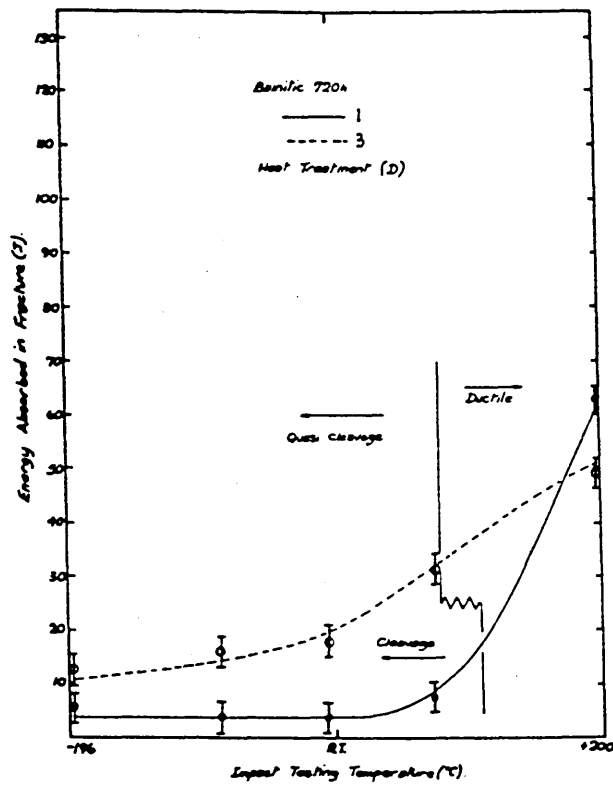
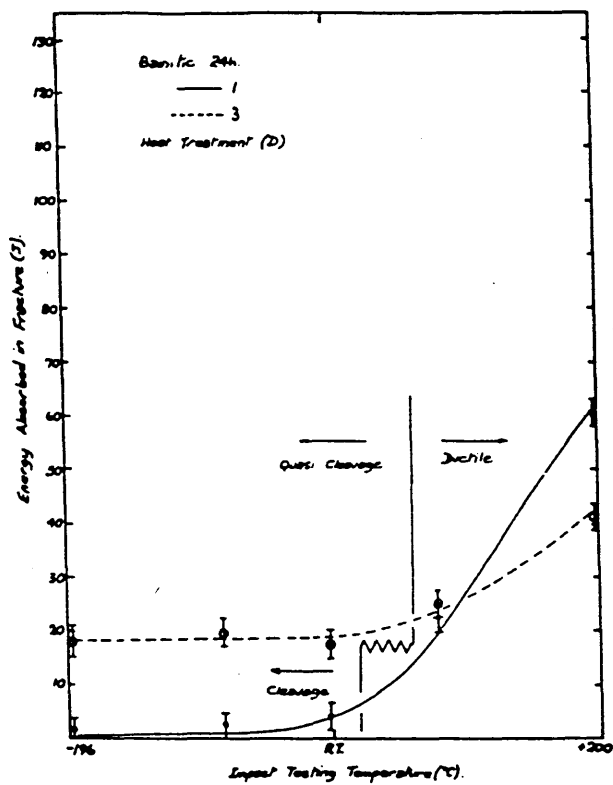


Fig. 61 Ageing curves for alloys 1 and 3 in the isothermally transformed bainitic condition (heat treatment D).

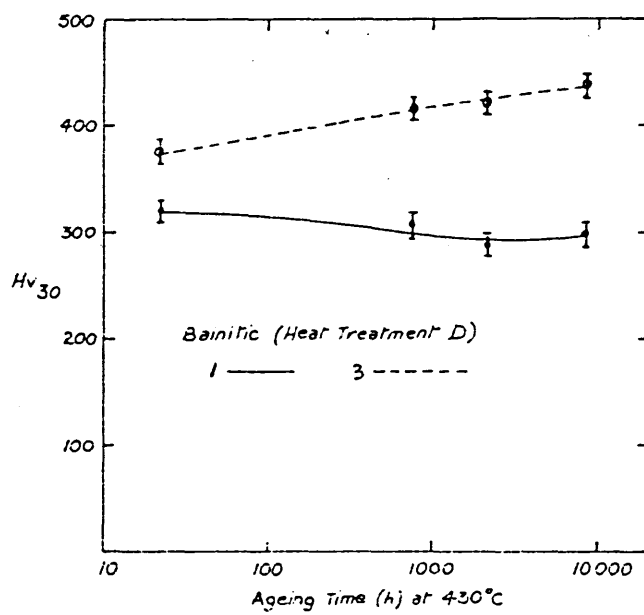


Fig. 62 DBTT curves for alloys 2 and 3 in the isothermally transformed bainitic condition (heat treatment A) with increasing ageing time.

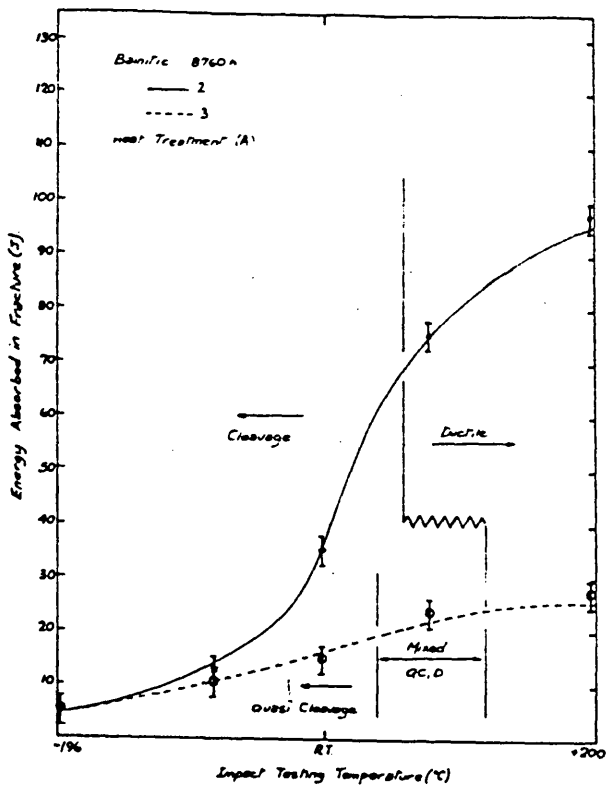
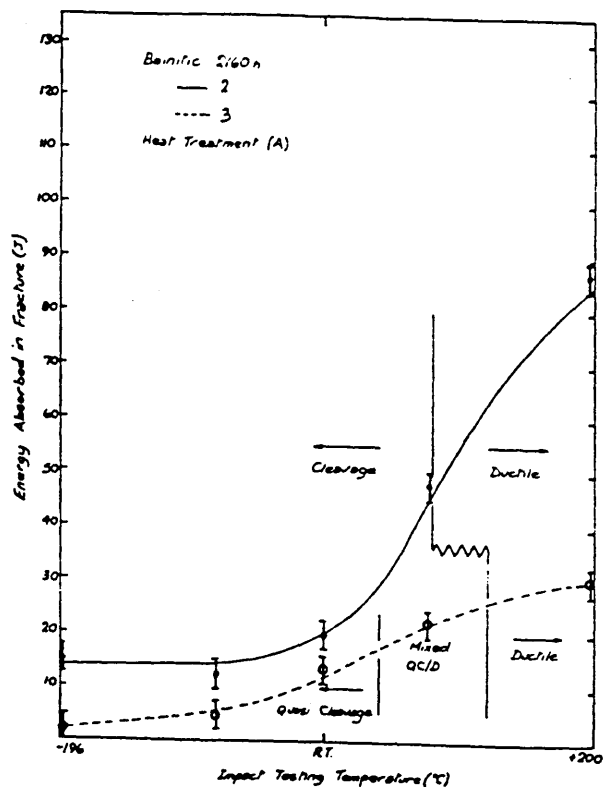
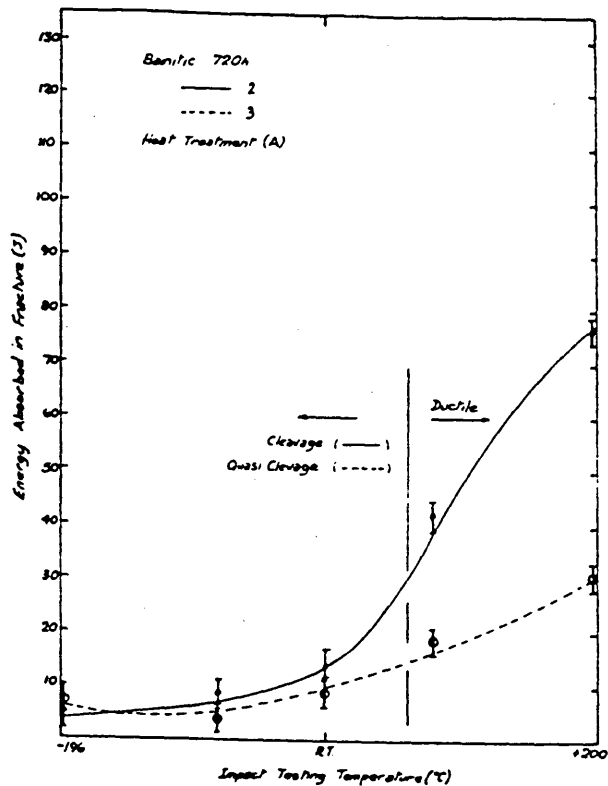
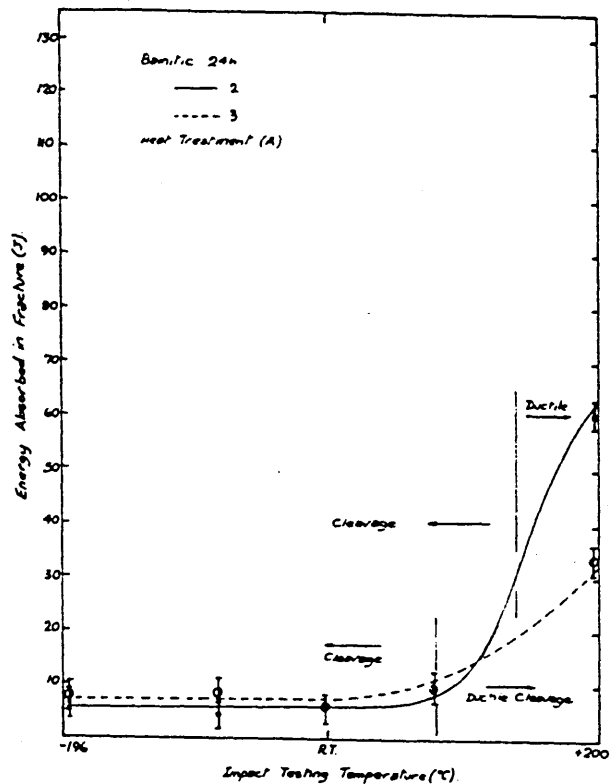


Fig. 63 DBTT curves for alloys 2 and 3 in the quenched and tempered martensitic (heat treatment B) condition with increasing ageing time.

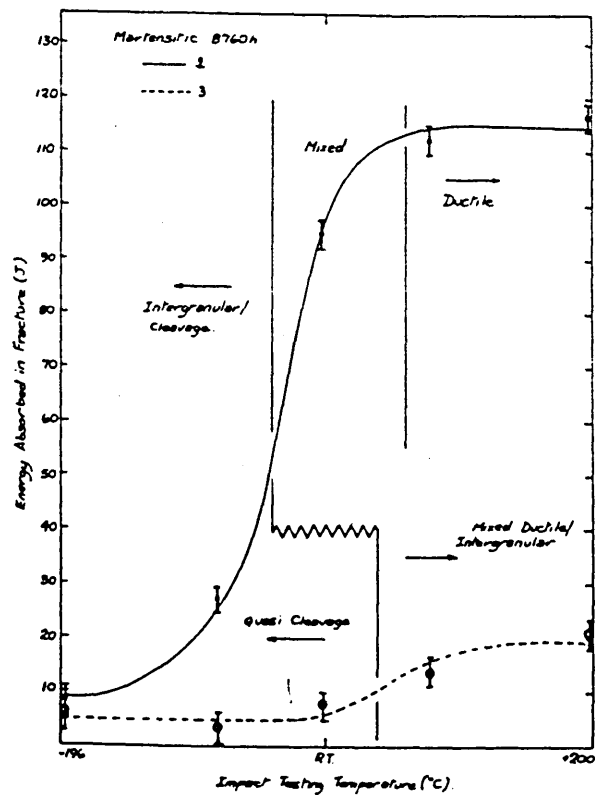
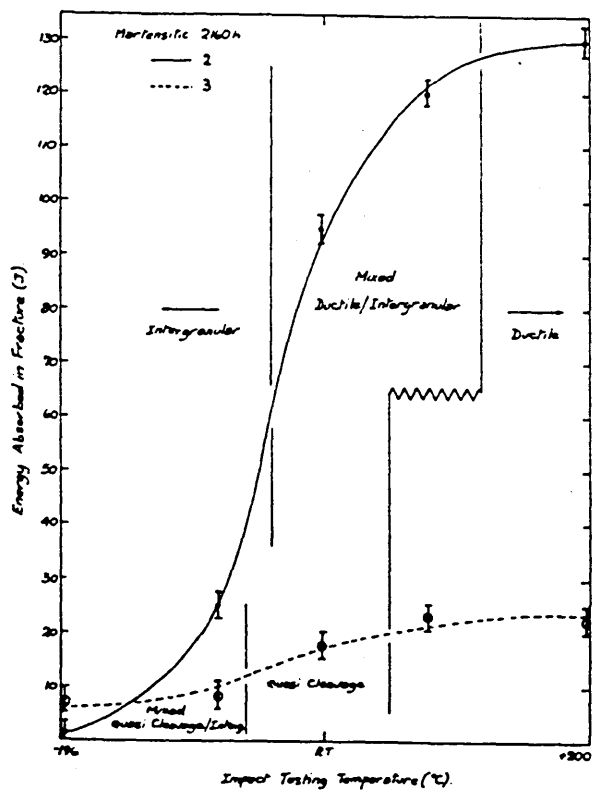
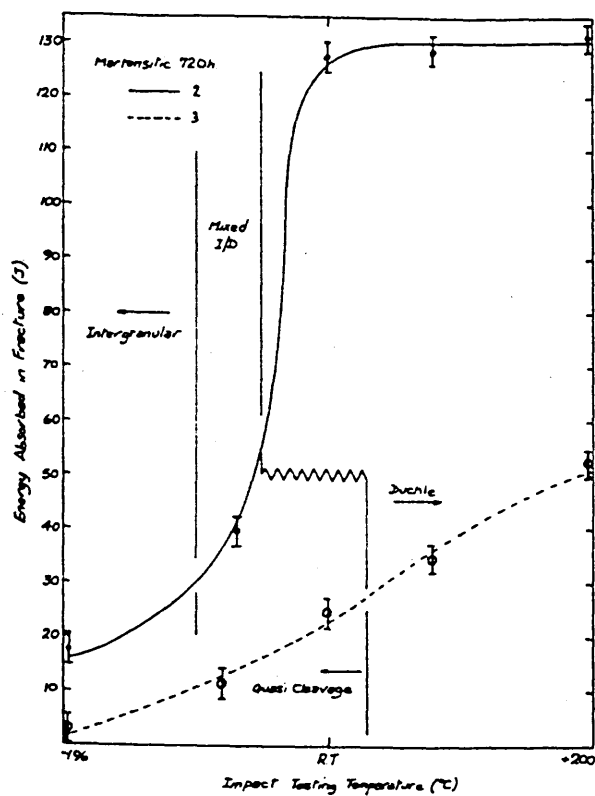
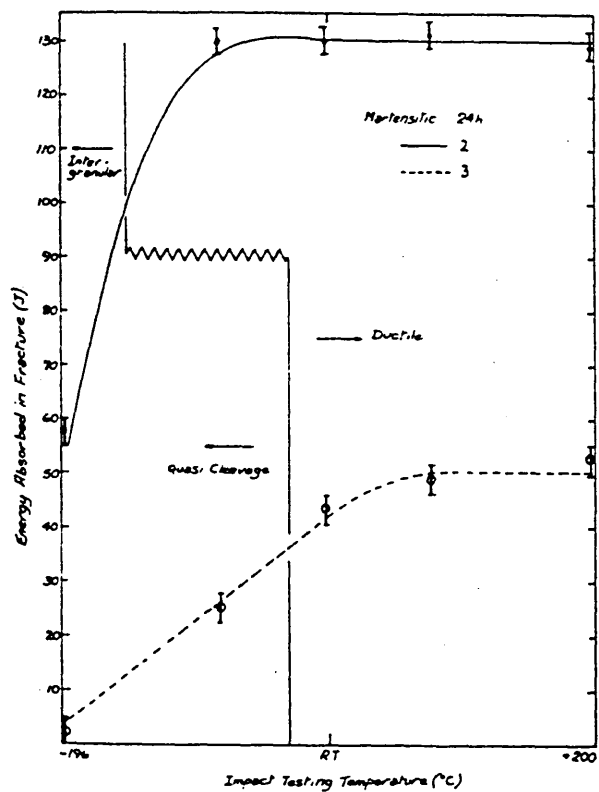
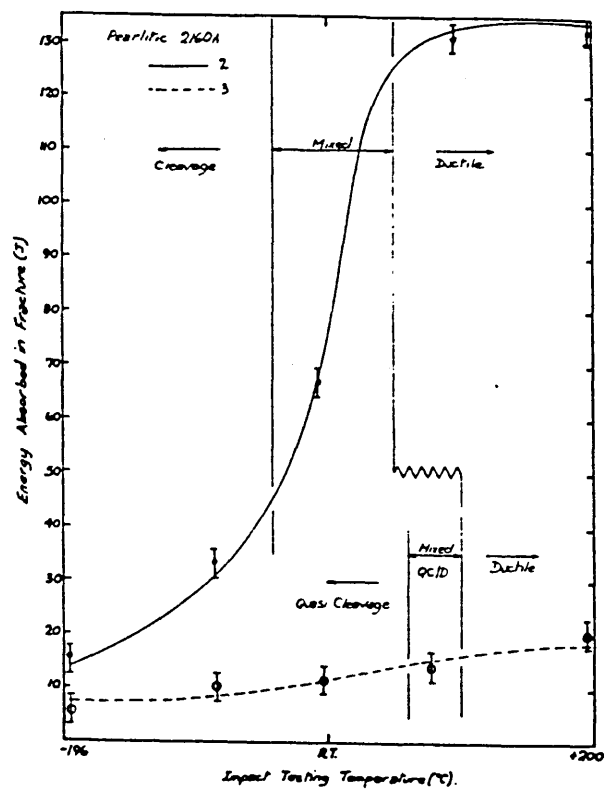
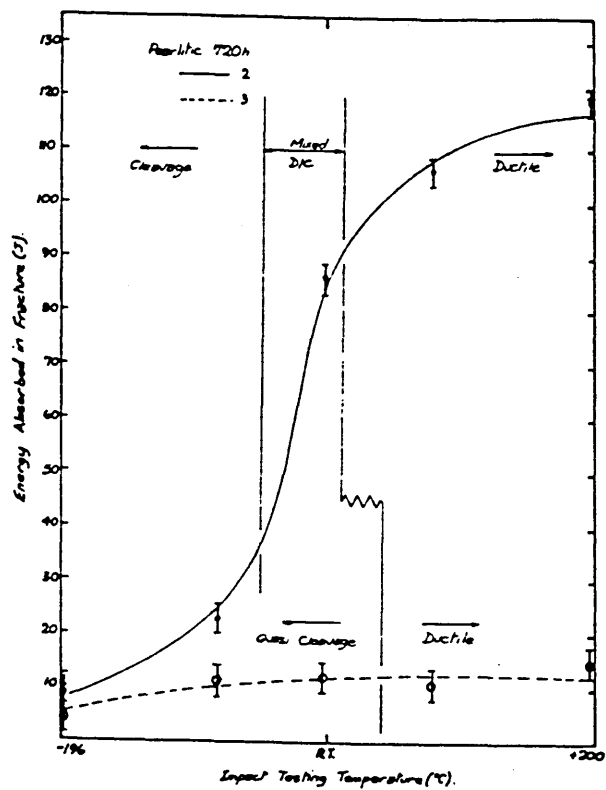
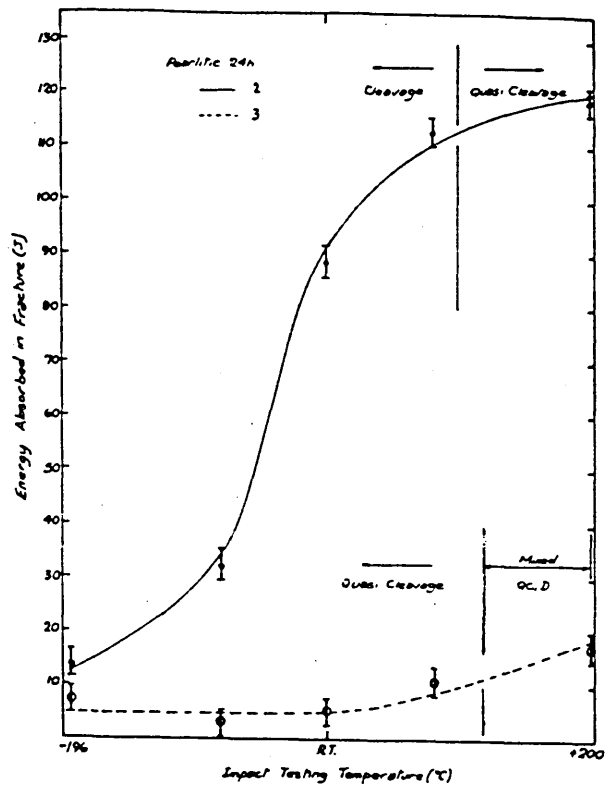


Fig. 64 DBTT curves for alloys 2 and 3 in the pearlitic condition (heat treatment C) with increasing ageing time.



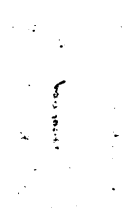


Fig. 65 DBTT curves for alloys 2 and 3 in the isothermally transformed bainitic condition (heat treatment D) with increasing ageing time.

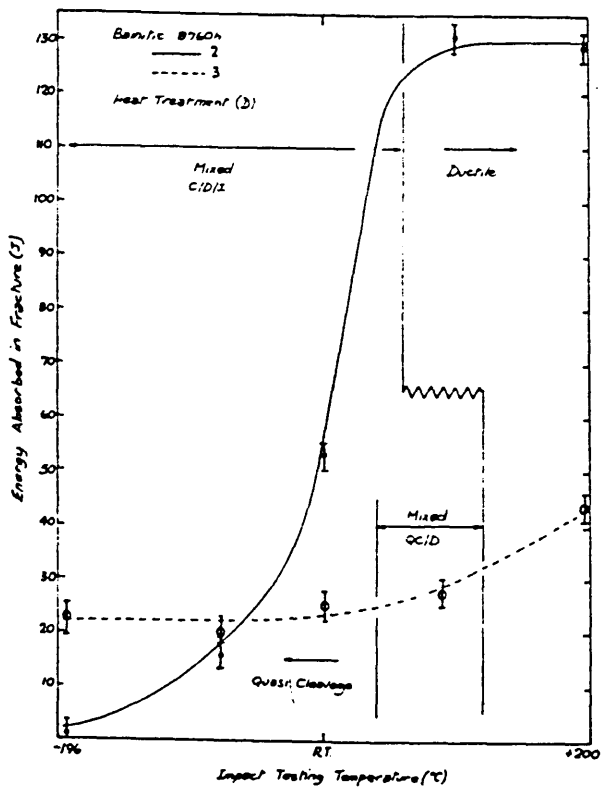
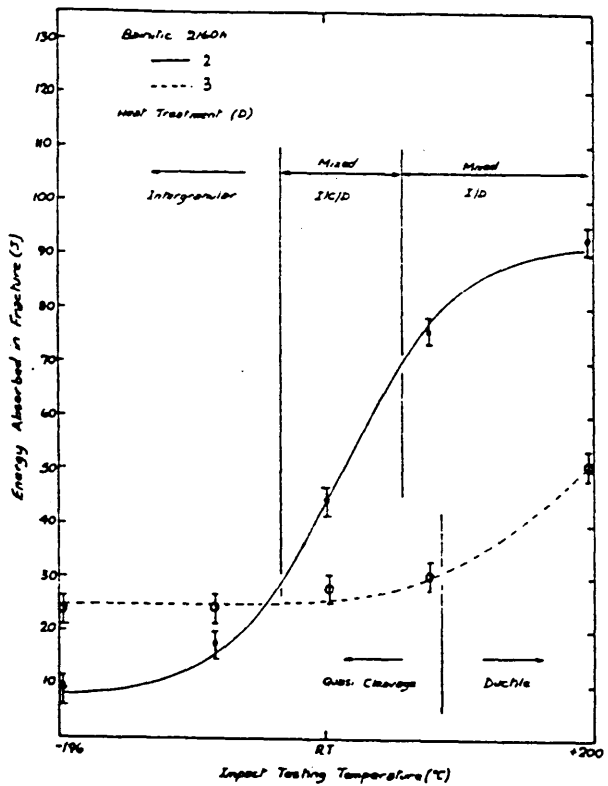
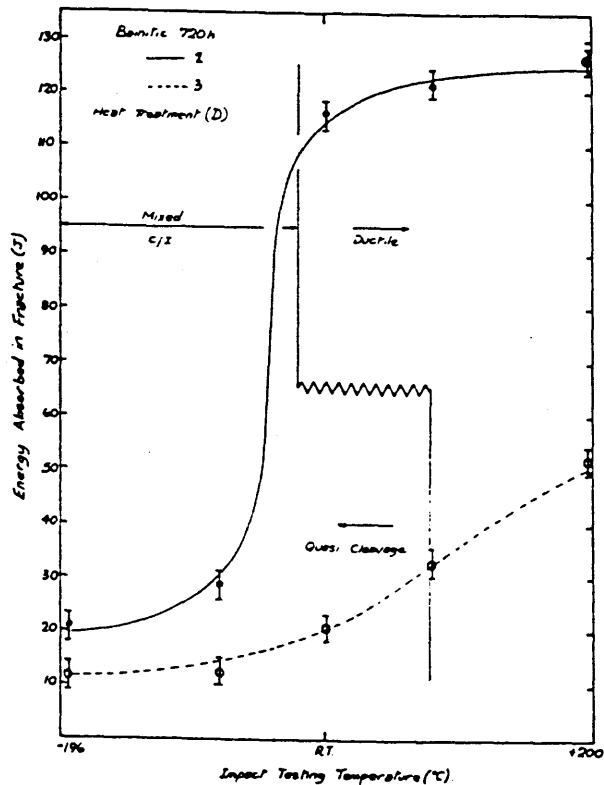
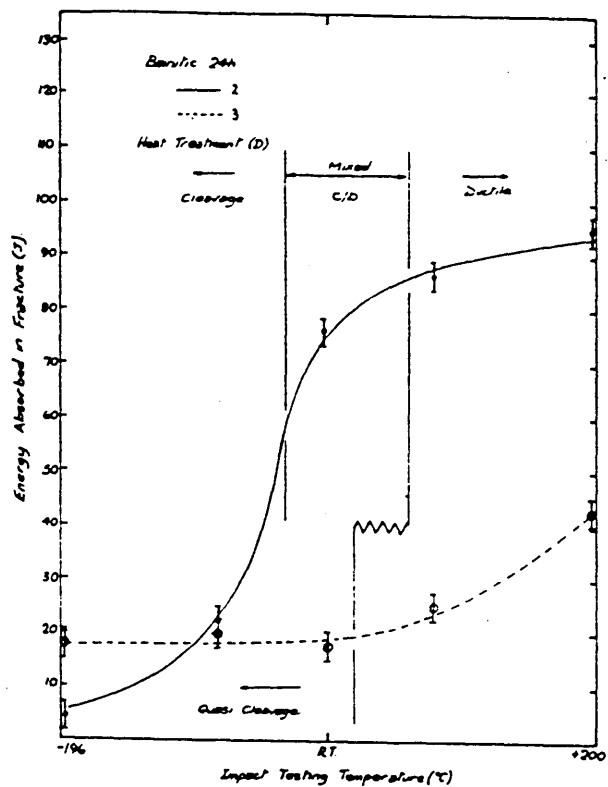
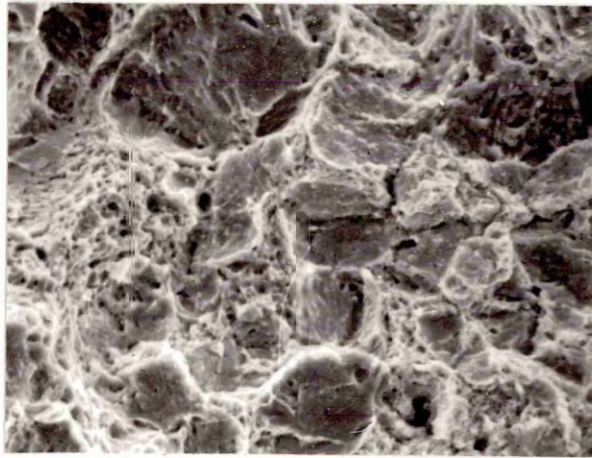
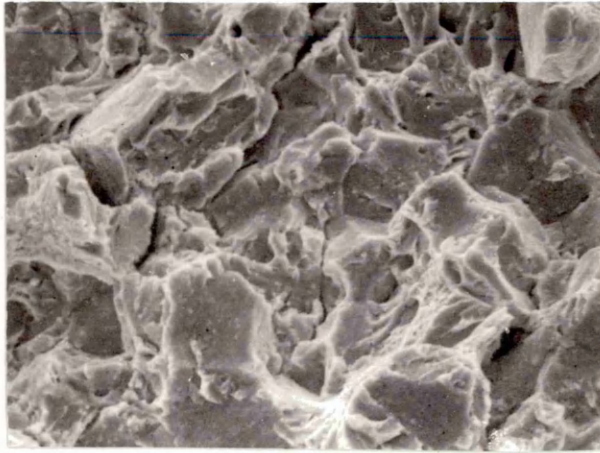


Fig. 66 Scanning electron micrograph of alloy 5, heat treatment B, aged for 8,760 hours at 430°C, impact tested at -196°C, mag. 800x.

Fig. 67 Scanning electron micrograph of alloy 5, heat treatment B, aged for 8,760 hours at 430°C, impact tested at +200°C, mag. 800x.



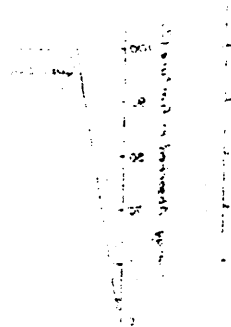
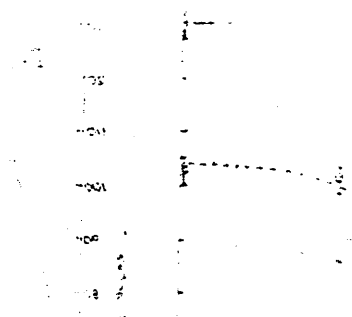


Fig. 68 DBTT curves for alloys 4 and 5 in the quenched and tempered condition (heat treatment B), with increasing ageing time.



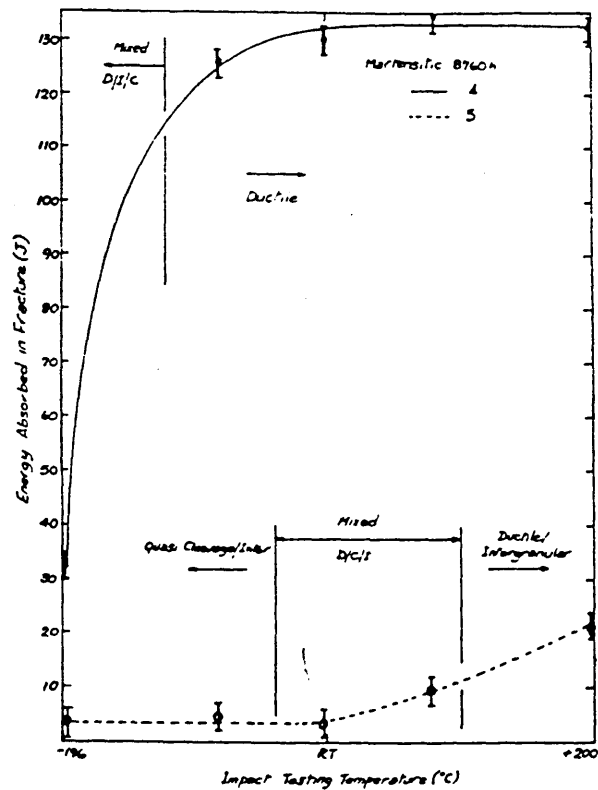
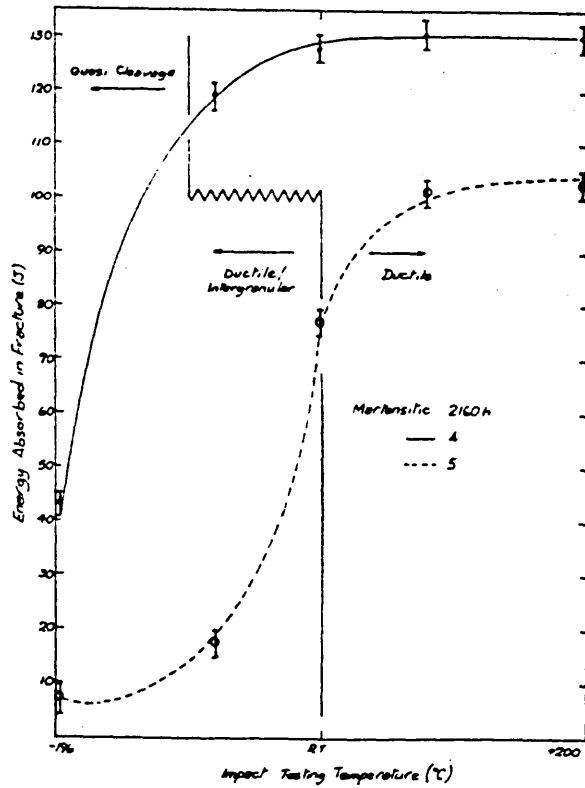
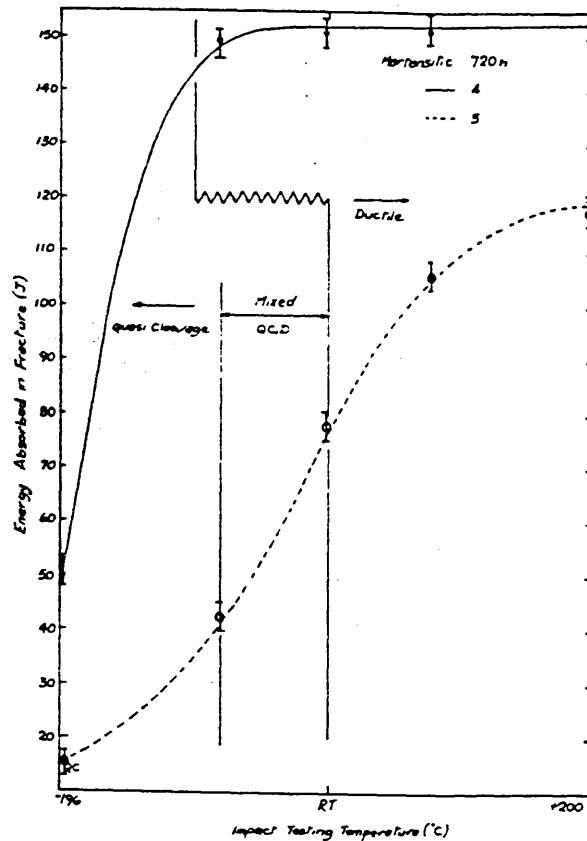
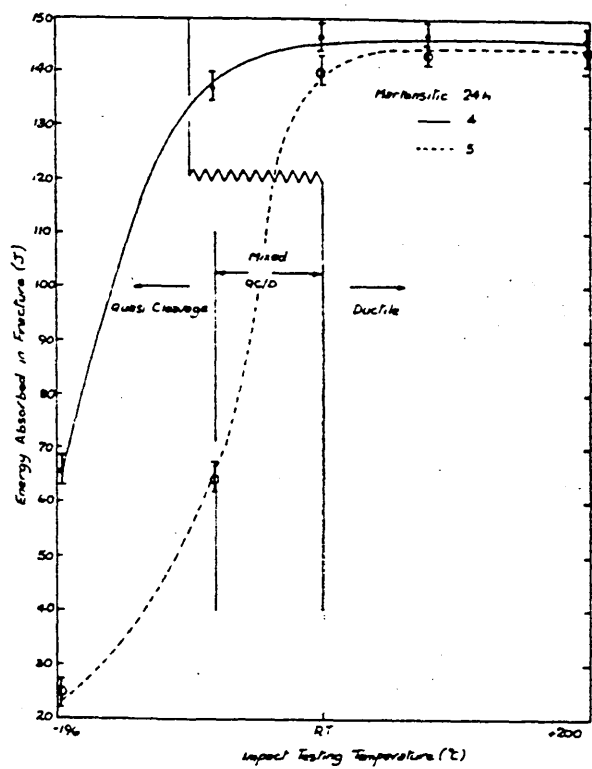


Fig. 69 Scanning electron micrograph of alloy 5, heat treatment B, aged for 2,160 hours at 430°C, impact tested at ambient temperature, mag. 800x.

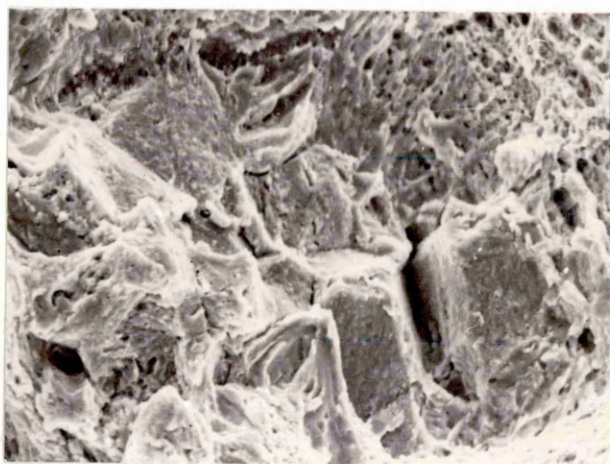


Fig. 70 Ageing curves for alloys 4 and 5 in the quenched and tempered martensitic condition (heat treatment B).

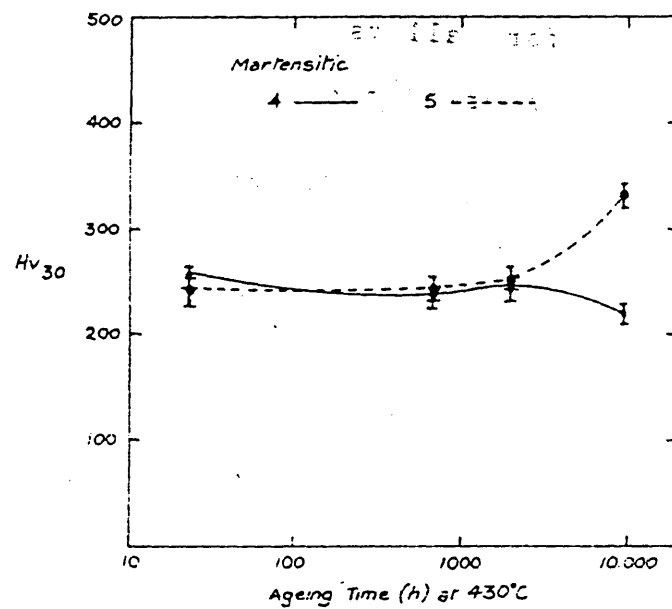


Fig. 71 Transmission electron micrograph of alloy 4 in the quenched and tempered martensitic condition (heat treatment B) aged for 2,160 hours at 430°C.

Fig. 72 Transmission electron micrograph of alloy 4 in the quenched and tempered martensitic condition (heat treatment B), aged for 8,760 hours at 430°C.

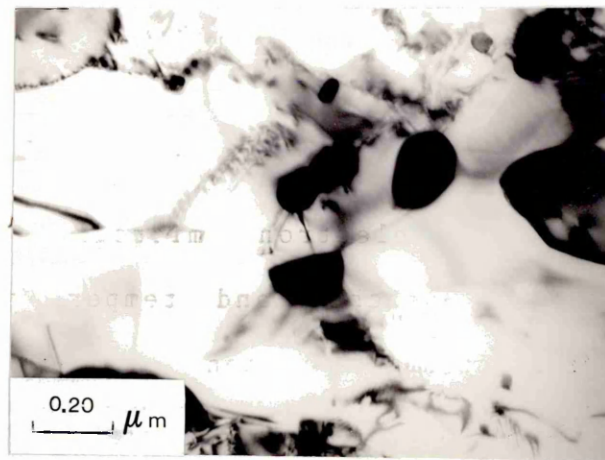
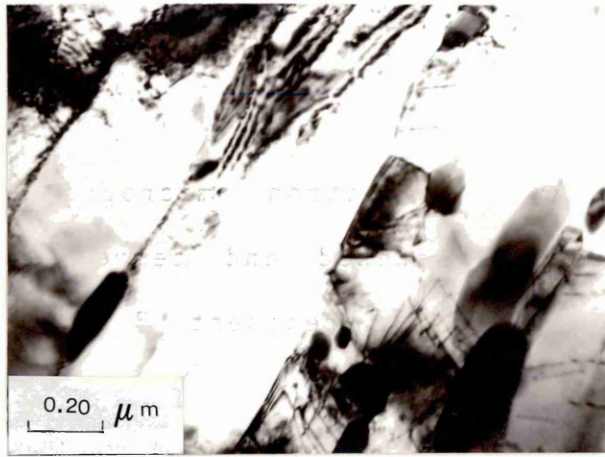
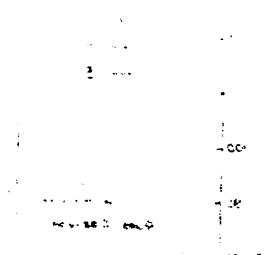


Fig. 73 DBTT curves for alloys 4 and 5 in the isothermally transformed bainitic condition (heat treatment D), with increasing ageing times.



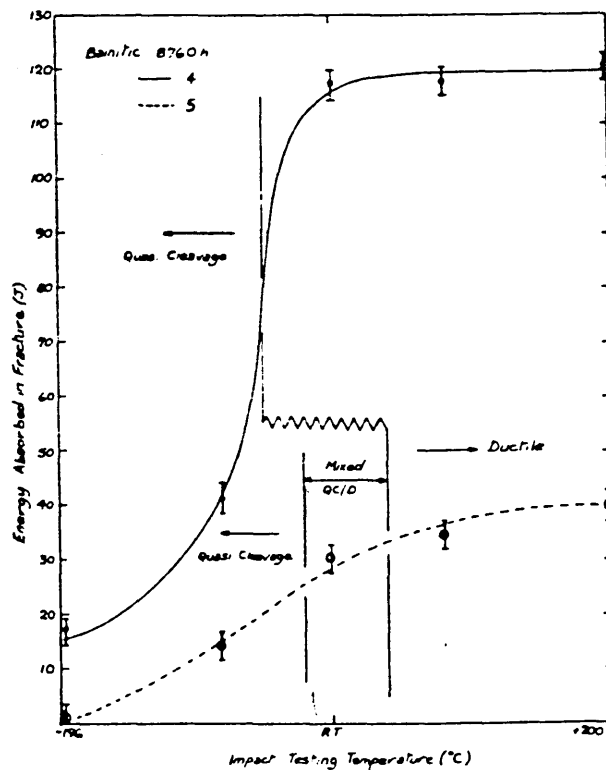
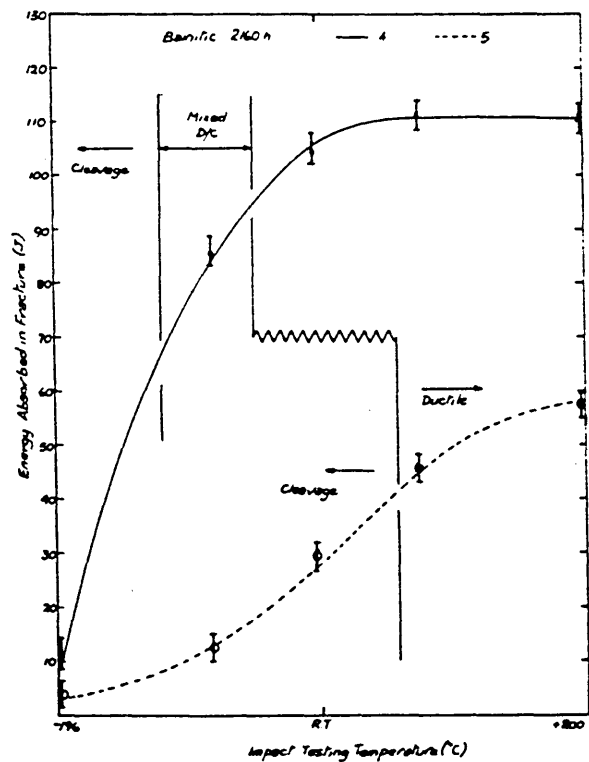
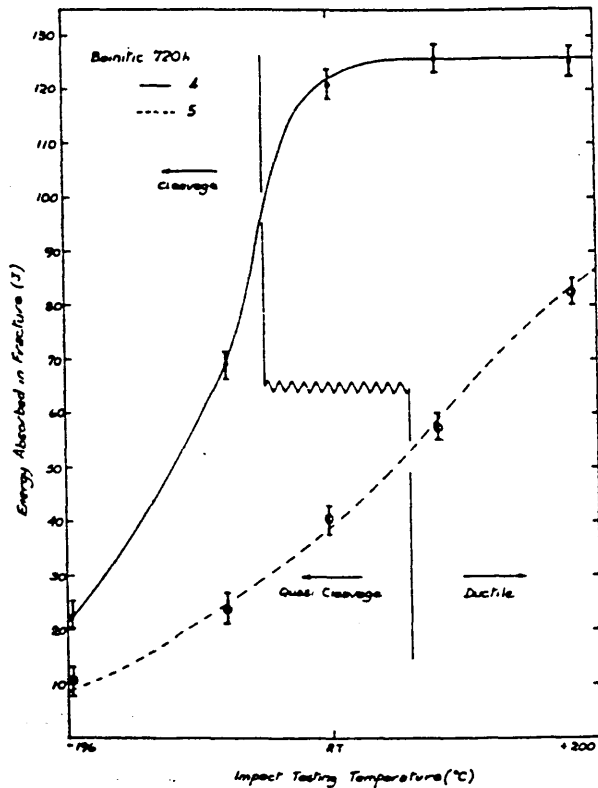
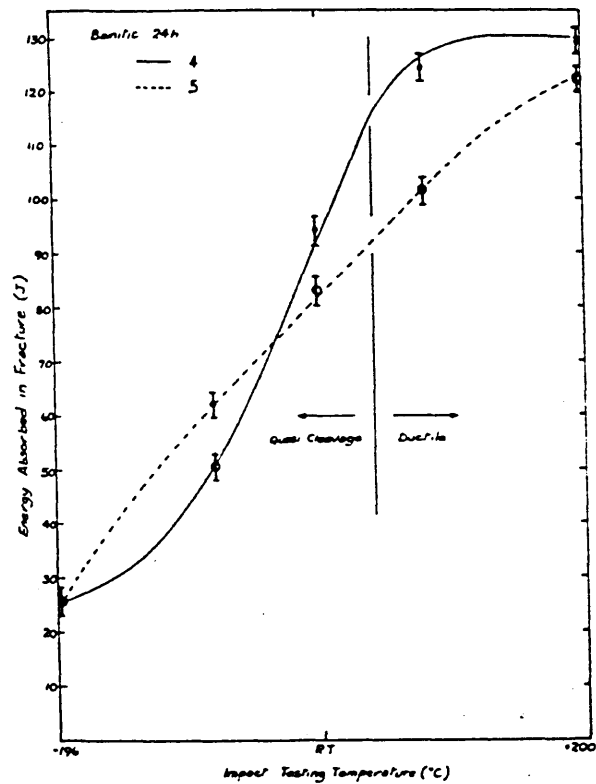


Fig. 74 Scanning electron micrograph of alloy 5, heat treatment D, aged for 24 hours at 430°C, impact tested at -196°C, mag. 950x.

Fig. 75 Scanning electron micrograph of alloy 5, heat treatment D, aged for 8,760 hours at 430°C, impact tested at -196°C, mag. 950x.

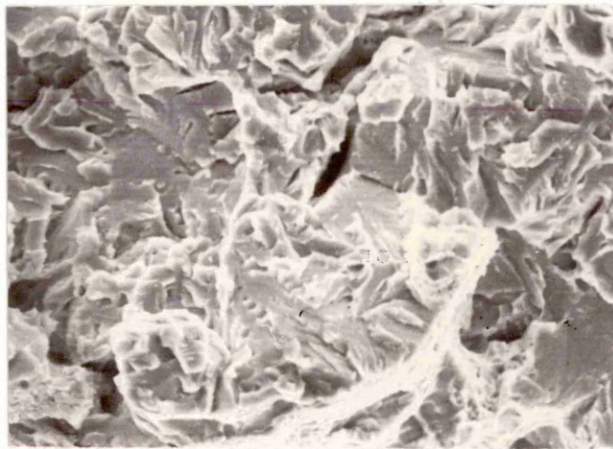
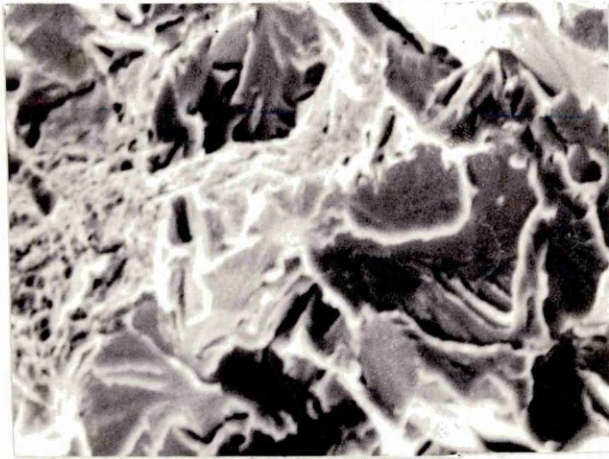


Fig. 76 Ageing curves for alloys 4 and 5 in the isothermally transformed bainitic condition (heat treatment D).

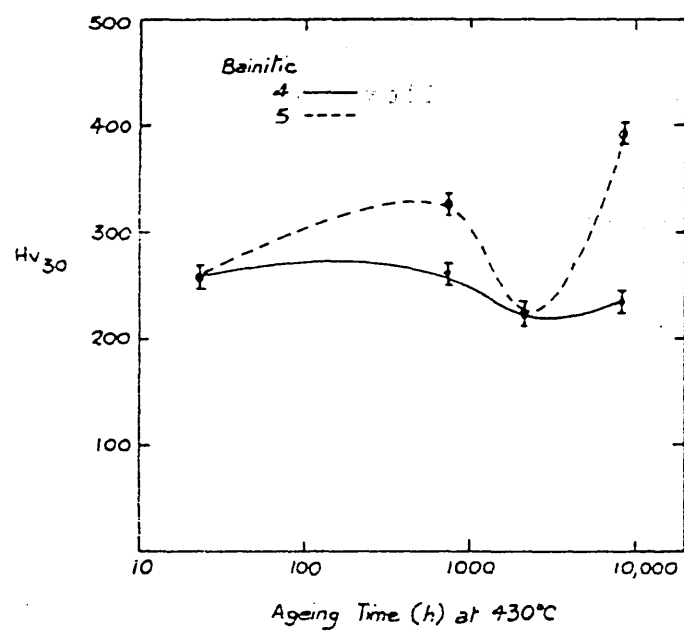


Fig. 77 Scanning electron micrograph of alloy 4 in the isothermally transformed bainitic condition (heat treatment D) aged for 24 hours at 430°C, mag. 1200x.

Fig. 78 Scanning electron micrograph of alloy 5 in the isothermally transformed bainitic condition (heat treatment D) aged for 24 hours at 430°C, mag. 1200x.

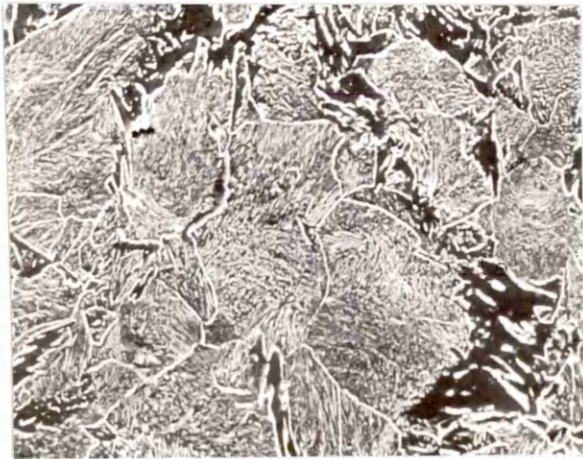
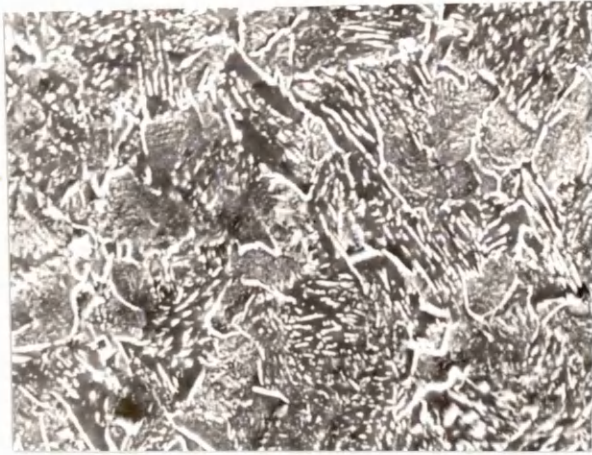


Fig. 79

Fig. 79 DBTT curves for alloys 6 and 7 in the quenched and tempered martensitic condition (heat treatment B) with increasing ageing times.

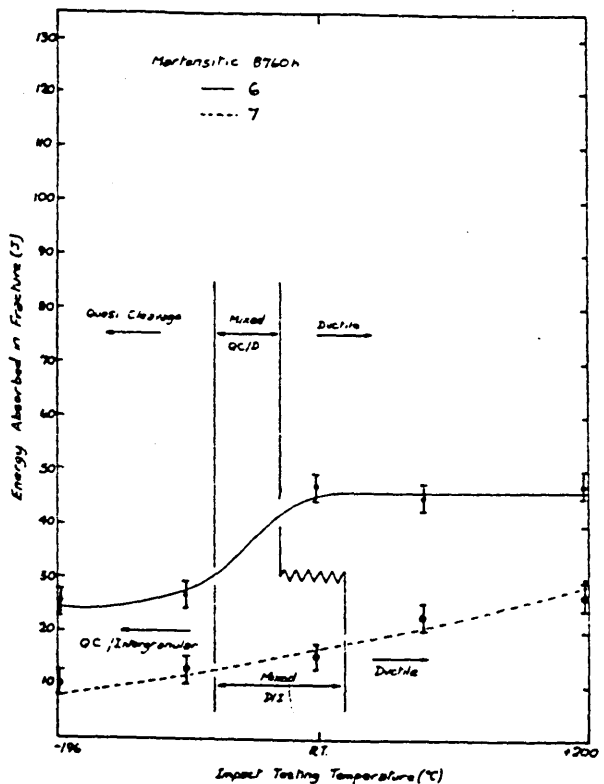
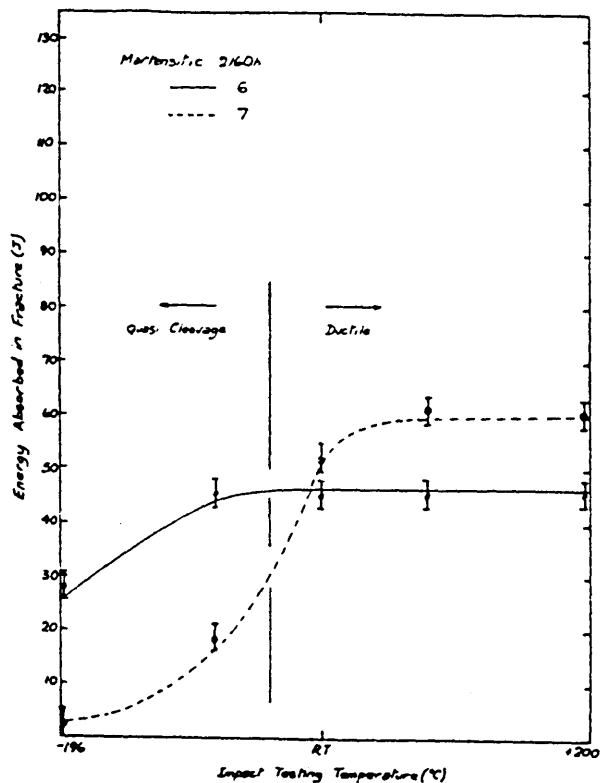
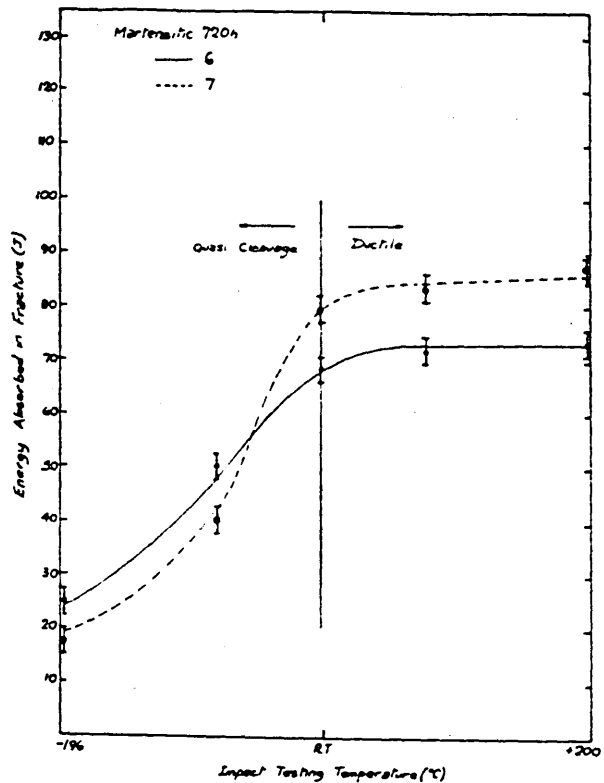
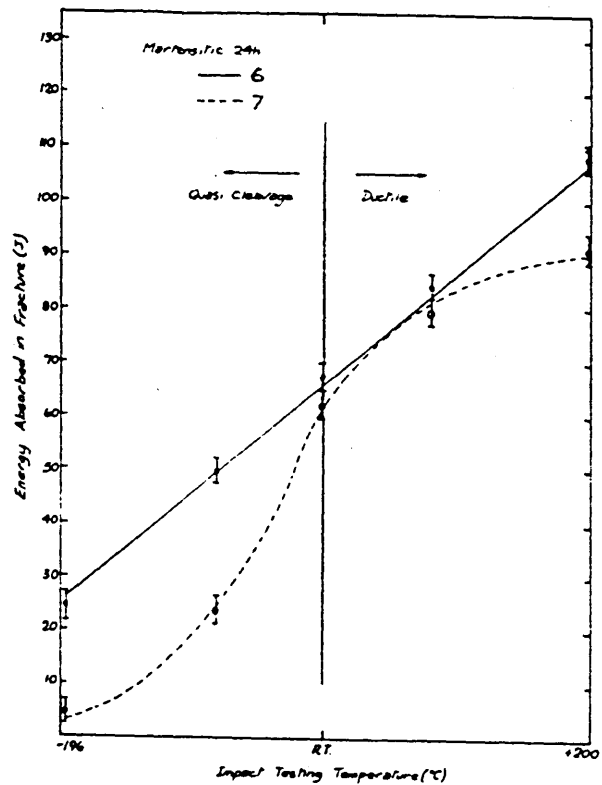
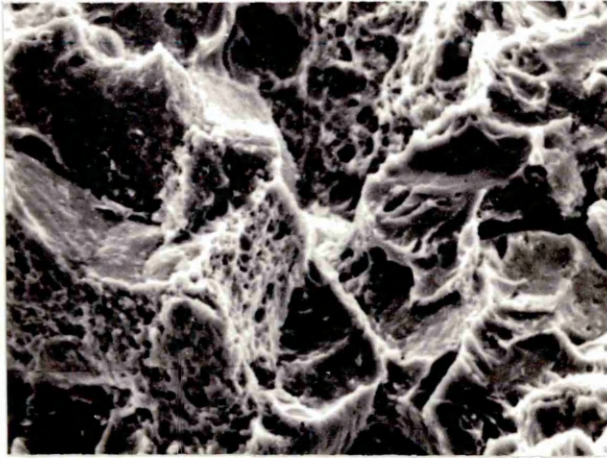
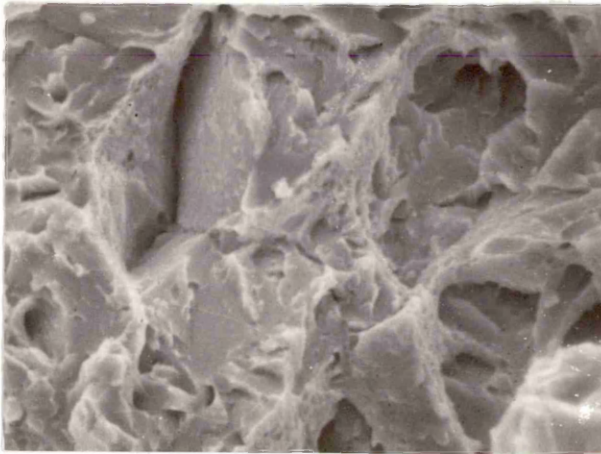


Fig. 80 Scanning electron micrograph of alloy 7, heat treatment B, aged for 8,760 hours at 430°C (a) impact tested at ambient temperature, mag. 1000x, (b) impact tested at -196°C, mag. 1000x.



a



b

Fig. 81 Ageing curves for alloys 6 and 7 in the quenched and tempered martensitic condition (heat treatment B).

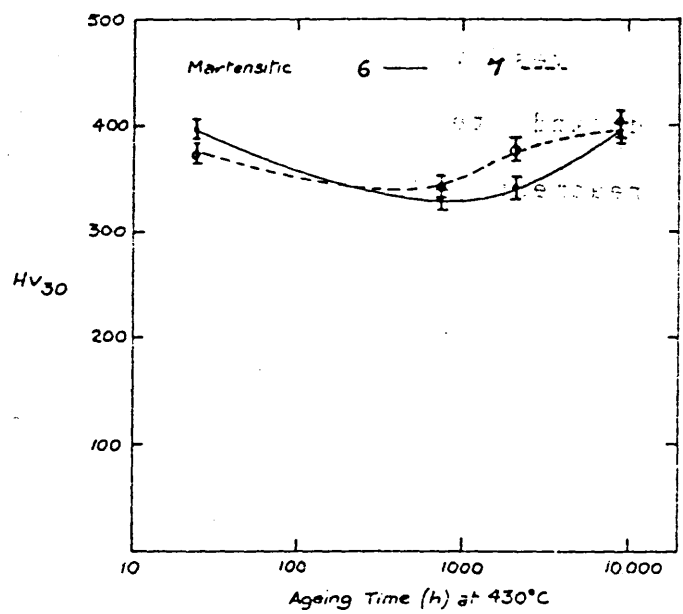


Fig. 82 Transmission electron micrograph of alloy 6 in the quenched and tempered martensitic condition (heat treatment B) aged for 8,760 hours at 430°C.

Fig. 83 Transmission electron micrograph of alloy 7 in the quenched and tempered martensitic condition (heat treatment B) aged for 8,760 hours at 430°C.

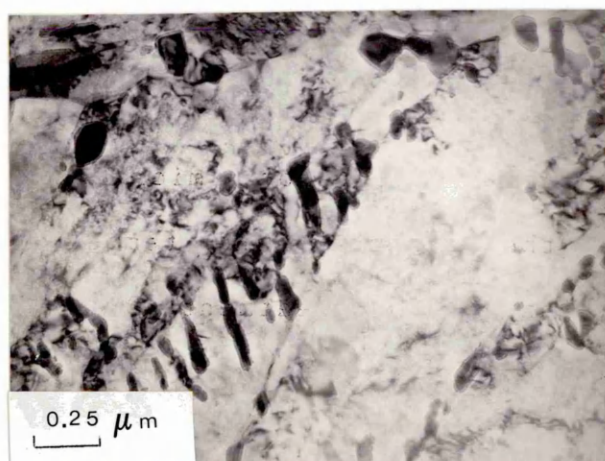
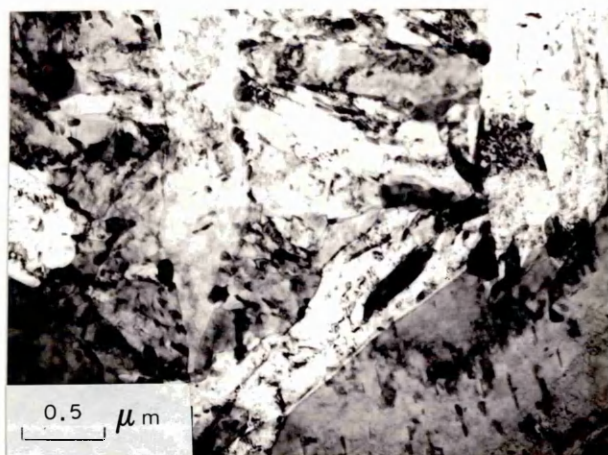


Fig. 84 DBTT curves for alloys 6 and 7 in the isothermally bainitic condition (heat treatment D) with increasing ageing times.

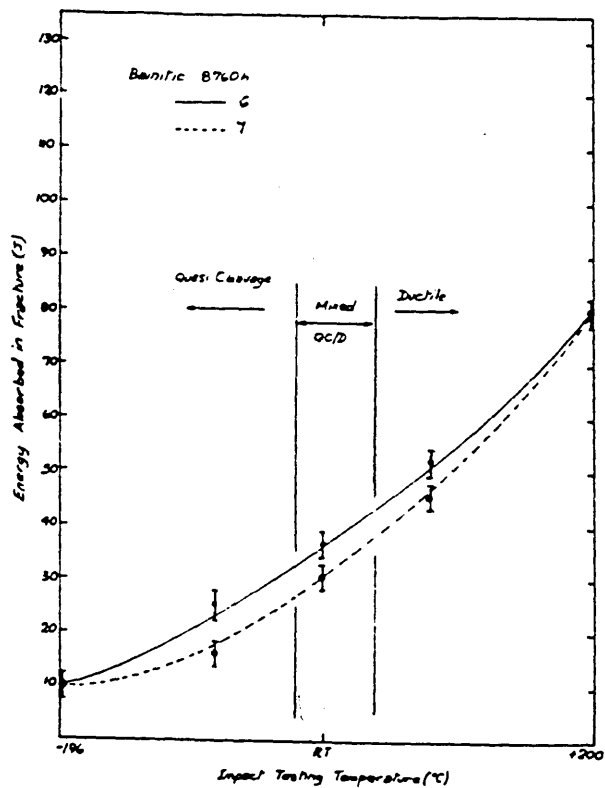
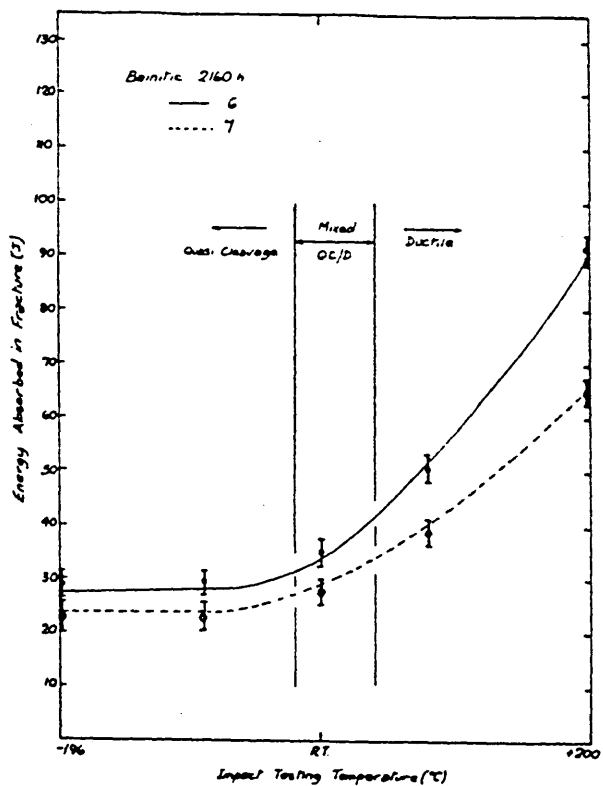
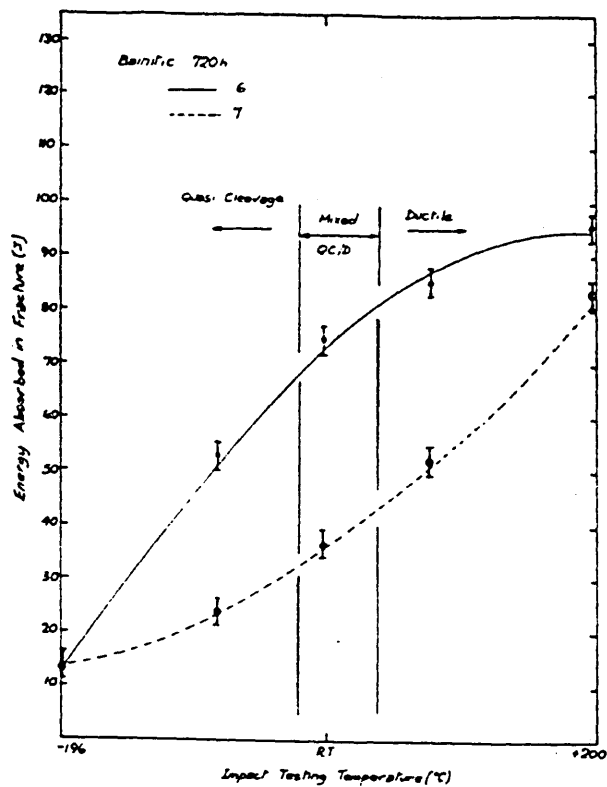
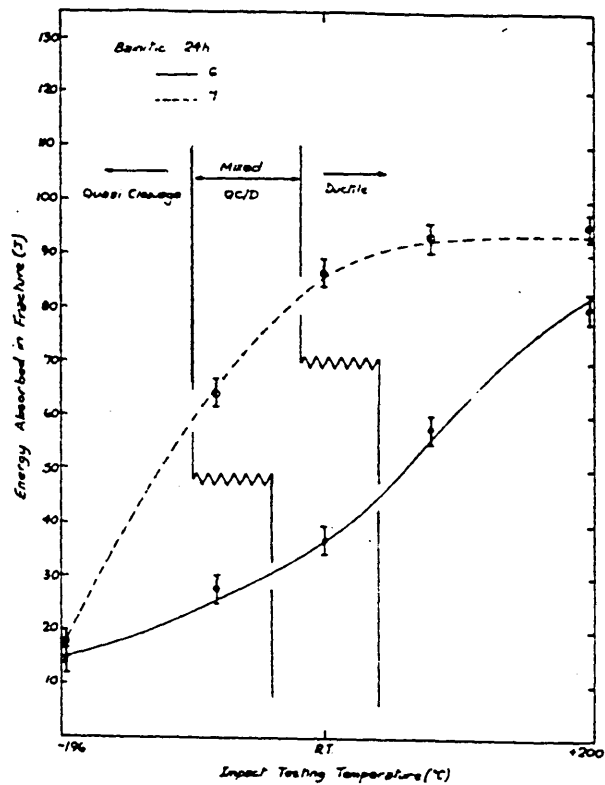
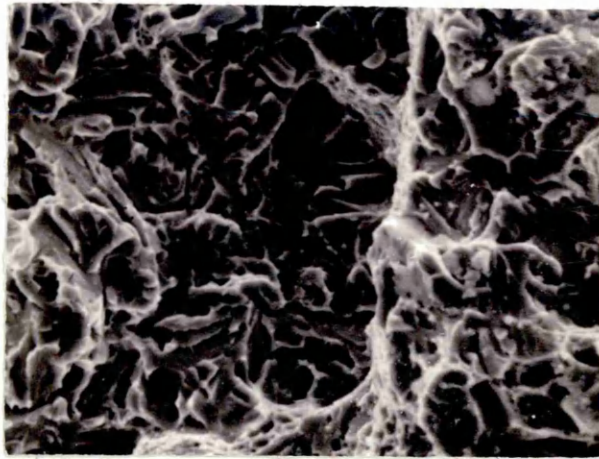
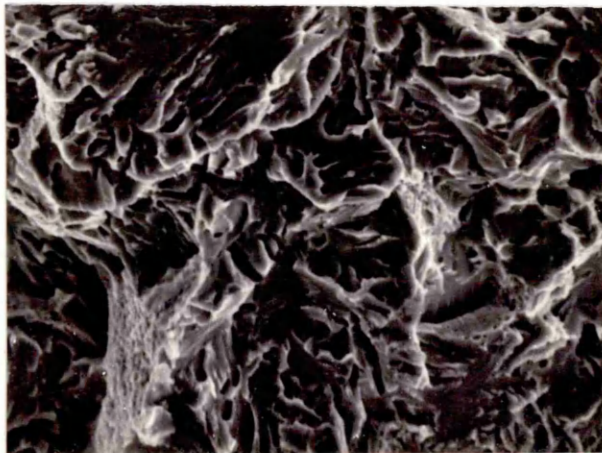


Fig. 85 Alloys 6 and 7, heat treatment D, aged for 24 hours at 430°C (a) alloy 6, impact tested at -80°C, mag. 950x, (b) alloy 7, impact tested at -196°C, mag. 950x.

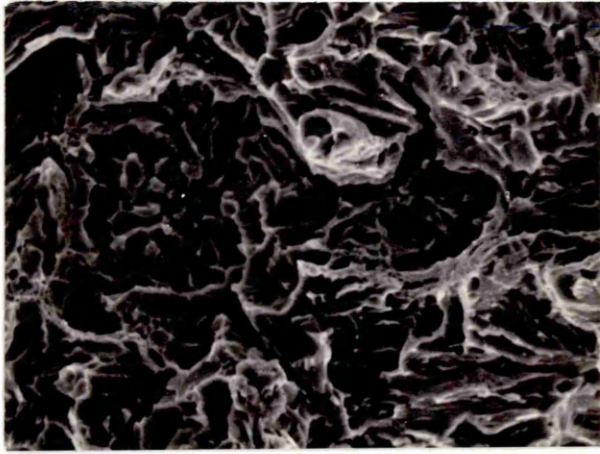


a

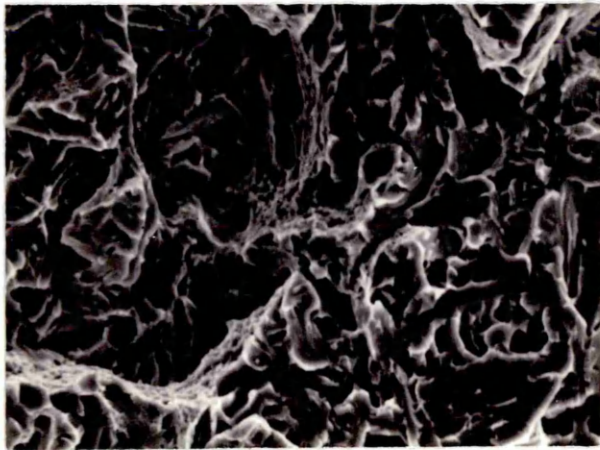


b

Fig. 86 Alloys 6 and 7, heat treatment D, aged for 8,760 hours at 430°C (a) alloy 6, impact tested at -196°C, mag. 900x, (b) alloy 7, impact tested at -196°C, mag. 900x.



a



b

Fig. 88 Scanning electron micrograph of alloy 8, heat treatment B, aged for 24 hours at 430°C, impact tested at ambient temperature, mag. 1400x.

Fig. 89 Scanning electron micrograph of alloy 9, heat treatment B, aged for 24 hours at 430°C, impact tested at ambient temperature, mag. 1500x.

Fig. 90 Scanning electron micrograph of alloy 8, heat treatment B, aged for 8,760 hours at 430°C, impact tested at ambient temperatures, mag. 1200x.

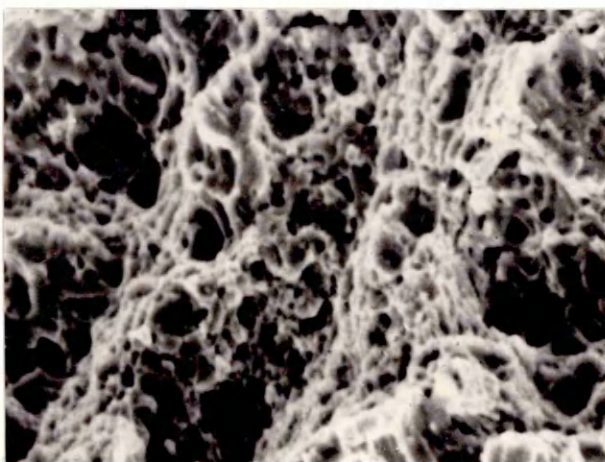
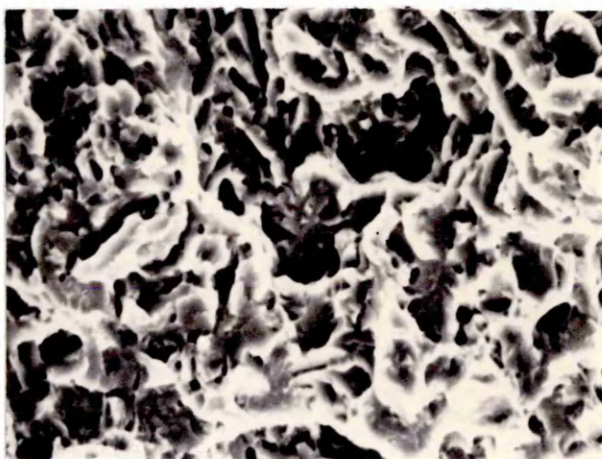
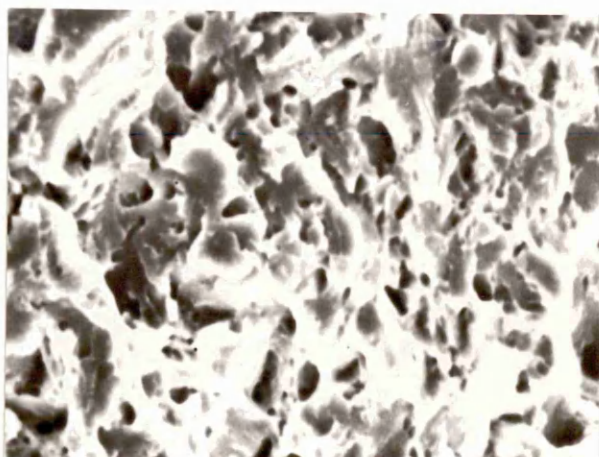


Fig. 87 Ageing curves for alloys 6 and 7 in the isothermally transformed bainitic condition (heat treatment D).

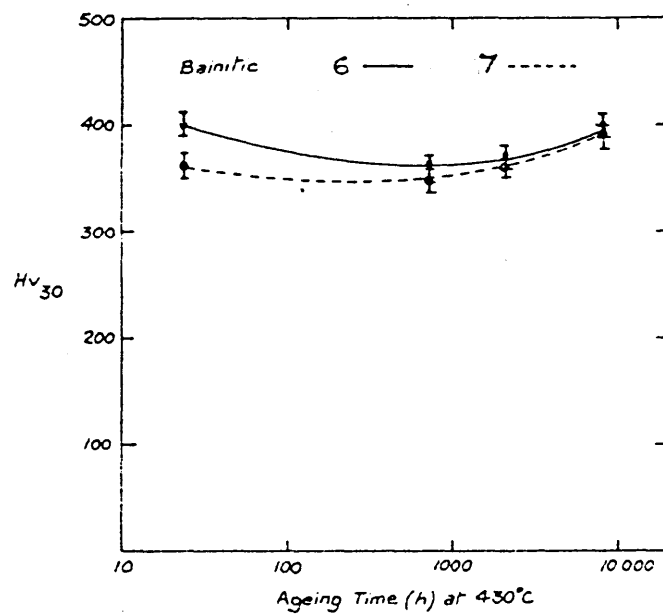


Fig. 91 Scanning electron micrograph of alloy 9, heat treatment B, aged for 8,760 hours at 430°C, impact tested at ambient temperature, mag. 1600x.

Fig. 92 Scanning electron micrograph of alloy 8, heat treatment B, aged for 24 hours at 430°C, impact tested at +200°C, mag. 1700x.

Fig. 93 Scanning electron micrograph of alloy 8, heat treatment B, aged for 8,760 hours at 430°C, impact tested at +200°C, mag. 1600x.

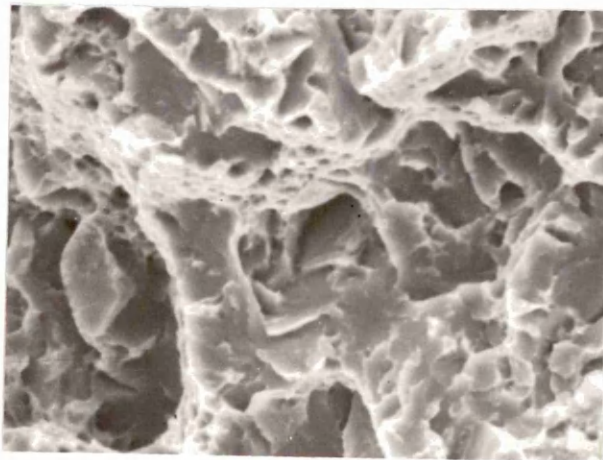
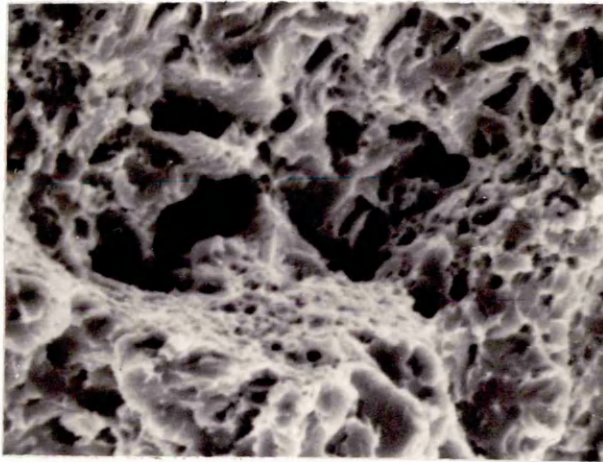
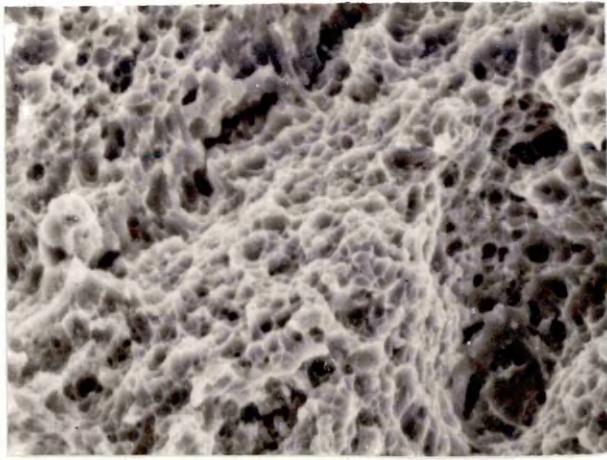


Fig. 94 Scanning electron micrograph of alloy 9, heat treatment B, aged for 24 hours at 430°C, impact tested at +80°C, mag. 1400x.

Fig. 95 Scanning electron micrograph of alloy 9, heat treatment B, aged for 8,760 hours at 430°C, impact tested at +200°C, mag. 1400x.

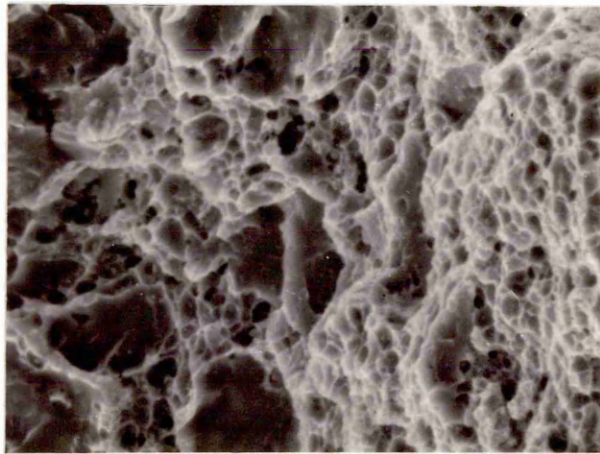
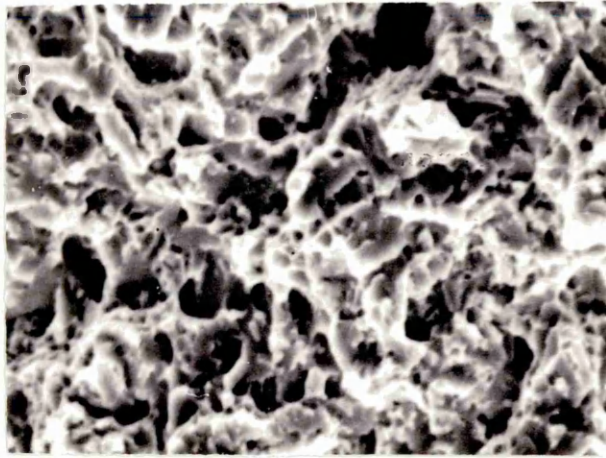


Fig. 96 DBTT curves for alloys 8 and 9 in the quenched and tempered martensitic condition, (heat treatment B) with increasing ageing times.

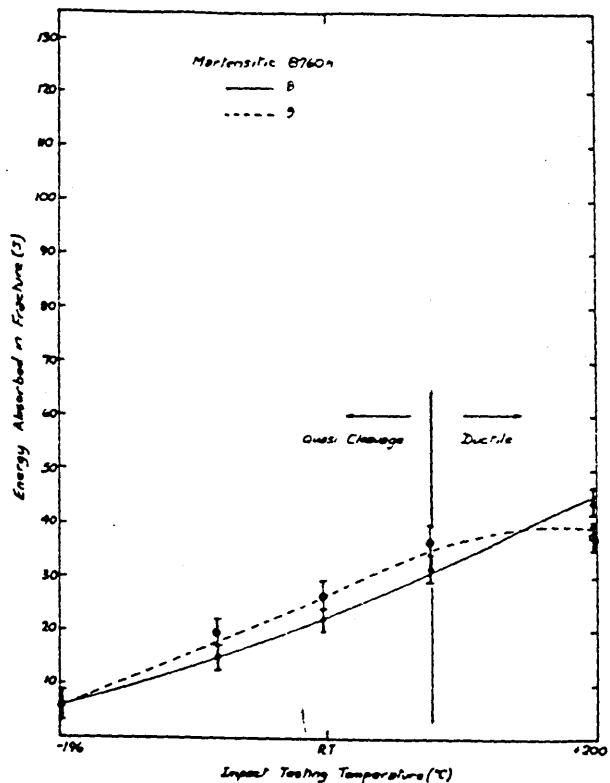
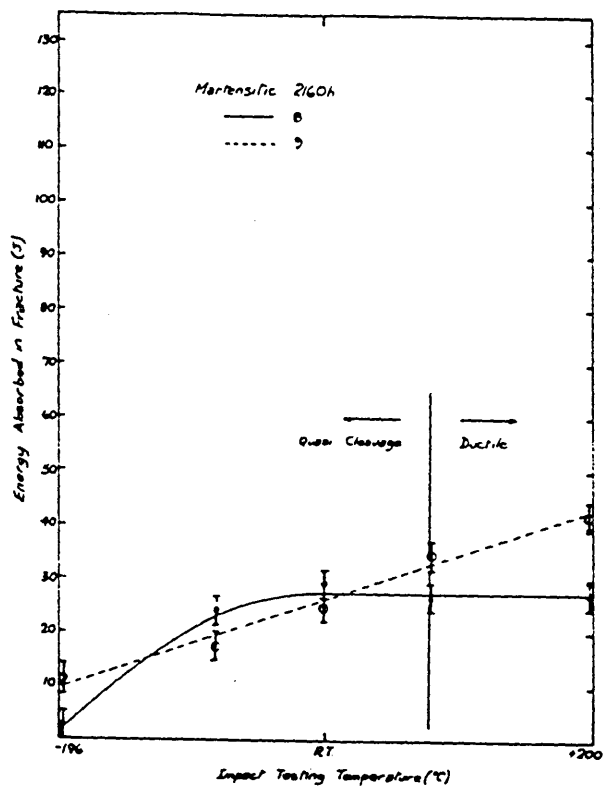
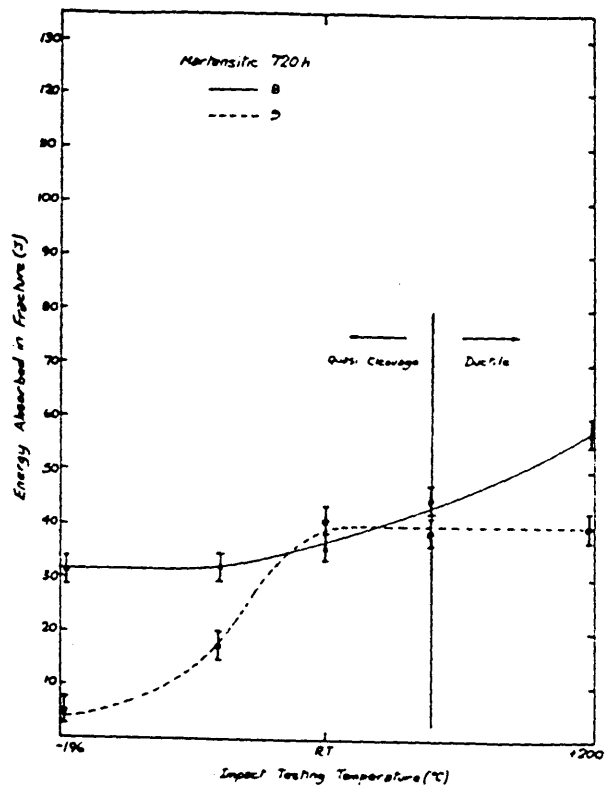
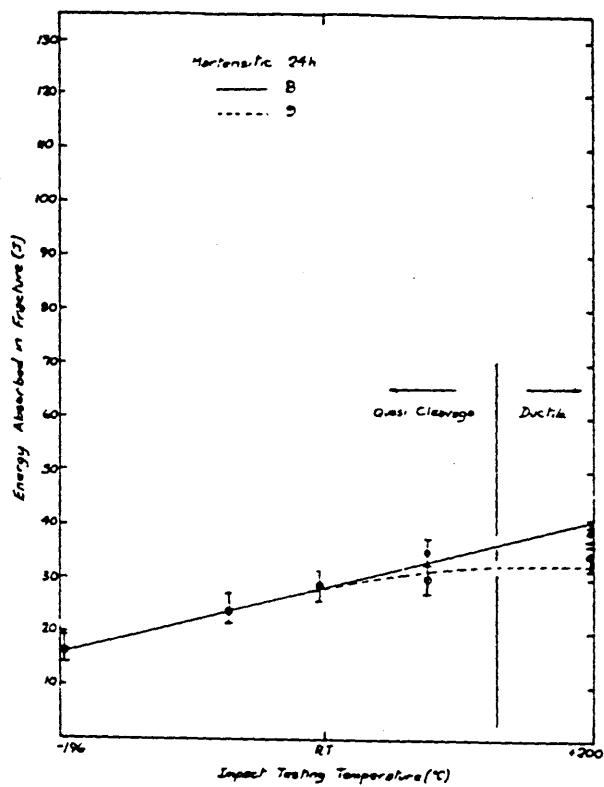


Fig. 97 Ageing curves for alloys 8 and 9 in the
quenched and tempered martensitic condition
(heat treatment B).

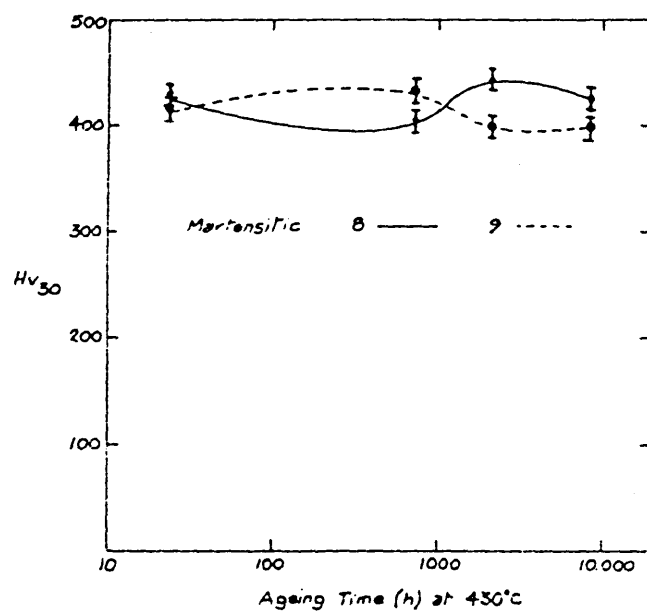
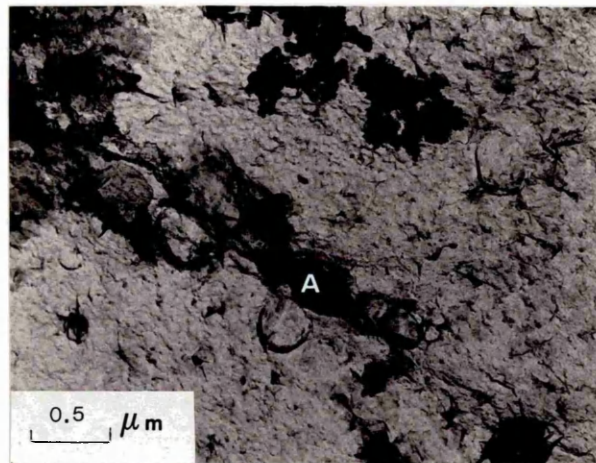
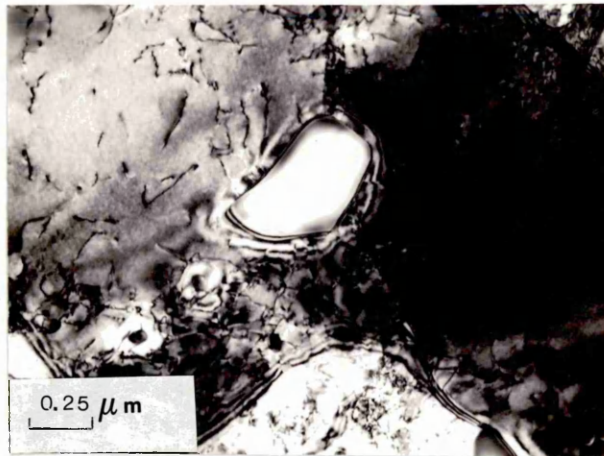


Fig. 98 Transmission electron micrograph of alloy 9 in the quenched and tempered martensitic condition (heat treatment B) aged for 8,760 hours at 430°C.

Fig. 99 Carbon extraction replica of the microstructure obtained for alloy 9 in the as-quenched condition, showing M₆C particle (particle A).



100

Fig. 100 DBTT curves for alloys 8 and 9 in the isothermally transformed bainitic condition (heat treatment D) with increasing ageing times.

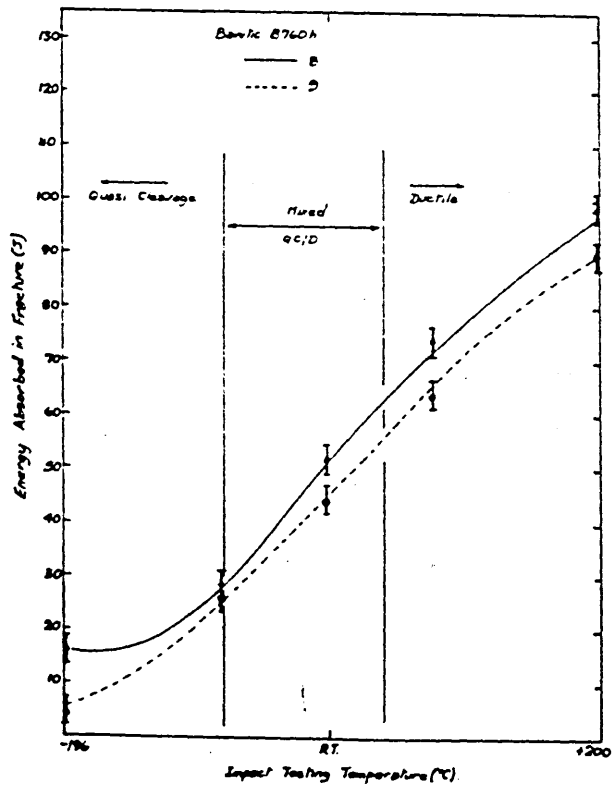
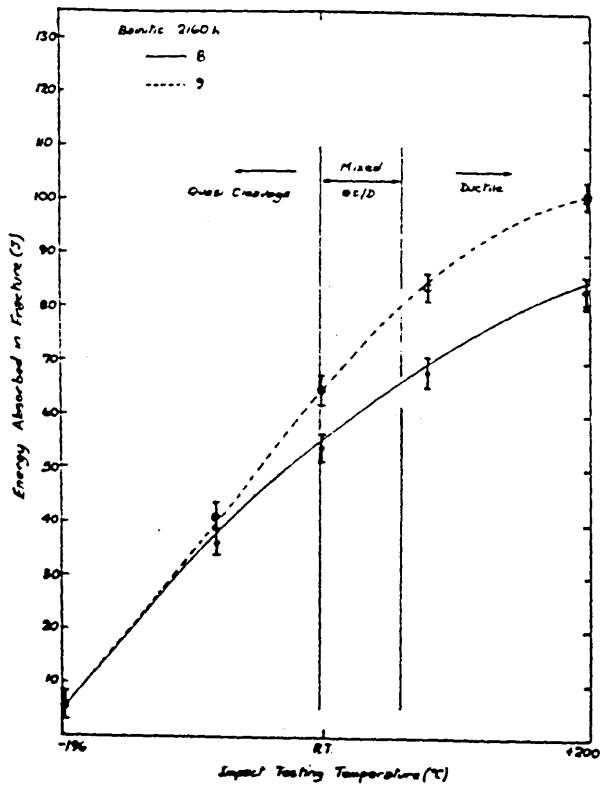
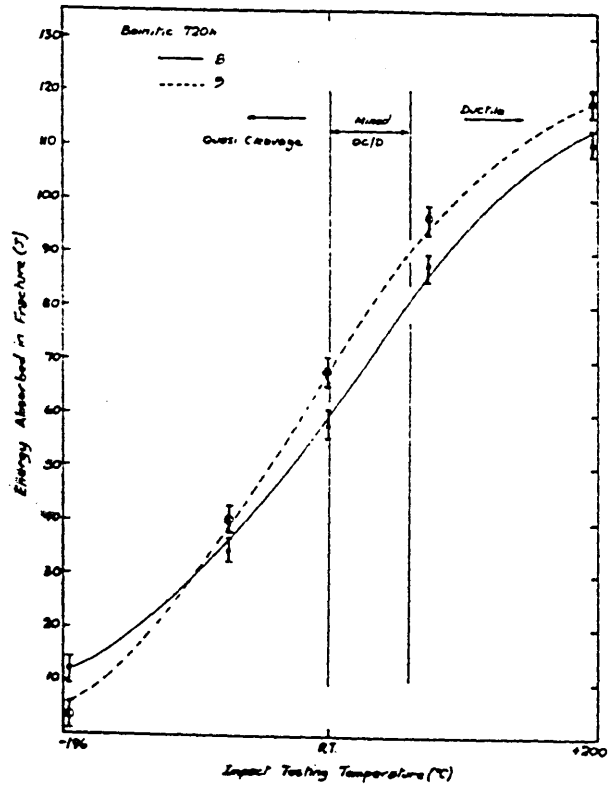
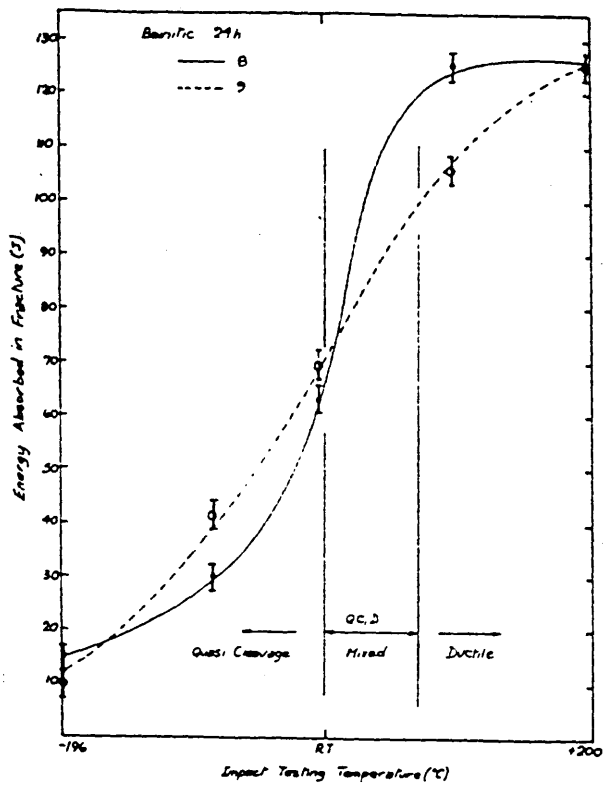


Fig. 101 Ageing curves for alloys 8 and 9 in the isothermally transformed bainitic condition (heat treatment D).

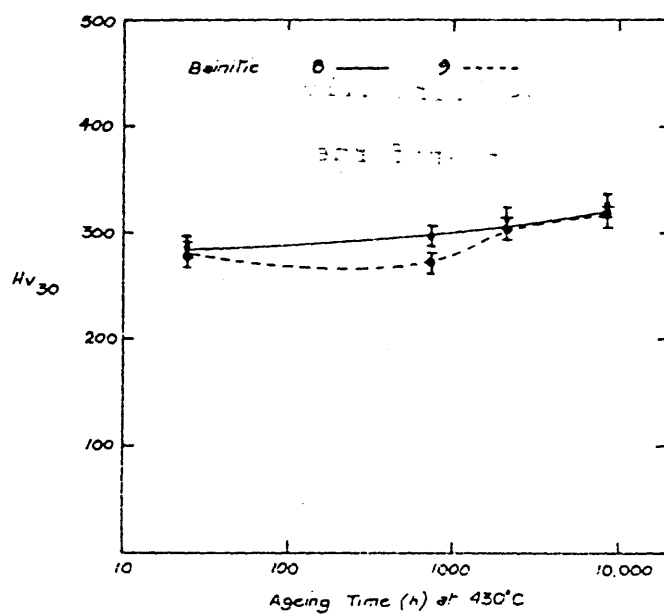


Fig. 102 Transmission electron micrograph of alloy 8 in the isothermally transformed bainitic condition (heat treatment D) aged for 24 hours at 430°C.

Fig. 103 Transmission electron micrograph of alloy 8 in the isothermally transformed bainitic condition (heat treatment D) aged for 8,760 hours at 430°C.

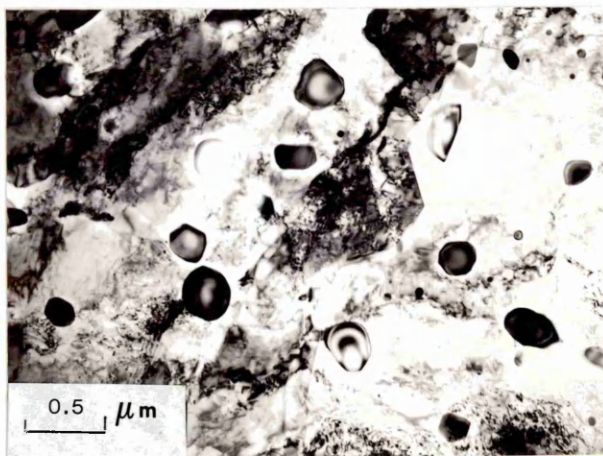
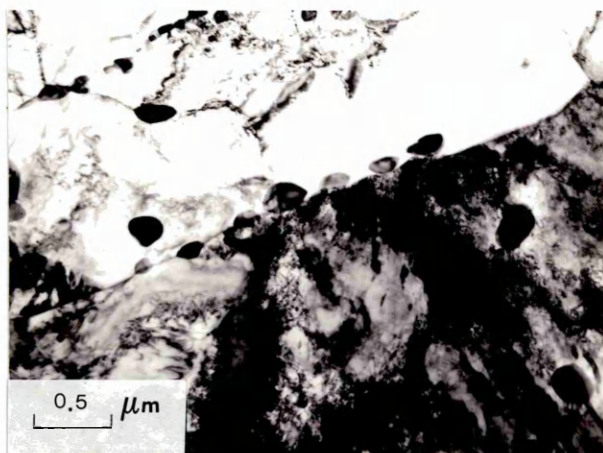


Fig. 104 Scanning electron micrograph of alloy 11,
heat treatment B, aged for 2,160 hours at
430°C, impact tested at ambient temperature,
mag. 800x.

Fig. 105 Scanning electron micrograph of alloy 10,
heat treatment B, aged for 8,760 hours at
430°C, impact tested at -196°C, mag. 800x.

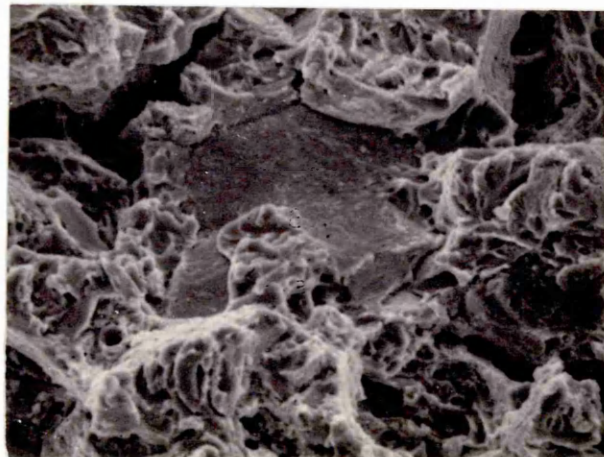
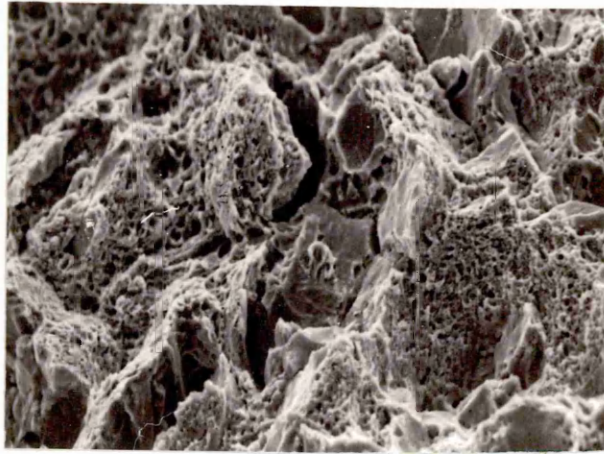


Fig. 106 DBTT curves for alloys 10 and 11 in the quenched and tempered martensitic condition (heat treatment B) with increasing ageing times.

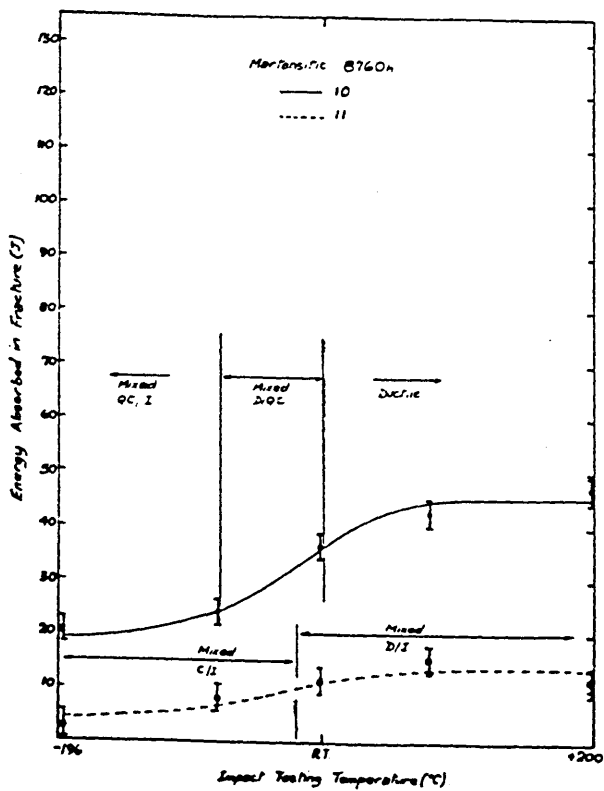
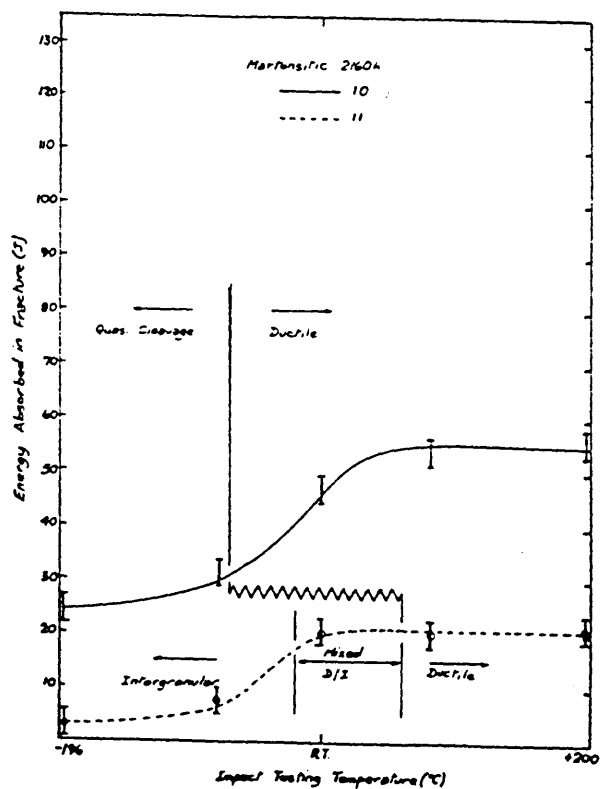
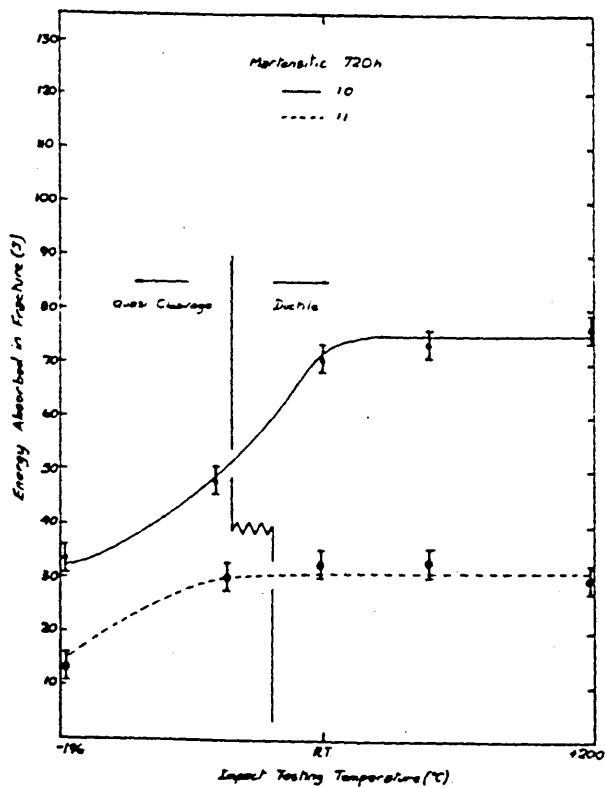
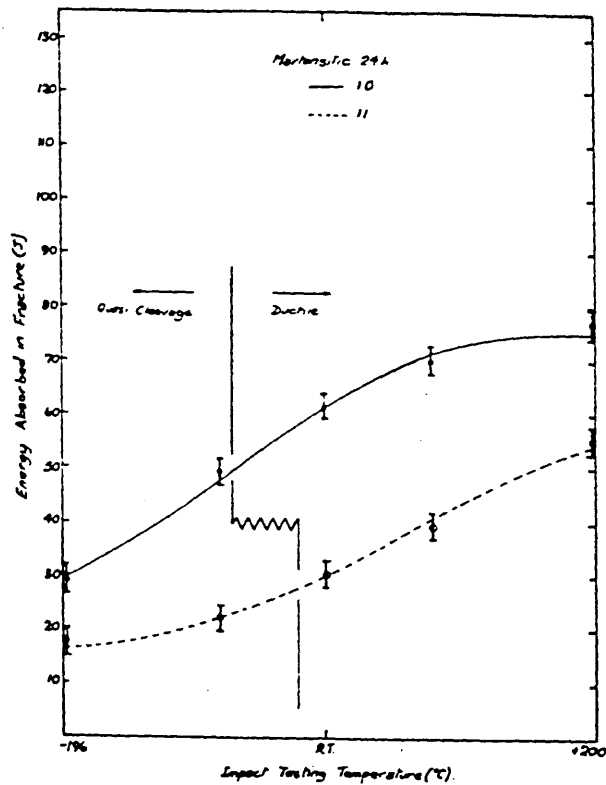


Fig. 107 Ageing curves for alloys 10 and 11 in the quenched and tempered martensitic condition (heat treatment B).

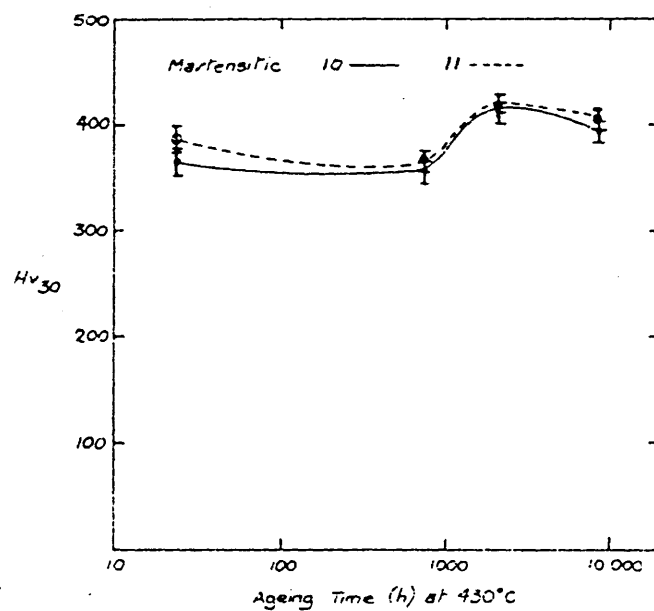


Fig. 108 Transmission electron micrograph of alloy
11 in the quenched and tempered martensitic
condition (heat treatment B) aged for 8,760
hours at 430°C.

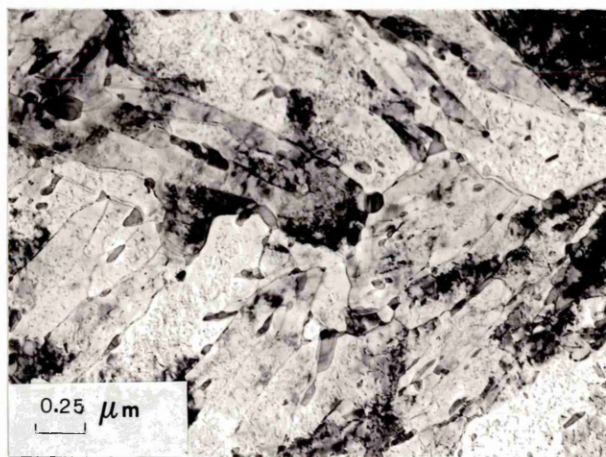


Fig. 109 DBTT curves for alloys 10 and 11 in the isothermally transformed bainitic condition (heat treatment D) with increasing ageing times.

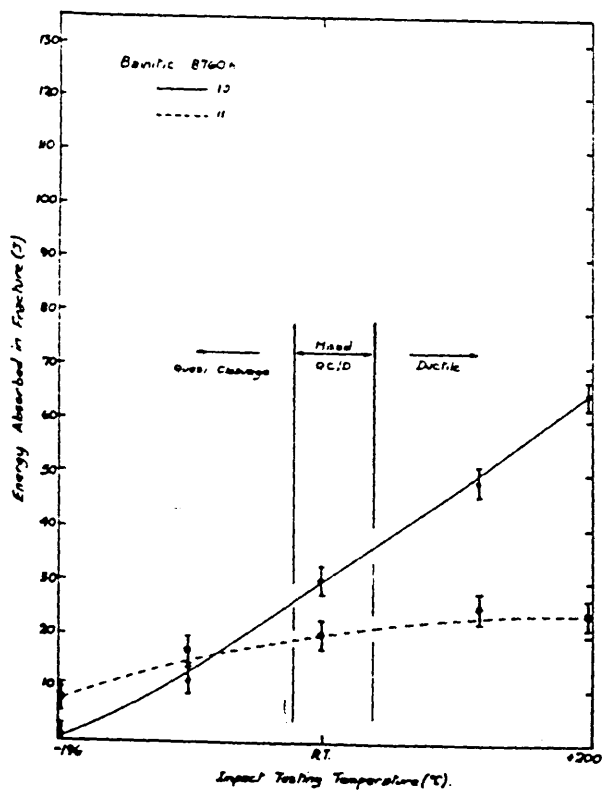
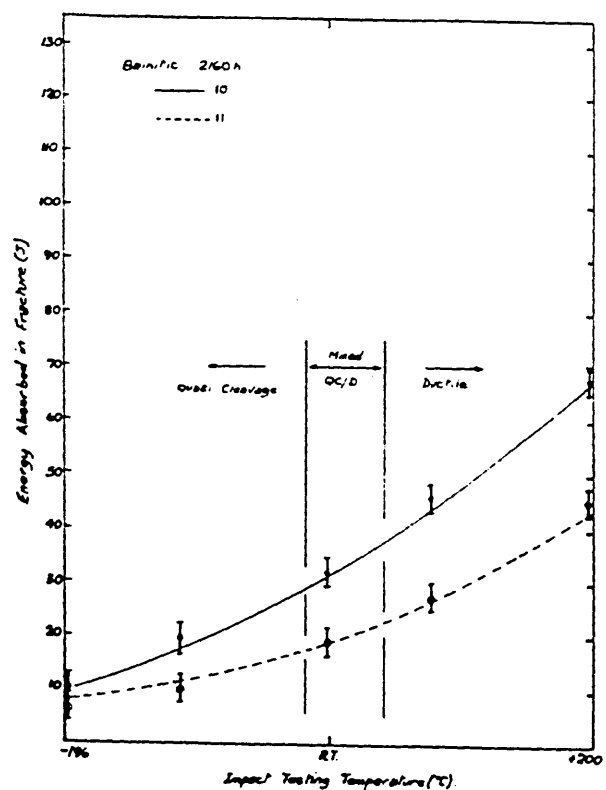
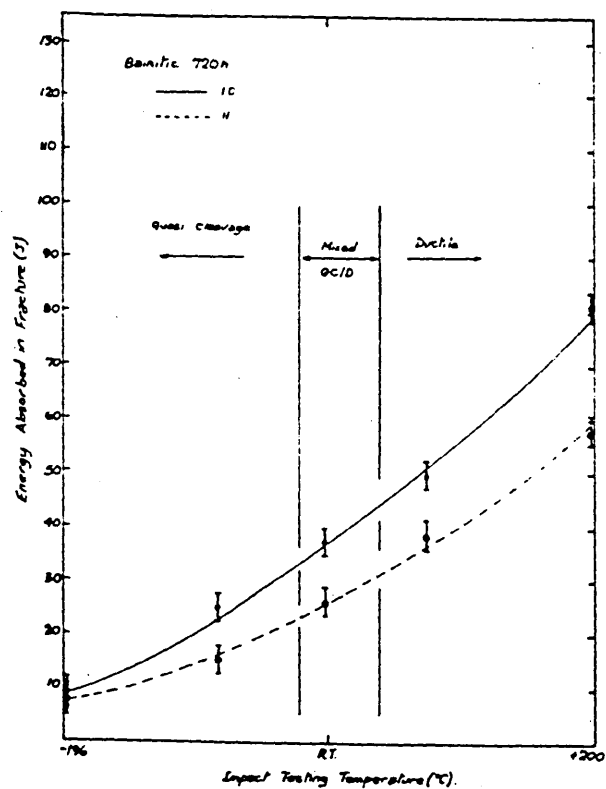
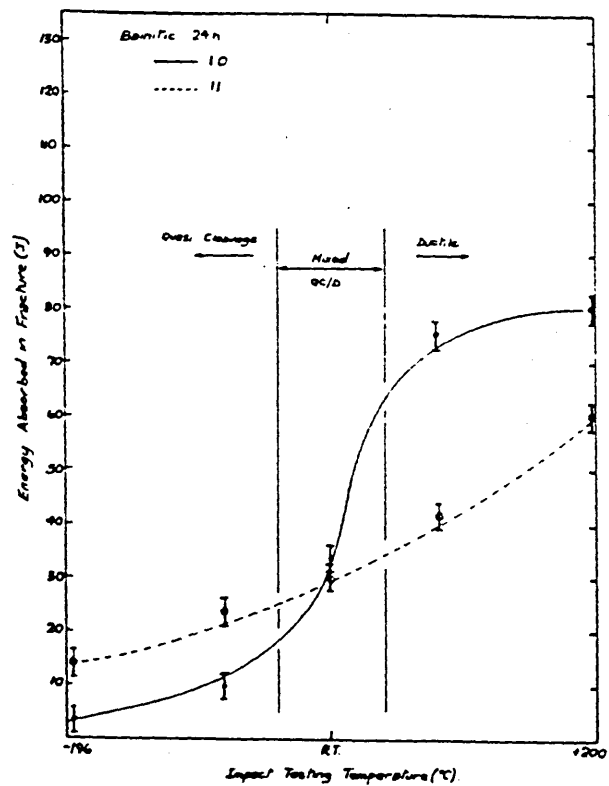


Fig. 110 Ageing curves for alloys 10 and 11 in the isothermally transformed bainitic condition (heat treatment D).

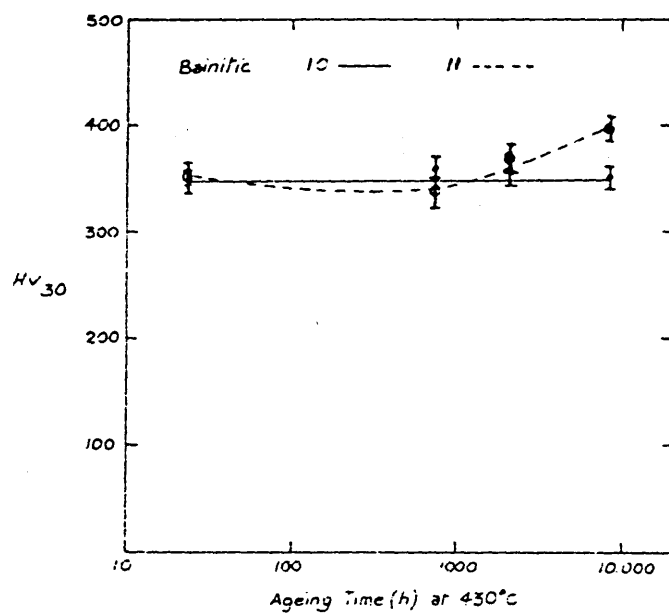


Fig. 111 Scanning electron micrograph of alloy 10,
heat treatment D, aged for 720 hours at
430°C, impact tested at -196°C, mag. 900x.

Fig. 112 Scanning electron micrograph of alloy 10,
heat treatment D, aged for 8,760 hours at
430°C, impact tested at -196°C, mag. 900x.

Fig. 113 Scanning electron micrograph of alloy 11,
heat treatment D, aged for 24 hours at 430°C,
impact tested at -196°C, mag. 900x.

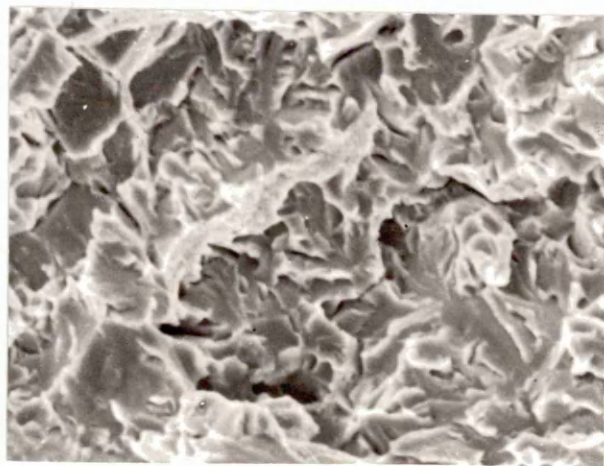
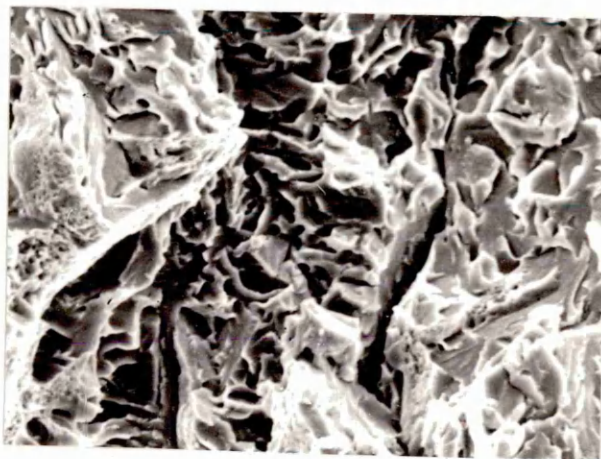
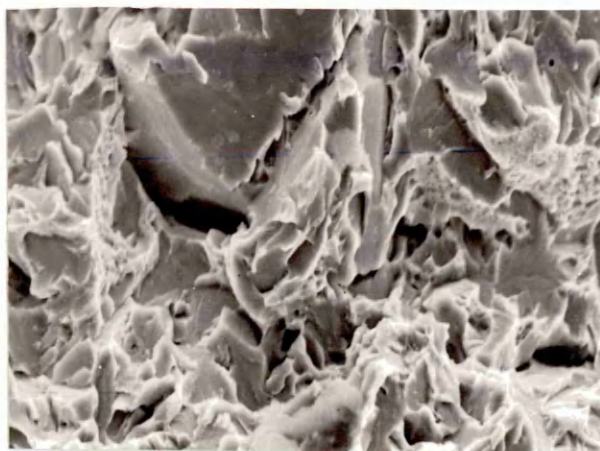


Fig. 114 Scanning electron micrograph of alloy 11,
heat treatment D, aged for 8,760 hours at
430°C, impact tested at -196°C, mag. 900x.

Fig. 115 Transmission electron micrograph of alloy
11 in the isothermally transformed bainitic
condition (heat treatment D) aged for 8,760
hours at 430°C.

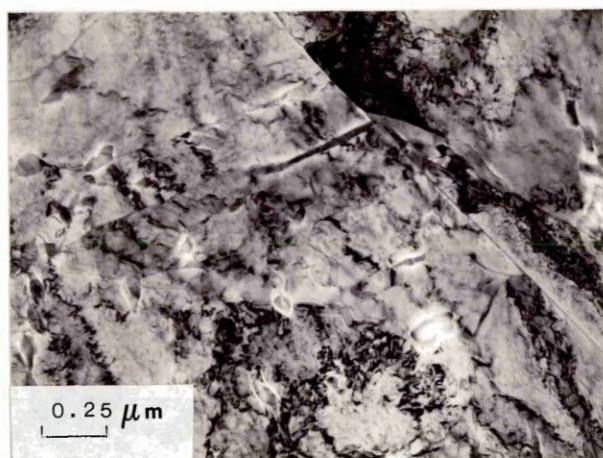
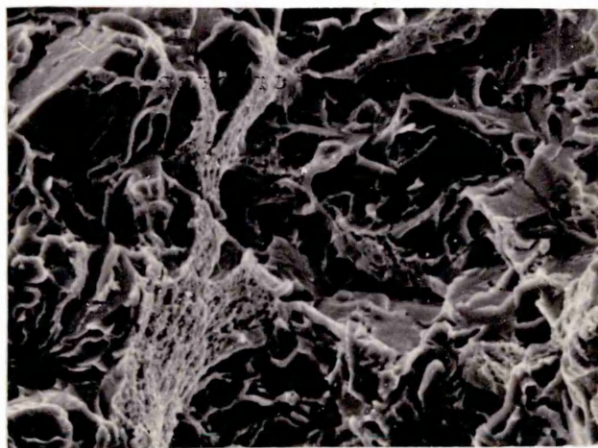


Fig. 116 Auger analysis (average over 1.5mm^2) taken from alloy 1 in the isothermally transformed bainitic condition (heat treatment A) aged for 720 hours at 430°C and embrittled for 16 hours at 200°C in hydrogen atmosphere.

Fig. 117 Auger analysis taken from an intergranular fracture surface area of alloy 1 after 8,760 hours ageing at 430°C for heat treatment A.

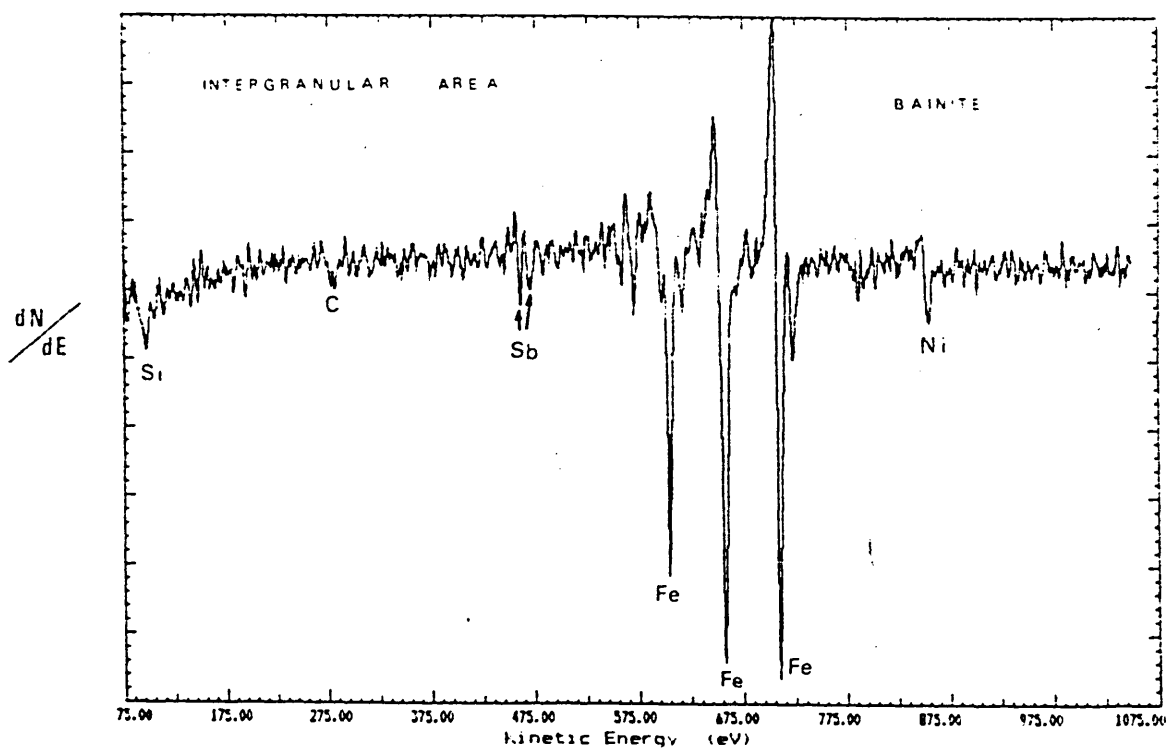
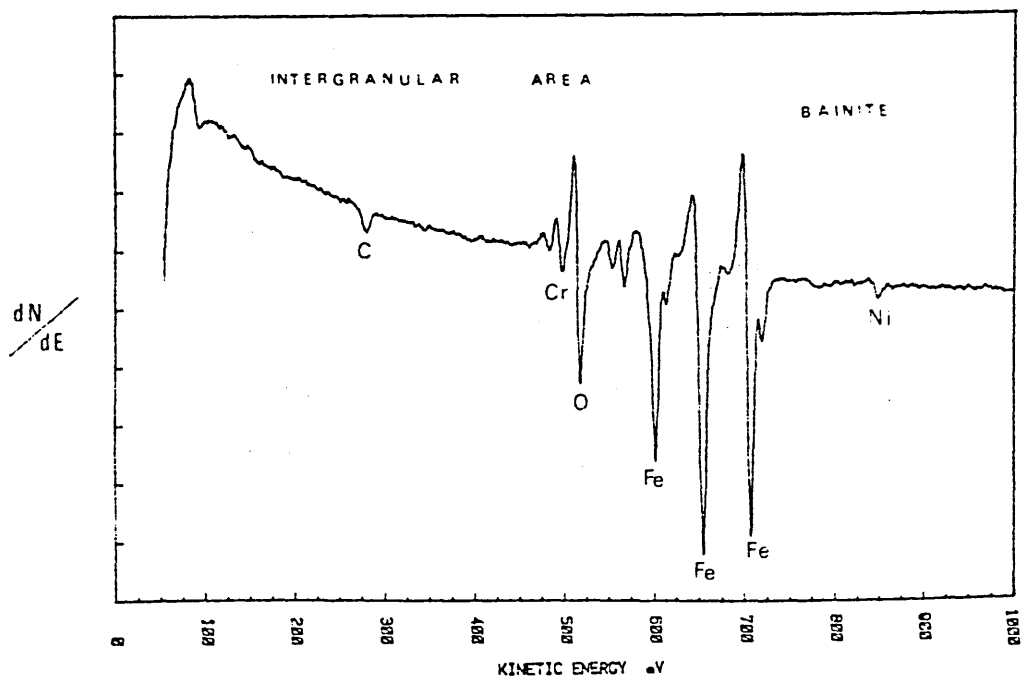


Fig. 118 Auger spectrum obtained from a mixed fracture surface area of alloy 1 including intergranular cleavage and ductile, after 8,760 hours ageing at 430°C for heat treatment A.

3 11.977

Fig. 119 Auger spectrum obtained from an intergranular fracture surface area of alloy 1, after 17,520 hours ageing at 430°C for heat treatment A.

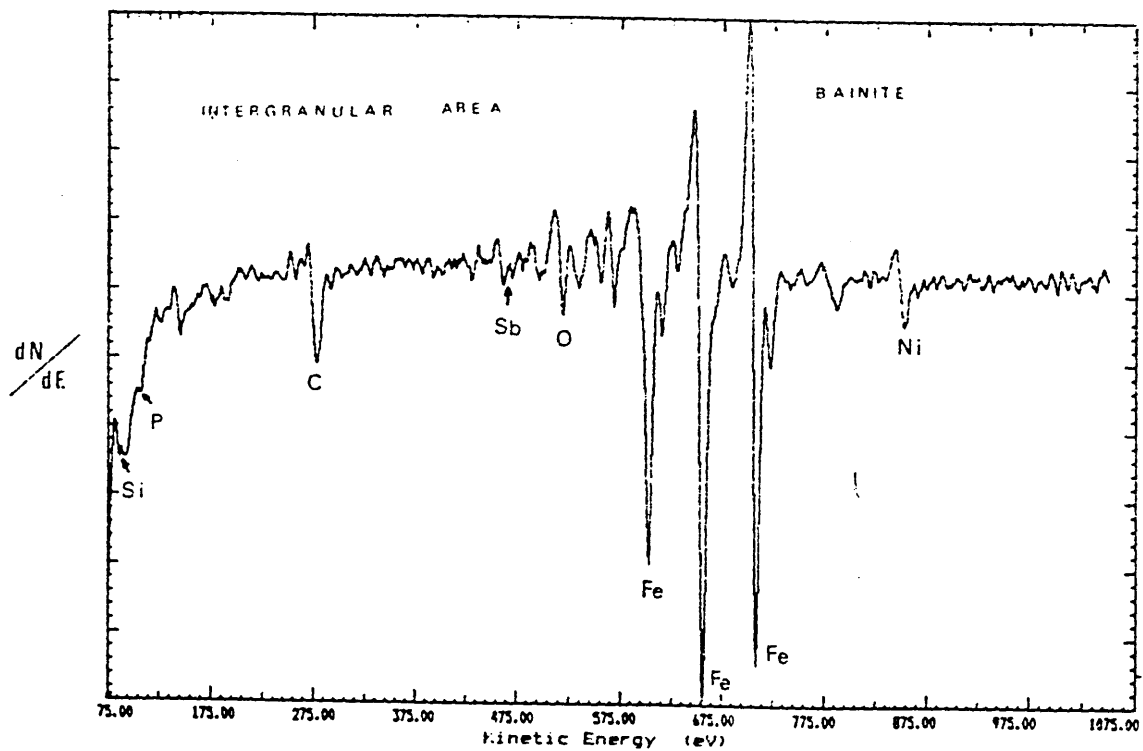
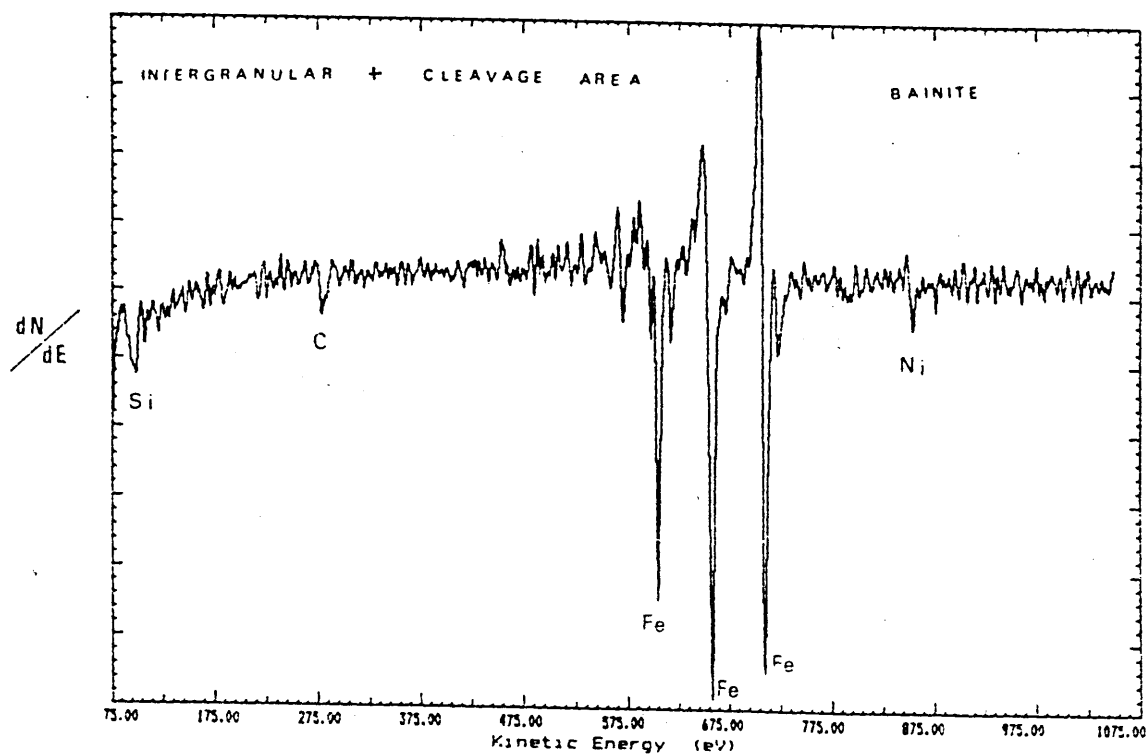


Fig. 120 Auger spectrum obtained from a cleavage fracture surface area of alloy 1 after 17,520 hours ageing at 430°C for heat treatment A.

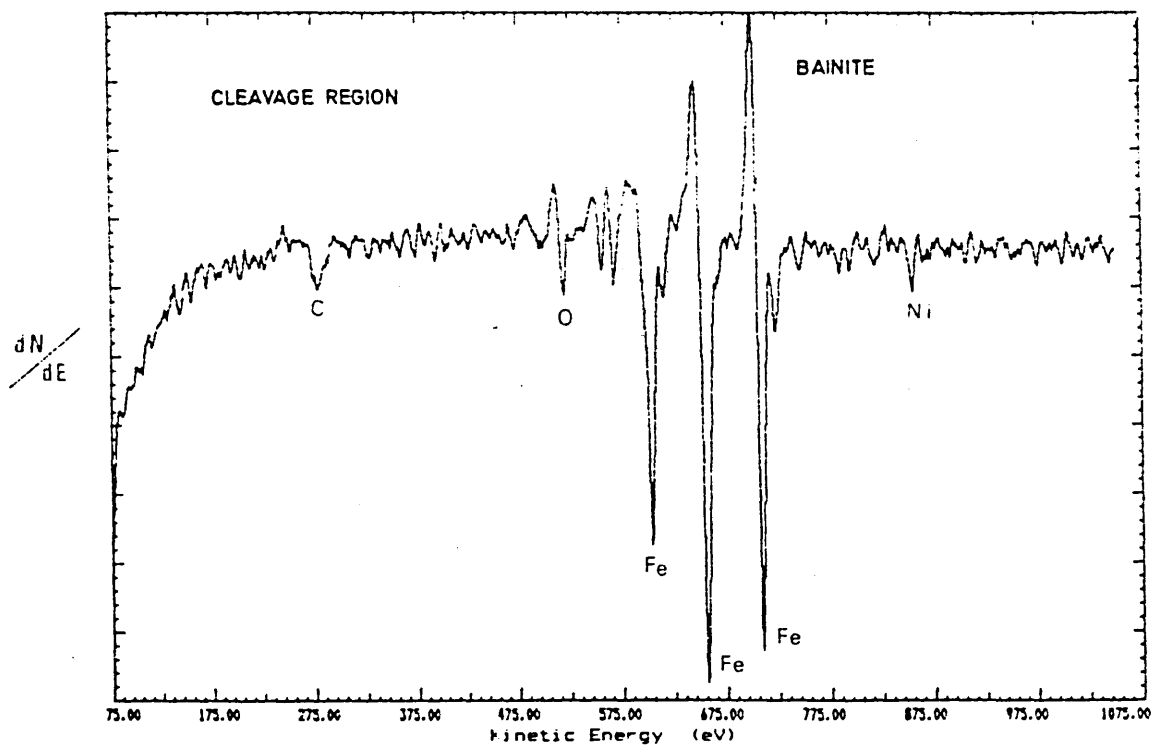
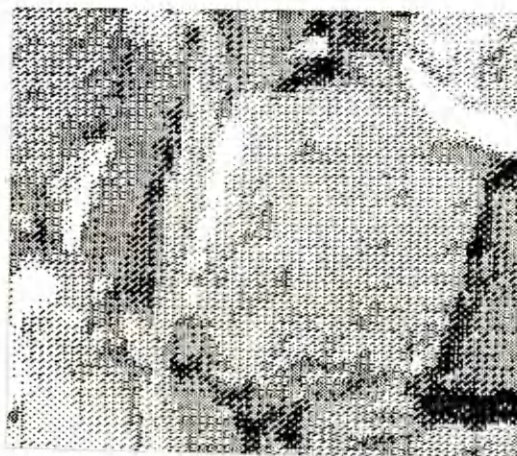
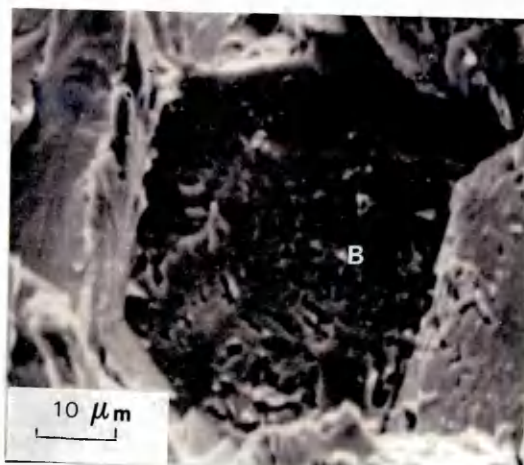


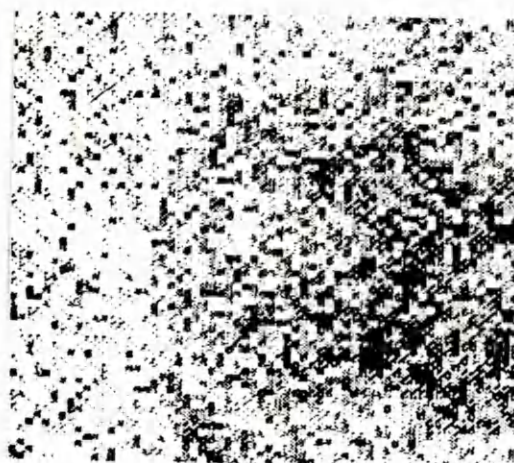
Fig. 121 Secondary electron image from the intergranular fracture surface of alloy 1 aged for 17,520 hours at 430°C.

Fig. 122 Auger map of background signal for area shown in Fig. 121.

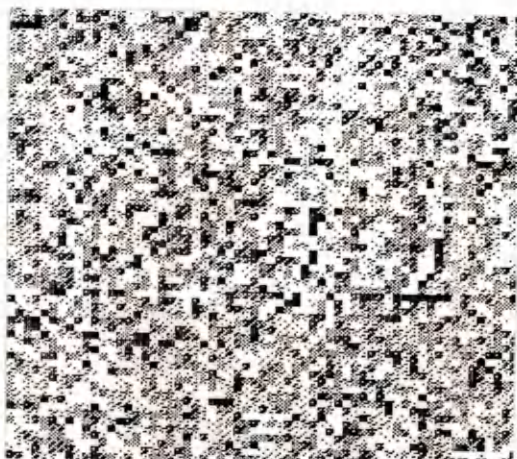
Fig. 123 Auger maps giving the distribution of the elements Sb(a), Ni(b), Cr(c) and P(d) on the region depicted in Figs. 121 and 122.



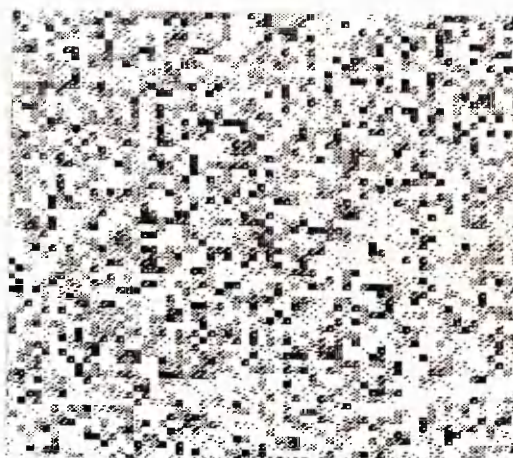
a



b



c



d

Fig. 124 Energy dispersive X-ray analysis of the particle (B) (M_3C) found on the intergranular fracture surface of the structure shown in Fig. 121.

Fig. 125 Positive secondary ion mass distribution of species sputtered from a cleavage fracture surface of embrittled isothermally formed bainite (heat treatment A) aged for 1,000 hours at 430°C.

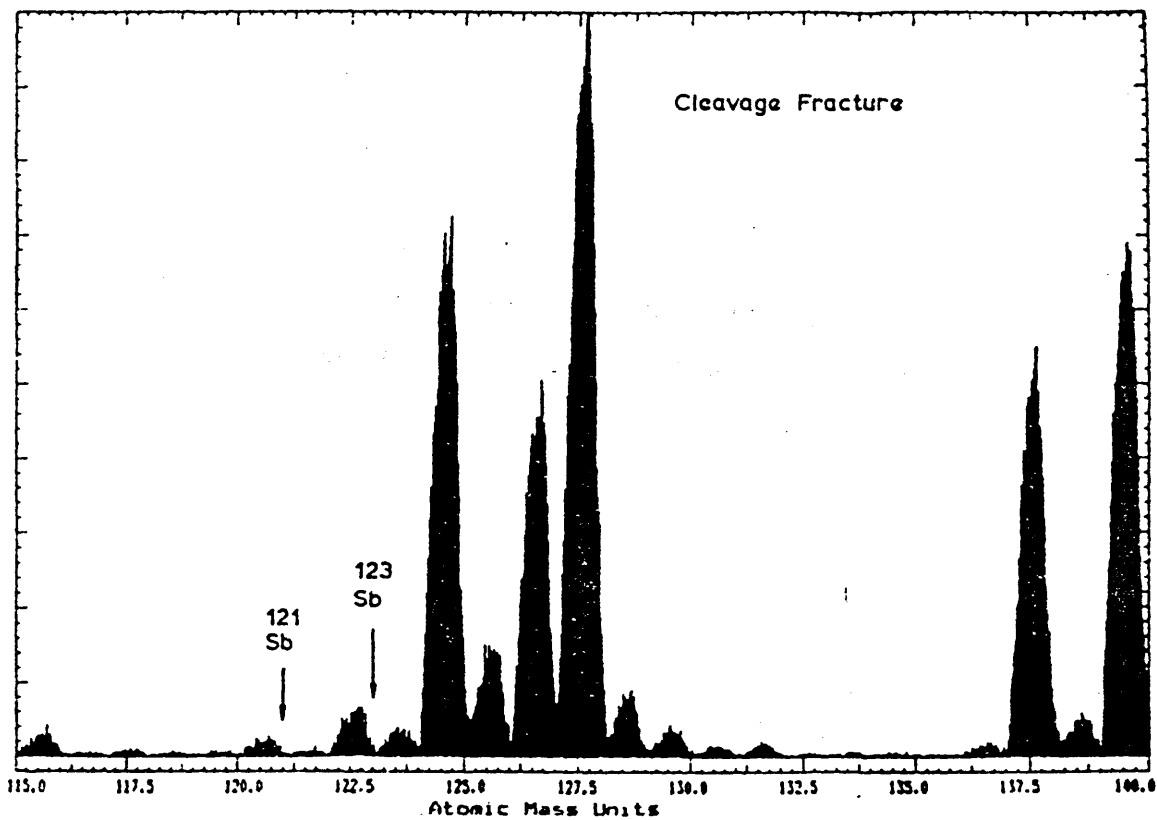
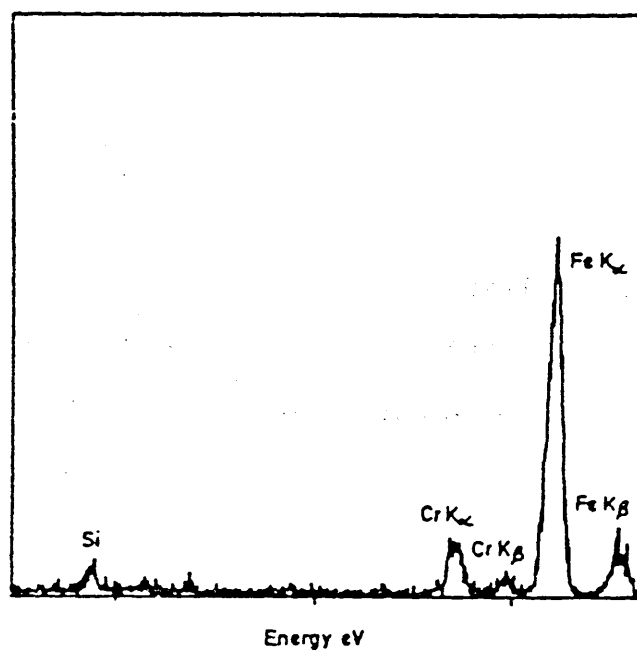


Fig. 126 Secondary electron image of alloy 1 in the isothermally transformed bainitic condition (heat treatment A) aged for 8,760 hours at 430°C, after ion beam sputtering.

Fig. 127 Topographical image from the ion-etched surface shown in Fig. 126.

Fig. 128 Auger map showing the Sb distribution of the area shown in Fig. 126.

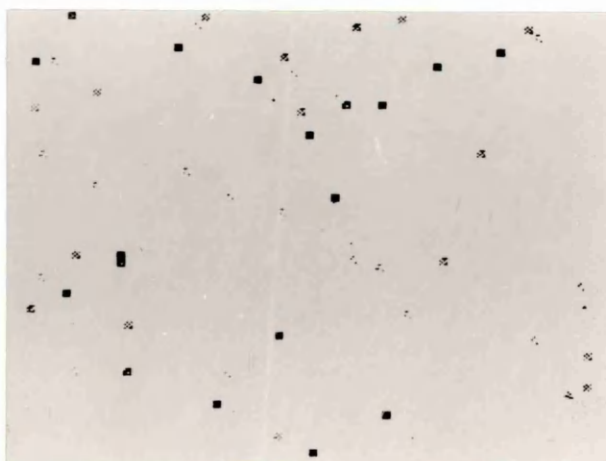
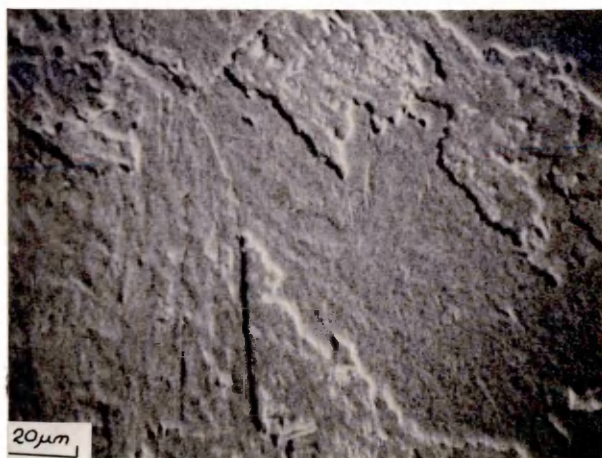


Fig. 129 Auger spectrum from an intergranular fracture surface area of alloy 1 in the quenched and tempered martensitic condition (heat treatment B) aged for 24 hours at 430°C.

Fig. 130 Auger spectrum for a ductile fracture surface area of alloy 1 (heat treatment B) aged for 24 hours at 430°C.

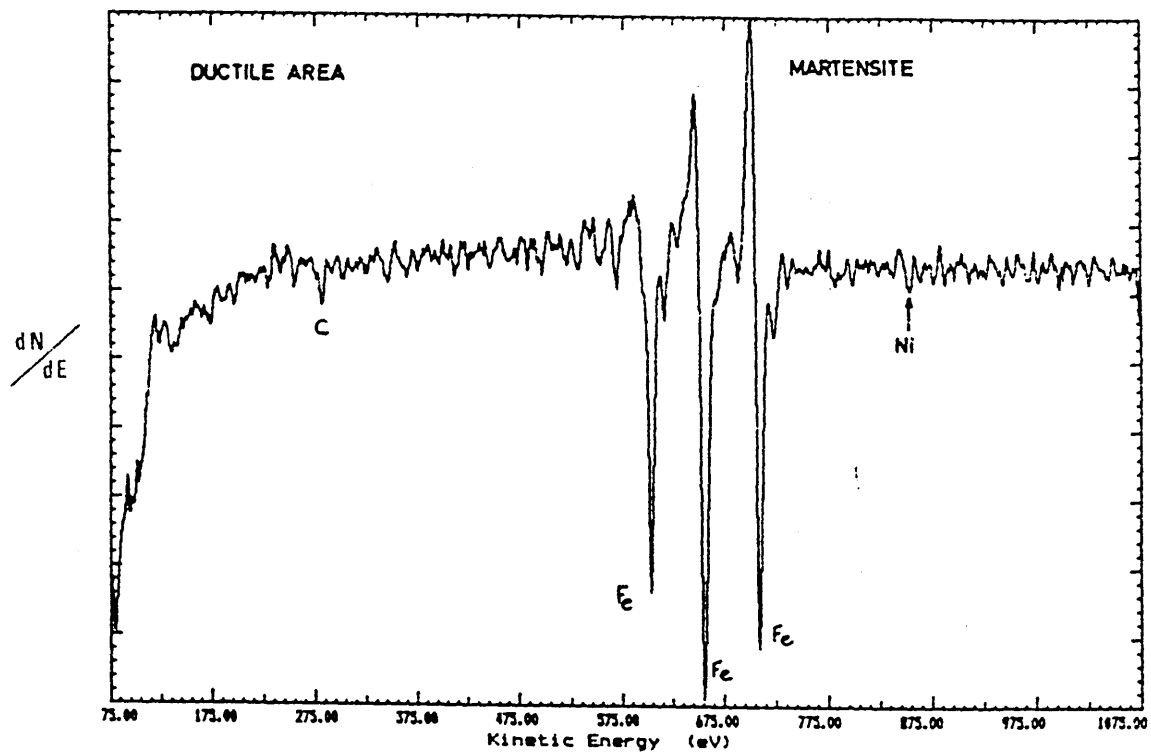
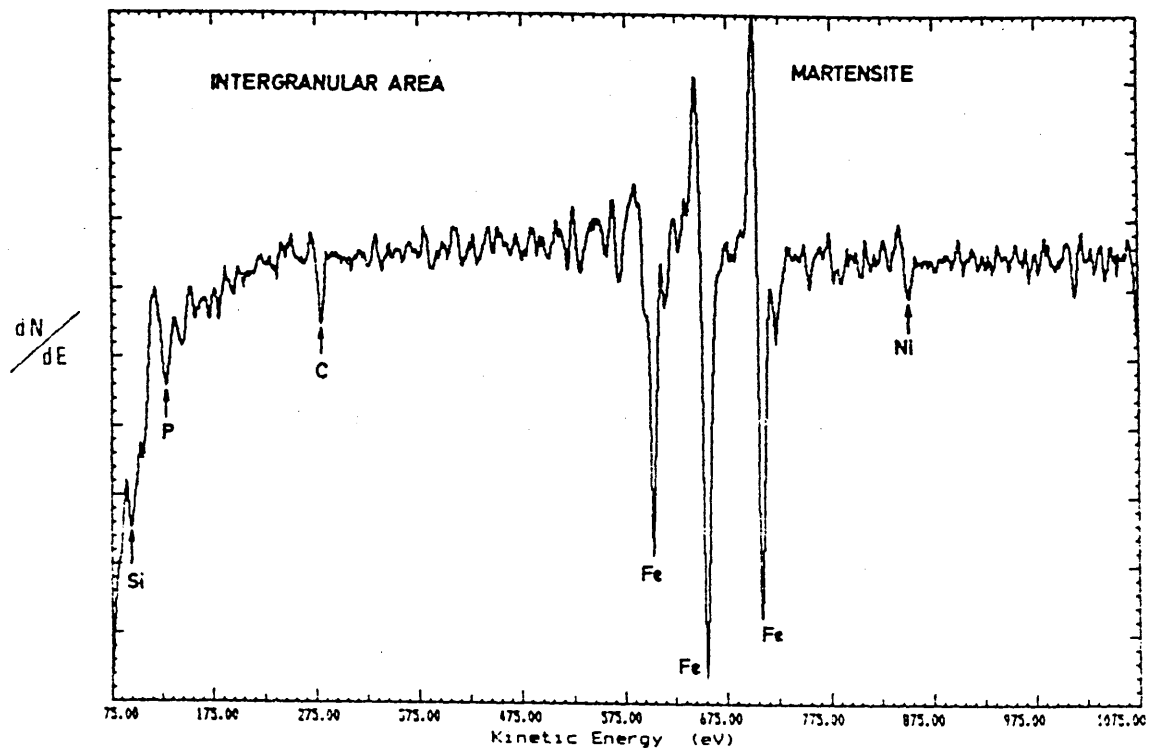


Fig. 131 Topographical image from the intergranular fracture surface area of alloy 1 after being aged for 24 hours at 430°C for heat treatment B.

Fig. 132 Auger map distribution of the element Ni on the intergranular fracture surface shown on Fig. 131.

Fig. 133 Auger map distribution of the element P on the intergranular fracture surface shown on Fig. 131.

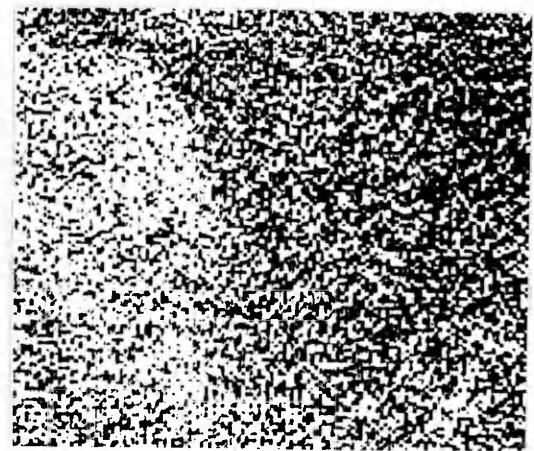
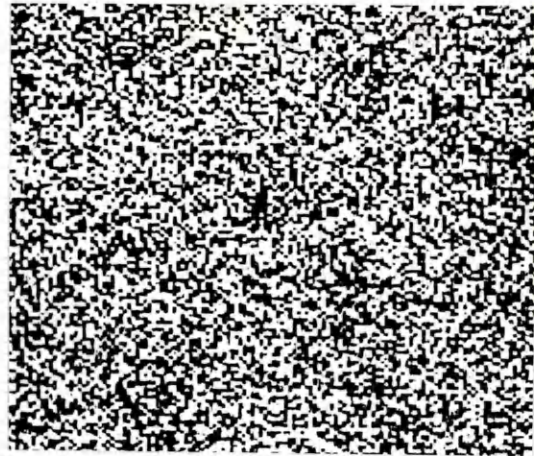
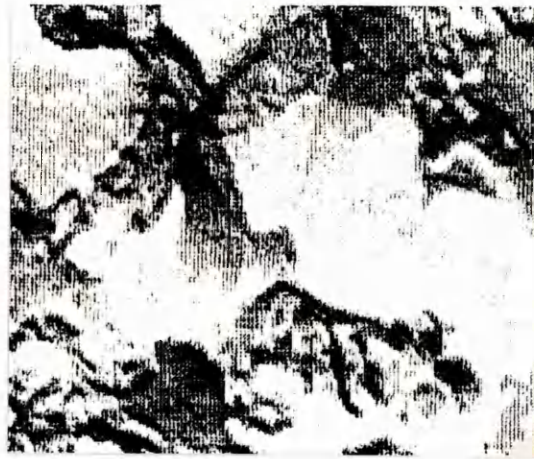


Fig. 134 Secondary electron image from fracture surface of alloy 1 as shown in Fig. 131, in the quenched and tempered martensitic condition (heat treatment B) aged for 24 hours at 430°C.

Fig. 135 Energy dispersive X-ray analysis of a particle (C) (M_7C_3), found on an intergranular surface fracture shown on Fig. 134.

Fig. 136 X-ray map for CrK α of the region shown in Fig. 134.

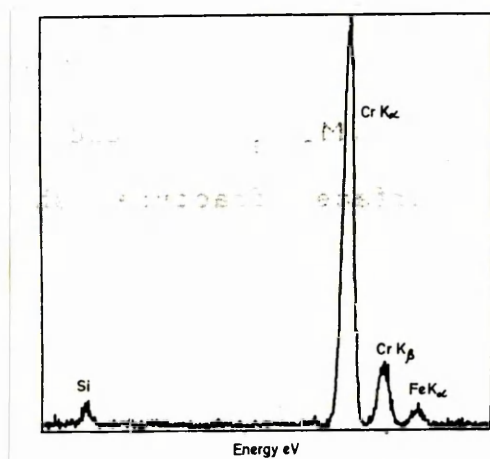
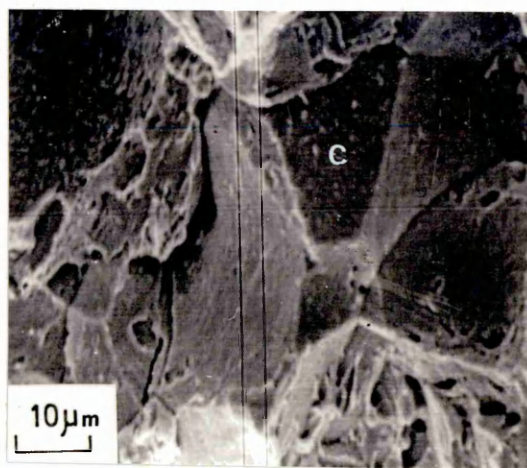


Fig. 137 Positive secondary ion mass distribution of species sputtered from intergranular fracture surface of alloy 1 in the quenched and tempered martensitic condition aged for 1,000 hours at 430°C.

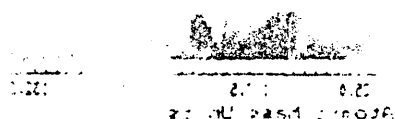
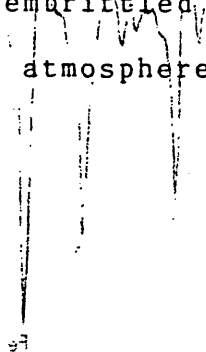


Fig. 138 Auger analysis taken from alloy 1 in the quenched and tempered martensitic condition (heat treatment B) aged for 2,160 hours at 430°C and embrittled for 16 hours at +200°C in hydrogen atmosphere.



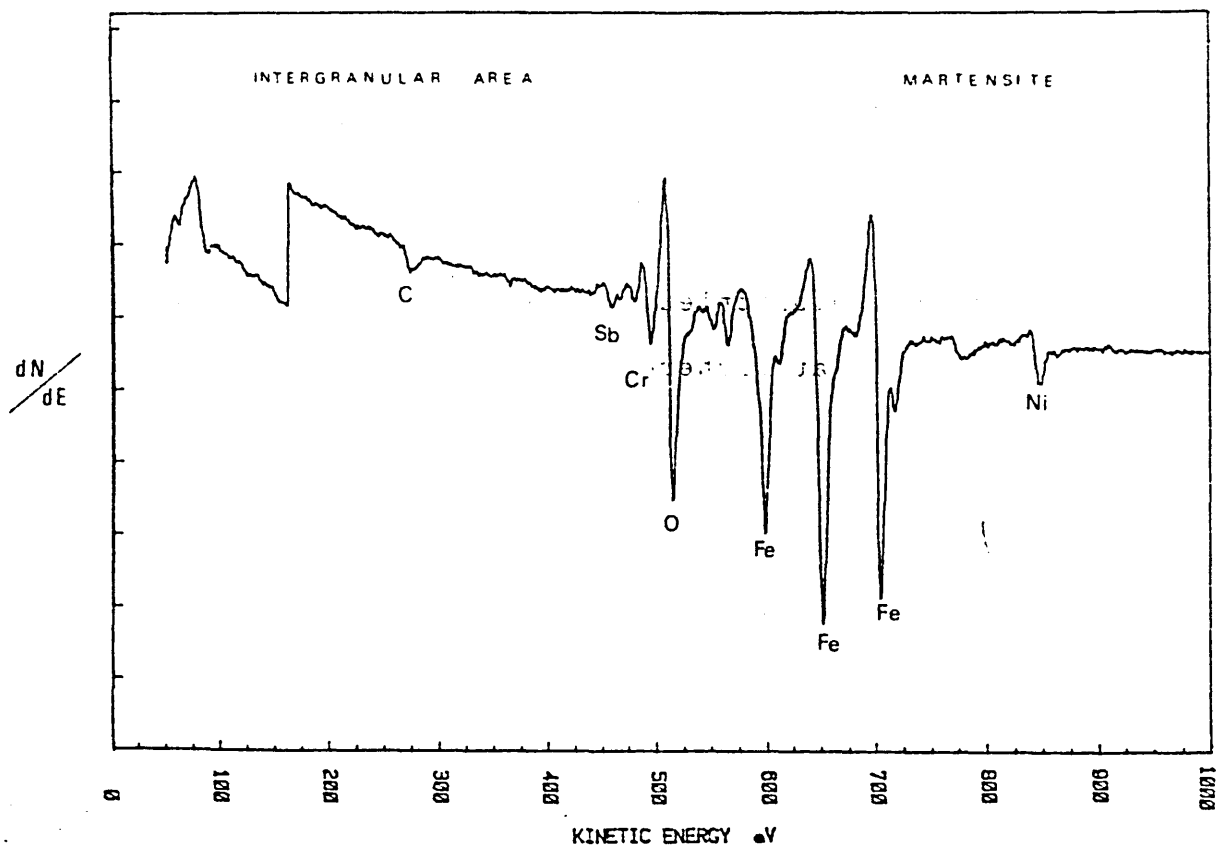
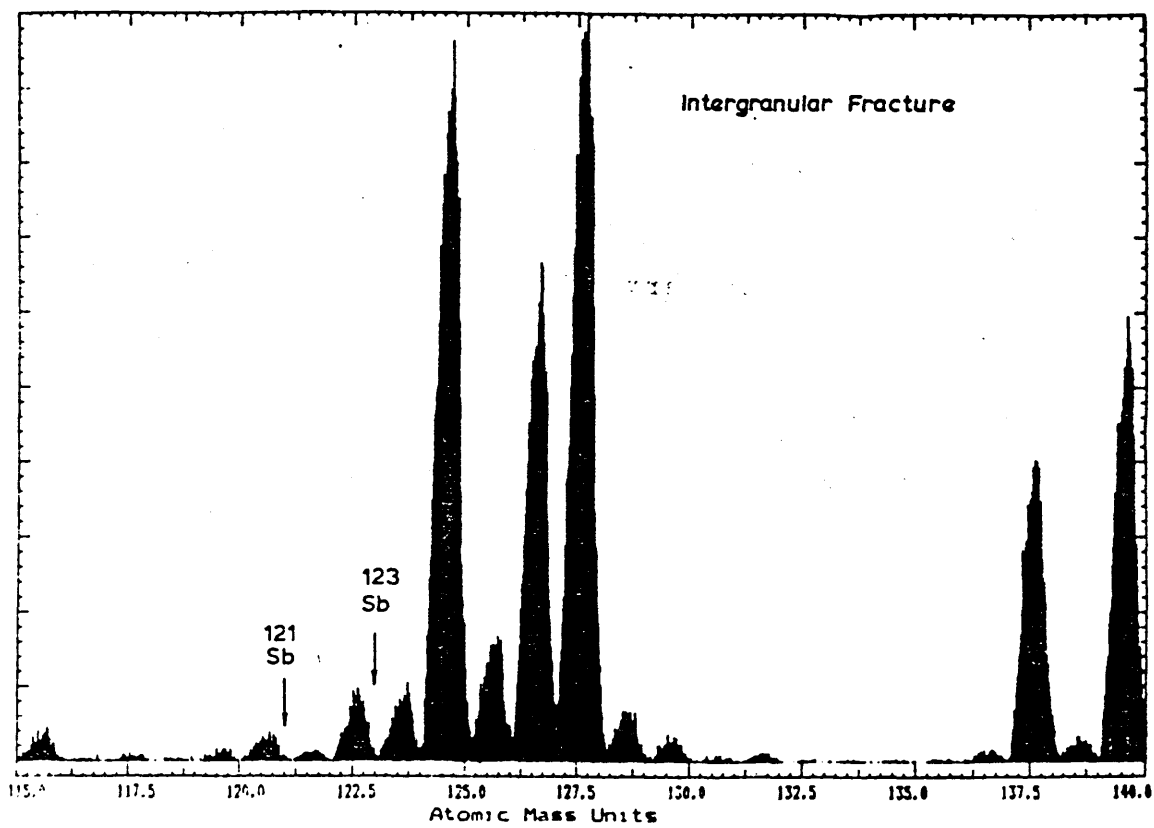


Fig. 139 Energy dispersive analysis for Mn-containing G-phase at prior austenite boundary of alloy 1 in the quenched and tempered martensitic condition (heat treatment B) aged for 8,760 hours at 430°C.

Fig. 140 Auger spectrum taken from alloy 1 in the quenched and tempered martensitic condition (heat treatment B) aged for 17,520 hours at 430°C.

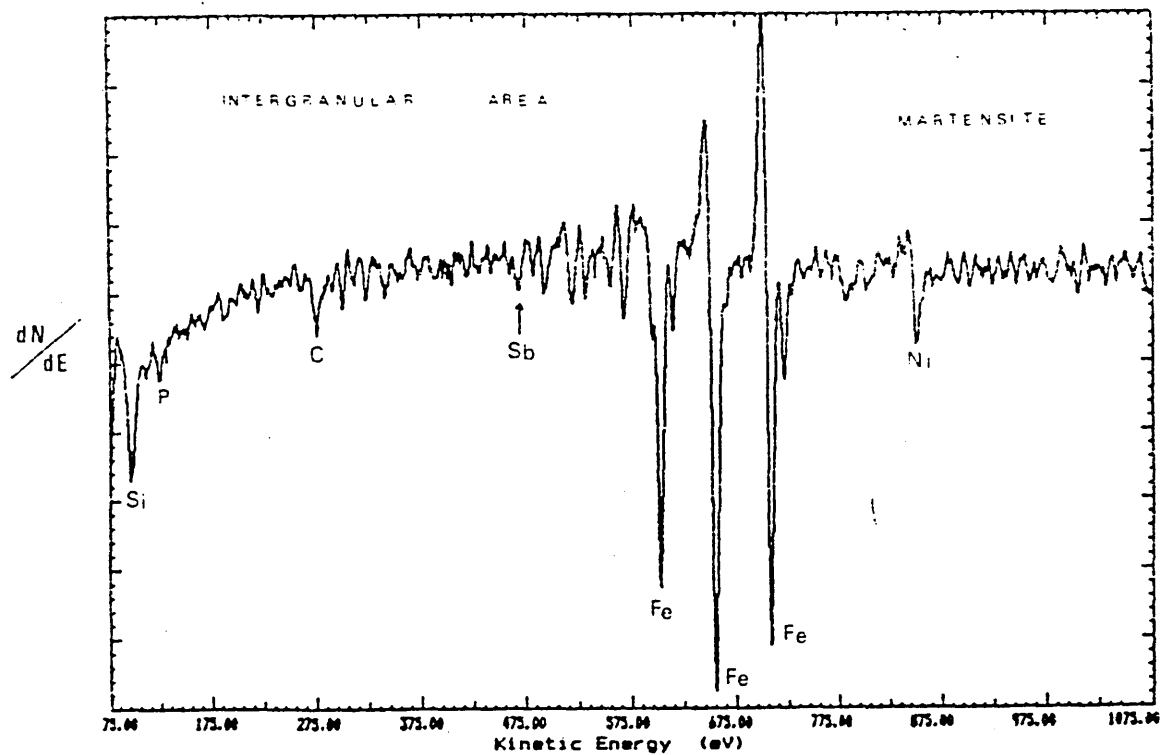
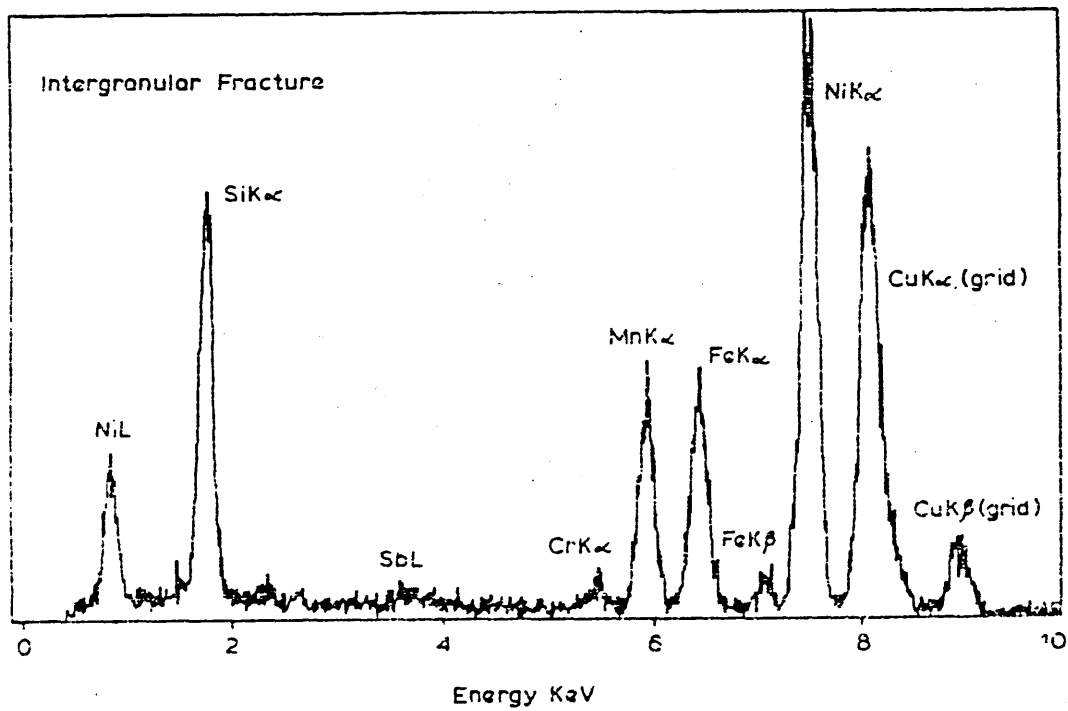
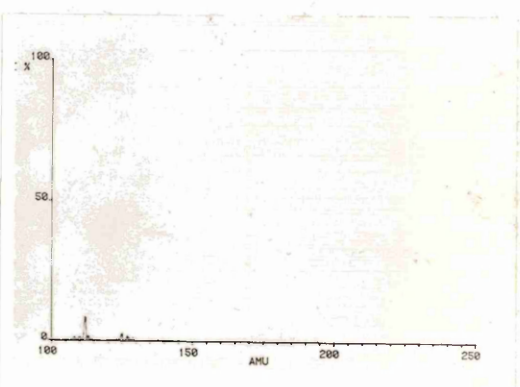
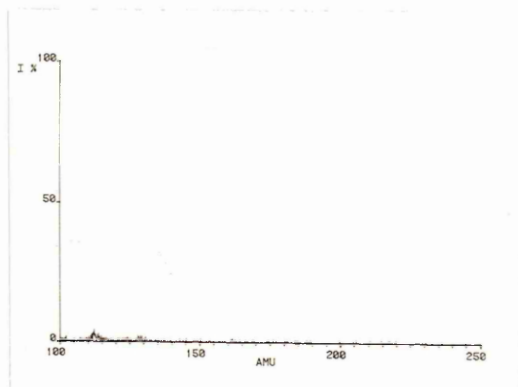
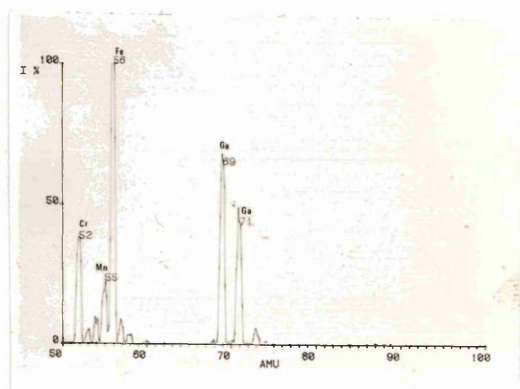
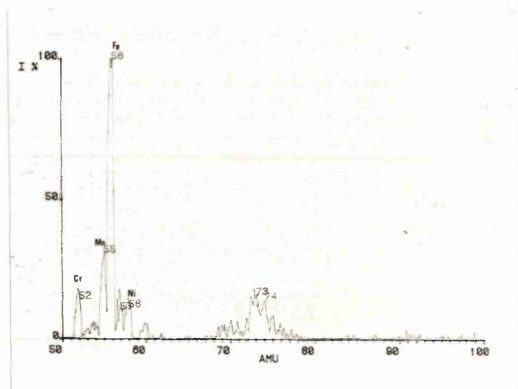
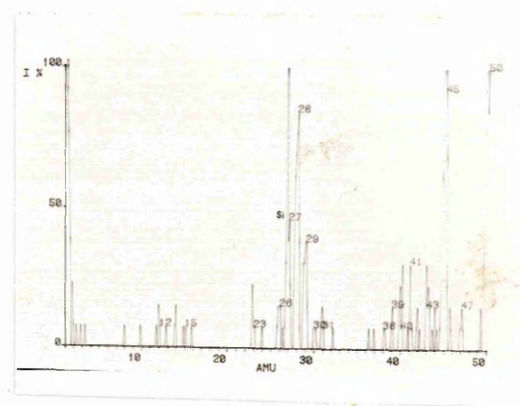
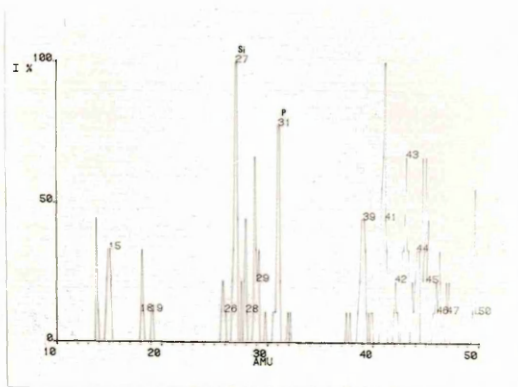


Fig. 141 Depth profile spectrum for alloy 1 aged
for 17,520 hours at 430°C (a) first scan,
(b) second scan.



a

b

Fig. 142a

Auger spectrum obtained from alloy 5 aged for 8,760 hours at 430°C in the quenched and tempered martensitic condition (heat treatment B).

Aug. 142a

Aug. 142a

Fig. 142b

Auger spectrum obtained from an intergranular region of a surface fracture of alloy 7 in the quenched and tempered martensitic condition (heat treatment B) aged for 8,760 hours at 430°C

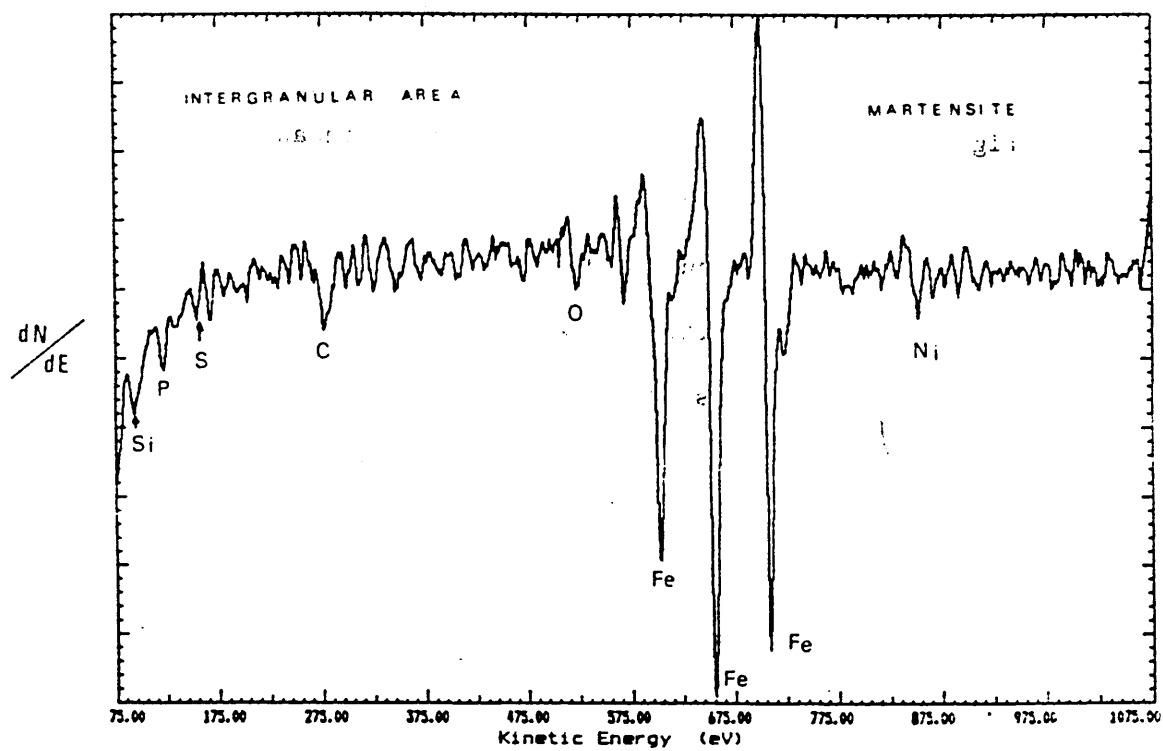
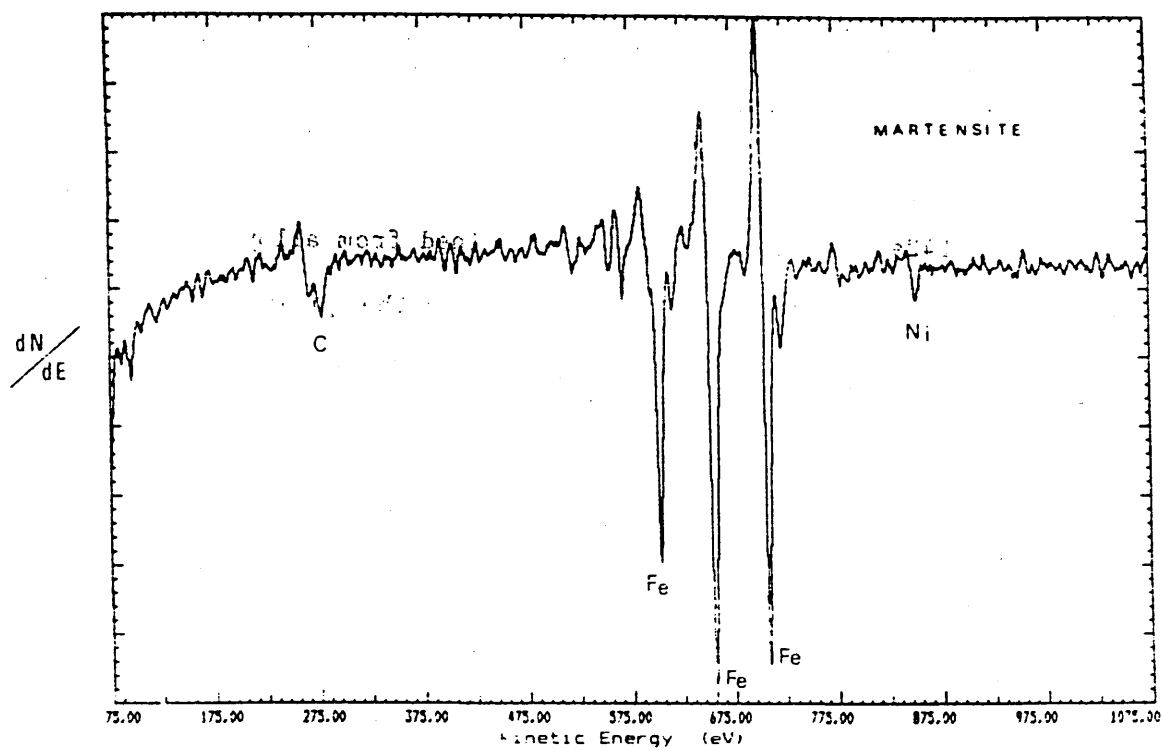


Fig. 143 Auger spectrum taken from a cleavage area of fracture surface of alloy 7 in the quenched and tempered martensitic condition (heat treatment B) aged for 8,760 hours at 430°C

Fig. 144 Energy dispersive analysis of M_6C particle extracted from alloy 9 in the as-quenched condition.

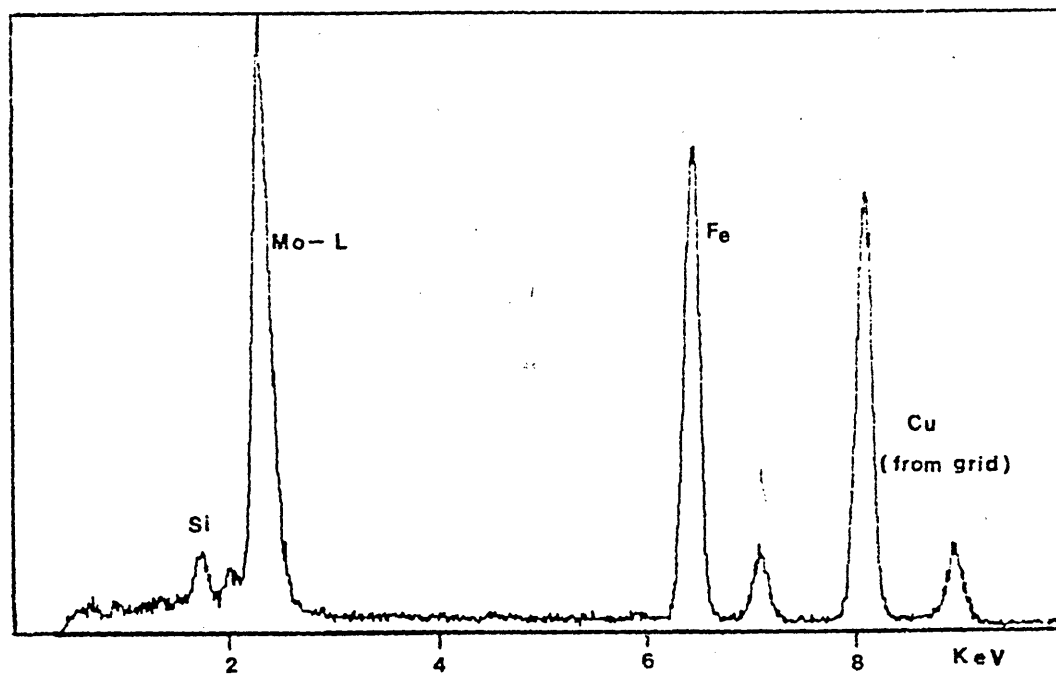
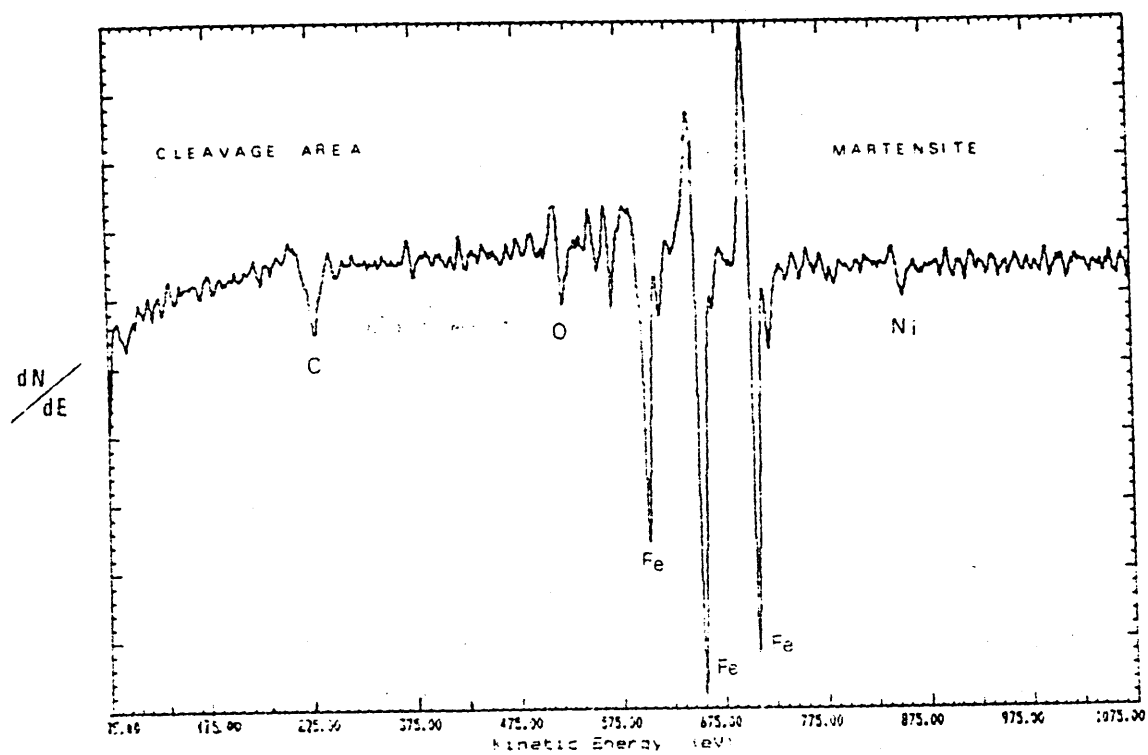


Fig. 145(a)

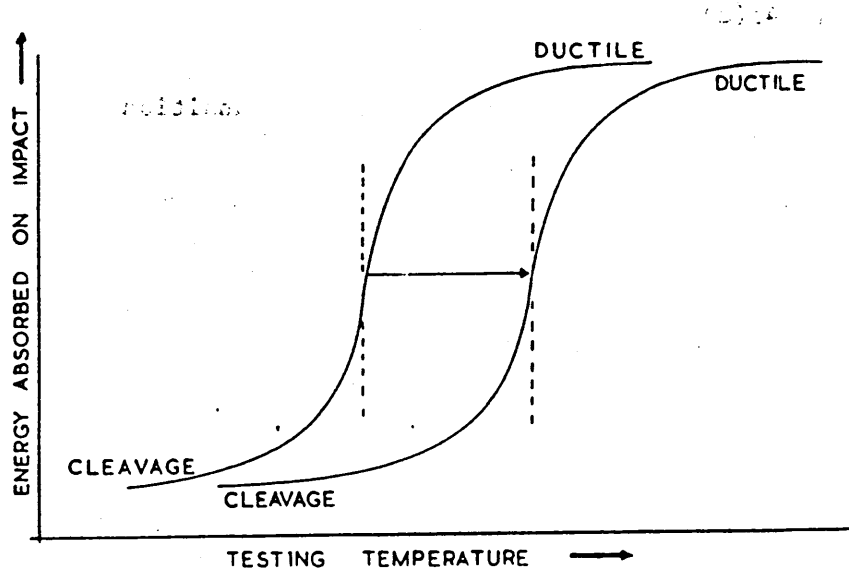
Schematic representation of the types of
embrittlement observed

331000

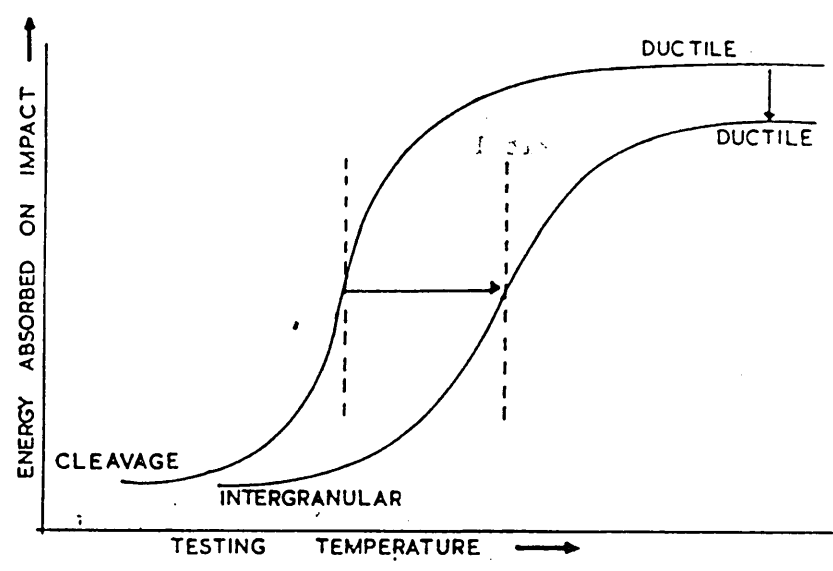
(1) Cleavage-ductile transition

(2) Temper embrittlement

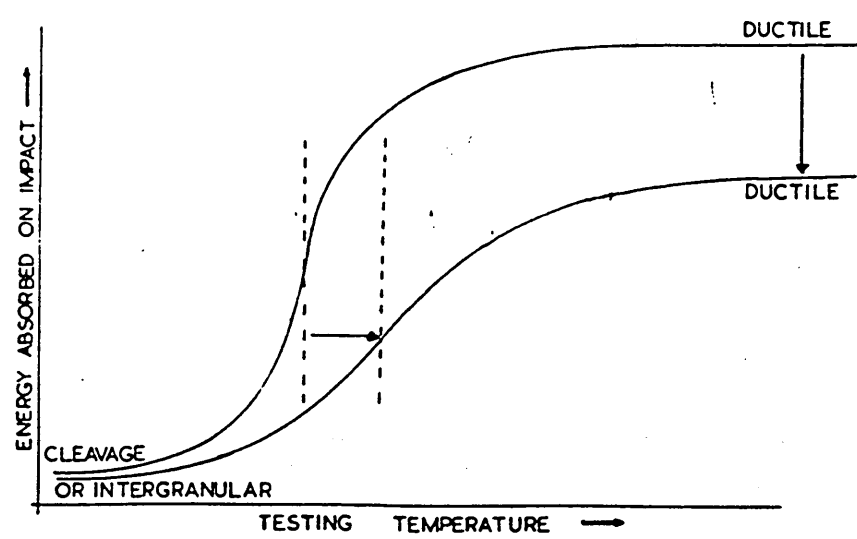
(3) Reduction of the upper shelf energy



1.



2.



3.

Fig. 145b

Histogram showing the degree of embrittlement
as measured by the shift in transition
temperature between the embrittled and
unembrittled condition.

12 115

115

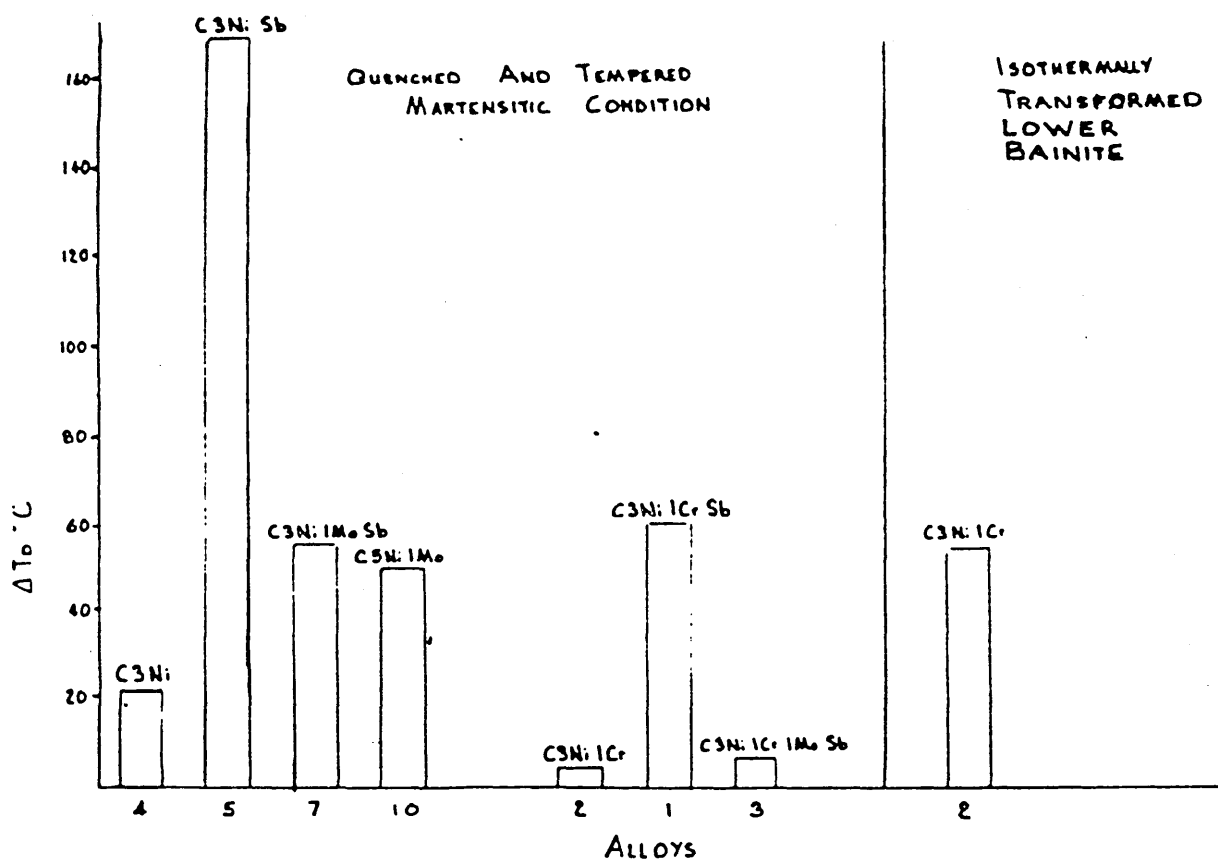


Fig. 146:

Transition temperature curves for alloys
8(C-4Mo) and 9(C-4Mo-Sb) for the quenched and
tempered martensitic and isothermally
transformed lower bainitic condition.

Fig. 147

Fig. 147

Schematic representation of the relationship
between softening segregation and variation
in transition temperature.

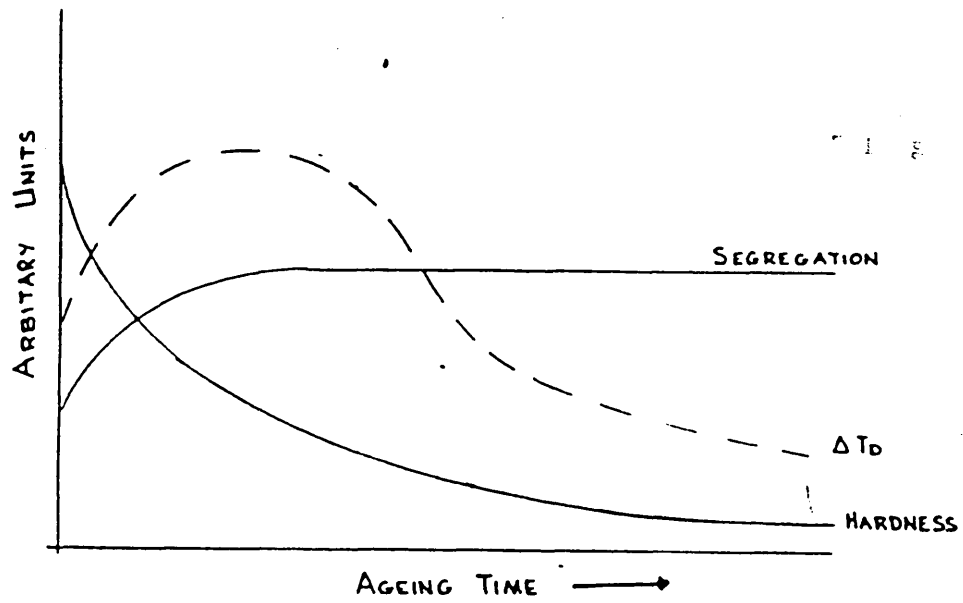
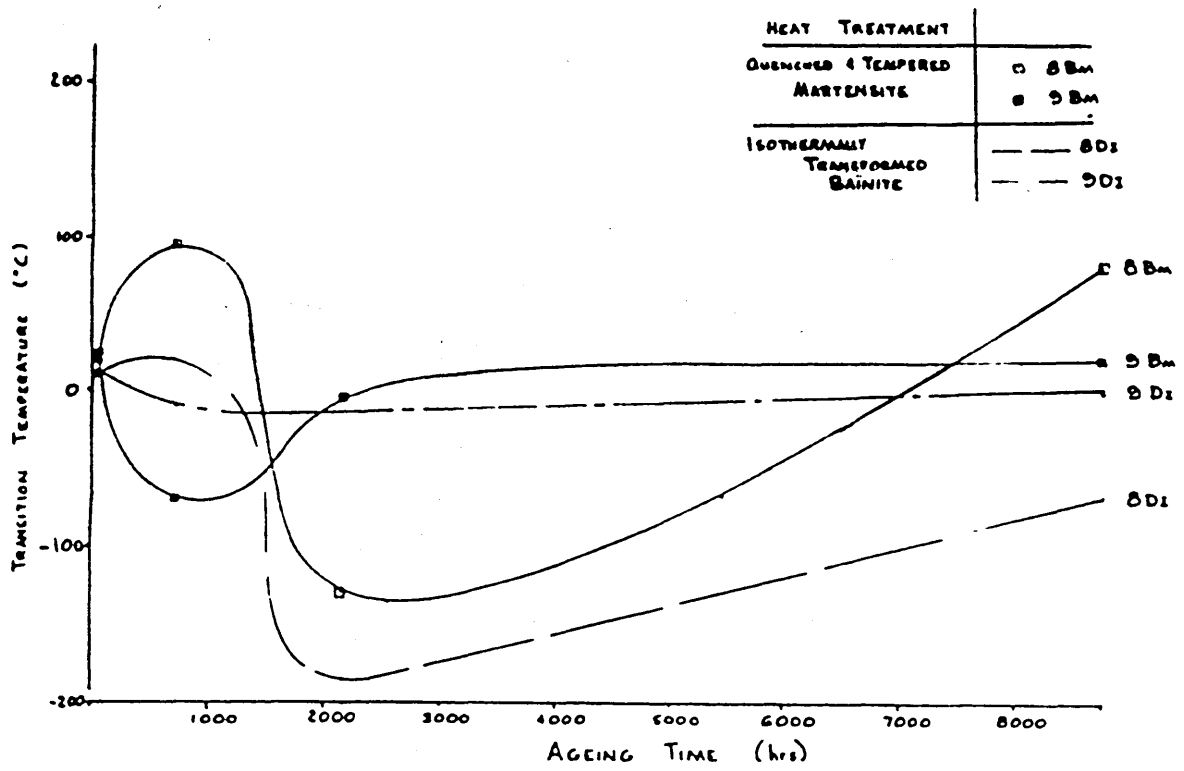


Fig. 148 Effect of tempering at 650°C on embrittlement
 and segregation behaviour of a Ni-Cr steel
 0.4 mass% C 0.06 mass% P, aged at 520°C.
 After Mulford et al(76).



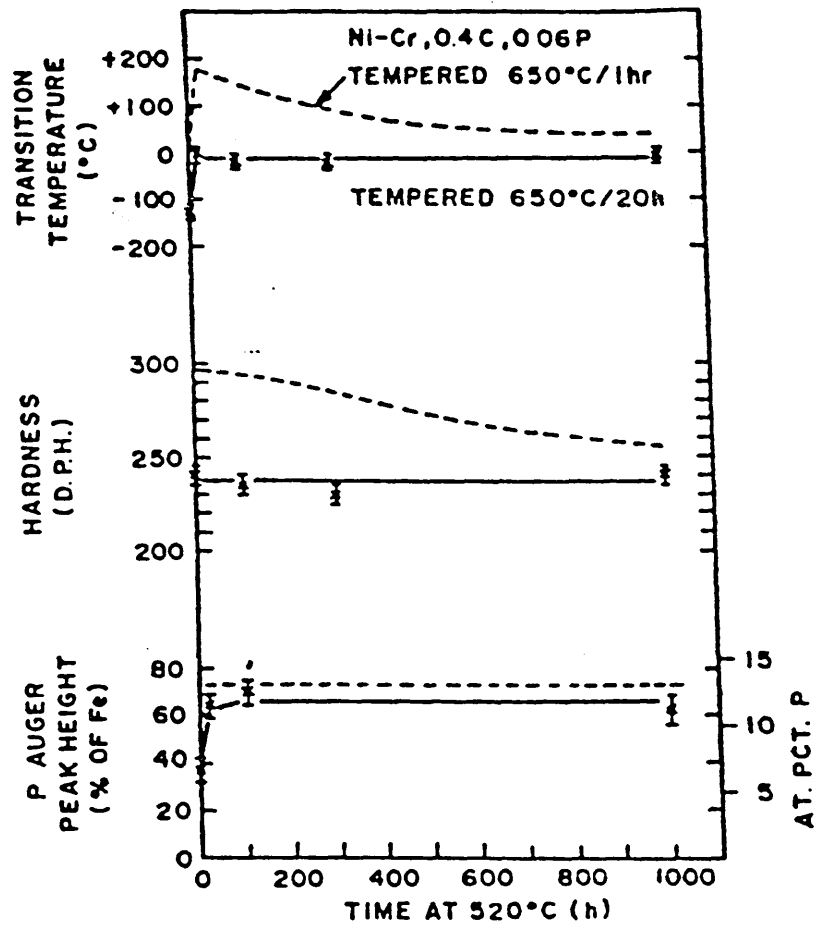


Fig. 149

Schematic representation of the mechanism of
void growth and coalescence related to the
upper shelf energy.



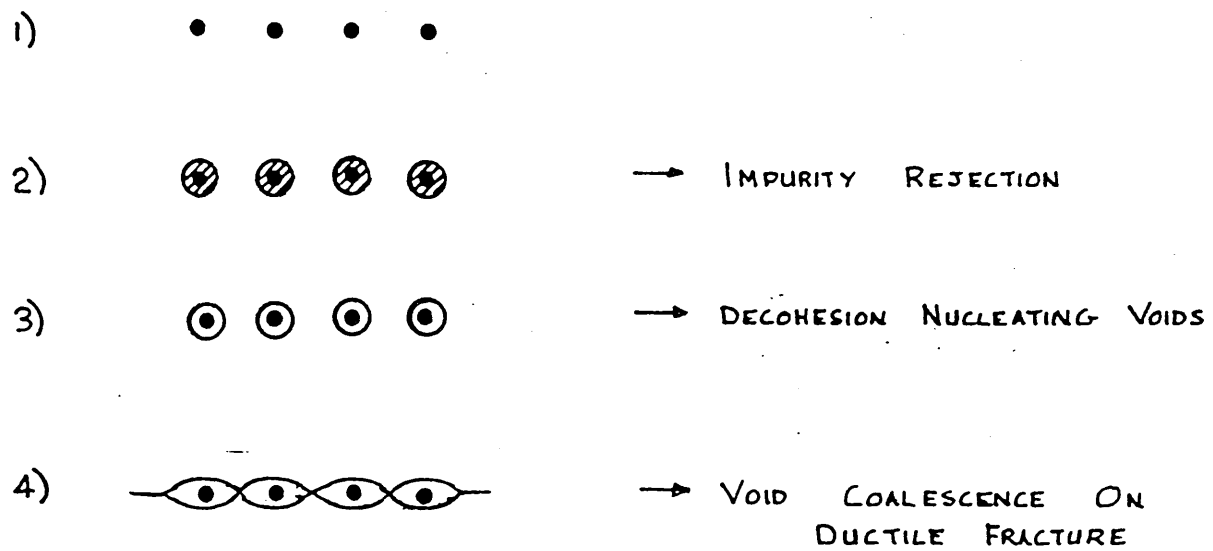
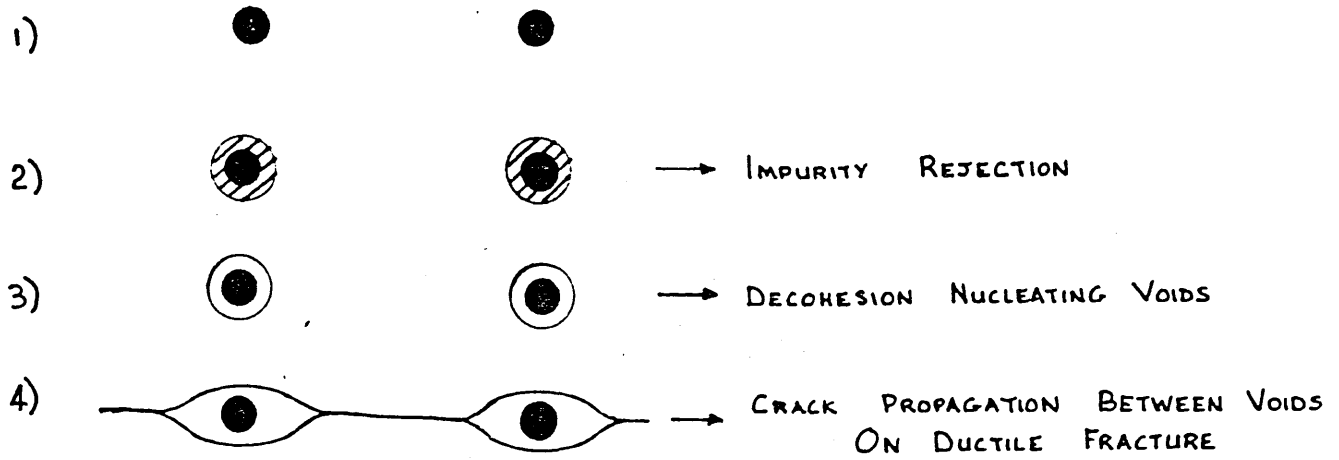
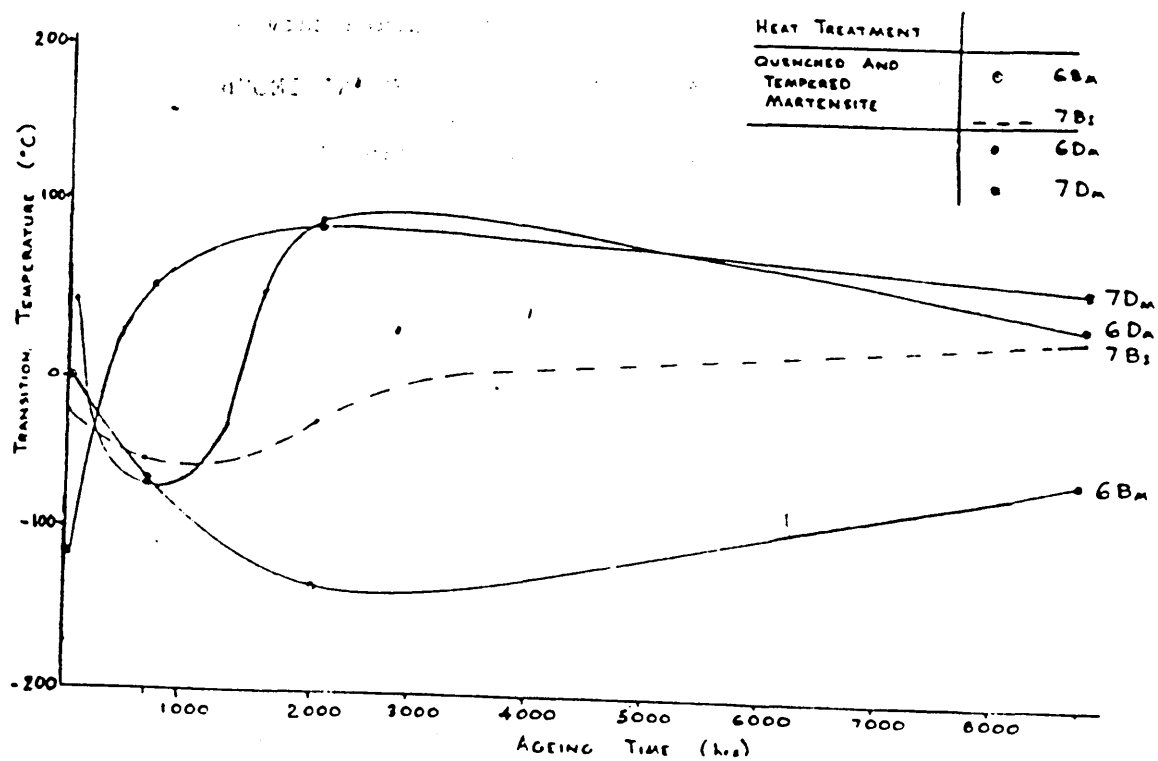
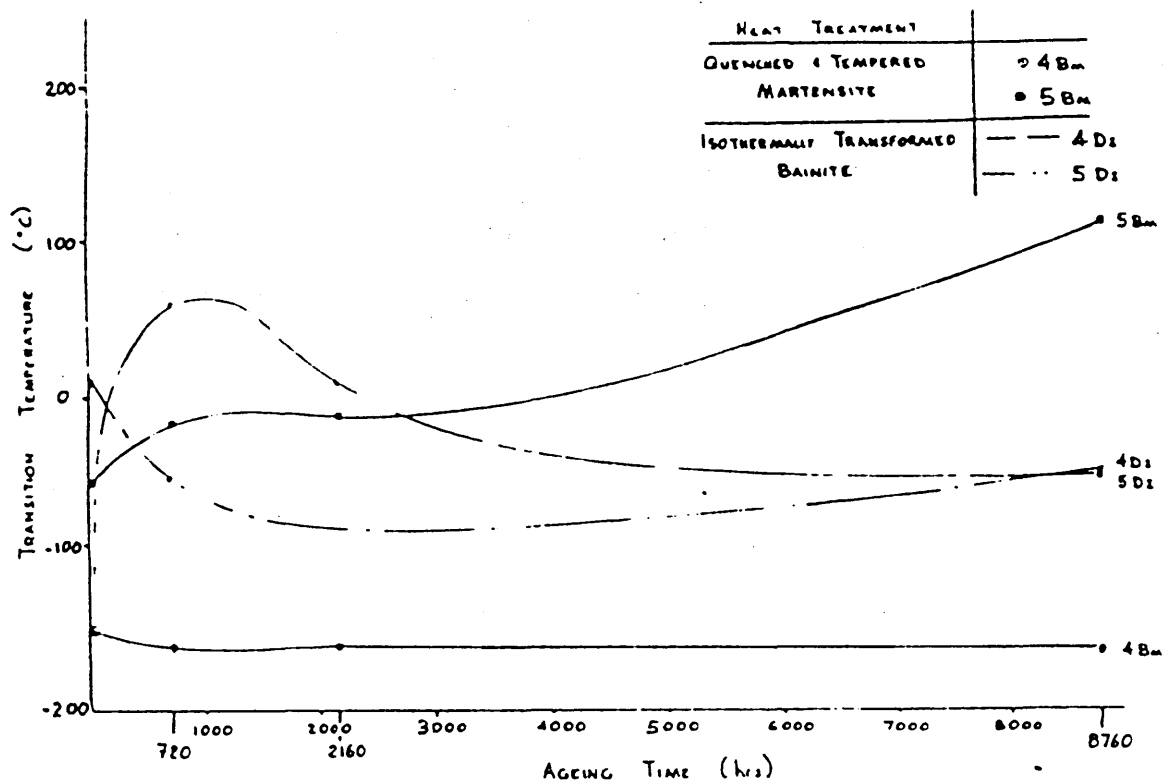


Fig. 150

Transition temperature curves for alloys
4(C 3Ni) and 5(C 3NiSb) for the quenched and
tempered martensitic and isothermally
transformed lower bainitic conditon.

Fig. 151

Transition temperature curves for alloys
6(C 3Ni 1Mo) and 7(C 3Ni 1MoSb) in the
quenched and tempered martensitic and
isothermally transformed lower bainitic
condition.



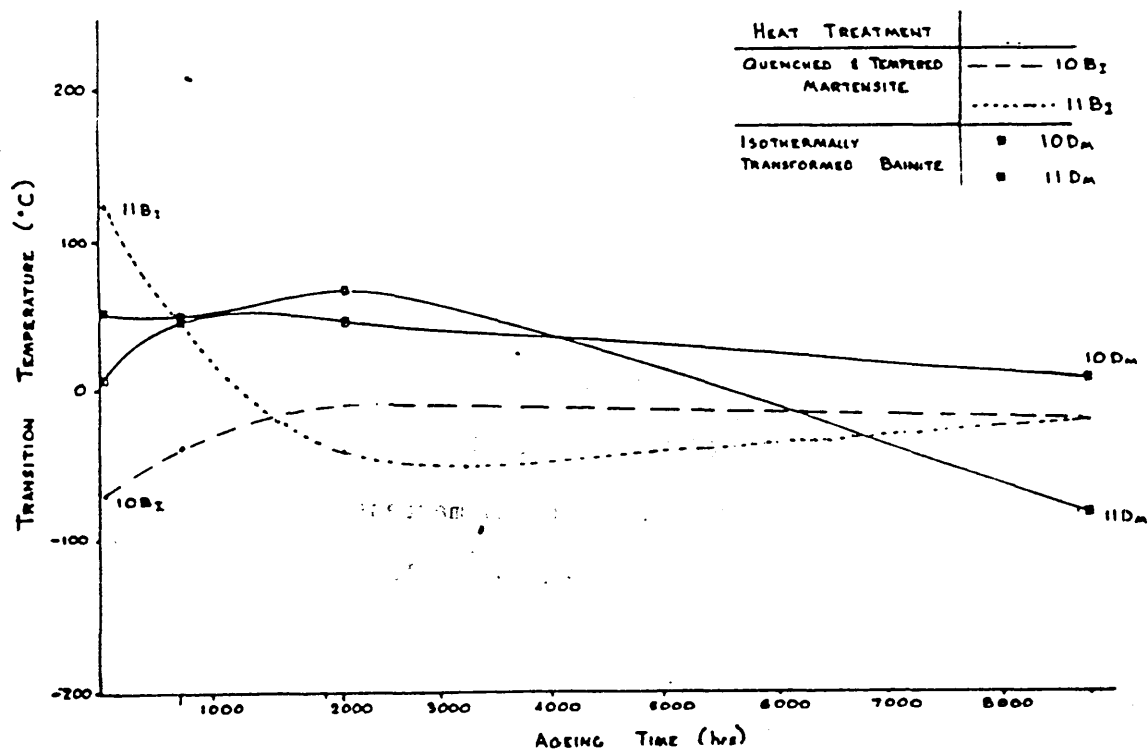


Fig. 152 Transition temperature curves for alloys
10(C 5Ni 1Mo) and 11(C 5Ni 1MoSb) in the
quenched and tempered martensitic and
isothermally transformed lower bainitic
condition.

Fig. 153

Impact energy versus temperature curves

(a) A 5% Ni steel quenched and tempered at
620°C for 2h

(b) A 9% Ni steel quenched and tempered at
520°C for 25h. After Norström and
Vingsbo(135).

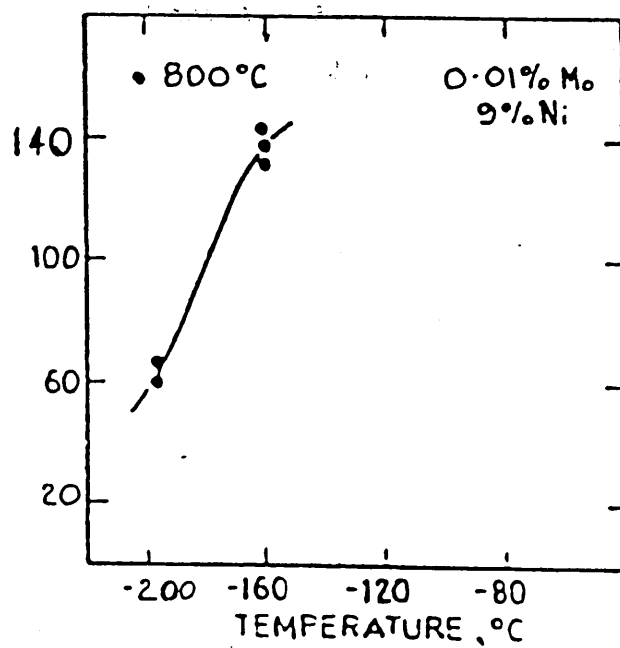
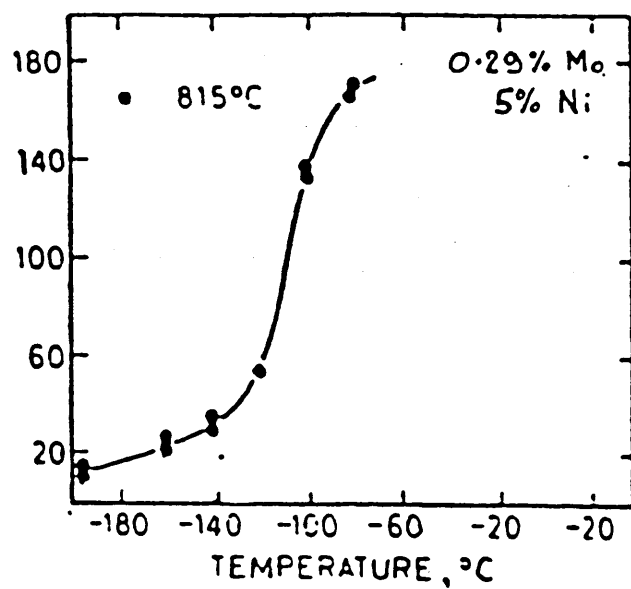


Fig. 154 Transition temperature curves for alloys
2(3Ni 1Cr), 1(3Ni 1CrSb) and 3(3Ni 1Cr 1MoSb)
in the isothermally transformed ferrite-
pearlite and upper bainitic condition.

Fig. 155 Transition temperature curves for alloys
2(3Ni 1Cr), 1(3Ni 1CrSb) and 3(3Ni 1Cr 1MoSb)
in the quenched and tempered martensitic and
isothermally transformed lower bainitic
condition.

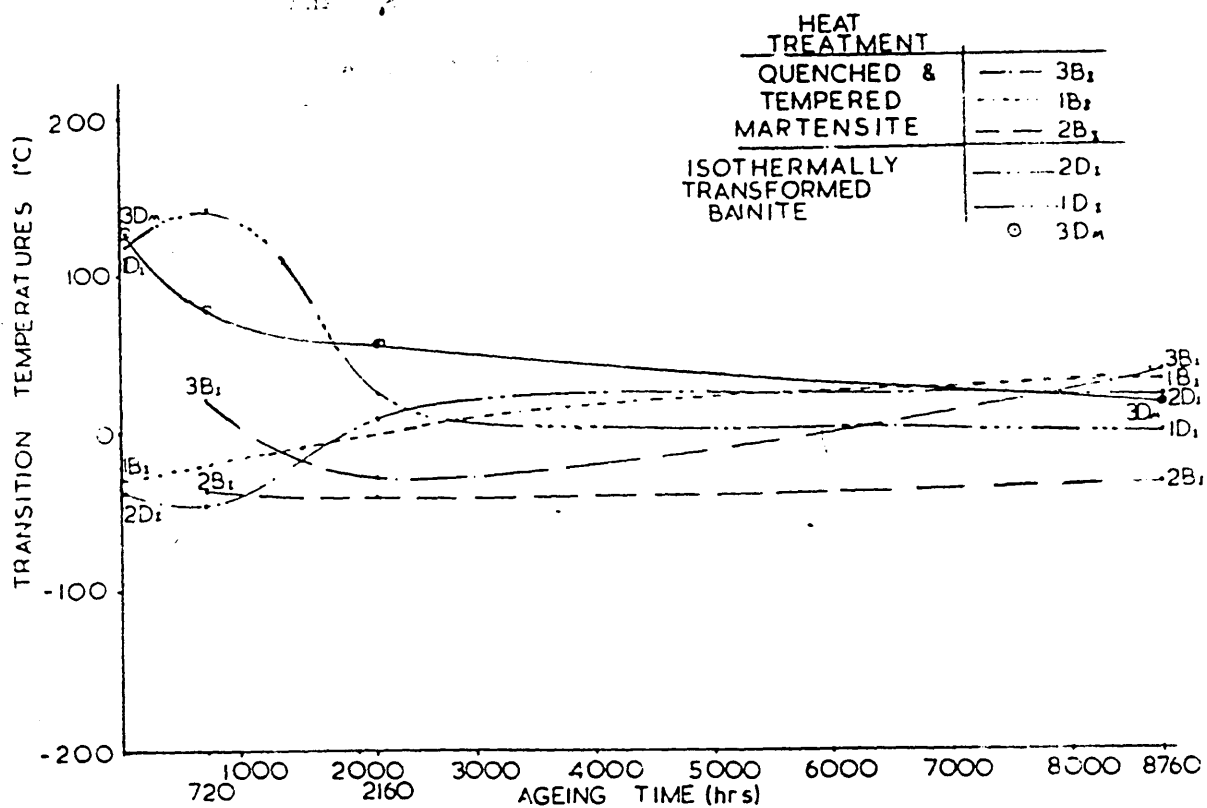
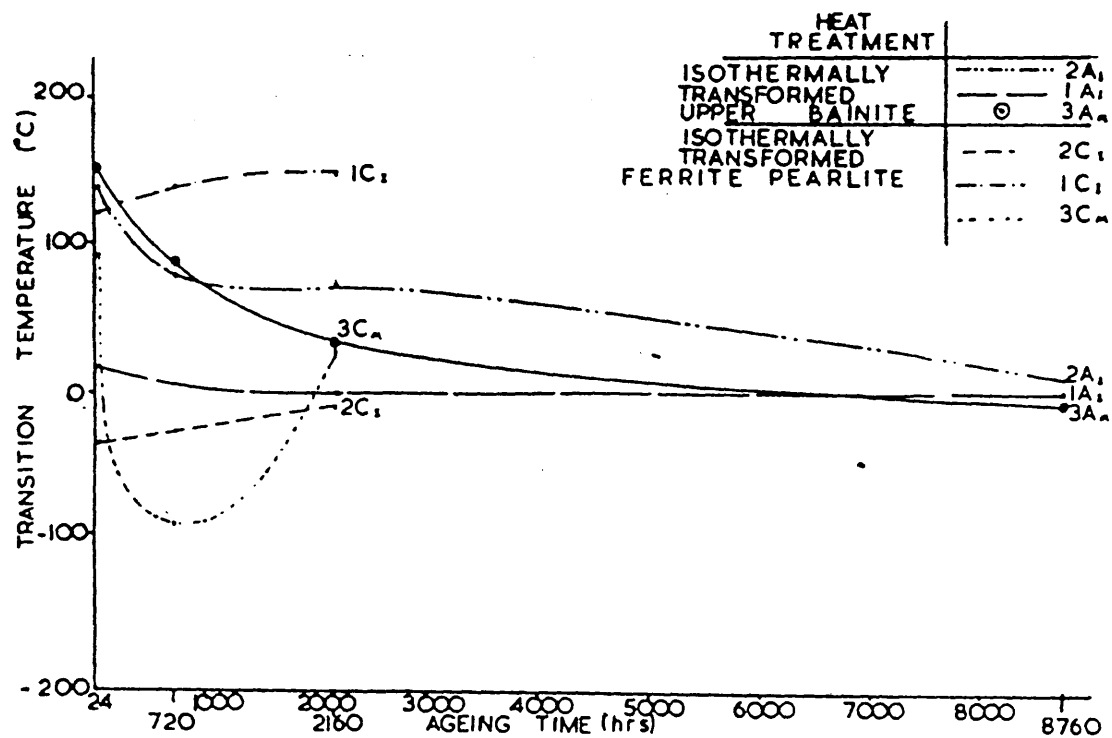


Fig. 156 Effect of P concentration on rate and amount
of P segregation to grain boundaries in Ni-Cr
steel with 0.4 mass% C.
After Mulford et al⁽⁷⁶⁾.

Fig. 157 Variations in transition temperature and
grain boundary concentrations according with
increasing ageing time for alloy 1 in the
isothermally transformed upper bainitic.

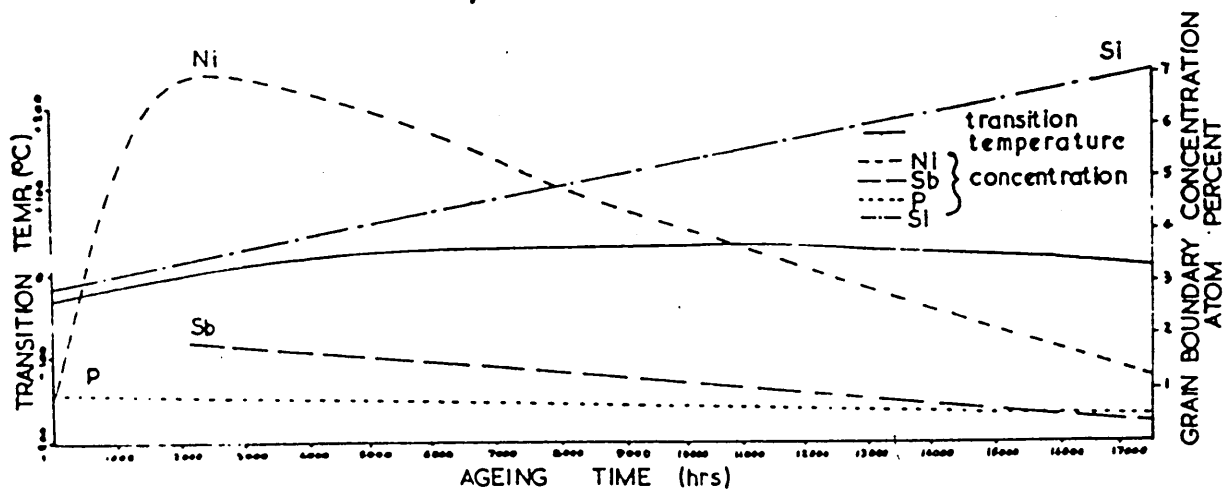
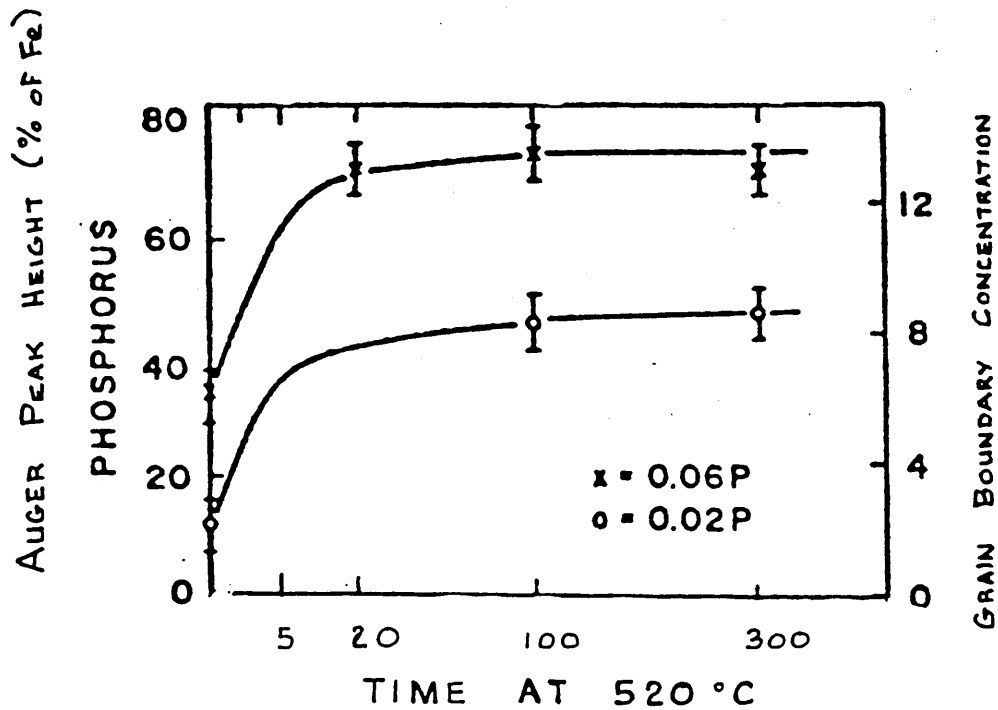


Fig. 158

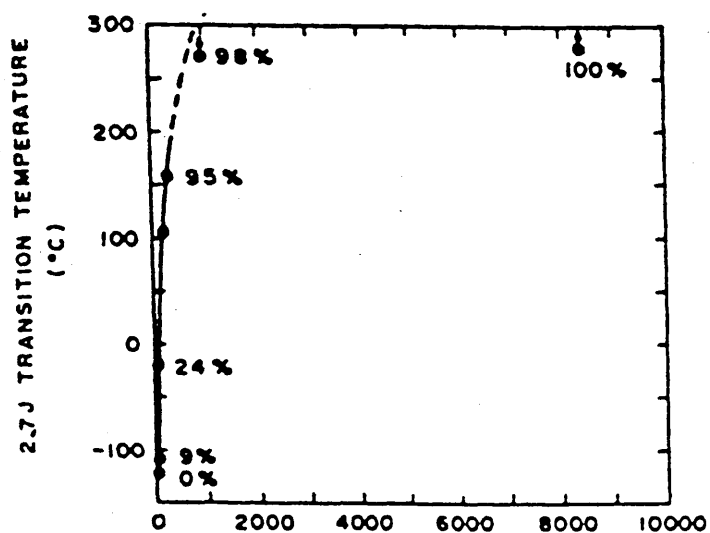
(a) Increase in transition temperature and percent intergranular fracture with time of ageing at 520°C.

(b) Corresponding increase in the grain boundary concentrations of Sb and Ni. After McMahon et al⁽⁹⁰⁾.

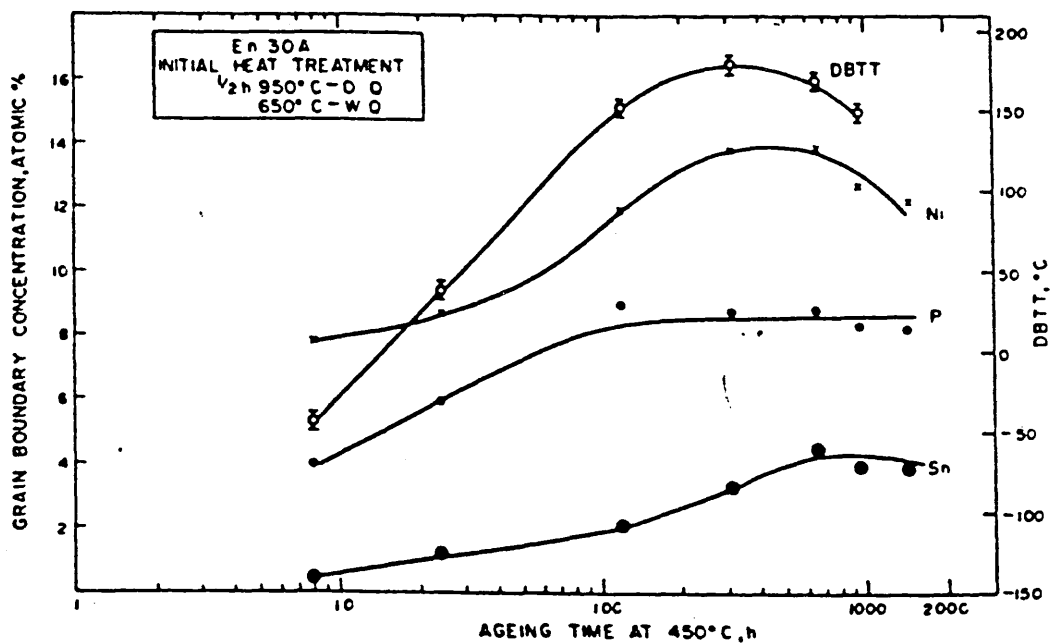
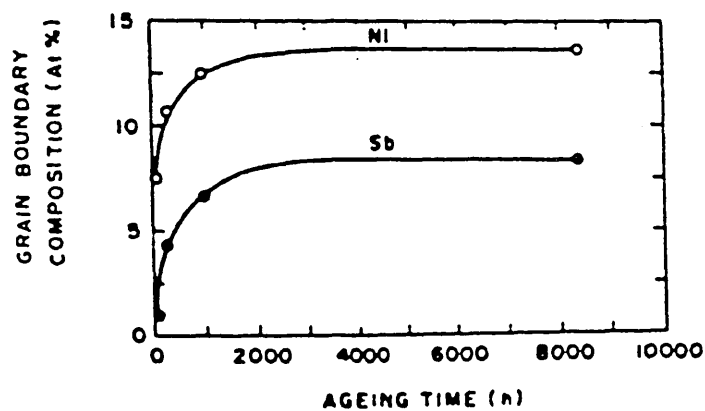
Fig. 159

Grain boundary composition as a function of ageing time at 450°C. After Edwards et al⁽¹⁶⁾.

(a)



(b)



Simultaneous Analysis of Fracture Surfaces by Auger and Energy Dispersive X-ray Mapping

A. Wirth, I. Andreoni and G. Gregory

Metals and Materials Engineering Department, Sheffield City Polytechnic, Pond Street, Sheffield S1 1WB, UK

The grain boundary segregation of the metalloid impurities antimony and phosphorus to the prior austenite grain boundaries of an Fe-3.5 Ni-1Cr alloy during embrittlement at 430°C has been studied by simultaneous Auger and energy dispersive x-ray analysis. The segregating species were found to be related to the tempering characteristics of the unembrittled microstructures. Initial intergranular embrittlement in a quenched and tempered martensite microstructure was associated with the presence of phosphorus whereas the initial embrittlement in a bainitic microstructure was associated with the segregation of antimony. The difference in behaviour between the two microstructures has been explained in terms of site competition at the grain boundaries. In the case of the tempered martensite microstructure the carbon activity is reduced as a consequence of the formation of chromium rich precipitates at the grain boundary. Carbon activity is reduced as a consequence of the formation of chromium rich precipitates at the grain boundary. The reduction in carbon activity allowed phosphorus migration to the boundary producing intergranular embrittlement. In bainites the predominant precipitate M_3C increased the carbon activity with a resultant decrease in phosphorus concentration the grain boundary and the absence of intergranular failure in the early stages of embrittlement. Prolonged embrittlement of the bainites produced a low energy intergranular failure. Increased nickel and antimony concentrations at the grain boundaries were associated with the formation of a fine grain boundary precipitate low in chromium. The increased carbon activity continued to prevent appreciable phosphorus segregation but was not sufficient to inhibit the cosegregation of nickel and antimony.

INTRODUCTION

Much attention has been focused in recent years on the understanding of the relationship between microstructure and grain boundary segregation characteristics in a wide range of steels which fail prematurely in an intergranular manner. Correlation of the information obtained from microstructural and surface analytical studies has often proved extremely difficult in the past mainly because of the problems of carrying out surface analysis in one electron optical system and then microstructural analysis of the fracture surface in a different electron optical system with the resultant repositioning problems that specimen transfer involved. Examining the composition and distribution of grain boundary precipitates by energy dispersive x-ray mapping techniques simultaneously with Auger mapping of the same region during depth profiling has provided the authors with valuable information which is helping towards further improving their understanding of the relationship between precipitate composition, grain boundary segregated species and intergranular fracture characteristics of both ferritic and austenitic steels.

The aim of this paper is to relate in more detail the relationship between segregating species and grain boundary precipitate composition in a low alloy steel susceptible to intergranular failure during tempering at 430°C.

EXPERIMENTAL PROCEDURE

The composition of the vacuum melted material studied in this investigation was Fe 3.56 at %Ni, 1.04 at %Cr, 0.36 at %C, 0.24 at %Mn, 0.10 at %Si, 0.06 at %Sb, 0.002 at %S, <10 ppm As, <10 ppm Sn.

Auger fracture specimens 30 mm in length and 5 mm in diameter and notched 15 mm from one end were manufactured from the remains of izod samples previously fractured at ambient temperature. The izod samples had been heat treated to produce either tempered martensite or bainite and then embrittled alongside each other for up to 2 years at 430°C.

Auger and energy dispersive x-ray analysis were carried out simultaneously on the freshly broken Auger samples in a VG Microlab 500 Simslab fitted with a Link Systems energy dispersive x-ray analysis system.

Auger spectra were obtained using 3–20 kV electrons and specimen currents of 5–20 nA. Auger and x-ray mapping used a 10–20 kV electron beam energy and 10 nA specimen current.

Auger maps were processed using the ratio $\frac{P-B}{B}$ to minimize the effects of topography on the results.

RESULTS AND DISCUSSION

Previous examination of low alloy steels susceptible to reversible temper embrittlement (RTE) has highlighted the different low energy fracture morphologies

observed in embrittled quenched and tempered martensites and bainites.^{1,2}

For example, embrittled, quenched and tempered martensite invariably fractures to produce a fracture morphology of intergranular, ductile intergranular or ductile dimpling. The amount of each type of morphology depending upon the temperature at which fracture occurs. Embrittled bainites on the other hand rarely contain intergranular or ductile intergranular modes of failure unless the alloy contains large amounts of metalloid impurity and has been embrittled for periods of time of the order of 1000 hours. Figures 2(a) and 3(a) show typical examples of the different fracture characteristics of embrittled bainites and tempered martensites.

Extensive transmission microscopical studies of the

different embrittled microstructures, reported elsewhere,³ showed significantly different prior austenite grain boundary precipitate types, distribution and morphologies. The authors suggested that changes in the precipitation sequence during the tempering of tempered martensite and bainite was responsible for a difference in the rate of diffusion of antimony to the tempered martensite and bainite prior austenite grain boundaries.

Clearly the presence of antimony after long tempering times would then promote the tendency to intergranular failure, hence the difference between the fracture morphologies of tempered martensites and bainites in the early stages of the embrittlement process. Similarly Erhart and Grabke⁴ showed recently that the grain boundary phosphorus concentration was

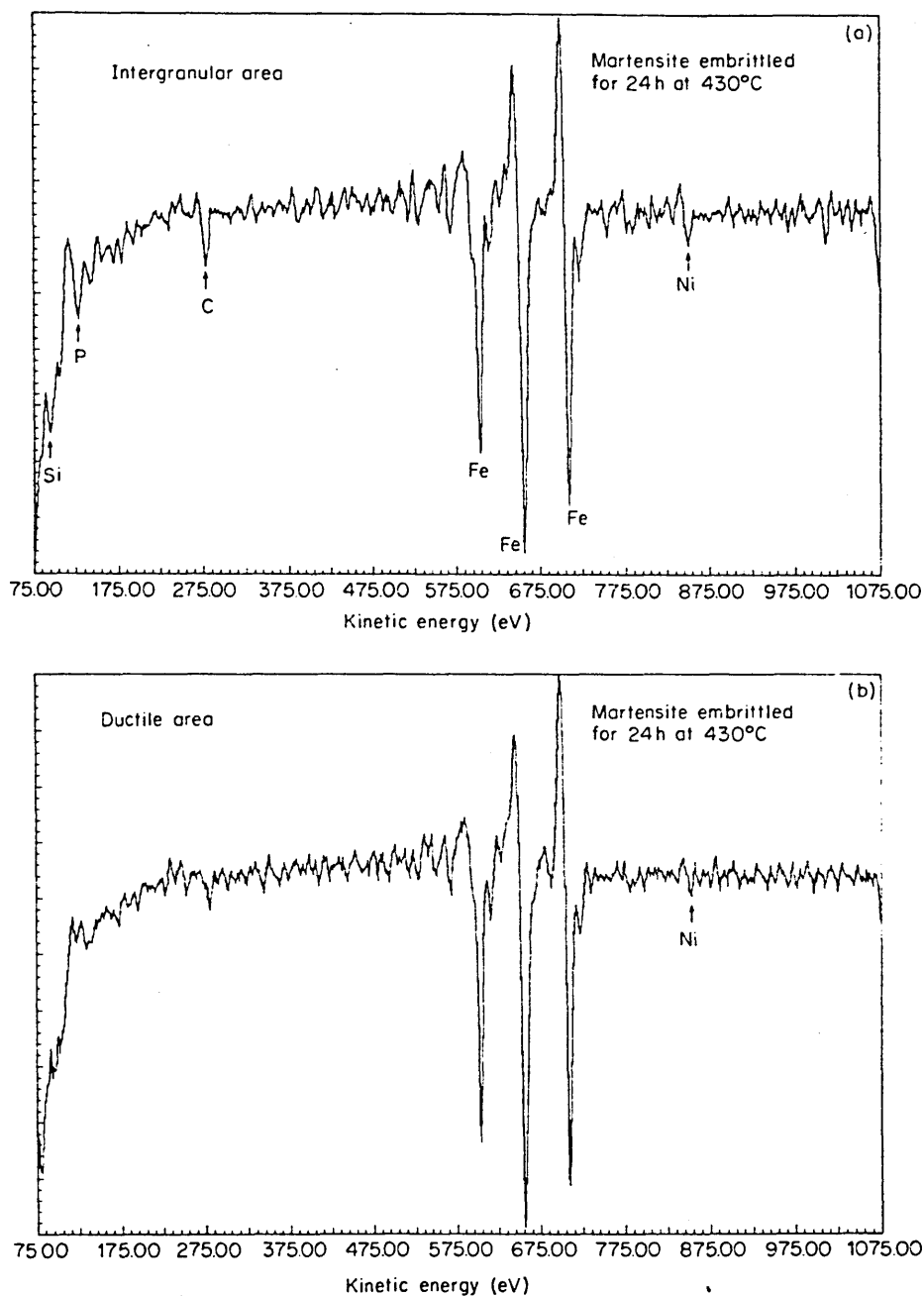


Figure 1. (a) Auger spectrum from intergranular area shown in Fig. 2(a); (b) Auger spectrum from ductile area shown in Fig. 2(a).

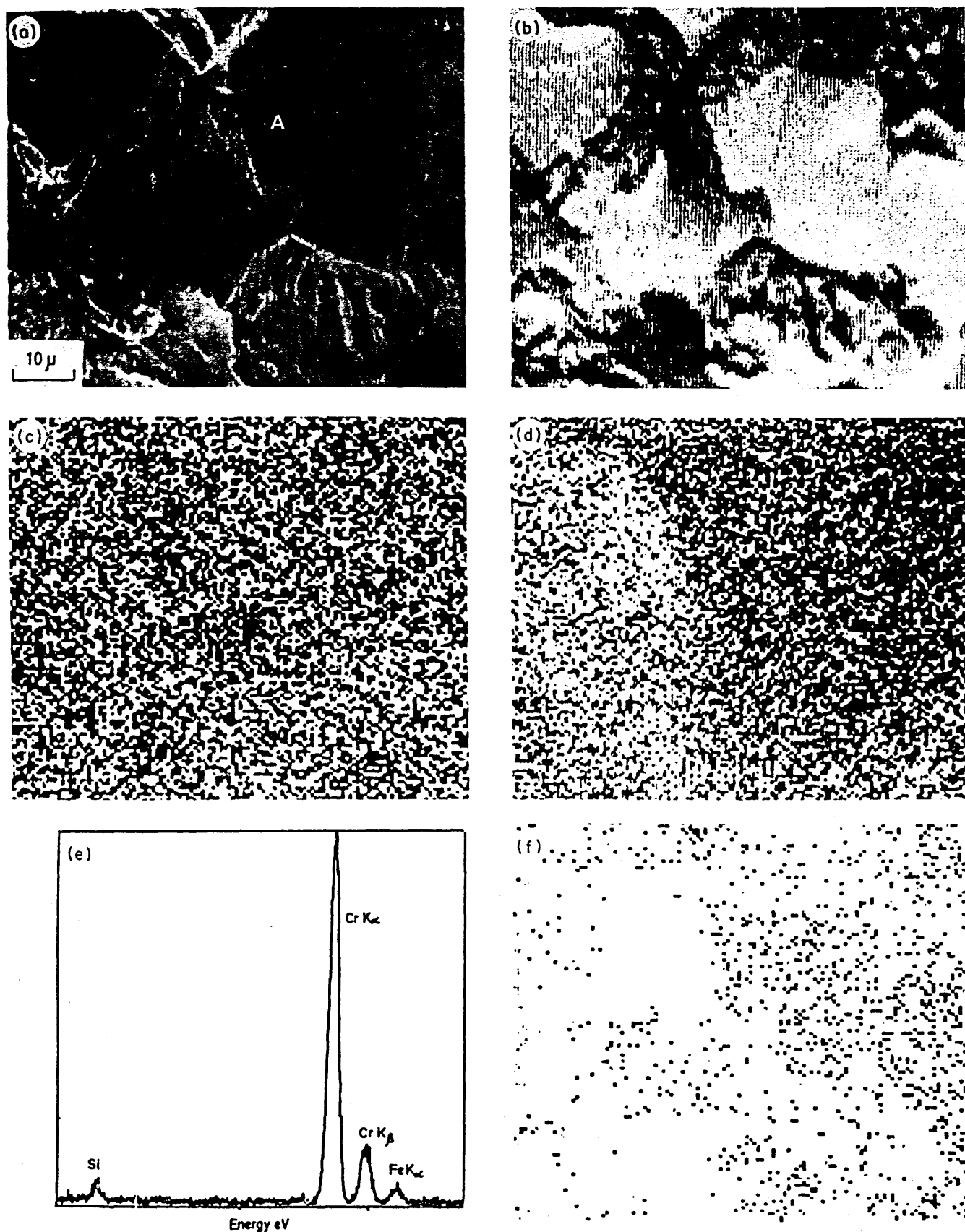


Figure 2. (a) Secondary electron image from fracture surface of embrittled martensitic material; (b) Auger map of background signal for area shown in Fig. 2(a); (c) Auger map showing nickel distribution on fracture surface shown in Fig. 2(a); (d) Auger map showing phosphorus distribution on fracture surface shown in Fig. 2(a); (e) energy dispersive x-ray analysis of particle A on intergranular fracture surface shown in Fig. 2(a); (f) Cr K x-ray map for area shown in Fig. 2(a).

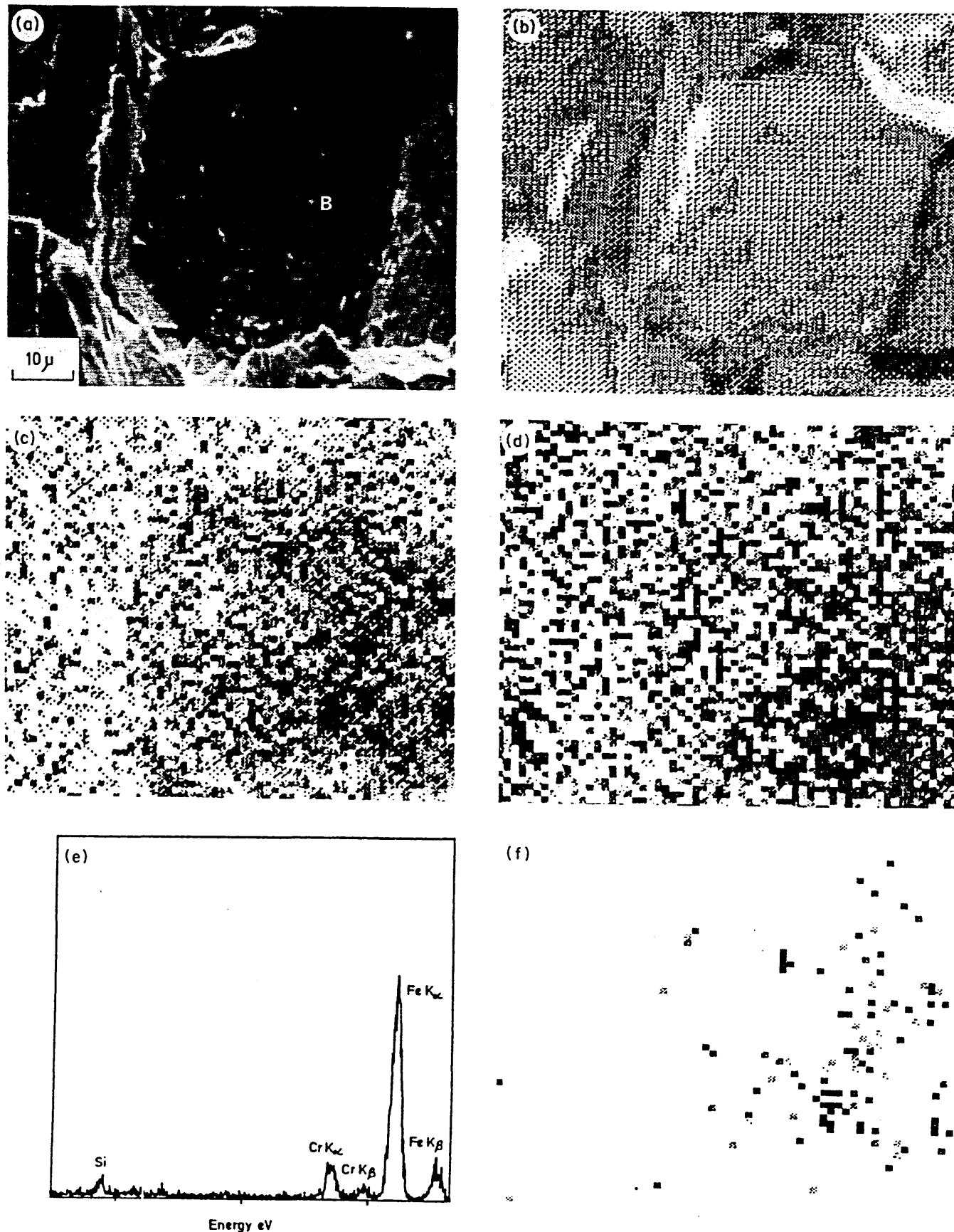


Figure 3. (a) Secondary electron image from fracture surface of embrittled bainitic material; (b) Auger map of background signal for area shown in Fig. 3(a); (c) Auger map showing nickel distribution on fracture surface shown in Fig. 3(a); (d) Auger map showing antimony distribution on fracture surface shown in Fig. 3(a); (e) energy dispersive x-ray analysis of particle on intergranular surface shown in Fig. 3(a); (f) Cr K x-ray map for area shown in Fig. 3(a).

dependent upon the carbide type present at the grain boundary. They reported that competition between carbon and phosphorus for grain boundary sites was related to the bulk concentration of free carbon. Using this argument Erhart and Grabke concluded that a strong carbide former, chromium reduces the carbon activity at grain boundaries in an Fe-C-P alloy allowing increased phosphorus segregations and intergranular failure. Conversely alloying elements e.g. nickel which increase the carbon activity ought to reduce grain boundary phosphorus segregation although they had no evidence available when going to press to confirm their view.

Examination of the Auger spectra shown in Fig. 1(a) and 1(b) from the intergranular and ductile areas shown in Fig. 2(a) indicates that interpretation becomes more complex when both chromium and nickel are present because the phosphorus and carbon concentrations are significantly higher on the intergranular facets compared with the ductile dimple region. Furthermore, examination of the nickel and phosphorus Auger maps Fig. 2(c) and 2(d) suggests that the distribution of phosphorus is not significantly related to the distribution of nickel even though the nickel concentration in the intergranular spectrum is approximately twice the value in the ductile spectrum (compare Fig. 1(a) and 1(b)). What may be of greater significance, and in agreement with the results of Erhart and Grabke is that the chromium rich carbides are concentrated in the same area where the phosphorus concentration is greatest (compare Fig. 2(d) and 2(f)).

In the case of embrittled bainites the situation becomes even more complex when the low energy fracture changes to the intergranular type because the antimony metalloid impurity rather than phosphorus is associated with an increase in the nickel concentration on the intergranular facets compared with the cleavage region (see Fig. 3). The predominant precipitate associated with the intergranular facets contains much less chromium (see Fig. 3(e)) than the precipitate observed at the grain boundaries in the quenched and tempered material although the Auger peak height ratio $P_{\text{C}}/P_{\text{Fe}}$ is similar for both bainite and tempered martensite intergranular facets.

It could be argued that the bainitic grain boundary precipitate which is low in chromium acts in a similar manner to Fe_3C in Fe-C-P alloy⁴ in as much as the high

carbon activity prevented the phosphorus migrating to the bainitic prior austenite grain boundaries during the early stages of tempering at 430°C. Antimony on the other hand because of its ability to form nickel-antimony precipitates and has a bulk concentration in the alloy of some thirty times greater than the phosphorus content may explain why antimony segregates to the bainitic prior austenite grain boundaries to promote intergranular failure after extensive tempering. It should also be remembered that the relatively clean prior austenite boundaries observed after short embrittling times contain M_3C precipitates after long tempering times,³ although there is no reason to suppose the carbon activity will have changed significantly with the precipitation of the M_3C at the grain boundaries. Consequently embrittled bainites will always fail with a low energy cleavage mode in the early stages of tempering because the prior austenite grain boundaries are relatively free from precipitates and segregated impurities and the interface between the large matrix M_3C and the ferrite is a more probable area for inducing failure by cleavage.

Clearly there is a need for a great deal of further careful work to be carried out in order to resolve the factors relating grain boundary precipitate composition with the amount and composition of embrittling grain boundary species if intergranular embrittlement is to be understood in multiphase systems.

CONCLUSIONS

Simultaneous Auger and x-ray mapping of fracture surfaces produced *in situ* showed that the segregated species responsible for intergranular embrittlement in an Fe-3½%Ni-1 at%Cr steel tempered at 430°C was related to the precipitate composition at the prior austenite grain boundaries. Increasing the chromium content of the grain boundary precipitate resulted in a decrease in grain boundary phosphorus concentration and an increase in the antimony concentration.

Acknowledgement

One of us, I. Andreoni would like to thank CNPQ-MIC-STI (Brazil) for their continued support.

REFERENCES

1. A. Wirth and B. Clarke, *Advances in Physical Metallurgy and Applications of Steels*, University of Liverpool, September 1981.
2. R. Viswanathan and R. Joshi, *Met. Trans.* **6A**, 2289-2296 (1975).
3. A. Wirth, I. Andreoni and J. Titchmarsh, *Inst. Phys. Conf. Ser. No. 68*, 297-300 (1983).
4. H. Erhart and H.J. Grabke, *Met. Sci.* **15**, 401-408 (1981).